

STAVEBNÍ OBZOR

ČÍSLO 3/2018

Obsah čísla:

NON-DESTRUCTIVE TESTING AND X-RAY DIFFRACTION ANALYSIS OF HIGH-TEMPERATURE DEGRADED CONCRETE

Richard Dvořák, Zdeněk Chobola

BOND PERFORMANCE OF DEFORMED REBAR IN STEEL FIBER REINFORCED LIGHTWEIGHT-AGGREGATE CONCRETE AFFECTED BY MULTI-FACTORS

Mingshuang Zhao, Xiaoyan Zhang, Kai Yan, Teng Fei, Shunbo Zhao

TEMPERATURE ANALYSIS OF HIGH LATITUDES AND LOW ALTITUDE ISLAND PERMAFROST DURING THE CONSTRUCTION OF CFG PILE

Liu Jin-liang, Jia Yan-min

THE EFFECT OF PORE DISTRIBUTION IN HISTORIC MASONRY ON THE GROUTING METHOD AND GROUTING MIX SELECTION

Jiří Witzany, Radek Zigler, Klára Kroftová, Tomáš Čejka, Jan Kubát, Milan Holický, Jiří Karas

STUDY ON THE SEISMIC PERFORMANCE OF RECYCLED AGGREGATE CONCRETE-FILLED LIGHTWEIGHT STEEL TUBE FRAME WITH DIFFERENT ASSEMBLY JOINTS

Liu Wenchao , Cao Wanlin , Qiao Qiyun , Ren Lele , Wang Ruwei

STUDY ON THE EFFECT OF THREE KINDS OF FILTER AID ON THE DEHYDRATION PERFORMANCE OF MICROCYSTIS AERUGINOSA

Yang Zong-zheng, Zhang Meng-yao, Cao Jing-guo, Liu Honglei, Han Chao-xi, Tian Xin

THE EFFECT OF GAMMA-RAY IRRADIATION ON MECHANICAL PROPERTIES OF EARLY-AGE CEMENT MORTAR

Yuliia Khmurovska, Petr Štemberk, Svyatoslav Sikorin, Yuliya Kaladkevich, Eryk Pavalanski, Viktor Fatseyeu

STUDY ON A NEW DESIGN OF GROUTING PUMP FOR MANAGING WATER INRUSH IN KARST TUNNELS

Li Shucai, Li Mengtian, Zhang Xiao, Zhang Qingsong

EVALUATION OF FLEXURAL CAPACITY AND DUCTILITY ON HIGH-STRENGTH CONCRETE BEAMS REINFORCED WITH FRP REBAR AND STEEL FIBER

Jinzhong Li

PARALOID B72 NANODISPERSION PREPARATION TECHNOLOGY AND ITS POSSIBILITIES FOR USE IN THE MONUMENT CARE

David Škoda, Renata Pučalíková, Ivo Kuřitka, Klára Kroftová

RANKING OF MAJOR HAZARDS SUITABLE FOR THE GOVERNMENT SUPERVISION

Hao Yu , Sun Chaolun

RELIABILITY EVALUATION IN CONSTRUCTION QUALITY BASED ON COMPLEX VAGUE SOFT EXPERT SET METHOD

Xiaoping Bai, Hongyue Zhao

HISTORICAL ORTHOPHOTOS CREATED ON BASE OF SINGLE PHOTOS - SPECIFICS OF PROCESSING

Jindřich Hodač, Anna Zemánková

THE EFFECT OF AXIAL COMPRESSION RATIO ON SEISMIC BEHAVIOR OF INFILLED REINFORCED CONCRETE FRAMES WITH PROFILED STEEL SHEET BRACING

Feng Ningning, Wu Changsheng, Ma Junyue, Mao Xiaotian

IN-SERVICE CONDITION ASSESSMENT OF LONG-SPAN BRIDGES BASED ON TRAFFIC LOAD EFFECTS USING MONITORING DATA

Rui-feng Nie, Yi-jie Huang, Song-hui Li

OPTIMIZATION OF RECLAIMED ASPHALT AND FT PARAFFIN FOR PERMANENT DEFORMATION AND MOISTURE DAMAGE OF ASPHALT MIXES

Fazal Haq, Arshad Hussain, Muhammad Bilal Khurshid

NON-DESTRUCTIVE TESTING AND X-RAY DIFFRACTION ANALYSIS OF HIGH-TEMPERATURE DEGRADED CONCRETE

Richard Dvořák, Zdeněk Chobola

Brno University of Technology, Faculty of Civil Engineering, Institute of Physics, Brno, Veveří 331/95, Czech Republic; dvorak.r1@vutbr.cz, chobola.z@fce.vutbr.cz

ABSTRACT

In the field of civil engineering a diagnostics acoustic non-destructive testing is widely used and in the past years it was used even in testing of high-temperature degraded concrete structures. These methods can provide specific information about the physical-mechanical state of material; however physical-chemical changes in microstructure are measurable to a limited extent. This article is focused on non-destructive and destructive testing of high-temperature degraded concrete test beams of dimensions $0.1 \times 0.1 \times 0.4$ m fired at $200 - 1200$ °C. The Impact-Echo method and ultrasonic velocity pulse method measurements are compared with destructive test results. Testing of measured changes in the p-m properties of reference and fired samples is then supplemented by X-ray diffraction analysis, in order to document mineralogical physical-chemical changes of tested material.

KEYWORDS

Impact-Echo method, Concrete, Coarse aggregate, High-temperature degradation, Non-destructive testing, X-ray diffraction analysis

INTRODUCTION

The presented paper investigates the potential application of non-destructive acoustic methods of testing as a diagnostic tool, used in the retrofitting process of thermally degraded concrete structures. Due to its composition, plain concrete has good fire-resistant properties, it does not produce smoke in elevated temperature, it is non-flammable and non-combustible. Its specific heat capacity is approximately $1020 \text{ J}\cdot\text{kg}^{-1}\cdot\text{K}^{-1}$ and coefficient of thermal conductivity is $1.0 - 1.5 \text{ W}\cdot\text{m}^{-1}\cdot\text{k}^{-1}$ and thus behaves as a fine thermal insulant in case of fire [1]. Concrete is heterogeneous composite and each of the compounds, like aggregate and cement matrix, react differently to high temperature [2]. We can observe these changes by non-destructive testing. It is synergic effect of physical-mechanical and physical-chemical changes, affecting both macrostructure and microstructure. The aim of this paper is to compare the results of non-destructive testing with changes in mineralogical composition of high temperature degraded concrete.

METHODOLOGY

A total of 63 test specimens of diameter $0.1 \times 0.1 \times 0.4$ m were manufactured and divided into 7 temperature sets. First reference set was kept at temperature of 20 °C and the remaining 6 sets were divided in multiples from 200 °C 1200 °C. The composition of each mixture used in the investigation can be seen in Table 1. All tests specimens were kept in water container for 28 days.

Then each test specimen was pre-dried in laboratory dryer oven at 110 °C for 72 hours before being fired in a furnace. The length time used for pre-drying was chosen according to initial measurements of designed mixture, whereby the weight was monitored during drying until samples achieved a maintained weight. By this step we got rid of residual free water and prevented possible explosive spalling for sets degraded by 400 °C and higher [3]. The furnace temperature was set to rise at a rate of 5 °C/min and upon reaching maximum temperature for each set was maintained for 1 hour. Afterwards the specimens were cooled by atmospheric air to room temperature, inside the furnace.

*Tab. 1 - Mixture design**

| Compounds | Amount of each compound for 1 m ³ [kg] |
|---------------------------------------|---|
| Cement CEM I 42.5 R | 345 |
| Fine aggregate Žabčice 0/4 mm | 896 |
| Coarse aggregate Olbramovice 8/16 mm | 521 |
| Coarse aggregate Olbramovice 11/22 mm | 391 |
| Superplastizer Sica Viscocrete 2030 | 2.5 |
| Mix water | 173 |

*Compressive strength after 28 days at 20 °C was 75.1 MPa

For non-destructive testing, both, Impact-Echo (IE) and ultrasonic pulse velocity method (US) were used. IE method is based on the excitation of low-frequency mechanical waves created within the test specimen upon mechanical impact. The test specimens begin to vibrate as the mechanical waves are reflected and refracted within their structure; these vibrations are then recorded using a suitable receiver [4].

The signal recorded in the time domain is then converted using the Fast Fourier transform [5] to the frequency spectrum, which can be easily analysed (Figure 1 and Figure 2).

Measurement by Impact-Echo was conducted as test specimens were placed on rubber pads and struck by a spherical hammer of total mass 25.5 g. The produced vibrations were recorded by a piezoelectric sensor MIDI 446s12. A digital oscilloscope Handyscope HS3 with sampling speed set at 0.2 MHz was used for signal processing.

Ultrasonic pulse velocity method is based on measuring time needed for and US pulse to travel through tested material. The presence of defects, cracks and inhomogeneity alter the ultrasonic signal, which then refracts and thus travels by longer path. Using this investigation, we can evaluate different types of degradation and localize defects within the tested structure. With knowledge of acoustic velocity in the tested medium, as well as density, and diameters of tested specimen, we can compute a dynamic modulus of elasticity [6]. For US measurement an Ultrasonic Pulse Analyser 58-E4900 was used.

By using these methods, we can evaluate the physical-mechanical state of structure, however these changes originate from changes of mineralogical composition and thus the non-destructive measuring is supplement by X-ray diffraction analysis. This method is based on subjecting the specimen to X-rays, which is reflected from each crystalline surface. According to Braag's equation, at the point of maximum reflection of X-rays, a peak is formed in the diffractogram [7]. Each peak is then identified using mineralogical libraries. Specimens for this

analysis were taken from the ends of test beams. The samples of aggregate and cement matrix were grinded to a fraction below the 0.063 mm. X-ray diffraction analysis was conducted at AdMaS centre in Brno.

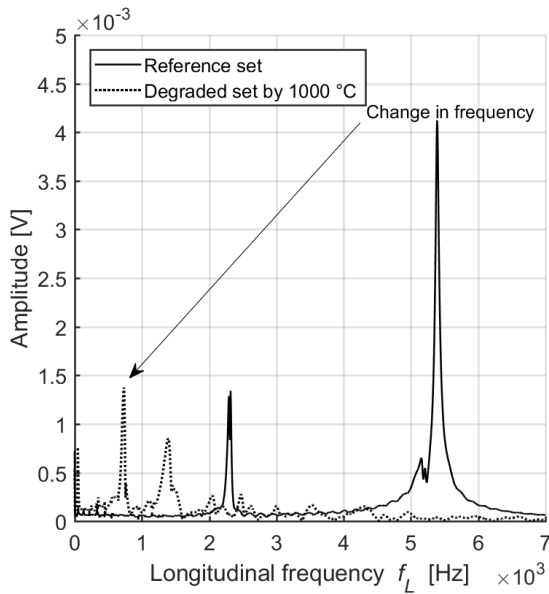


Fig. 1 – Change of dominant frequency for reference test specimen and test specimen degraded at 1200 °C.

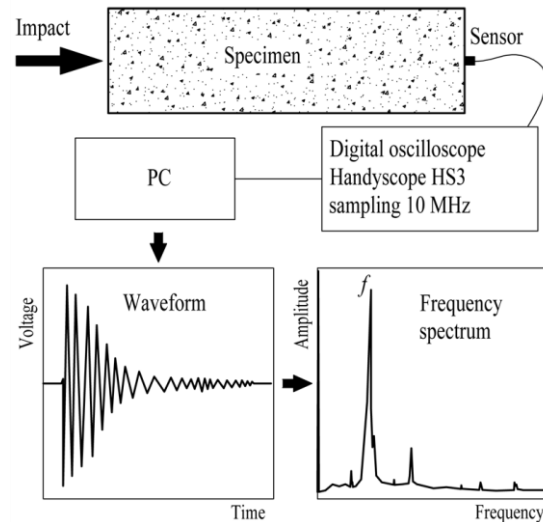


Fig. 2 – Testing setup of Impact-echo measurement.

RESULTS

The fresh concrete prepared for manufacturing of test specimens had slump test result of S4 (60 – 70 mm) and did not show any signs of bleeding or segregation of coarse aggregate. The fresh concrete was completely compacted via a vibration table in 14 s on average. Density of concrete in its hardened state was 2380 kg·m⁻³. The measured change in density between non-degraded and thermally degraded state is shown in Figure 3.

The largest drop in density 11 % was observed in the temperature set of 1200 °C. The main cause of density loss is dehydration of free and chemically bounded water in aggregate and cement compounds. This smallest decrease can be observed in temperature range from 20 to 400 °C. Moreover, a decay of portlandite at 480 – 560 °C and decay of coarse and fine carbonates (CaCO₃ → CaO + CO₂) at temperature 930 – 960 °C also accompany the loss of density [8]. From temperature 600 °C up to 1000 °C a linear trend of loss in density is observed. After the 1200 °C a steep change occurs caused by degradation of aggregate minerals and formation of ceramic bonds between melted compounds.

In terms of macroscopic changes, the thermally degraded specimens change in colour from cement grey to ochre shade of brown colour with the presence of cracks. Sets degraded at 200 °C did not show any signs of cracking, however at 400 °C, the first signs of cracking appeared. At 1000 °C the concrete became brittle and fragile to mechanic manipulation. Whole scales of dried, shrunk and cracked cement matrix were falling off, in this state the diameter of cracks reached nearly 4 mm and covered the whole body of test specimens. At 1200 °C the test specimens changed colour to brown and were recompacted by forming the ceramic bonds between the aggregate and cement matrix. The test specimens bend due to effect of transient creep [9], with total difference of middle section to edges by 2 – 5 mm.

These mechanical changes can be observed through dynamic modulus of elasticity. It is seen in Figure 4. The reference sets reached modulus of 44 GPa. From this point the designed mixture showed a decrease in measured dynamic modulus of elasticity for higher degradation temperatures. The first significant decrease in dynamic modulus of elasticity occurred between 400 and 600 °C, from 29 GPa to 14 GPa.

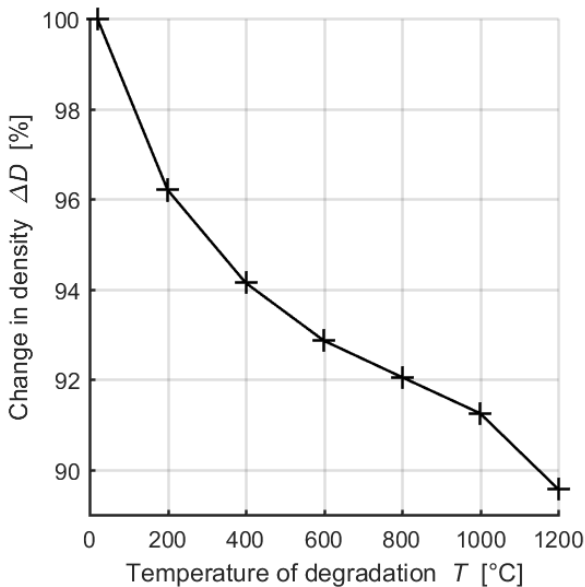


Fig. 3 – Loss in density of thermally degraded temperature sets.

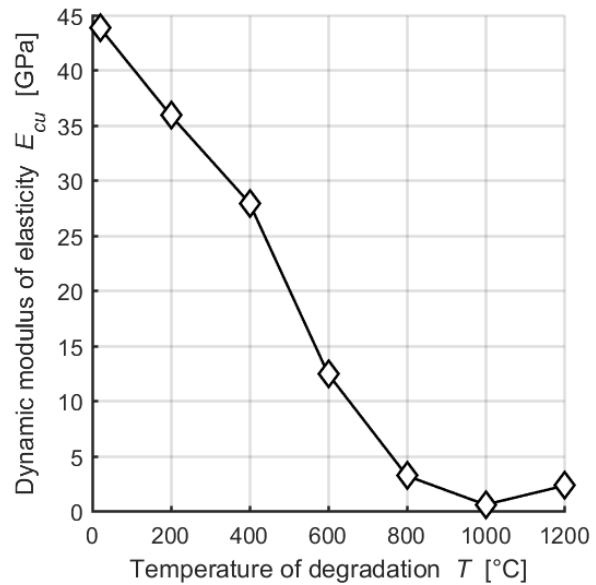


Fig. 4 – Measurement of dynamic modulus of elasticity.

From 600 °C the decrease tendency is similar and lowest measured value is 1 GPa for 1000 °C temperature set. At this temperature the test specimens had the lowest measured physical-mechanical properties.

Slightly similar results can be observed in Impact-Echo measurement shown in Figure 5. The reference sets had a resonance frequency of 5.37 kHz longitudinally and 2.30kHz transversely for the first resonance and 8.37 kHz for the second resonance frequency. The decrease in frequency was similar to change in dynamic modulus of elasticity.

The lowest frequencies were measured at 1000 °C with longitudinal frequency of 0.63 kHz and a transverse frequency of 0.32 kHz and 1.23 kHz.

Both US and IE method have confirmed the changes in physical-mechanical properties with the same trend of measured values. When we compare these results with different studies of this topic [10] the presented measured values correspond with other publications. Impact-Echo measurements have shown the ability to determine the extent of high-temperature damage.

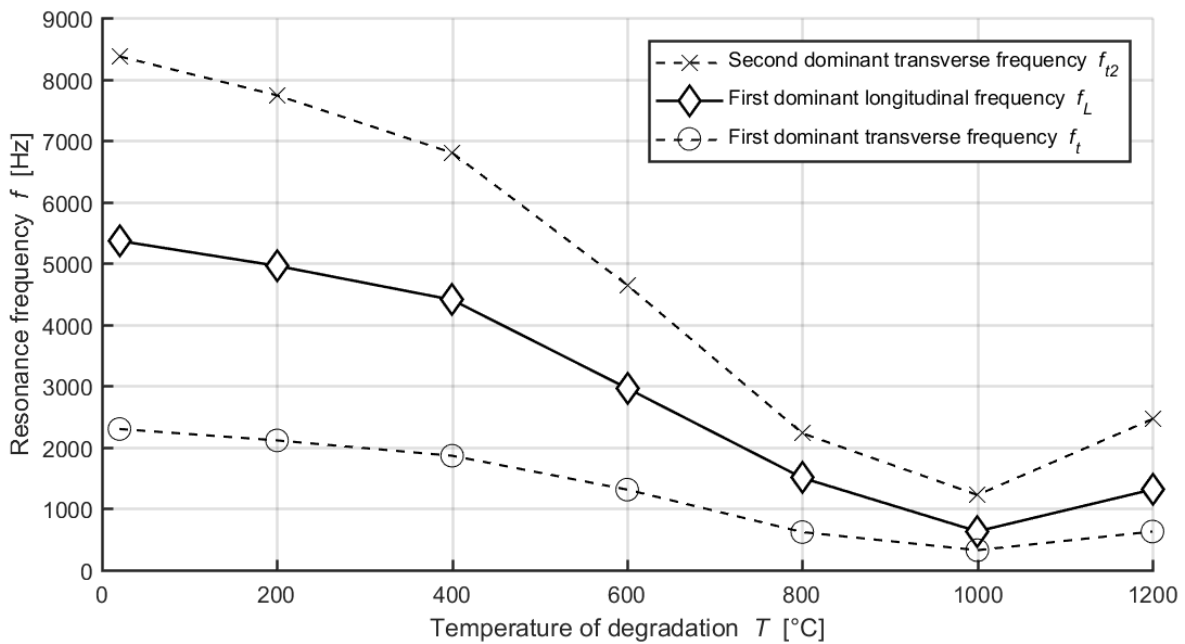


Fig. 5 – Average resonance frequencies of each temperature sets.

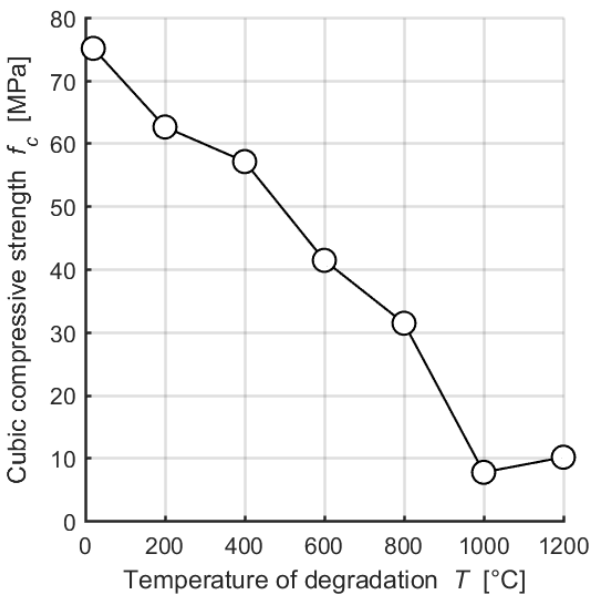


Fig. 6 – Cubic compressive strength of thermally degraded sets.

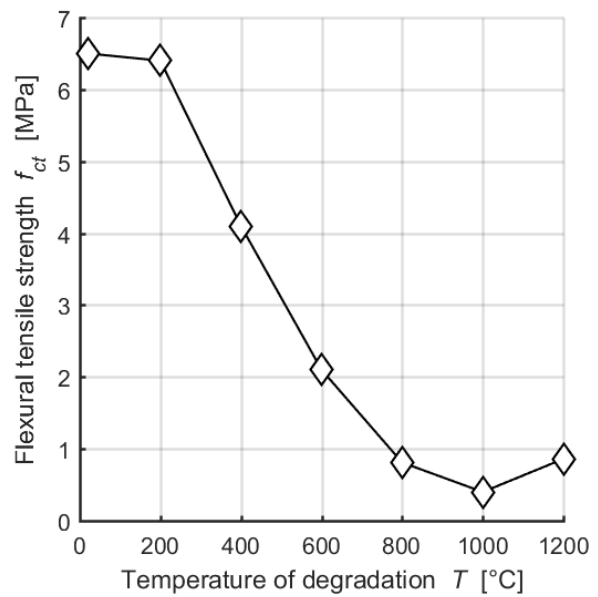


Fig. 7 – Flexural tensile strength of thermally degraded sets.

The same results can be seen in destructive tests shown in Figure 6 and Figure 7. According to destructive tests, test specimens degraded at 1200 °C had higher tensile strength than temperature sets 800 °C and 1000 °C. It seems that the tensile strength of tested material is more affected by temperature degradation than compressive strength.

Table 1 - Correlation coefficients for each measured parameter of tested material.

| | D | f_L | f_{t2} | f_{t1} | E_{cu} | f_c | f_{ct} |
|------------------------------------|--------|---------------|---------------|---------------|---------------|--------|----------|
| Density D | 1 | 0.8891 | 0.8858 | 0.8891 | 0.9415 | 0.9239 | 0.9168 |
| Longitudinal f_L | 0.8891 | 1 | 0.9985 | 0.9993 | 0.9806 | 0.9732 | 0.9707 |
| Transverse f_{t2} | 0.8858 | 0.9985 | 1 | 0.9995 | 0.9828 | 0.9612 | 0.9746 |
| Transverse f_{t1} | 0.8891 | 0.9993 | 0.9995 | 1 | 0.9809 | 0.9666 | 0.9714 |
| Dynamic modulus E_{cu} | 0.9415 | 0.9806 | 0.9828 | 0.9809 | 1 | 0.9532 | 0.9899 |
| Cubic compressive strength f_c | 0.9239 | 0.9732 | 0.9612 | 0.9666 | 0.9532 | 1 | 0.9313 |
| Flexural tensile strength f_{ct} | 0.9168 | 0.9707 | 0.9746 | 0.9714 | 0.9899 | 0.9319 | 1 |

After the non-destructive and destructive parameters were measured a table of correlation coefficients was created with results in Table 2. Apart from high values of correlation coefficients between measured frequencies we can distinguish high correlation between destructive and non-destructive tests where correlation coefficients reached values from 0.95 up to 0.97 for compressive strength and 0.97 up to 0.98 for tensile strength.

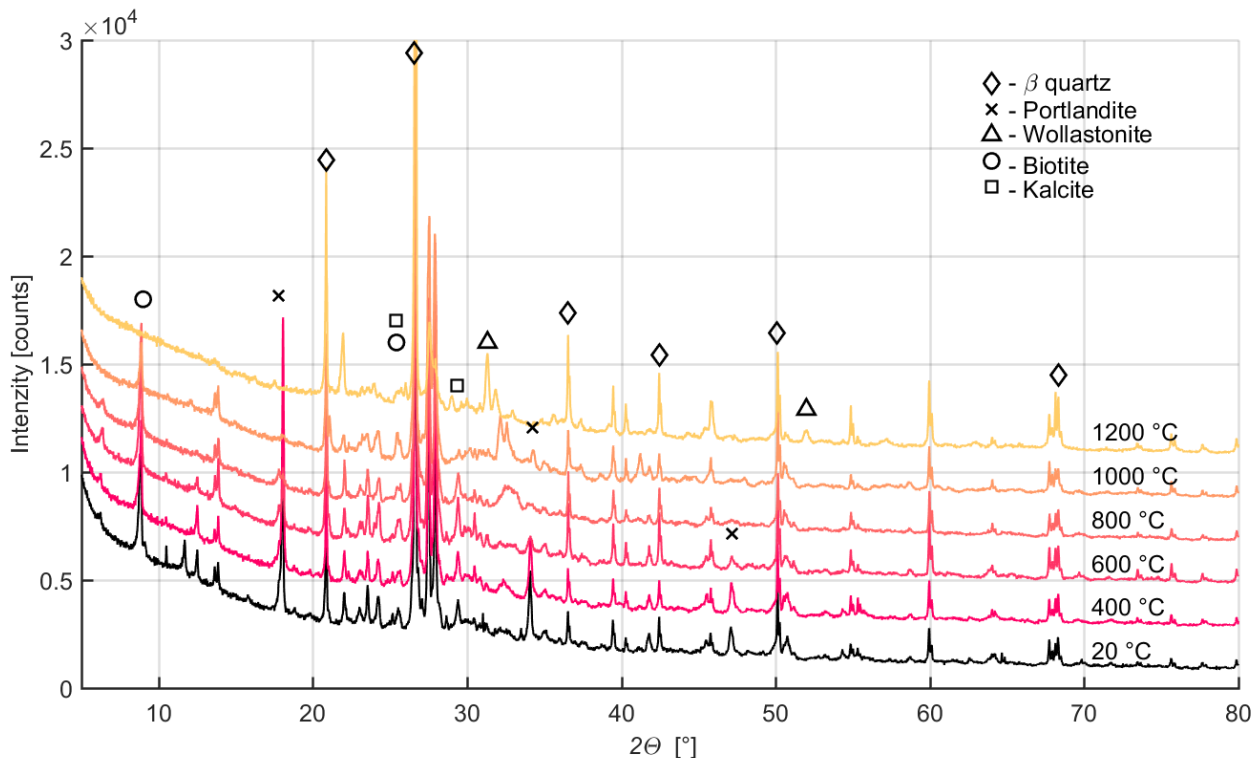


Fig. 8 – X-ray diffraction analysis of tested concrete specimens

Changes of physical-mechanical properties are based on change of microstructure and mineralogical composition of concrete specimens. For this purpose, the specimens were submitted to X-ray diffraction analysis. The measured results of reference set and temperature set from 400 to 1200 °C is shown in Figure 8. During this mineralogical analysis the presence of several minerals from both, used aggregate and cement were found. From aggregate: biotite, calcite,

kaolinite and β -quartz were found, while from cement: portlandite, β -quartz and wollastonite were found. All diffractograms were moved apart by 2000 counts for clarity. We can recognize that most changes appear between 400 and 800 °C and between 400 and 600 °C a decomposition of portlandite takes place.

Studies [11] have shown that, portlandite decomposed from 400 °C, which has been confirmed. Portlandite was recognizable with a much lower intensity at 800 °C and at 1000 °C no presence of portlandite was observed. Biotite, which is a mineral found in used aggregate decomposed between 920 and 960 °C [12], at 1200 °C biotite was not found in the diffractogram.

The hydraulic bonds between cement matrix and aggregate after 1000 °C are substituted by ceramic bonds which begin to form between calcium and quartz compounds [13]. After 1100 °C the low-melting quartz compounds start to melt and concrete shows partial sintering and forming of wollastonite $\text{CaO}\cdot\text{SiO}_2$. The presence of wollastonite was confirmed as it can be seen in the diffractogram from the 1200 °C set. This process is mainly responsible for recompacting of the test specimens and higher residual tensile and compressive strength.

CONCLUSION

This paper presented an investigation designed to test the applicability of a non-destructive method as a diagnostic tool for evaluation of thermally degraded concrete test specimens. As a test method, an Impact-Echo and ultrasonic pulse velocity method was used and compared with destructive tests such as cubic compressive strength test and flexural tensile strength test. These measurements aim to compare physical-mechanical changes with physical-chemical changes in microstructure.

Non-destructive measurement shows a strong correlation with destructive tests with lowest measured values for test specimens degraded at 1000 °C. After the 1200 °C, a slight increase in residual physical-mechanical properties was observed. Partial sintering at 1200 °C of concrete test specimens was observed and was accompanied by the formation of wollastonite at 1200 °C temperature sets. Apart from the formation of wollastonite, a presence of different minerals connected with used aggregate and cement was also confirmed. A decay of portlandite at 400 - 800 °C was observed, as well as decay of biotite between 800 and 1000 °C. The Impact-Echo testing seems to be more suitable to reveal a physical-mechanical condition of thermally degraded concrete than ultrasonic pulse velocity method.

The Conducted investigation has proved the theoretical assumptions of high-temperature degradation mechanisms of concrete, on the level of microstructure, in the scope of non-destructive testing.

High coefficients of correlation between destructive and non-destructive tests indicate suitability of acoustic non-destructive testing in the field of high-temperature Cementous composites such as concrete. This ability was also suggested and proved in the abroad studies [10].

The possibility of non-destructive assessment of material is convenient approach not only in the field of building diagnostics, but also in the development of new silicate and cementous fireproof materials. The possibility of combination of results from acoustic signal, processing tools with easy and cheap resonance methods of testing and X-ray diffraction analysis can unveil specific behaviour of material which can be key in the stage of development or quality control of new materials.

ACKNOWLEDGEMENTS

This publication was developed under the project No. LO1408 "AdMaS Up – Advanced Materials, Structures and Technologies" supported by the Ministry of Education, Youth and Sports under the „National Sustainability Programme I" and under the project GAČR No.16-02261S supported by Czech Science Foundation and under the project FAST-J-18-5275 supported by Faculty of Civil Engineering of VUT. We also thank Ms. Donnelly for English revision.

REFERENCES

- [1] PROCHÁZKA, Jaroslav, Radek ŠTEFAN a Jitka VAŠKOVÁ. *Navrhování betonových a zděných konstrukcí na účinky požáru*. Vyd. 1. V Praze: České vysoké učení technické, 2010.
- [2] CHOBOLA, Zdenek, Kristyna SRAMKOVA a Danieala STEFKOVA. The Use Acoustic Methods for Non-destructive Testing of High-temperature-degraded Cement- based Composite. In: *Mechanics and Control Engineering: Applied Mechanics and Materials*. 2014. Switzerland: Trans Tech Publications, b.r., s. 1395-1399
- [3] OZAWA, M., S. UCHIDA, T. KAMADA a H. MORIMOTO. Study of mechanisms of explosive spalling in high-strength concrete at high temperatures using acoustic emission. *Construction and Building Materials*. 2012, **37**, 621-628.
- [4] MALHOTRA, V. a Nicholas CARINO. *Handbook on nondestructive testing of concrete*. 2nd ed. Boca Raton, Fla.: CRC Press, 2004. ISBN 08-031-2099-0.
- [5] BRACEWELL, R. *The Fourier Transform & Its Applications*. 3. USA: McGraw-Hill Science/Engineering/Math, 1999.
- [6] ČSN 73 1371. *Non-destructive testing of concrete – Method of ultrasonic pulse testing of concrete*. Prague: Czech normalization institue, 1983.
- [7] VENKATARAMAN, Ganesan, Debendranath SAHOO a Venkataraman BALAKRISHNAN. *Beyond the Crystalline State an Emerging Perspective*. Berlin, Heidelberg: Springer Berlin Heidelberg, 1989.
- [8] ZHANG, Q. a G. YE. Dehydration kinetics of Portland cement paste at high temperature. *Journal of Thermal Analysis and Calorimetry*. The Netherlands, 2012, , 6. DOI: 10.1007/s10973-012-2303-9.
- [9] GERNAY, T. a J.M. FRANSEN. A Comparison Between Explicit and Implicit Modelling of Transient Creep Strain in Concrete Uniaxial Constitutive Relationships. *Fire and Materials 2011*. London: Interscience Communications Ltd, 2011, **31**, 405-416.
- [10] HAGER, I. Post-fire assessment of mechanical properties of concrete with the use of the impact-echo method. *Construction and Building Materials*. 2015, **2015**, 9.
- [11] GRAVES, H. L. A Review of the Effects of Elevated Temperature on Concrete Materials and Structures. *Volume 1: Plant Operations, Maintenance and Life Cycle; Component Reliability and Materials Issues; Codes, Standards, Licensing and Regulatory Issues; Fuel Cycle and High Level Waste Management*. ASME, 2006, , 615-624.
- [12] ROUXHET, P.G., J.L. GILLARD a J.J. FRIPIAT. Thermal decomposition of amosite, crocidolite and biotite. *Mineralogical magazine*. Belgium: Laboratoire de Physico-Chimie Minérale, 1972, **38**, 583-592.
- [13] BODNÁROVÁ, L., J. ZACH, J. HROUDOVÁ a J. VÁLEK. Methods for Determination of the Quality of Concretes with Respect to their High Temperature Behaviour. *Procedia Engineering*. 2013, **65**, 260-265.

BOND PERFORMANCE OF DEFORMED REBAR IN STEEL FIBER REINFORCED LIGHTWEIGHT-AGGREGATE CONCRETE AFFECTED BY MULTI-FACTORS

Mingshuang Zhao¹, Xiaoyan Zhang², Kai Yan¹, Teng Fei¹, Shunbo Zhao¹

- 1. Henan Province International United Lab of Eco-building Materials and Engineering, North China University of Water Resources and Electric Power, No. 36 Beihuan Road, 450045 Zhengzhou, China; E-mail: 1287827643@qq.com (Mingshuang Zhao), 1743767554@qq.com (Yan), 1751447427@qq.com (Fei), sbzhao@ncwu.edu.cn (Shunbo Zhao)*
- 2. School of Civil Engineering and Communication, North China University of Water Resources and Electric Power, No. 136 Jinshui East Road, 450046 Zhengzhou, China; E-mail: zxyanzi@ncwu.edu.cn*

ABSTRACT

For the innovation of building materials, a new high-performance Steel Fiber Reinforced Lightweight-Aggregate Concrete (SFRLAC) made of 100% fine and coarse expanded shales has been developed. In view of the importance of reliable bond properties between deformed rebar and this new SFRLAC, the experimental study of 39 specimens was conducted by using the modified pull-out test method with the evaluation of different slips at loading-end and free-end. In which the influencing factors were considered as the volume fraction of steel fiber, the water-cement ratio, the rebar diameter, the bond length of rebar, the strength of coarse expanded shales and the fine expanded shale replaced by manufactured sand. The complete bond stress-slip curves were measured, the bond failure modes of specimens were observed. Based on the bond mechanism of adhesion, friction and bearing action of deformed rebar in SFRLAC, the bond performance characterized by the bond strength and peak-slip, the differential of bond slip between loading-end and free-end, the bond sustainability in descending portion and the bond failure mode observed are analyzed. The recommendations are proposed for the design of SFRLAC structures related to the bond performance.

KEYWORDS

Steel fiber reinforced lightweight-aggregate concrete, Bond performance Modified pull-out test, Bond stress-slip curve, Bond strength, Peak-slip, Bond sustainability

INTRODUCTION

As a green building materials, lightweight-aggregate concrete (LAC) has been applied in civil engineering to lighten the self-weight of building structures and get other benefits such as better earthquake resistance and thermal insulation [1, 2]. However, owing to the different lightweight aggregates such as expanded clay aggregate, expanded shale aggregate, cold-bonded fly ash aggregate, sintered pulverized fuel ash aggregate, pelletized blast furnace slag aggregate, pumice aggregate, oil palm shell aggregate, etc., the properties of LAC may be varied in a great extent [3, 4]. In aspect to utilize the local expanded shale as lightweight aggregate, a new LAC dealt with 100% expanded shales as fine and coarse aggregates was innovated. Experimental

studies on the basic mechanical properties [5-7], strength development and carbonation [8], and shrinkage [9] of this LAC mixed with steel fibres were finished, and a new Steel Fiber Reinforced Lightweight-Aggregate Concrete (SFRLAC) with high structural performances was developed [10-12].

For the structural application, the bond performance of rebar in this new SFRLAC is important to ensure their working together. Similar to the reports about the bond properties of plain rebar in LAC [13], two kinds of actions affect the bond performance between plain rebar and this new SFRLAC: the adhesion referred to the chemical bonding of set cement is dominant before the bond stress reaches the ultimate; after that, the friction arising from the roughness of the interface becomes control. From the bonding mechanism, both the adhesion and the friction rely on the strength of set cement adhered on the interface. Therefore, the bond stress-slip behaviour is affected obviously by the water-binder ratio, and the bond strength increases mainly with the decrease of water-binder ratio. The bond strength trends a slight increment with the increasing volume fraction of steel fiber, while the bond sustainability rises after the peak-slip in descending portion of bond stress-slip curve. Meanwhile, the bond performance is less influenced by the strength of coarse expanded shale and the different fine aggregates tested [14].

As the deformed rebar is popular used for the main reinforcement, the bond performance of deformed rebar in this new SFRLAC should also be reasonably evaluated. In this respect, the studies on bond properties of LAC dealt with expanded shale provide good references [15-22], and the enhancement of steel fibres on the bond of SFRLAC presents a bright prospect [23-27].

Except the adhesion and friction on bond interface, the bearing action due to the anchorage of ribs against LAC surface benefits much more to the bond between deformed rebar and LAC [1, 13]. As the rib surface is not perpendicular to the longitudinal axis of rebar, the bearing action is resulted from the comprehensive effects of LAC under compression, tension and shear. Therefore, the issues were focused on the types of lightweight-aggregate and the strength of LAC (or water-binder ratio). Clarke and Birjandi [15] did not observe significant difference in the bond strengths of LAC using coarse expanded shale and other coarse lightweight aggregates such as expanded clay and pelletized blast furnace slag aggregates. König *et al.* [16] found higher bond strength of LAC with coarse expanded shale compared to the LAC with coarse expanded clay due to the higher compressive and splitting tensile strength of the former LAC. Lachemi *et al.* [17] reported that under the conditions of equivalent workability and compressive strength, the bond properties of LAC with coarse expanded shale was significantly enhanced compared to the LAC with coarse lightweight slag aggregate. Wu *et al.* [18] reported that the LAC with coarse expanded shale exhibited higher bond strength compared to the LAC with sintered pulverized fuel ash aggregate when equal water-binder ratio was used for both mixes. Meanwhile, the bond strength between deformed rebar and LAC with coarse expanded shale increases with the increasing tensile and/or compressive strength of LAC [19-22], and is higher than that of ordinary concrete in the same strength grade due to the lower water-binder ratio of LAC [19, 20].

Regardless of types of coarse lightweight-aggregate used such as cold-bonded fly ash, expanded clay, oil palm shell and expanded shale aggregates, the addition of steel fiber enhances the bond strength of deformed rebar in SFRLAC. This may be due to the increased confinement effect which altered the failure mode from splitting to pull-out failure [23], the bridging effect of steel fiber which restrained the widening of cracks appeared on surface of SFRLAC to improve the splitting failure [24, 25], or the strengthening effect which arrested the propagation of internal micro-cracks in pull-out failure [25]. The enhancements depend on the different conditions of concrete cover, rebar diameter, volume fraction of steel fiber and strength of SFRLAC. Meanwhile, Zhang *et al.* [26] observed that the peak-slip increased slightly with the increasing volume fraction of steel fiber, while the bond-stress in descending portion reduced slowly with higher loading resistance. Mo *et al.* [27] reported that the peak-slip increased with the increasing volume fraction

of steel fiber, while the bond stress-slip curve did not affected.

Given above, the bond performances of deformed rebar in SFRLAC are not fully recognized. This leads to the specially focuses on the bond performance of deformed rebar in the new high-performance SFRLAC in this paper. In the experimental study, the effects of such factors as the volume fraction of steel fiber, the water-cement ratio, the rebar diameter, the bond length of rebar, the strength of coarse expanded shales and the fine expanded shale replaced by manufactured sand were considered. The complete bond stress-slip curves and bond failure modes are measured by using the modified pull-out test method. Based on the analyses of test results, some beneficial recommendations are proposed for the safeguard design relating to the bond of high-performance SFRLAC structures.

EXPERIMENT

Raw materials

Grade P.O. 42.5 ordinary silicate cement was used, the physical and mechanical properties are listed in Table 1. Two kinds of sintering expanded shale in continuous gradation with maximum size of 20mm were used as coarse aggregate which sieved based on the maximum density principle, their physical and mechanical properties are presented in Table 2. The fine aggregate was the lightweight fine sintering expanded shale and the manufactured sand respectively in continuous gradation with size of 1.6-5 mm, their physical properties are listed in Table 3. Meanwhile, Table 4 presents the tested water absorption of coarse and fine expanded shales.

Tab. 1 - Physical and mechanical properties of cement

| Strength grade | Water requirement of normal consistency (%) | Setting time (min) | | Compressive strength (MPa) | | Tensile strength (MPa) | |
|----------------|---|--------------------|-------|----------------------------|------|------------------------|-----|
| | | initial | final | 3d | 28d | 3d | 28d |
| 42.5 | 26.4 | 150 | 248 | 22.8 | 50.8 | 4.1 | 8.0 |

Tab. 2 - Physical and mechanical properties of expanded shale

| Identifier | Apparent density (kg/m ³) | Bulk density (kg/m ³) | 1h water absorption (%) | Mud content (%) | Cylinder compressive strength (MPa) |
|------------|---------------------------------------|-----------------------------------|-------------------------|-----------------|-------------------------------------|
| N | 1274 | 800 | 6.1 | 0.2 | 5.0 |
| H | 1471 | 917 | 6.5 | 0.2 | 6.2 |

Tab. 3 - Physical properties of lightweight sand and manufactured sand

| Identifier | Fineness modulus | Apparent density (kg/m ³) | Bulk density (kg/m ³) | 1h water absorption (%) | Mud content (%) | Stone powder (%) |
|------------|------------------|---------------------------------------|-----------------------------------|-------------------------|-----------------|------------------|
| L | 3.56 | 1659 | 946 | 9.0 | 1.5 | - |
| M | 2.50 | 2730 | 1930 | 0.90 | - | 7.9 |

Tab. 4 - Water absorption of aggregate with the change of time

| Aggregate | Term | 5 min | 10 min | 15 min | 30 min | 1 h |
|------------------|---------------------|-------|--------|--------|--------|-----|
| Expanded shale | Absorption (%) | 4.0 | 5.0 | 5.2 | 5.5 | 6.1 |
| | Relative to 1 h (%) | 65.6 | 82.0 | 85.2 | 90.2 | 100 |
| Lightweight sand | Absorption (%) | 8.0 | 8.4 | 8.7 | 8.8 | 9.0 |
| | Relative to 1 h (%) | 89.2 | 93.4 | 96.8 | 98.1 | 100 |

Steel fiber was milling type in length $l_f=30$ mm and equivalent diameter $d_f=0.8$ mm. The aspect ratio $l/d_f=37.5$. Others were the tap-water and the polycarboxylic acid superplasticizer with water-reducing rate of 19 %.

Mix proportion of SFRLAC

The variables of this study were considered as the volume fraction of steel fiber (ρ_f), the water-cement ratio (W/C), the strength of coarse lightweight aggregate and the type of fine aggregate. Table 5 lists their combinations, where the double letters of mix No. are the identifiers of expanded shale and fine aggregate, the following digits represent W/B and ρ_f .

The mix proportion of high-performance SFRLAC was designed in accordance with the specifications in China Standards [28, 29], where the absolute volume method was selected. For all mixes, the dosage of water reducer was 5.5 % cement in mass. All mixes had good workability with slump of 120mm~150mm.

Tab. 5 - Mix proportion, compressive and tensile strength of concrete

| Mix No. | W/C | Cement (kg/m ³) | Water (kg/m ³) | Steel fiber (kg/m ³) | Sand (kg/m ³) | Expanded shale (kg/m ³) | f_{cu} (MPa) | f_{ft} (MPa) |
|------------|------|-----------------------------|----------------------------|----------------------------------|---------------------------|-------------------------------------|----------------|----------------|
| NL0.30/0 | 0.30 | 460 | 138 | — | 491.1 | 519.8 | 41.7 | 1.59 |
| NL0.30/0.4 | 0.30 | 487 | 147 | 31.2 | 484.4 | 508.6 | 44.1 | 2.03 |
| NL0.30/0.8 | 0.30 | 513 | 155 | 62.4 | 478.7 | 497.5 | 46.4 | 2.23 |
| NL0.30/1.2 | 0.30 | 541 | 164 | 93.6 | 472.4 | 485.7 | 47.3 | 2.81 |
| NL0.25/0.8 | 0.25 | 543 | 136 | 62.4 | 466.2 | 526.8 | 50.4 | 2.49 |
| NL0.35/0.8 | 0.35 | 483 | 169 | 62.4 | 499.4 | 477.9 | 44.4 | 1.87 |
| NM0.30/0.8 | 0.30 | 513 | 155 | 62.4 | 787.7 | 497.5 | 59.2 | 2.15 |
| HL0.30/0.8 | 0.30 | 513 | 155 | 62.4 | 478.7 | 574.4 | 58.5 | 2.77 |

Preparation of specimens

The bond behaviour of deformed rebar in high-performance SFRLAC was experimented by using the modified central pull-out test method [30-32]. The deformed rebar was steel bar with crescent-ribs. Table 6 lists their mechanical properties.

Tab. 6 - Mechanics properties of rebar

| Type | d (mm) | Yield strength (MPa) | Ultimate tensile strength (MPa) | Fracture elongation (%) |
|--------|----------|----------------------|---------------------------------|-------------------------|
| HRB335 | 12 | 365 | 565 | 21.2 |
| HRB335 | 16 | 371 | 561 | 23.9 |
| HRB335 | 20 | 375 | 563 | 24.6 |

The bond length of rebar was placed in the central part of specimen with the bond-breakers in length of 35 mm at the ends. Realized by PVC tubes and sealed with paraffin, the bond-breakers simulated the real condition of rebar in concrete, and eliminated the local compression on loading surface. The normal section of specimen was 150 mm×150 mm, the bond length of rebar $l_a=2d$, $5d$, $8d$ and $11d$ (where d is rebar diameter), the length of specimen $l=l_a+70$, the steel bar at loading end was kept long enough for pull-out purpose. Thirteen groups of specimen were designed, each group had 3 specimens. The group No.means the variables of bond length, rebar diameter followed by mix No. (Table 7).

Tab. 7 - List of specimens

| Group No. | Mix No. | ρ_x (%) | d (mm) | l_a (mm) | l (mm) | Aggregates |
|-----------------|------------|--------------|----------|------------|----------|------------|
| 5d16NL0.30/0 | NL0.30/0 | 0 | 16 | 80 | 150 | N+L |
| 5d16NL0.30/0.4 | NL0.30/0.4 | 0.4 | 16 | 80 | 150 | N+L |
| 5d16NL0.30/0.8 | NL0.30/0.8 | 0.8 | 16 | 80 | 150 | N+L |
| 5d16NL0.30/1.2 | NL0.30/1.2 | 1.2 | 16 | 80 | 150 | N+L |
| 5d16NL0.25/0.8 | NL0.25/0.8 | 0.8 | 16 | 80 | 150 | N+L |
| 5d16NL0.35/0.8 | NL0.35/0.8 | 0.8 | 16 | 80 | 150 | N+L |
| 5d16HL0.30/0.8 | HL0.30/0.8 | 0.8 | 16 | 80 | 150 | H+L |
| 5d16NM0.30/0.8 | NM0.30/0.8 | 0.8 | 16 | 80 | 150 | N+M |
| 5d12NL0.30/0.8 | NL0.30/0.8 | 0.8 | 12 | 60 | 130 | N+L |
| 5d20NL0.30/0.8 | NL0.30/0.8 | 0.8 | 20 | 100 | 170 | N+L |
| 2d16NL0.30/0.8 | NL0.30/0.8 | 0.8 | 16 | 32 | 102 | N+L |
| 8d16NL0.30/0.8 | NL0.30/0.8 | 0.8 | 16 | 128 | 198 | N+L |
| 11d16NL0.30/0.8 | NL0.30/0.8 | 0.8 | 16 | 176 | 246 | N+L |

The specimens were prepared and cured in the lab. Steel moulds with holes at central of opposite plates ensured the placement of rebar [32]. The SFRLAC was put into the moulds and vibrated on the vibration platform. After cast for 24 hours, the specimens were moved from moulds and placed in the standard curing room for 28 days. To get the real compressive and tensile strengths of SFRLAC, six cubes in dimension of 150 mm for each mix were cast at the same time and cured in the same condition with specimens.

Test Method

On test platform, the loading-end of rebar passed successively through the steel plate, steel tube, load meter and locked at the end of hydraulic jack. All of them fixed together were adjusted with the axis of rebar to eliminate the eccentric effect of pull-out force. The bond slip at loading-end was measured by the displacement meter fixed on the rebar within the steel tube, which was corrected by accounting for the local elongation of the rebar. The slip at free-end was accounted by the relative displacement between rebar and concrete measured with two displacement meters. The displacement meters linked to the strain acquisition system. The initial load was exerted on the specimen to check the stability of test system, and then the static loading test was started. As specified in China Standard [30], the loading speed changes with different diameter (d) of steel bar, it was taken as $0.05d^2$ N/min.

The average bond stress (τ) was calculated from the pull-out force divided by the bond area within bond length, the maximum value was the bond strength (τ_u), that is:

$$\tau = F / (\pi d l_a) \quad (1)$$

Where, F is the pull-out force, l_a is the bond length of rebar, d is the diameter of rebar.

Tests for cubic compressive strength (f_{cu}) and splitting tensile strength (f_t) of SFRLAC were in accordance with the specifications of China Standard [33]. The results are presented in Table 5.

TEST RESULTS AND DISCUSSION

Failure states, bond strength & peak-slip

Except those specimens with $11d$ bond length failed due to the yield of rebar without pull-out from the SFRLAC, the LAC specimens (5d16NL0.30/0) failed due to the splitting of LAC after the pull-out load reached the maximum, while the others of SFRLAC specimens failed because of the pull-out of rebar accompanied with cracks appeared on side surfaces of SFRLAC. Therefore, the bond stress-slip curves of LAC specimens were obtained only before ultimate load, while the complete bond stress-slip curves of SFRLAC specimens were gotten.

Steel fibres protected the splitting of SFRLAC specimens into two or three parts as those of LAC, which led a ductile bond failure due to the successive pull-out of rebar. As the slip of rebar gradually transferred from loading-end to free-end, the loading-end slip was larger than the free-end slip until the pull-out load up to the maximum. After that, the increments of slip at free-end and loading-end were almost equal. During the pull-out process of rebar, cracks appeared and widened continuously on the side surface of SFRLAC specimens. With the increasing volume fraction of steel fiber, the crack width decreased due to the enhanced confinement of steel fibres on crack widening. Table 8 lists the maximum crack width measured on the side surface of specimens while the rebar was fully pull out of SFRLAC.

From the bond stress-slip curve, the maximum bond stress is the bond strength (τ_u), and the corresponding peak-slip is marked as s_u . Table 9 lists test values of the bond strength (τ_u) and the peak-slips at free-end ($s_{f,u}$) and loading-end ($s_{l,u}$). The mean values are computed for the specimens failed without yield of rebar according to the statistical analysis principle of the deviation within 20 %. The value of peak-slip (s_u) is taken as the mean value of peak-slips at free-end and loading-end, to generally analyse the bond stress-slip relationship.

Tab. 8 - Maximum crack width appeared on side surface of specimen (mm)

| Group no. | Specimen no. | | |
|----------------|--------------|------|------|
| | 1 | 2 | 3 |
| 5d16NL0.30/0.4 | 3.50 | 3.30 | 2.00 |
| 5d16NL0.30/0.8 | 2.00 | 2.50 | 1.10 |
| 5d16NL0.30/1.2 | 1.50 | 0.38 | 0.45 |

Tab. 9 - Test result of bond strength and slip

| Group no. of specimens | τ_u (MPa) | | $s_{l,u}$ (mm) | | $s_{f,u}$ (mm) | | s_u (mm) | Failure mode* |
|------------------------|----------------|------|----------------|------|----------------|------|------------|---------------|
| | test value | mean | test value | mean | test value | mean | | |
| 5d16NL0.30/0 | 14.5/13.2/14.0 | 13.9 | 0.37/0.35/0.38 | 0.37 | 0.26/0.27/0.28 | 0.27 | 0.32 | S/S/S |
| 5d16NL0.30/0.4 | 15.5/16.5/14.5 | 15.5 | 0.74/0.86/0.68 | 0.76 | 0.50/0.60/0.54 | 0.55 | 0.66 | P/S/P |
| 5d16NL0.30/0.8 | 17.0/16.1/17.7 | 16.9 | 1.06/0.91/0.94 | 0.97 | 0.57/0.51/0.54 | 0.54 | 0.76 | P/P/P |
| 5d16NL0.30/1.2 | 18.9/19.8/19.1 | 19.3 | 1.19/1.13/1.16 | 1.16 | 0.41/0.38/0.40 | 0.40 | 0.78 | P/P/P |
| 5d16NL0.25/0.8 | 18.5/18.3/19.1 | 18.6 | 1.08/0.94/1.05 | 1.02 | 0.46/0.50/0.45 | 0.47 | 0.75 | S/P/P |
| 5d16NL0.35/0.8 | 15.1/17.4/16.5 | 16.3 | 0.85/0.93/0.96 | 0.91 | 0.62/0.60/0.64 | 0.62 | 0.77 | P/S/P |
| 5d16HL0.30/0.8 | 17.5/19.1/17.8 | 18.1 | 1.05/1.01/1.01 | 1.02 | 0.48/0.40/0.46 | 0.45 | 0.74 | S/P/P |
| 5d16NM0.30/0.8 | 17.3/16.3/16.5 | 16.7 | 0.62/0.61/0.67 | 0.63 | 0.55/0.60/0.56 | 0.57 | 0.60 | P/P/P |
| 5d12NL0.30/0.8 | 17.8/16.7/17.5 | 17.3 | 0.78/0.79/0.90 | 0.82 | 0.49/0.52/0.55 | 0.52 | 0.67 | P/P/P |
| 5d20NL0.30/0.8 | 15.1/16.5/17.2 | 16.3 | 0.72/0.79/0.71 | 0.74 | 0.53/0.50/0.61 | 0.55 | 0.65 | P/S/S |
| 2d16NL0.30/0.8 | 17.0/15.7/17.5 | 16.7 | 0.58/0.60/0.55 | 0.58 | 0.44/0.46/0.52 | 0.47 | 0.53 | P/P/P |
| 8d16NL0.30/0.8 | 13.2/12.6/12.9 | 12.9 | 1.20/1.19/1.21 | 1.20 | 0.35/0.33/0.40 | 0.36 | 0.78 | P/S/S |

Note: *S-splitting of LAC or SFRLAC; P-pull-out of rebar.

Effect of steel fibres

As shown in Figure 1, the bond stress-slip (τ - s) curves of rebar pull-out of SFRLAC contain three portions with the characteristics of micro-slip, slip and descending. In the micro-slip portion, the slip increased elastically due to the continuous loss of adhesion between rebar and SFRLAC. In the slip portion, the bond stress increased nonlinearly with slip as the SFRLAC in front of the ribs of rebar became into the nonlinear deformation under compression, tension and shear. Accompanied with the internal broken of SFRLAC in front of the ribs of rebar, the splitting cracks appeared on the side surface of specimen, the bond stress reached the ultimate with the peak-slip, and the bond stress-slip curve went into the third portion.

Similar to the reported study [26, 27], due to the restraint of steel fibres to the propagation of internal cracks of SFRLAC, the slip of rebar kept persistently with the successive shear fracture and compressive broken of SFRLAC along the rebar.

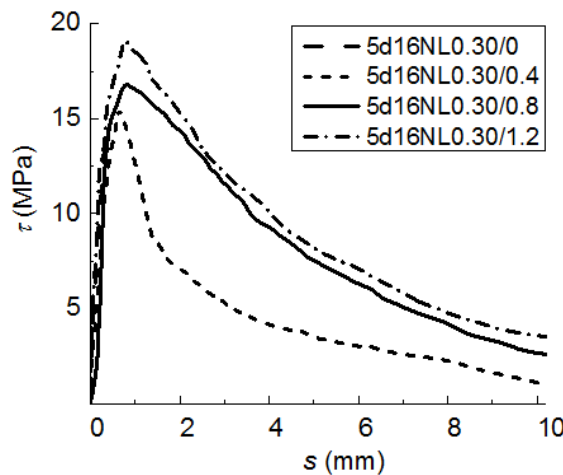


Fig. 1 - Bond stress-slip curves of specimens with different volume fraction of steel fiber

Normally, the bond strength (τ_{u0}) between deformed rebar and LAC is expressed as a function of compressive strength (f_{c0}) or tensile strength (f_{t0}) of LAC [13, 17, 19], which can be generally shown as:

$$\tau_{u0} = a f_{c0}^b \tag{2}$$

$$\tau_{u0} = c f_{t0} \tag{3}$$

Where a , b and c are the fitness coefficients depended on the test parameters.

Considering that the tensile strength (f_{ft}) of SFRLAC is always expressed as linearly to the content characteristic value (λ_f) of steel fiber, that is [7, 10, 29]

$$f_{ft} = (1 + \alpha_t \lambda_f) f_{t0} \tag{4}$$

Where α_t is the fitness coefficient. $\lambda_f = \rho_f \cdot k / d_f$, ρ_f is the volume fraction of steel fiber, k/d_f is the aspect ratio of steel fiber.

Suppose Equation 3 is also fit for the bond strength (τ_u) between deformed rebar and SFRLAC, the following equation can be deduced as:

$$\tau_u = (1 + \alpha_b \lambda_f) \tau_{u0} \tag{5}$$

The reasonability of Equations 4 and 5 can be verified by the test results shown in Figure 2. Where the tensile strength ratio, bond strength ratio and compressive strength ratio are f_{ft}/f_{t0} , τ_u/τ_{u0} and f_{cd}/f_{c0} , respectively. Obviously, the increment of bond strength is lower than that of tensile strength with the same increment of the volume fraction of steel fiber. The addition of 0.4%, 0.8% and 1.2% steel fibres resulted in increase of 11.5%, 21.6% and 38.9% in the bond strength of SFRLAC, while the increase of 27.6%, 40.2% and 76.7% in the tensile strength. This means the coefficient $\alpha_b < \alpha_t$, and explains that the enhancement of steel fibres on bond strength not only depended on the strengthening of tensile strength, but also on the compressive strength. The less strengthening of compressive strength reduced the resistance of SFRLAC in front of the ribs of rebar under compression. In this aspect, Equation 2 has certain reasonability reflecting the comprehensive effect of LAC strength on bond strength by using the exponential function of compressive strength.

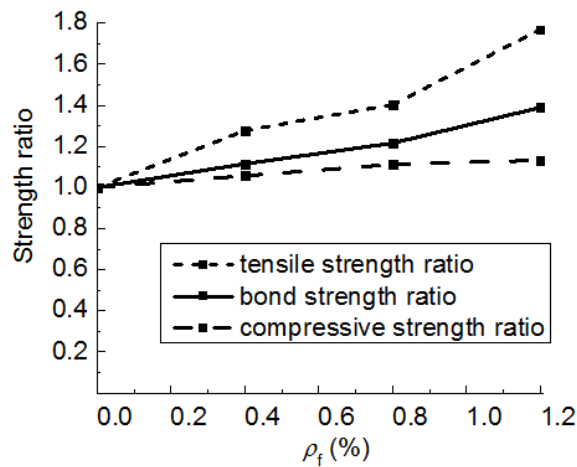


Fig. 2 - Bond strength affected by the volume fraction of steel fibres

Figure 3 shows that with the increasing volume fraction of steel fiber, the mean values of peak-slip (s_u) were almost equal, however the slip at loading-end increased and the slip at free-end became smaller, which resulted in the increased deviation of slips at loading-end and free-end. This illustrates that the steel fibres in SFRLAC restrained the internal splitting of SFRLAC along rebar and led to the continuously increment of bond stress from loading-end to free-end [31, 32], resulted in the enhancement of the sustainability of bond between deformed rebar and SFRLAC.

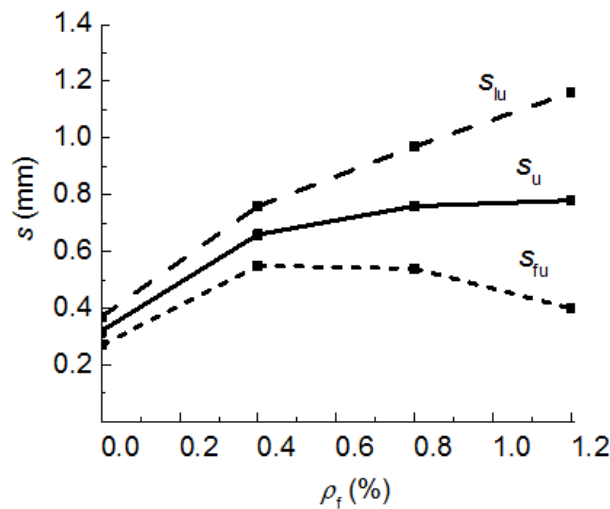


Fig. 3 - Bond slip affected by the volume fraction of steel fibres

In this paper, the bond sustainability of deformed rebar in SFRLAC is in direct proportion to the normalized bond stress τ_r/τ_u . Where τ_r is the bond stress at point of bond stress-slip curve in descending portion, normally called as residual bond strength. As shown in Figure 4, when the same slip took place in descending portion of bond stress-slip curve, τ_r/τ_u was higher with the volume fraction of steel fiber no less than 0.8 %. This result is different from Mo *et al.* reported [27] that the addition of steel fiber did not affect the bond stress-slip curve, where the oil palm shell was used as coarse lightweight-aggregate. With the lower volume fraction of steel fiber as 0.4%, the bond sustainability was poor although the brittleness of bond failure was improved obviously.

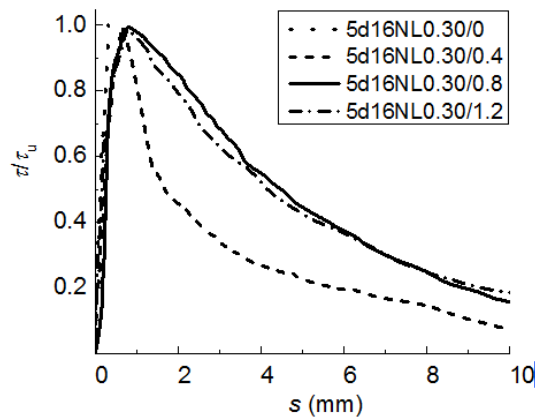


Fig. 4 - Bond sustainability affected by the volume fraction of steel fibres

Effect of SFRLAC strength

In the test, the different of SFRLAC strength depended on the different water-cement ratio. From Table 5, the compressive and splitting tensile strengths of SFRLAC increased with the decrease of water-cement ratio. This provided the good condition to enhance the bond performance of deformed rebar in SFRLAC. As listed in Table 9, the bond strength increased with the decreasing water-cement ratio, the differential of slips at loading-end and free-end become larger in spite of the almost equal mean value of peak-slip. More directly, Figure 5 presents the increasing trend of bond performance with the decrease of water-cement ratio.

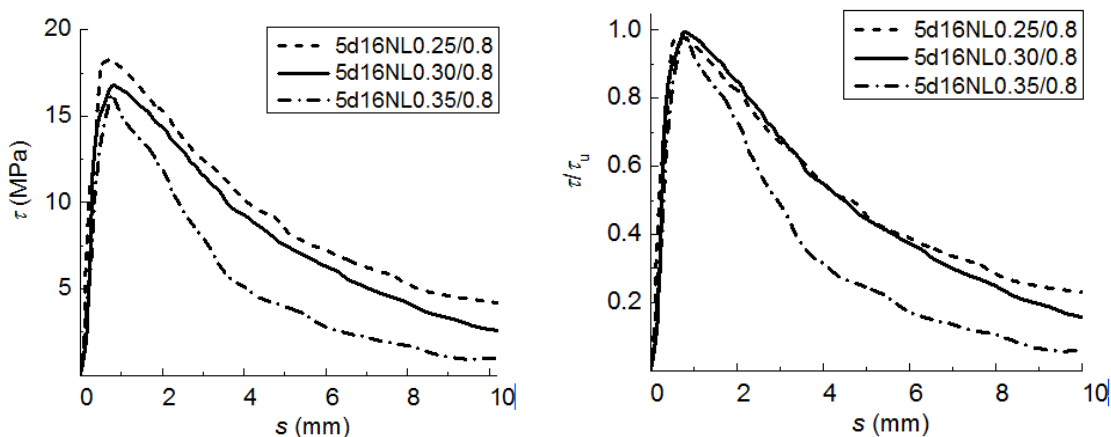


Fig. 5 - Bond stress-slip curve and bond sustainability affected by the water-cement ratio

Figure 5 also shows the bond sustainability of SFRLAC with different water-cement ratio. Due to the complex action of SFRLAC under compression and shear in front of ribs and along bond length of rebar, the bond sustainability was almost equal when the water-cement ratio was 0.25 and 0.30, while the lower bond sustainability was for the water-cement ratio of 0.35.

Effect of rebar diameter

From Table 9, the bond strength reduced slightly with the increase of rebar diameter, the mean value of peak-slip decreased with the reduced differential of peak-slips between loading-end

and free-end. Compared the bond strength of rebar $d=12\text{mm}$, the bond strength of rebar $d=16\text{mm}$ and 20mm decreased for 2.31% and 5.78%. From Figure 6, the bond stress of rebar $d=20\text{mm}$ drop down quickly with the increased slip in descending portion of bond stress-slip curve, which was bad for the bond sustainability. These may be due to the reduction of bearing capacity of SFRLAC in front of ribs, as the height of ribs relatively reduced and the space of ribs increased with the increasing diameter of rebar [1, 2]. Another reason may be owing to the changes of concrete cover from 5.75, 4.19 to 3.25 times the rebar diameter, which led to the increasing trend of the splitting failure of SFRLAC and decreased the lateral restraint to the bond surface. Similar regulations of bond strength of LAC reduced with the increasing rebar diameter are reported in previous studies [16-20]. As the proof, two of three specimens with 20mm rebar failed in splitting of SFRLAC in this test.

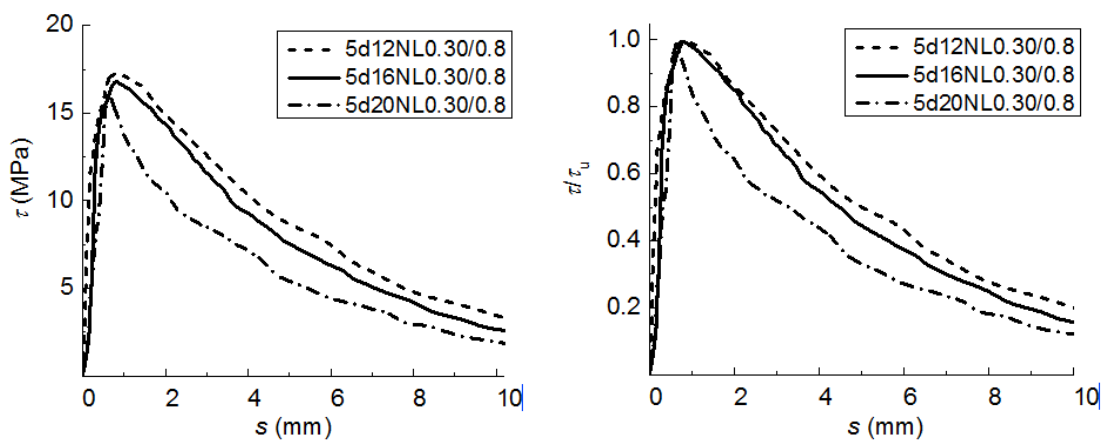


Fig. 6 - Bond stress-slip curves and bond sustainability affected by diameter of rebar

Effect of aggregate types

The SFRLAC (HL0.30/0.8) with higher strength expanded shale had greater compressive and tensile strengths than the SFRLAC (NL0.30/0.8) with normal strength expanded shale (Table 5). This resulted in the higher bond strength, the larger differential of peak-slip between loading-end and free-end (Table 9) and the relative fullness of bond stress-slip curve (Figure 7). Taken an observation on the failure of bond interface, the expanded shales were directly sheared as a plain. This demonstrated that the strength of expanded shales played an important role resisting the complex action under shear and compression.

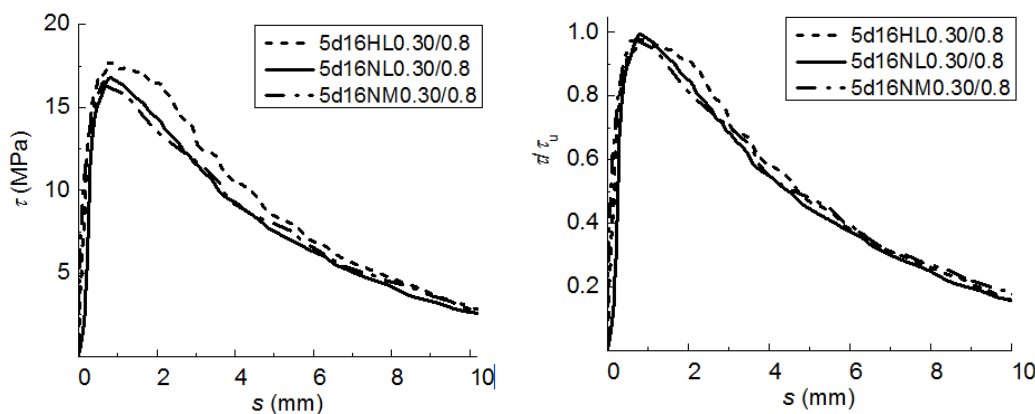


Fig. 7 - Bond stress-slip curves affected by types of coarse and fine aggregates

The SFRLAC (NM0.30/0.8) with manufactured sand had greater compressive strength and slightly lower tensile strength than the SFRLAC (NL0.30/0.8) with normal strength expanded shale (Table 5). This resulted in the almost equal bond strength with some differential of slip (Table 9), and the similar bond stress-slip curve and bond sustainability (Figure 7).

Therefore, the strength of coarse expanded shale affected the bond performance in much more extent, while the effect of fine expanded shale replaced by manufactured sand could be eliminated.

Effect of bond length

With the increase of bond length, the pull-out load increased. This led to the increase of tensile stress of rebar over the yield strength as well as ultimate strength, and finally resulted in the fracture of rebar when the bond length reached $11d$. Combined with test data in Table 9 and bond stress-slip curves in Figure 8, the bond strength of rebar with $2d$ bond length was equal to that with $5d$ bond length, while the bond strength of rebar with $8d$ bond length was lower about 30%. The fullness of bond stress-slip curve in descending portion of rebar with $2d$ bond length was better than those of rebars with $5d$ and $8d$ bond length. The rebars with $5d$ and $8d$ bond length presented the similar bond stress-slip curve and bond sustainability, although the latter has a greater differential of peak-slips between loading-end and free-end. Meanwhile, it should be noted that the bond sustainability of rebar with $8d$ bond length at the initial part of descending portion of τ/τ_u - s curve was greater, which provided a higher reliability to sustain the bond strength with a greater peak-slip.

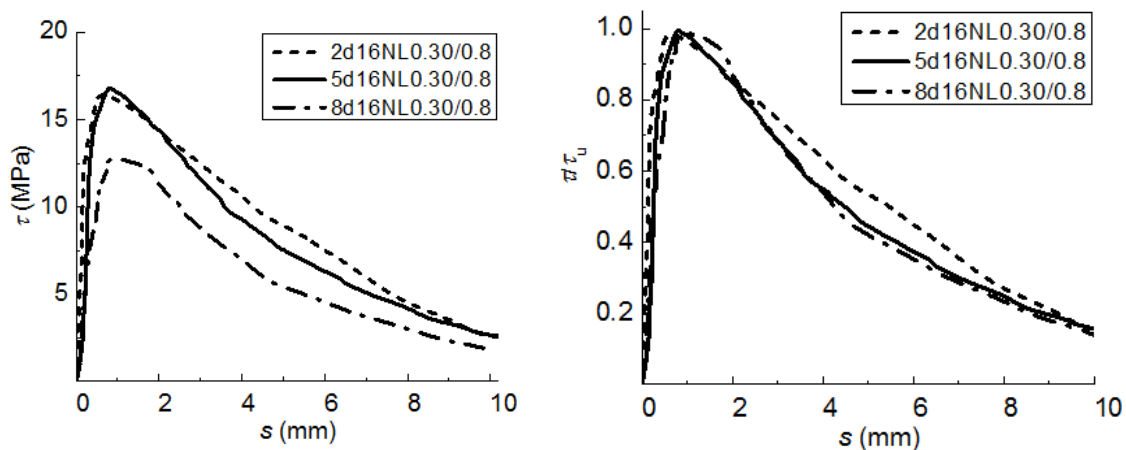


Fig. 8 - Bond stress-slip curves and bond sustainability affected by bond length of rebar

The above differences may be concluded to the different bond mechanism affected by bond length. As the rib space is about $0.7d$, the number of ribs took part in the bearing action is about 3, 7 and 11 corresponding to the rebar with $2d$, $5d$ and $8d$ bond length. Because of the transfer of bond slip from loading-end to free-end, the bearing action of ribs took place successively from the one near the loading-end. For the rebar with $2d$ bond length, the bearing action of ribs could be simultaneous easily and led the bond stress up to the ultimate; after that, the slip increased with the crushing deformation of SFRLAC in front of ribs and the complete shear failure of coarse expanded shales in a plain along the bond length. This exhibited that the even distribution of bond stress along the bond length and the straight reduction of bond stress in descending portion.

For the rebars with $5d$ and $8d$ bond length, the much more number of ribs gave the opportunity of the redistribution of bond stress along bond length with the transfer of slip from

loading-end to free-end [17-20, 26], which let the SFRLAC work successively into effective states. In this condition, the bond reliability was higher because the ribs seceded bearing action one by one with the increasing slip, the obvious reduction of bond stress gave the forebode to avoid related damages.

CONCLUSION

In the test, multi-factors were considered to study their effects on the bond performance of deformed rebar in high-performance SFRLAC. The complete bond stress-slip curves of specimens are obtained by using modified pull-out test with the detection of the slips at loading-end and free-end. The compressive and splitting tensile strength of SFRLAC were also tested. Based on the analyses of test results, the conclusion can be drawn as follow:

- (1) Three kinds of actions affected the bond performance of deformed rebar in high-performance SFRLAC: the adhesion referred to the chemical bonding of set cement, the friction arising from the roughness of the interface and the bearing action due to the anchorage of ribs against SFRLAC surface. To completely and reasonably evaluate the bond behaviours, the differential of bond slip between loading-end and free-end, the bond failure mode and the bond stress-slip curve characterized by bond strength, peak-slip and bond sustainability are analysed.
- (2) Steel fibers in LAC benefited to the ductile failure of bond test specimens by altering the failure mode from splitting to pull-out. The width of cracks appeared on surface of SFRLAC specimens decreased obviously with the increase of volume fraction of steel fiber. When the bond length reached $11d$, the fracture of rebar took place without failure of SFRLAC specimens.
- (3) The strengthening effect of steel fiber on bond strength is lower than that on tensile strength. With the increase of volume fraction of steel fiber, the peak-slips were almost equal while the deviation of slips at loading-end and free-end increased, the bond sustainability in descending portion was improved. When the volume fraction of steel fiber was no less than 0.8%, the bond sustainability was higher with the ductile bond failure.
- (4) The bond performance was improved by decreasing the water-cement ratio. The bond strength increased, the mean values of peak-slip were almost equal with the greater differential of slips at loading-end and free-end. The bond sustainability was almost equal when the water-cement ratio was 0.25 and 0.30, while the lower one was for the water-cement ratio of 0.35.
- (5) Compared the bond strength of rebar $d=12\text{mm}$, the bond strength of rebar $d=16\text{mm}$ and 20mm decreased for 2.31% and 5.78%. With the increase of rebar diameter, the mean value of peak-slip decreased with the reduced differential of slips between loading-end and free-end, the bond sustainability reduced. Except the difference of rebar dimension, the different concrete cover should be considered.
- (6) The higher strength of coarse expanded shale led to the higher bond strength, the larger differential of slip between loading-end and free-end and the higher bond sustainability. The effect of fine expanded shale replaced by manufactured sand on bond performance could be eliminated.
- (7) The bond strength of rebar with $2d$ bond length was equal to that with $5d$ bond length, while the bond strength of rebar with $8d$ bond length was lower about 30%. The rebars with $5d$ and $8d$ bond length presented the similar bond stress-slip curve and bond sustainability, while the better behaviors was exhibited for the rebar with $2d$ bond length. Meanwhile, the bond sustainability of rebar with $8d$ bond strength at the initial part of descending portion was greater, which provided a higher reliability to sustain the bond strength with a greater peak-slip.

ACKNOWLEDGEMENTS

This study was financially supported by the NCWU Innovation Funds for Doctoral Candidate (201714402), the Key Research Project in University of Henan Province, China (14B560004, 16A560024), and the Science and Technology Innovation Team of Eco-building Material and Structural Engineering in University of Henan Province, China (13IRTSTHN002) .

REFERENCES

- [1] JGJ12, 2006. Design Specification for Lightweight Aggregate Concrete Structures (China Building Industry Press) 62 pp.
- [2] CECS 202:2006, Technical Specification for Lightweight Aggregate Concrete Bridges, China Plan Press, Beijing, China, 2006.
- [3] Zhao M.S., Ma Y.Y., Pan L.Y., Li C.Y., 2015. An overview of study on natural lightweight aggregate for concrete in China. In: 3rd International Conference on Civil Engineering, Architecture and Sustainable Infrastructure, Edited by Zhang X.Q., Zhao S.B. & Xie Y.M., DEStech Publications, Inc., 125-133
- [4] Hassanpour M., Shafigh P., Mahmud H.B., 2012. Lightweight aggregate concrete fiber reinforcement –A review. *Construction and Building Materials*, No. 37: 452-461
- [5] Zhao S.B., Li C.Y., Qian X.J., 2011. Experimental study on mechanical properties of steel fiber reinforced full lightweight concrete. *Geotechnical Special Publication*, No. 212: 233-239
- [6] Pan L.Y., Yuan H., Zhao S.B., 2011. Experimental study on mechanical properties of hybrid fiber reinforced full lightweight aggregate concrete. *Advanced Materials Research*, Vol. 197-198: 911-914
- [7] Shen Z., Chen M.H., Zhao M.S., Li X.K., 2015. Experimental study on tensile properties of steel fiber reinforced lightweight-aggregate fly-ash flowable concrete. In: *Architectural Engineering and New Materials*, Edited by Badorul H.A.B., Meor O.H. & Noridah M., DEStech Publications, Inc: PA, USA, 1-8
- [8] Li X.K., Zhang X.Y., Li M.Q., Zhao M.S., Li C.Y., 2017. Experiments on development of strength and carbonization of steel fiber reinforced full-lightweight concrete. *Journal of Civil Engineering and Management*, Vol. 34, No. 2: 46-50
- [9] Zhao S.B., Li C.Y., Zhao M.S., Zhang X.Y., 2016. Experimental study on autogenous and drying shrinkage of steel fiber reinforced lightweight-aggregate concrete. *Advances in Material Science and Engineering*, Vol. 2016, Article ID2589383, pages 10
- [10] Li C.Y., Zhao S.B., Chen H., Gao D.Y., Ding X.X., 2015. Experimental study on flexural capacity of reinforced SFRFLC superposed beams. *Journal of Building Structures*, Vol. 36, Suppl. 2: 257-264
- [11] Li C.Y., Ding X.X., Zhao S.B., Zhang X.Y., Li X.K., 2016. Cracking resistance of reinforced SFRFLC superposed beams with partial ordinary concrete in compression zone. *The Open Civil Engineering Journal*, No. 10: 727-737
- [12] Pei S.W., Du Z.H., Li C.Y., Shi F.J., 2013. Research of punching performance of reinforced SFRLAC superposed two-way slabs. *Applied Mechanics and Materials*, Vols. 438-439: 667-672
- [13] Mo K.H., Alengaram U.J., Jumaat M. Z., 2016. Bond properties of lightweight concrete -A review. *Construction and Building Materials*, No. 112: 478-496
- [14] Li F.L., Yu Y.N., Yu K.F., Chen J.Q., 2014. Experimental study on bond properties of plain steel bar with SFRLAC. *Journal of Hebei University of Technology*, Vol. 43, No. 6: 93-96
- [15] Clarke J.L., Birjandi F.K., 1993. Bond strength tests for ribbed bars in lightweight aggregate concrete. *Magazine of Concrete Research*, Vol. 45, No. 163: 79-87
- [16] Konig G., Dehn F., Holschemacher K., Weibe D., 2002. Determination of the bond creep coefficient for lightweight aggregate concrete (LWAC) under cyclic loading. In: *Concrete for Extreme Conditions. Proceedings of the International Conference Held at the University of Dundee, Scotland, UK*, 673-683
- [17] Lachemi M., Bae S., Hossain K. M. A., Sahmaran M., 2009. Steel-concrete bond strength of lightweight self-consolidating concrete. *Materials and Structures*, No. 42: 1015-1023
- [18] Wu X., Wu Z., Zheng J., Zhang X., 2013. Bond behavior of deformed bars in self-compacting lightweight concrete subjected to lateral pressure. *Magazine of Concrete Research*, Vol. 65, No. 23: 1396-1410

- [19] Wei J., Ma J., Yue J., 1993. Experimental study of bond and anchorage of concrete and deformed bars. *Journal of Harbin Architecture & Civil Engineering Institute*, Vol. 26, No. 1: 95-100
- [20] Lu C., Wang W., Li P., 2007. Experimental research on bond behavior between deformed bar and lightweight concrete. *Journal of Guangxi University (Nat Sci Ed)*, Vol. 32, No. 1: 6-9
- [21] Zhang D., Yang W., 2015. Experimental research on bond behaviors between shale ceramsite lightweight aggregate concrete and bars through pullout tests. *Journal of Materials in Civil Engineering*, Vol. 27, No. 9, Article ID 06014030
- [22] Gu C., Zheng X., Zhang W., Chang H., 2017. Test research on bond properties between reinforcing bar and lightweight aggregate concrete. *Journal of Railway Science and Engineering*, Vol. 14, No. 3: 528-535
- [23] Ali A., Iqbal S., Holschemacher K., Bier T., 2016. Effect of fibers on bond performance of lightweight reinforced concrete. *Periodica Polytechnica: Civil Engineering*, Vol. 60, No. 1: 97-102
- [24] Guneyisi E., Gesoglu M., Ipek S., 2013. Effect of steel fiber addition and aspect ratio on bond strength of cold-bonded fly ash lightweight aggregate concrete. *Construction and Building Materials*, No. 47: 358-365
- [25] Campione G., Cucchiara C., Mendola L., Papia M., 2005. Steel-concrete bond in lightweight fiber reinforced concrete under monotonic and cyclic actions. *Engineering Structures*, Vol. 27, No. 6: 881-890
- [26] Zhang H., Lv Z., Liu Y., 2016. Experimental research on bond behavior between steel fiber reinforced high-strength ceramsite concrete and rebar. *Building Structure*, Vol. 46, No. 4: 79-84
- [27] Mo K.H., Goh S.H., Alengaram U.J., Visintin P., Jumaat M.Z., 2017. Mechanical, toughness, bond and durability-related properties of lightweight concrete reinforced with steel fibers. *Materials and Structures*, No. 50:46, pages 14
- [28] JGJ 21, 2002, Technical Specification for Lightweight Aggregate Concrete (China Building Industry Press) 52 pp.
- [29] JG/T 472, 2015. Steel Fiber Reinforced Concrete (China Standard Press) 16 pp.
- [30] GB 50152, 2012. Standard for Test Method of Concrete Structures (China Building Industry Press) 26 pp.
- [31] Zhao S.B., Ding X.X., Li C.M., Li C.Y., 2013. Experimental study on bond properties between deformed steel bar and concrete with machine-made sand. *Journal of Building Materials*, Vol. 12, No. 3: 191-196
- [32] Li C.Y., Zhao M.L., Ren F.C., Liang N., Li J., Zhao M.S., 2017. Bond Properties between full-recycled-aggregate concrete and deformed steel bar. *The Open Civil Engineering Journal*, Vol. 11: 685-698
- [33] GB/T 50081, 2002. Standard for Test Method of Mechanical Properties on Ordinary Concrete (China Building Industry Press) 28 pp.

TEMPERATURE ANALYSIS OF HIGH LATITUDES AND LOW ALTITUDE ISLAND PERMAFROST DURING THE CONSTRUCTION OF CFG PILE

Liu Jin-liang, Jia Yan-min

*Northeast Forestry University, School of civil engineering, Harbin, 150040, China;
jinliangliu_2015@126.com, yanminjia2008@126.com*

ABSTRACT

Cement fly ash gravel (CFG) pile composite foundation is an effective and economic foundation treatment approach, which is significant to building a foundation, subgrade construction, and so forth. The present paper aims to investigate the temperature behaviours of high latitudes and low altitude island permafrost when the CFG pile was constructed, in which FEM and field temperature monitoring of permafrost was utilized. The proposed findings demonstrate that the temperature disturbance of permafrost is obvious when the CFG pile was constructed, and the temperature variation of CFG pile and permafrost in FEM has a good agreement with the results of field temperature monitoring. Additionally, the influence of different height subgrade on the temperature field of CFG pile composite foundation was analyzed by FEM. The proposed findings demonstrate that the height of subgrade affects the maximum temperature increase of permafrost and the re-frozen time of permafrost after the construction of CFG pile composite foundation.

KEYWORDS

High latitudes and low altitude island permafrost, CFG pile composite foundation, Temperature monitoring, Finite element model, Height of subgrade

INTRODUCTION

Permafrost means various rock and soil below zero degrees centigrade and containing ice [1], it is widely distributed in the extreme northern locations of Eurasia, North American continent and many islands of the Arctic Ocean [2-3]. Permafrost has the feature of the rheological property, and its long-term intensity is far less than the instantaneous intensity. Because of these features, two significant risks must be faced by the engineering buildings in the permafrost zone: frost heave and thaw collapse [4-5]. Due to little cold source, the high latitude and low altitude island permafrost are more easily affected by heat disturbance. In the freeze-thawing process of permafrost, the foundation of a building may sink, crack and be lifted by frost [6]. During the highway construction, an engineer often uses pile foundation to stiffen permafrost structure, to increase the bearing capacity of subgrade [7-8]. As a kind of essential pile foundation, CFG pile composite is widely applied in the treatment for permafrost foundation owing to the following advantages: little heat radiation, excellent freeze-thawing resistance, large lifting amplitude of bearing capacity, simple construction, short construction period and low cost [9-14]. Foundation Institute of China Academy of Building Research developed a CFG pile composite foundation in the early 1990s [15], which greatly facilitated the development of composite foundation theory and design method. CFG pile is a high bond strength pile formed by cement, fly ash, gravel, aggregate chips, sand, and a moderate amount of water, together with soil between piles and cushion to form the composite foundation.

Permafrost is a kind of unique soil extremely sensitive to temperature change, its series of physical properties including specific heat, heat conductivity coefficient, and density vary following the change of temperature [16]. When a building is constructed in the permafrost, the hydration heat of concrete and the heat disturbance in construction may affect the stability of the permafrost below ground. After a building has been constructed, the permafrost will refreeze after long time, the building and the permafrost will lie under the state of heat balance again. In the process, the thermal properties of permafrost also change unceasingly, the changing properties of permafrost bring a lot of unstable factors for the construction above ground and the bearing capacity of permafrost foundation [17-19], even it will make the disturbed permafrost unable refreeze or the destruction of permafrost structure. Therefore, it has an important reality significance to research the effect of the construction process of building on the distribution and change law of the temperature field of permafrost. In the past years, many scholars started to pay attention to and research the disturbance effect of the construction of building on permafrost temperature and the re-frozen law of permafrost. On the basis of considering the effect of water on the temperature field of pile foundation, Harlan [20] amended the one-dimensional linear temperature field equation, added in the water field of pile foundation and raised the water-heat coupling equation set on pile foundation, in addition, elaborated the solution method in detail. Sun et al. [21] introduced the application of cast-in-site bored pile in Qinghai-Tibet Railway, analysed the heat disturbance theory of cast-in-site pile in permafrost layer and the factors affecting the re-frozen time of permafrost, the results show that cast-in-site bored pile is suitable for the application in the permafrost region. Zhao [22] researched the temperature change of a pile foundation in permafrost region under the influence of the construction disturbance of a single pile and the change of climatic conditions, put forward different temperature regulation & control measures used for the construction period and subsequent curing period. The study of [23] revealed that, the temperature of pile foundation changed dynamically under the coupling effect of hydration heat and ground temperature of permafrost, in addition, the temperature of permafrost below the upper limit tended to the ground temperature of permafrost in the local region after pile foundation refroze. Through model test, Zhai [24] researched the law of the effect of the hydration heat of cast-in-site bored pile on the upper temperature field of pile circumference under different permafrost temperatures. Fu et al. [25] researched the early-stage refrozen law of large-diameter cast-in-site bored pile in the permafrost region of Qinghai-Tibetan Plateau, it was suggested that the construction time of pile should be arranged in warm season, so as to provide excellent conditions for concrete curing. Shang et al. [26] researched the effect of the hydration heat of the cast-in-site bored pile in the permafrost region of Qinghai- 1m below ground kept stable at about 10°C, Tibetan Plateau on the temperature of soil around pile circumstance. The results of Shang et al. [26] explored that hydration heat of concrete has a large effect on the temperature of the permafrost located at 0.6m and 0.9m from the pile, while a little effect on the temperature of the permafrost located at 2m from the pile.

In the construction of CFG pile composite foundation, it should be avoided that the permafrost cannot be re-frozen or the permafrost was destroyed. Thus, it is of great necessity to explore the temperature performance characteristics of the permafrost when CFG pile foundation construction. Therefore, this paper compares the monitoring results of CFG pile construction temperature by finite element method and analyses the temperature characteristics of island permafrost and CFG pile during pile foundation construction, which can provide experience to the design and construction of the CFG pile composite foundation in island permafrost or permafrost with less cold source.

EXPERIMENT ON TEMPERATURE OF CFG PILE AND PERMAFROST

Engineering overview

Yichun-Suihua expressway is located in Heilongjiang Province, China. The route has to pass or go through an island permafrost region from k44+400 to k44+575 where is located in high latitudes and low altitude areas (as shown in Figure 1). Because the bearing capacity could not meet design requirements in the permafrost region, and the CFG pile composite foundation was applied, which showed the best reinforcement effect among the treatments. Because of the peculiarity of island permafrost, the depth and thickness of the permafrost at different locations are different. In this time, the zone where the temperature of permafrost was monitored was the region with central pile No. K44+525. According to the data on geotechnical test and geological survey, in the test area, the uppermost layer was the humus with 1.2m thick. Within the area 1.2m-3.2m from the top was richly frozen powdery soil with low liquid limit. Within the area of 3.2m-4.7m from the top was richly frozen clay with low liquid limit. In the area below 4.7m from the top was richly frozen granular sand, the thaw collapse is weak, this layer can be deemed as the bearing layer. The physical properties of all soil layers are listed in Table 1.

Because of a few cold sources, the high-latitude low-altitude island permafrost is easily disturbed by the external environment and the stability is inferior. The hydration heat of fly ash concrete is different from that of conventional concrete, and the past experiences are not applicable. In order to assure the stability and safety of island permafrost consolidated by CFG pile, a CFG pile was cast in the island permafrost region, the temperature of the CFG pile and permafrost were monitored. The temperature measurement point of the pile was embedded in the centre of the pile, from the pile bottom, for every other upward 1m, one temperature sensor was embedded. Temperature sensors were also embedded at the positions 0.6m, 1.0m and 1.4m from the centre of the CFG pile, the sensors were laid from the location 5m underground, for every other upward 1m, one sensor was embedded, five sensors were provided in every row. Figure 2 shows the layout diagram of the temperature sensor in the monitoring area.

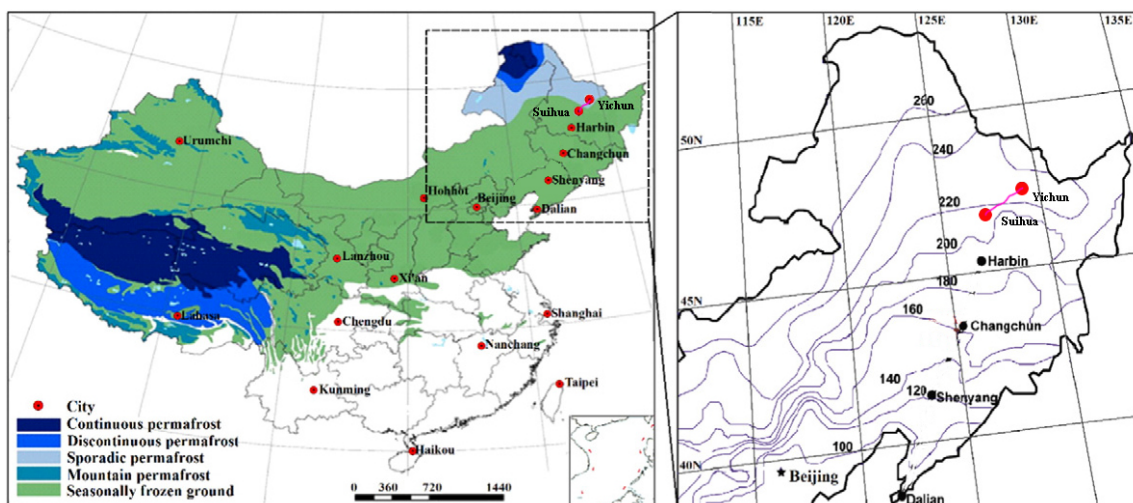


Fig. 1 - The position of expressway and permafrost

Tab. 1 - Physical parameters of permafrost [25]

| Geological condition | Water content | Dry density kg/m ³ | Thermal conductivity W/(m·K) | Specific heat capacity J/(kg·K) | Intent heat of phase change KJ/m ³ | c_p J/(kg·K) | c_{up} J/(kg·K) |
|---|---------------|----------------------------------|---------------------------------|------------------------------------|--|----------------------|----------------------|
| Humus | 22.70% | 1700 | 1.72 | 2825.82 | 127.8 | 2.23×10 ⁵ | 2.11×10 ⁵ |
| Low liquid limit silt Ice-rich frozen soil | 27% | 1575 | 1.008 | 2011.34 | 140.85 | 2.55×10 ⁵ | 2.33×10 ⁵ |
| Grade of thaw settlement: III | | | | | | | |
| Low liquid limit clay Ice-full frozen soil | 42.90% | 1400 | 1.38 | 3458.48 | 198.92 | 2.82×10 ⁵ | 2.14×10 ⁵ |
| Grade of thaw settlement: IV | | | | | | | |
| Sand grains Multi ice frozen soil | 19.80% | 1670 | 2.077 | 2573.225 | 109.52 | 5.69×10 ⁵ | 5.31×10 ⁵ |
| Grade of thaw settlement: II | | | | | | | |
| CFG Pile | - | 2500 | 1.74 | 2300 | 103 | - | - |

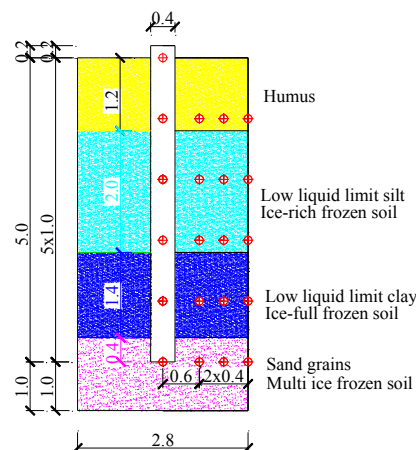


Fig. 2 - Layout diagram of temperature sensor in monitoring area (unit: m)

Analysis on temperature monitoring results

By monitoring the temperature of permafrost field and pile body in the construction process of CFG pile, the change trend and amplitude of the temperature of the permafrost beside pile can be known in the process of casting fly ash concrete. In addition, the curing temperature of the CFG

pile at the time when the strength of fly ash concrete achieves can also be known. According to the researches of the scholars for the application of pile foundation in permafrost, after pile concrete has been cast for one day, the temperature rise of the peripheral permafrost temperature field reaches the maximum value [26-27], therefore, after CFG pile was constructed, the temperature of the pile body and peripheral permafrost were measured in every day and at the same weather temperature. Figure 3 gives the temperature monitoring results of the pile and the permafrost within 140cm away from the pile centre on the 1st day, the 2nd day, the 3rd day, the 5th day, the 10th day and the 15th day.

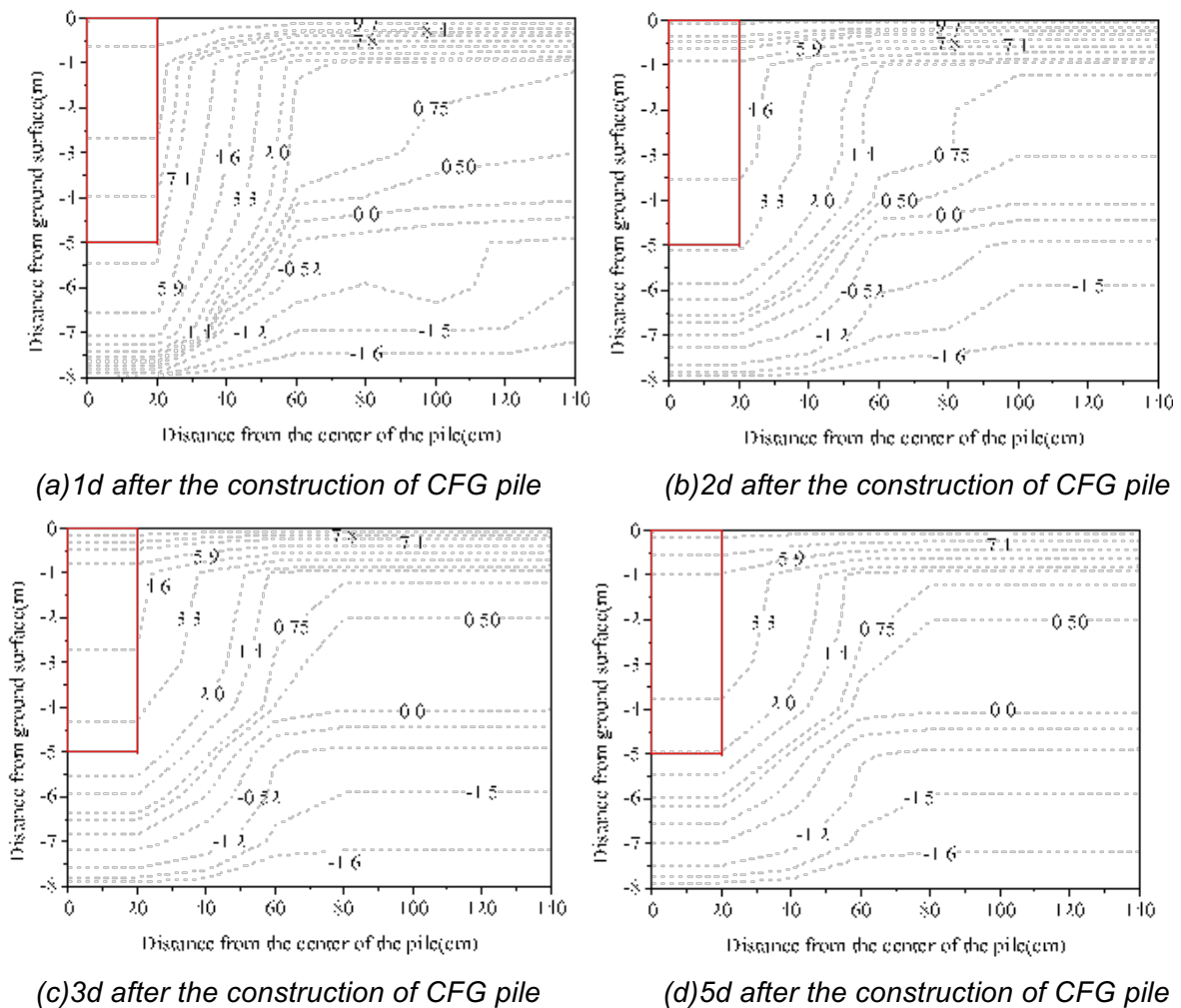


Fig. 3 - The variation of temperature field for CFG pile and permafrost with time

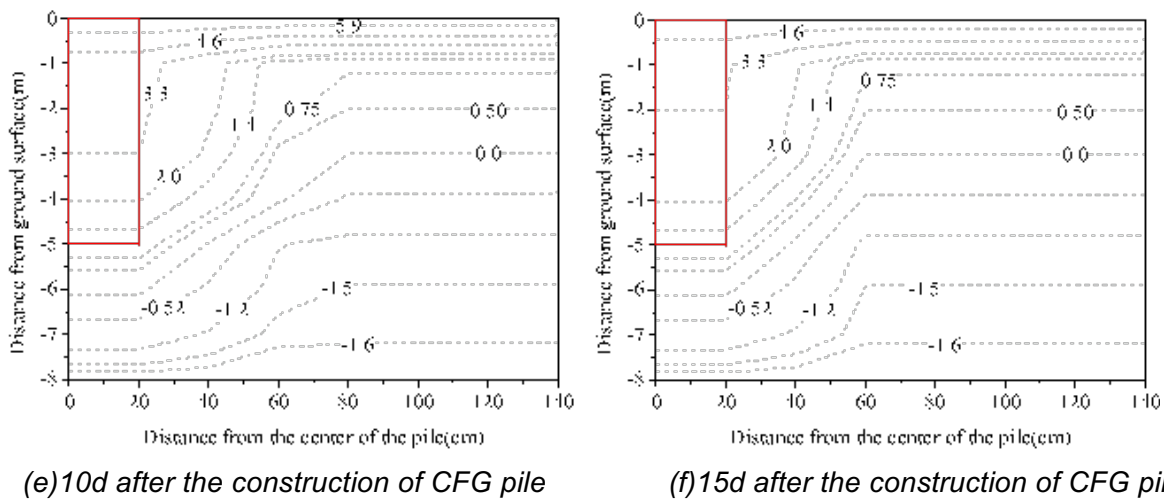


Fig. 3 - The variation of temperature field for CFG pile and permafrost with time

Figure 3 shows that 15 days after the CFG pile had been constructed, the temperature of the CFG pile decreased from 7.8°C~9.7°C to 2.0°C~3.8°C, also, the distribution of the effect caused by the temperature of peripheral permafrost to pile body was not even. Therefore, when CFG pile is designed, the effect of low-temperature curing environment on the strength of fly ash concrete shall be considered. Because the temperature of peripheral permafrost apparently affects the pile temperature, pile cracking and pile breakage caused by uneven temperature distribution of CFG pile shall be avoided. Due to the influence of the initial heat and hydration heat of fly ash concrete, the temperature of the permafrost beside pile rose apparently, the maximum value reached 7.1°C~9.7°C. The change of the thermal properties of the permafrost in this stage shall be considered in the design process. Following the unceasing release of the own heat of fly ash concrete and the hydration heat, the temperature of permafrost beside piles gradually decreased, the permafrost at the pile bottom unceasingly refroze upward. After CFG pile had been constructed for 15 days, the temperature changes of the permafrost beside pile tended to stability. The atmospheric heat continually transferred heat energy to permafrost via CFG pile, therefore, the permafrost beside pile kept at about 2.0°C and was hard to fully refreeze. It is suggested to prohibit applying a load in the permafrost zone beside pile within 15 days since construction of the CFG pile to avoid the settlement of peripheral permafrost under unstable state. From the temperature rise distribution area of the permafrost beside pile, it can be seen that the construction of CFG pile disturbed the permafrost within the scope of 1.5~2.0 times of pile diameter.

NUMERICAL METHOD

The construction of cast-in-site pile foundation in the permafrost region can bring heat for permafrost, the geothermal field will change correspondingly and the stable freezing state of permafrost will be destroyed, especially the hydration heat in concrete cast-in-site pile can cause serious thermal disturbance to stable permafrost, while fly ash concrete has unique feature of hydration heat. The research on the effect on the permafrost beside pile caused in the strength generation process of fly ash concrete is of extreme significance for the permafrost consolidation works. Therefore, it is considered to apply the 3D unsteady finite element with phase change for analysing the thermal disturbance caused by hydration heat to the temperature field of pile foundation in the construction of fly ash concrete cast-in-site pile; the result can provide a reference for the design and construction of CFG composite pile foundation in permafrost.

Numerical analysis model

According to the engineering background introduced in the above text, a numerical calculation model on CFG pile and permafrost was established, as shown in Figure 4. The model matched single-pile test. In the numerical calculation model on permafrost, the diameter of the CFG pile is 40cm, the pile length is 5.0m, the model involves in the scope of 1.4m away from the pile centre and the simulated depth of permafrost is 6.0m.

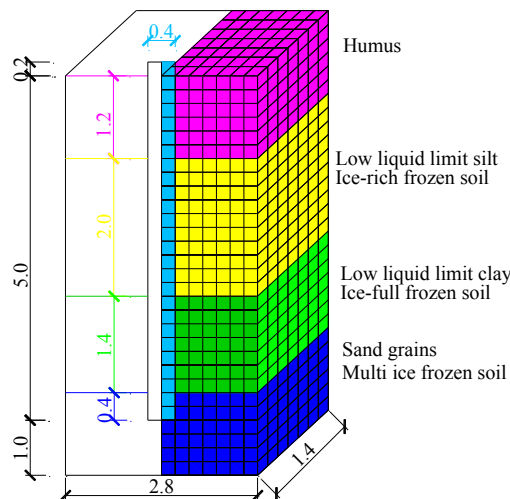


Fig. 4 - Numerical calculation model

Control equation and initial conditions on pile body temperature field

The CFG pile is made of fly ash concrete. Because mixed materials are added into concrete, the heat released in its hydration reaction stage is different from common concrete [28]. After fly ash has been added in, the hydration heat of concrete will decrease, the temperature field control equation of CFG pile at hydration heat are listed as follows:

$$\frac{\partial}{\partial x} \left(k_{fc} \frac{\partial T_{fc}}{\partial x} \right) + \frac{\partial}{\partial y} \left(k_{fc} \frac{\partial T_{fc}}{\partial y} \right) + \frac{\partial}{\partial z} \left(k_c \frac{\partial T_{fc}}{\partial z} \right) + q_v = \rho_{fc} c_{fc} \frac{\partial T_{fc}}{\partial t} \quad (1)$$

$$q_v = \rho_{fc} c_{fc} \frac{d\theta}{dt} = \frac{\rho_{fc} c_{fc} k_T \theta_u}{[1 + k_T (t - t_0)]} \quad (2)$$

In the formula, k_{fc} is the heat conductivity coefficient of fly ash concrete; T_{fc} is the temperature of fly ash concrete; q_v is the hydration heat of unit volume of fly ash concrete within unit time; c_{fc} is the specific heat of fly ash concrete; ρ_{fc} is the density of fly ash concrete; θ is the adiabatic temperature rise of fly ash concrete with different initial temperature and different age($^{\circ}\text{C}$), θ_u is the maximum adiabatic temperature rise of fly ash concrete($^{\circ}\text{C}$) [29-30]; k_T is the chemical reaction speed of the hydration heat of fly ash concrete at the initial temperature of T_0 (d-1), Carino [31] was used to describe the expression reflecting the effect of temperature on the hydration reaction of fly ash concrete, $k_T = Ae^{BT}$, A is a constant. For fly ash concrete, $A = 0.1362 \text{ d}^{-1}$; B is the temperature sensitivity coefficient($^{\circ}\text{C}^{-1}$), $B = 0.0553 \text{ }^{\circ}\text{C}^{-1}$; t is the actual curing time in adiabatic temperature rise (d); t_0 is the starting time of adiabatic temperature rise (d).

The initial condition of the pile temperature, i.e., the casting temperature, apparently disturb the hydration heat of pile body and permafrost [32], therefore, when fly ash concrete is cast in site, the casting temperature of concrete shall be measured. In numerical calculation, the initial condition of pile temperature is shown as follows:

$$T(x, y, z, t)|_{t=0} = T_1(x, y, z) \quad (3)$$

According to the measurement results obtained in casting CFG pile in the site, the casting temperature of fly ash concrete is 35°C.

Control equation and initial conditions on permafrost temperature field

The thawing process of permafrost is a heat conduction process accompanied with phase change, the calculation on the phase change of permafrost is simulated by Sensible Heat Capacity Method [33]. The 3D unsteady-state temperature field control equation on permafrost accompanied with phase change is shown as follows:

$$\rho_p c_p \frac{\partial T_p}{\partial t} = \frac{\partial}{\partial x} \left(k_p \frac{\partial T_p}{\partial x} \right) + \frac{\partial}{\partial y} \left(k_p \frac{\partial T_p}{\partial y} \right) + \frac{\partial}{\partial z} \left(k_p \frac{\partial T_p}{\partial z} \right) + q_v + \rho_p L_p \frac{\partial f_s}{\partial t} \quad (4)$$

In the formula, c_p is the specific heat of permafrost; ρ_p is the density of permafrost; T_p is the temperature of permafrost; k_p is the heat conduction coefficient of permafrost; L_p is the latent heat of phase change of permafrost; f_s is the solid fraction, the increase(decrease) of solid fraction is directly proportional to the release(absorption) volume of latent heat of phase change. When $f_s = 0$, permafrost lies under the state of liquid phase; when $f_s = 1$, permafrost lies under the state of solid phase; when $0 < f_s < 1$, both phases coexist.

The main difference between permafrost and thawed soil is that permafrost contains ice. Therefore, the specific heat of permafrost can be calculated according to the weighted mean of the masses of all material compositions [31]:

$$\left. \begin{aligned} c_p &= \frac{c_{sp} + Wc_w}{1 + W} \\ c_{up} &= \frac{c_{sup} + (W - W_u)c_i + W_u c_w}{1 + W} \end{aligned} \right\} \quad (5)$$

In the formula, c_{sp} is the framework specific heat of permafrost; c_{up} is the specific heat of thawed permafrost; c_{sup} is the framework specific heat of thawed permafrost; c_w is the specific heat of water; c_i is the specific heat of ice; W is the content of ice in permafrost; W_u is the content of unfrozen water in permafrost. The final heat properties of permafrost are shown in Table 1.

The initial temperature of permafrost affects the final temperature rise, in addition, it also affects the refreezing time of permafrost. Therefore, the initial temperature of permafrost is significant for the analysis on the permafrost temperature field in the construction process of the CFG pile. The equation for the initial condition of permafrost is shown as follows:

$$T(x, y, z, t)|_{t=0} = T_2(x, y, z) \quad (6)$$

The differences among the thermal properties of all permafrost layers cause the difference of the temperatures of all layers. According to the site measurement on permafrost temperature, the initial temperature of all layers of permafrost was determined as -1.3°C.

Finite element model on the unsteady-state temperature field of foundation

The abovementioned governing differential equation is converted into the equivalent integral form:

$$\int_v \left[\rho c (\delta T) \left(\frac{\partial T}{\partial t} + \{v\}^T \{L\}^T \right) + \{L\}^T (\delta T) \right] d_v = \int_{S_1} (\delta T) q^* dS_1 + \int_{S_2} (\delta T) h (T_B - T) dS_2 \quad (7)$$

In the formula, $\{v\}$ is the volume vector of unit; q^* is the heat flow in permafrost; $[D]$ is the heat conduction matrix in permafrost, δT is the allowable actual temperature; T_B is atmospheric temperature; S_1 and S_2 are respectively the surface applying heat flow and convection.

Seeing that the above problem is a strong-nonlinearity problem and it is hard to obtain the analytic solution. Therefore, the finite element method can be utilized to firstly divide the fixed solution domain into several units, an equation is established for each unit, the Direct Stiffness Method is applied to integrate them into an integral balance equation, for which Calculus of Differences is applied for solution.

Boundary conditions for numerical calculation

The calculation scope of the numerical model is large; it is deemed that the permafrost at the boundary of calculation model lies under the steady state and heat exchange does not exist. Therefore, the established 1/2 model is dealt with according to heat insulation conditions at the interface [34]:

$$\left. \begin{aligned} k \frac{\partial T}{\partial x} = 0 \quad (x = 1.4) \\ k \frac{\partial T}{\partial y} = 0 \quad (y = 1.4) \end{aligned} \right\} \quad (8)$$

The upper boundary of pile foundation contacts with air, therefore, the temperature at the pile top is related to atmospheric temperature cycle, the following formula was defined:

$$k \frac{\partial T}{\partial z} = h (T_{\text{ground}} - T_{\text{air}}) \quad (z = 0) \quad (9)$$

$$T_{\text{ground}} = -0.25 + 2.28 \times 10^{-6} t_h + 12.2 \sin \left(\frac{2\pi}{8640} t_h + \frac{4\pi}{3} \right) \quad (10)$$

In the formula, h is the convectional heat exchange coefficient between air and ground; T_{ground} is the bottom temperature of the boundary layer below ground [35]; T_{air} is the atmospheric temperature above ground. According to local temperature statistics, $T_{\text{air}} = 2.0^\circ\text{C}$ was applied, t_h is the time in every day.

At the bottom of the model, permafrost transfers heat to pile body, at the time, the boundary condition applies heat flow q in permafrost. The boundary condition is shown as follows:

$$k \frac{\partial T}{\partial z} = q \quad (z = 5.0) \quad (11)$$

In the formula, the underground heat flow applies $q = 0.5 \text{ kJ/m}^2 \cdot \text{h}$.

Analysis of numerical calculation results

In order to verify the accuracy of parameter selection and material use in the numerical calculation model, the temperature of the pile body and the permafrost around the pile at the same time of testing piles were respectively calculated, the results are listed in Figure 5.

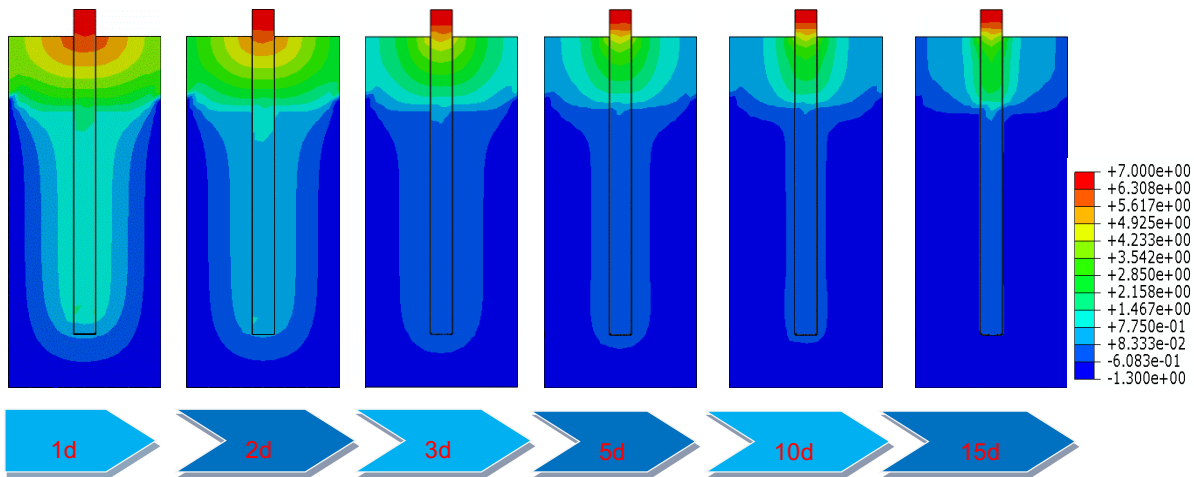


Fig.5 - The variation of temperature field for CFG pile and permafrost with time

The numerical analysis results show that (Figure 5), after CFG pile had been cast in site for one day, the temperature of pile body and its peripheral permafrost reached the highest value, the temperature of CFG pile was 0.7°C~2.1°C, the temperature of the permafrost beside the pile and within the scope of two times of pile interval rose to 1.4°C~4.2°C, the temperatures are basically consistent with the monitoring results in the temperature field of test pile. The simplified calculation for the initial temperature of the permafrost beside the pile causes the temperature rise of permafrost to be lower than the monitoring results. However, the disturbance scopes caused by pile casting to the temperature of peripheral permafrost are basically consistent. Following the gradual release of the initial heat and hydration heat of fly ash concrete, the permafrost beside the pile and at the pile bottom started to refreeze, the refreezing direction and scope of permafrost are consistent with the monitoring result in the temperature field. After CFG pile had been cast in site for 15 days, the heat exchange between pile body and peripheral permafrost terminated, the pile temperature was basically same as the temperature of peripheral permafrost, the pile temperature reached 0.8°C, and the permafrost around pile recovered to the initial temperature of -1.3°C. The numerical calculation result is a little lower than the monitoring result, the reason is shown as follows: for the simplification of numerical calculation, the process of transferring atmospheric heat to permafrost via CFG pile was not considered. In actual construction, after CFG pile and the permafrost beside pile refreeze basically, subgrade will be paved on the composite CFG pile foundation, while subgrade will isolate the path in which atmospheric heat is transferred into permafrost via pile. The permafrost beside pile can complete the refreezing process basically, and the simplified calculation is feasible in actual works. As mentioned above, the calculation values are in good agreement with the monitoring results in the temperature field of permafrost.

NUMERICAL SIMULATIVE ANALYSIS ON THE DISTRIBUTION OF TEMPERATURE FIELD OF PERMAFROST UNDER THE OPERATIONAL STATE

Numerical modelling

The effect of the construction of the CFG composite foundation on permafrost is not restricted in the construction process, the technical indices of roads and environmental factors will also affect the temperature of the reinforcement permafrost. However, due to restriction of personnel and fund, it is hard to collect enough data for analysis, the finite element software can be used for the numerical simulation of the technical indices of road and environment factors. The numerical calculation results can provide enough data for analyzing the effect of these factors on the change trend of permafrost temperature after construction of the CFG pile composite foundation. In this paper, ABAQUS, which was generally employed for geotechnical analysis, was used to develop the FE analysis.

According to the numerical analysis on the permafrost temperature field and the site monitoring results in the construction process of test pile, and the results of bearing test after the completion of test pile, on basis of the Design methods on Chinese Road Works [36], a design drawing on the CFG pile composite foundation constructed in the island permafrost region was determined, as shown in Figure 6. By utilizing the 2D heat processing module of ABAQUS, a thermotic finite element model on the subgrade, CFG pile composite foundation, raft and island permafrost was established. In the FE modelling (Figure 7), the location of the CFG pile and the distribution of permafrost layers are same as those shown in the design drawing (Figure 6). The physical parameters of all soil layers are shown in Table 1 and the properties of soil with temperature change base on REF. [37]. According to the site test results, the initial conditions of the model were exerted: the initial temperature of ground surface was 2°C, the initial temperature of permafrost was -1.3°C, the casting temperature of CFG pile was 35°C, the initial temperature of subgrade was 20°C.

The finite element numerical simulation will analyse the effect of different height of subgrades of subgrade and atmospheric temperature cycle on the temperature distribution law of island permafrost. The calculation process is divided into two analytic steps: In the first step, heat exchange calculation for CFG pile composite foundation and island permafrost was carried out. In the means of body heat flux, the hydration heat of fly ash concrete was exerted onto the pile as temperature load, the calculation time was 76 days. The analytic results will be taken as the initial conditions of the second analytic step. In the second analytic step, the soil of subgrade will be added into the calculation, according to the local monthly average temperature, the atmospheric heat cycle will be added into the calculation in the means of boundary conditions and the time span used for calculation is 12 months.

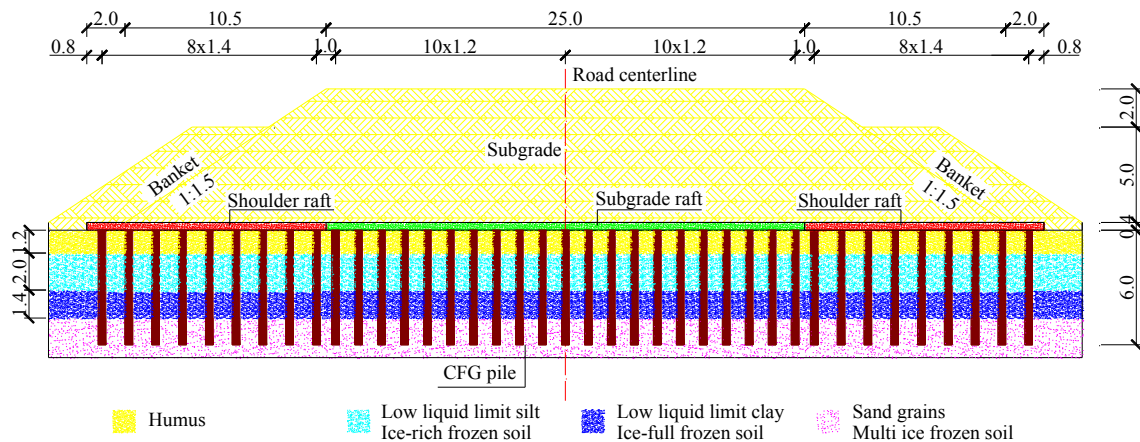


Fig. 6 - Cross section of permafrost was reinforced by CFG pile composite foundation in monitoring area (unit: m)

Raft(0.4m)

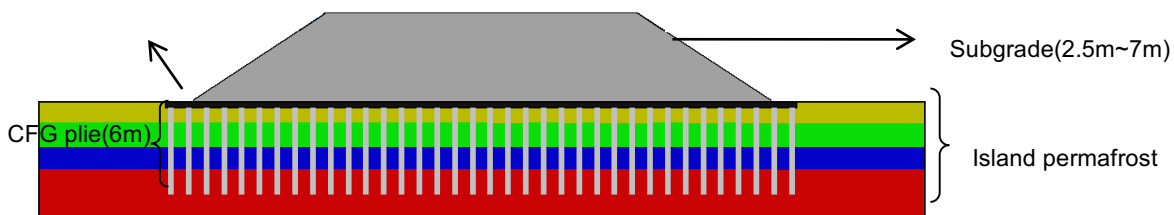


Fig. 7 - Finite element model

Effect of subgrade height on the distribution of permafrost temperature field

When a high-grade expressway is designed, in order to assure running safety and comfort, strict requirements are applied for route and lane slope, so different height of subgrades will be used for assuring reasonable longitudinal slope of the route [38]. The above analysis shows that the temperature of permafrost is significantly affected when subgrade is constructing. In order to analyse the process that different height of subgrades affect the temperature and the re-frozen time of permafrost, the paper established a finite element model respectively for the subgrade height of 2.5m, 3m, 4m, 5m, 6m, and 7m. In the analysis, the temperature change law of the permafrost layer 1m, 3m and 6m below ground were investigated. The finite element numerical calculation values are shown in Figure 8.

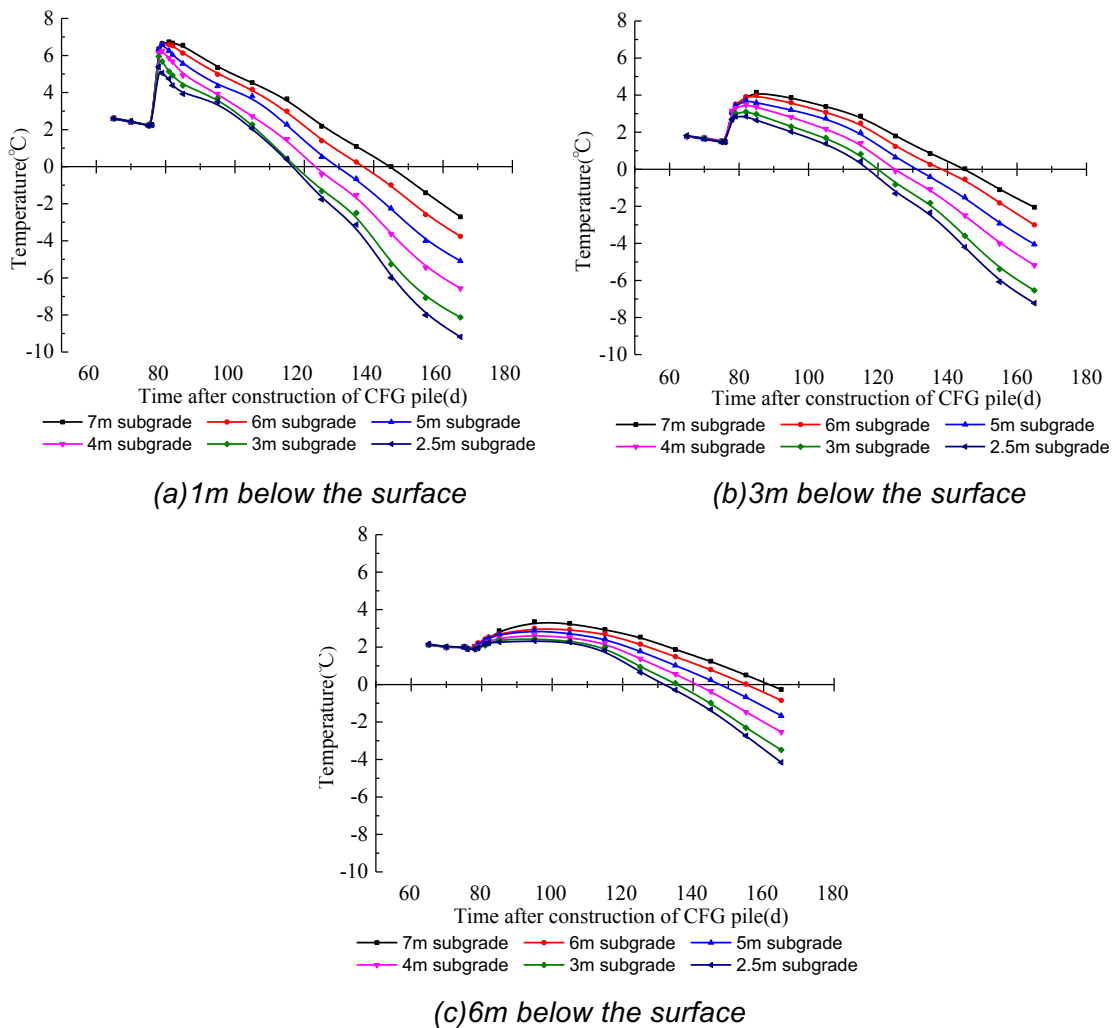


Fig. 8 - The temperature of permafrost varies with the height of subgrade

Figure 8 demonstrates that the subgrade fill apparently affected the temperature of island permafrost. The numerical simulation for 76d subgrade construction shows that, when the subgrade was 7m high, the temperature rose by 4.1°C at the location 1m below ground; when the subgrade was 2.5m high, the temperature rose by 3.1°C at the location 1m below ground. Following the increase of subgrade height, more heat was brought, and the effect on the depth of permafrost temperature became large. When the subgrade was 7m high, the temperature rose by 4.1°C, 2.7°C, and 1.5°C at the below ground location of 1m, 3m, and 2.5 respectively. the temperature rose by 4.1°C at the location 1m below ground, the temperature rose by 2.7°C at the location 3m below ground, and the temperature rose by 1.5°C at the location 6m below ground; While the subgrade was 2.5m high, the temperature rose by 3.1°C at the location 1m below ground, the temperature rose by 1.18°C at the location 3m below ground and the temperature analyzed the change rose by 0.4°C at the location 6m below ground. Following the increase of subgrade height, the heat transfer depth became large, and the decrease speed of permafrost temperature became slow. When the subgrade was 7m high, the temperature decrease speed at the location 1m below ground was 0.10°C/d; While the subgrade was 2.5m high, the temperature decrease speed at the location 1m below ground was 0.16°C/d. The subgrade height restricted the heat exchange between atmosphere and permafrost. Because of low subgrade height, the effect on permafrost temperature was small. Therefore, the re-frozen time of low subgrade was short. For the road

construction in permafrost area, traffic can be opened or load can be exerted in priority in the road segment with low subgrade height.

CONCLUSION

This paper studied the temperature characteristics of the CFG pile composite foundation in the application of high latitudes and low altitude island permafrost. The field temperature monitoring of permafrost was carried out to investigate the temperature variation of the CFG pile and permafrost during the construction of the CFG pile. FE modelling was used to discuss the temperature distribution of permafrost under the condition of different subgrade height and atmospheric temperature cycle. Based on the foregoing temperature characteristics studies, some of the main findings are summarized as follows:

(1) In the construction process of the CFG pile, the permafrost beside the pile reached the highest temperature of $7.1^{\circ}\text{C}\sim 7.9^{\circ}\text{C}$ after fly ash concrete had been cast for one day. 15 days later, the pile temperature and the temperature of permafrost beside pile realized a balance, the temperature of permafrost beside pile was 2.0°C . When the pile is applied for stiffening permafrost groundwork, the effect of low-temperature curing conditions on pile strength, pile cracking caused by uneven temperature or pile breakage shall be considered in the process of generating pile strength.

(2) The subgrade with different height had different effects on the temperature field of permafrost. When subgrade height decreased, the disturbance for permafrost temperature reduced, in addition, the re-frozen time of permafrost became short. The finite element calculation data show that, after subgrade construction, permafrost could complete refreezing only after one to two months. It is suggested that, within one to two months since subgrade filling, the surface construction or load exertion shall be reduced as far as possible, to make the permafrost at the bottom layer refreeze sufficiently, assure subgrade quality and reduce unnecessary economic loss.

The paper researched the effect of the construction process of CFG pile in island permafrost on the temperature of CFG pile and permafrost; the conclusions can provide a reference for the design on the CFG pile composite foundation used for consolidating permafrost. However, the changes of the physical properties of permafrost in freeze-thawing process are sometimes hard to control; this will lead to the destruction of the permafrost in use and affect road running. Therefore, the authores recommend future studies on the measures to reduce temperature disturbance in the construction of permafrost should be researched.

ACKNOWLEDGEMENTS

This work is financially supported by “the Fundamental Research Funds for the Central Universities” (Grant no. 2572017AB01), “Natural Science Foundation of Heilongjiang Province of China” (Grant no. E2017003), “Transportation Science and Technology Project of Heilongjiang Province Transportation Hall of China” (Grant no. 201519) and “Transportation Science and Technology Project of Liaoning Province of China” (Grant no. 201512 and Grant no. 201513).

REFERENCES

- [1] W. Ma, and D.Y. Wang, 2012. Studies on frozen soil mechanics in China in past 50 years and their prospect. *Chinese Journal of Geotechnical Engineering*, vol. 34, no. 4, pp.626-640.
- [2] V. S. Utkin, and L. A. Sushev, 2017. The Reliability Analysis of Existing Reinforced Concrete Piles in Permafrost Regions. *International Journal for Computational Civil and Structural Engineering*, vol. 13, no. 2, pp. 64-72.
- [3] G. Gabriel and Y. Yevgeniy, 2016. Estudio de las condiciones del techo del permafrost y de la capa activa del terraplén de asentamiento del Museo Otto Nordenskjöld, Isla Cerro Nevado, Antártida. *Revista de la Asociación Geológica Argentina*, vol.73, no. 4, pp. 552-562.
- [4] P. Perreault, and Y. Shur, 2016. Seasonal thermal insulation to mitigate climate change impacts on foundations in permafrost regions. *Cold Regions Science and Technology*, vol. 132, pp. 7-18.
- [5] J.F. Wang, K. Jia, R. Rafique, et al., 2016. Changes of backfill soil of tower foundation in the permafrost regions with warm ice-rich frozen soil on the Qinghai-Tibet Plateau. *Environmental Earth Sciences*, vol. 75, no. 21, Article ID 1416.
- [6] Y. M. Jia and D. Xu, 2013. Test and analysis of temperature field of CFG pile composite foundation in the island permafrost region. *Railway Engineering*, no. 10, pp. 80-83.
- [7] N. Khrenov, 2016. Some Recommendations for Ensuring the Stability of Pile Substructures for Above-Ground Routing of the Zapolyarno-Purpe Petroleum Pipeline. *Soil Mechanics & Foundation Engineering*, vol. 53, no. 2, pp. 139-142.
- [8] G. S. Crowther, 2015. Lateral Pile Analysis Frozen Soil Strength Criteria. *Journal of Cold Regions Engineering*, vol. 29, no. 2, Article ID 04014011.
- [9] A. J. Zhou and B. Li, 2010. Experimental study and finite element analysis of cushion in CFG pile composite foundation. *Rock and Soil Mechanics*, vol. 31, no. 6, pp. 1803- 1808.
- [10] F. Song, J. M. Zhang, and G. R. Cao, 2015. Experimental investigation of asymptotic state for anisotropic sand. *Acta Geotechnica*, vol. 10, no. 5, pp. 571-585.
- [11] X. Weng, Y. Nie, and J. Lu, 2015. Strain monitoring of widening cement concrete pavement subjected to differential settlement of foundation”, *Journal of Sensors*, vol. 2015, Article ID 679549,7 pages.
- [12] H. Yu, Y. Wang, C. Zou et al., 2017. Study on Subgrade Settlement Characteristics After Widening Project of Highway Built on Weak Foundation. *Arabian Journal for Science & Engineering*, vol. 7, no. 1, pp.1-10.
- [13] J. X. Lai, H. Q. Liu, J. L. Qiu et al., 2016. Stress Analysis of CFG Pile Composite Foundation in Consolidating Saturated Mine Tailings Dam. *Advances in Materials Science and Engineering*, vol. 2016, Article ID 3948754, 12 pages.
- [14] J. X. Lai, H.Q. Liu, J. L. Qiu, et al., 2016. Settlement Analysis of Saturated Tailings Dam Treated by CFG Pile Composite Foundation. *Advances in Materials Science and Engineering*, vol. 2016, Article ID 7383762, 10 pages.
- [15] L. Zhao, X. H. Wang, and H. B. Wu, 2008. Settlement calculation of CFG pile composite foundation under flexible foundation”, *Subgrade Engineering*, vol. 3, no. 138, pp. 147-149.
- [16] M. Christ, Y. C. Kim, J. B. Park, 2009. The influence of temperature and cycles on acoustic and mechanical properties of frozen soils. *Ksce Journal of Civil Engineering*, vol. 13, no. 3, pp. 153-159.
- [17] W. Nelson, A. Christopherson and D. Nottingham, 1992. Computer-based simulation of the ice fracture near a vertical pile. *International Journal of Offshore and Polar Engineering*, vol.2, no.2, pp.123-128.
- [18] X. X. Sun and H. Zhang, 2007. Experimental study on vertical pullout capacity of cast-in-site pile in permafrost region. *Rock and Soil Mechanics*, vol.28, no.10, pp. 2110-2116.
- [19] Q. B. Wang, 2014. Research For Bearing Capacity Of CFG Pile Raft Composite Foundation Of Road On The Permafrost [Ph.D. thesis], Northeast Forestry University, Harbin, China.
- [20] R. L. Harlan, 1973. Analysis of Coupled Heat-fluid Transport in Partially Frozen Soil. *Water Resources Research*, vol. 9, no.5, pp. 75-79.
- [21] C. X. Sun, A. M. Wang, X. Wang et al., 2007. Application of cast-in-place pile in permafrost regions of Qinghai-Tibet Railway. *Railway Engineering*, no. 11, pp. 65-67.
- [22] X. Y. Zhao, 2011. Numerical simulation of Pile Foundation Thermal Regime and Its Control Effect in Permafrost Regions [Master thesis], Chang’an University, Xi’an, China.
- [23] D. Z. Yu, 2015. Experimental Study of Bearing Capacity of Patchy Permafrost Pile Foundation in High Latitude Before and After Refrozen[Ph.D. thesis], Northeast Forestry University, Harbin, China.
- [24] Y. F. Zhai, 2016. Experimental research on thermal analysis and bearing behavior of cast-in-place bored in frozen soil foundation [Master thesis], Lanzhou Jiaotong University, Lanzhou, China.

- [25] D. Xu, 2013. The temperature field research of CFG composite foundation and the island permafrost [Ph.D. thesis], Northeast Forestry University, Harbin, China.
- [26] Xiong Wei, Liu Ming-gui, Zhang Qi-heng, Wang Zhi-ming, 2009. Temperature distribution along piles in permafrost regions. *Rock and Soil Mechanics*, no.6, pp.1658-1664.
- [27] X. H. Li, Y. P. Yang, Q. C. Wei, 2005. Numerical Simulation of Pile Foundation Conduction at Different Molding Temperature in Permafrost Regions. *Journal of Beijing Jiaotong University*, vol. 29, no.1, pp. 9-13.
- [28] Narmluk, Mongkhon, Nawa, Toyoharu, 2011. Effect of fly ash on the kinetics of Portland cement hydration at different curing temperatures. *Cement and Concrete Research*, vol.41, no.6, pp. 579-589.
- [29] Z. M. ZHANG, Z. T. SONG and H. Y. HUANG, 2002. New theory on adiabatic temperature rise and heat conduction equation of concrete. *Journal of Hehai University (Natural Sciences)*, vol.
- [30] J. C. WANG, P. Y. YAN, 2006. Experimental Analysis of Adiabatic Temperature Rise of Fly Ash Concrete", *Journal of Shenyang Jianzhu University (Natural Science)*, vol.22, no.1, pp.118-121.
- [31] L. Y. Tang, G. S. Yang and W. Y. YE, 2010. Thermal effects of pile construction on pile foundation in permafrost regions. *Chinese Journal of Geotechnical Engineering*, vol. 32, no.9, pp. 1350-1353.
- [32] Z. Y. Chen, C. Y. Li, Y. H. Mu, et al., 2014. Impact of molding temperature and hydration heat of concrete on thermal properties of pile foundation in permafrost regions along the Qinghai Tibet DC Transmission Line. *Journal of Glaciology and Geocryology*, vol. 36, no.4, pp. 818-827.
- [33] S. M. YANG and W. S. TAO, 2004. Heat transfer, Beijing: Higher Education Press.
- [34] Z. Zhuang, F. Zhang and S. Chen, 2009. Nonlinear finite element analysis and example of ABAQUS, Beijing: Science Press.
- [35] L.N. ZHU, 1988. Study of the adherent layer on different types of ground in permafrost regions on Qinghai-Xizang plateau. *Journal of Glaciology Geocryology*, no.1, pp.35-39.
- [36] Ministry of Communications of China, 2015. Design specification for Highway Subgrade (JTG D30-2015). China Communications Press: Beijing.
- [37] X. Z. Xu, J. C. Wang and L. X. Zhang, 2001. Permafrost physics, Science Press, Beijing, China.
- [38] C. Y. Zhuang, Y. F. Zhao, B. H. Pan et al., 2009. Research on Key Parameter of Highway Longitudinal Grade Design. *China Journal of Highway and Transport*, vol. 22, no.4, pp. 39-44.

THE EFFECT OF PORE DISTRIBUTION IN HISTORIC MASONRY ON THE GROUTING METHOD AND GROUTING MIX SELECTION

Jiří Witzany¹, Radek Zigler¹, Klára Kroftová², Tomáš Čejka¹,
Jan Kubát¹, Milan Holický³, Jiří Karas¹

1. CTU in Prague, Faculty of Civil Engineering, Department of Building Structures, Prague, Thákurova 7, Czech Republic; wizany@fsv.cvut.cz, zigler@fsv.cvut.cz, cejka@fsv.cvut.cz, jan.kubat.2@fsv.cvut.cz
2. CTU in Prague, Faculty of Civil Engineering, Department of Architecture, Prague, Thákurova 7, Czech Republic; klara.kroftova@seznam.cz
3. CTU in Prague, Klokner Institute, Prague, Šolínova 7, Czech Republic; milan.holicky@klok.cvut.cz

ABSTRACT

The NAKI II DG16P02M055 research project incorporates extensive experimental and theoretical research into the effect of grouting on the physical and mechanical characteristics of brick, stone and mixed masonry. The focus of the research is on the verification of particularly the reinforcing effect of selected grouting agents based on hydraulic lime (nanolime), resins and silicates. Selected materials are used for the monitoring of the effect of grouting on changes in the porosity, pore distribution, absorption capacity as compared to ungrouted masonry, and the reinforcing effect of grouting on historic brick, sandy marlstone, sandstone, trachyte, limestone and mixed masonry with a lime binder for different types of grouting agents as compared to ungrouted masonry.

KEYWORDS

Masonry, Grouting, Pore distribution, Stone, Brick, Experimental campaign

INTRODUCTION

The grouting of historic masonry with a degraded binder, damaged by cracks, or with high void contents and cavities represents a frequently applied rehabilitation method of historic masonry. Despite this, no objective background materials and procedures for the selection of the grouting method and mixture and the quantitative assessment of the grouting effect in terms of the physical and mechanical characteristics of the masonry have been elaborated to become a basis for the design and evaluation of the grouting effectiveness depending on the used grouting agent, grouting method and the properties of grouted masonry. The experimental verification of reinforcing grouting procedures abroad is primarily focused on multi-leaf masonry or masonry damaged by cracks. In [1], an empirical formula for the calculation of compressive strength of three-leaf masonry is derived as

$$f_{wc,i} = f_{wc,0} \left(1 + 1.25 \frac{V_i \sqrt{f_{gr,c}}}{V_w \cdot f_{wc,0}} \right) \quad (1)$$

where, $f_{wc,0}$ and $f_{wc,i}$ denote the compressive strength of the masonry before and after grouting; V_i and V_w the volume of the filling material and of the whole wall, respectively; and $f_{gr,c}$ is the compressive strength of the grout.

In [2], Valluzi used a formula for the calculation of the compressive strength of grouted masonry where the compressive strength of the grouted (filling) material is calculated as the function of the compressive strength of the grouting mix

$$f_{wc,i} = f_{wc,0} \left(1 + \frac{V_i f_{i,s}}{V_w f_{wc,0}} \right) \quad (2)$$

$$f_{i,s} = 0.31 \cdot f_{gr,c}^{1.18} \quad (3)$$

where, $f_{i,s}$ denotes the compressive strength of the grouted filling material.

The authors [1] conclude that the compressive strength of the mixture is not the crucial characteristic for the grouting effectiveness in the respective case of the filling material. Likewise, study [3] based on tests whose objective was to specify the mechanical properties of three-leaf stone masonry concluded that although the strength of ternary grouts is nearly twice the strength of the hydraulic lime-based grout, the strength of the grouting mixture does not principally affect the final compressive strength of the grouted wall. Due to the homogenization of multi-leaf masonry, improved mechanical characteristics of the masonry are achieved even in the case of a mixture that does not contain cement.

Based on observations, study [1] claims that the compressive strength of the grouted masonry also depends on the tensile strength of the grouting mix. The formula designed for the prediction of the compressive strength of the grouted filling material in [1] reads

$$f_{i,s} = 1.60 + 0.50 f_{gr,t} \quad (4)$$

where, $f_{gr,t}$ the bending tensile strength of the grout.

Mixtures based on hydraulic lime modified with admixtures are most commonly applied for historic masonry. In [4], experimental tests and in-situ applications (Crete) were performed with a mortar based on natural hydraulic lime (as a binding material), siliceous sand and crushed brick. Based on the results of the tests and measurements done three years later, further use of hydraulic lime mortars is recommended in [4].

In justified cases, a grouting mixture with small amounts of cement (5 to 10%), or with substances based on resins is also applied. In a similar way, study [5] verified lime-based grouts in several series with gradual additions of other components (pozzolan, clay, brick dust and their combinations). On the basis of the results of testing, a grouting mixture with the following composition: lime : brick dust : pozzolan, is, among others, recommended, which is effective in terms of strength development (measured at 28 and 90 days).

Modified admixtures of grouting mixes based on hydraulic lime such as pozzolan, lime, clay and brick dust are effective in modifying the rheological, volume changes and strength of the grouted masonry. The resulting properties of the grouted masonry may be, to some extent, affected by the non-compatibility of the original mortar and the grouting mix (different porosity, chemism, mineralogical and chemical characteristics). Adding pozzolan, lime or cement admixtures can affect both the tensile and shear strength, the bonding of the original binder and the grouting mix (new binder). Grouting agents based on minerals and hydraulic lime are suitable for the masonry of historic and particularly heritage buildings.

Local strengthening of material by modifying the masonry pore system's properties can be achieved by using mixes based on silicates. Like resin-based mixes, these mixes penetrate inside the pore system to a depth of 50 to 60 mm from the grouting borehole.

As part of the NAKI II research project (DG16P02M055 project "Research and development of materials, processes and techniques for the restoration, preservation and strengthening of historic masonry structures and surfaces and systems for preventive protection of historic and listed buildings threatened by anthropogenic effects"), extensive experimental and theoretic research is conducted investigating the effect of grouting on the physical and mechanical characteristics of the brick, stone and mixed masonry most commonly used in historic buildings. The analysis of the experimental and laboratory research is focused on the verification of the effect of the grouting method used (pressure and pressureless), the grouting agent type (agents based on minerals, resins and silicates) on the principal physical (pore system) and mechanical characteristics (strength, deformation characteristics) of the masonry. In the first research phase, test pieces of brick, stone and mixed masonry without an initial crack were tested (except for microcracks and structural cracks caused by volume changes of the binder, or by handling). In the second phase, the research will cover masonry columns with an initial crack and masonry columns with cavities.

The following parts present partial results of the first research phase investigating the effect of the grouting method, the masonry pore system, grouting agent's particle size, porosity on strength in concentric compression of the grouted masonry.

EXPERIMENTAL AND LABORATORY RESEARCH OF THE EFFECT OF GROUTING ON THE PHYSICAL AND MECHANICAL CHARACTERISTICS OF BRICK, STONE AND MIXED MASONRY

The subject of the experimental research into the effect of grouting on the principal physical characteristics of individual components of historic masonry was the identification of total porosity, pore distribution and integral pore system curves. The research focused on the principal mechanical characteristics included the identification of the strength characteristics of individual components of historic masonry, the strength (load-bearing capacity) of test pieces of ungrouted masonry and test pieces of grouted masonry. The analysis of the results was carried out on the basis of a limited number of masonry test pieces, which did not allow statistical analysis. With a view to this fact and considering the scattering of the physical and mechanical characteristics of the masonry, the results of this analysis need interpretation.

Research into the effectiveness of grouting involved masonry test pieces with dimensions of 300 x 450 x 420 to 450 mm, or 300 x 600 x 420 to 450 mm (brickwork columns) and 500 to 550 x 600 to 650 x 700 to 750 mm (stonework and mixed columns). The brickwork columns were walled with P20 solid burnt bricks on a lime mortar with a 5% admixture of MV 1 cement mixed in a 1:1 ratio with sand with a grain size of 0-2 mm. The stonework columns were built as irregular masonry of quarried stone – sandy marlstone, sandstone, limestone, trachyte, or as mixed masonry with sandy marlstone, limestone and bricks. The test pieces of stone masonry were walled on mortar with a lime binder (lime mortar 1:3 made from 5-year aged slaked lime and sand with a grain size of 0-4 mm).

The test pieces of brick, stone and mixed masonry are listed in Table 1 and Table 2 and displayed in Figure 1 and Figure 2.

After reaching the required mortar strength, all masonry columns were fitted with drilled holes 18 mm in diameter for pressure grouting and 22 mm in diameter for pressureless grouting inclined at ca 37° (27°) from the horizontal in the brickwork columns and running to a depth of 450 (600) mm, and at 30° from the horizontal in the stonework columns and terminated ca 50 mm from the masonry edge. The grout was applied as low-pressure (LP) using a low-pressure membrane pump for grouting suspensions and a piston grout pump for grouting resins, or as pressureless (PL) where the grout was applied by hydrostatic pressure. After the grouting procedure was

completed, the grout holes were filled with a mix with very low shrinkage (Oxal VP TK2). Individual sets of the test pieces included a so-called reference column, which had gone through all the preparatory phases in the same way as the grouted columns, i.e. drilling a grout hole and its filling with a mix with very low shrinkage (Oxal VP TK2). The tests of the grouted columns and the reference column were performed ca 3 to 4 weeks after the grouting procedure and filling the grout hole.

Tab. 1 - Overview of test pieces – brick masonry

| Label | Dimensions width/ thick./height | | | Mortar | $f_{tension, m}$ | $f_{compr, m}$ | $f_{compr, b}$ | $f_{k, masonry}$ accord. EC6 | grouting mixture | grouting method |
|------------|------------------------------------|-----|-----|------------|------------------|----------------|----------------|---------------------------------|---------------------|--------------------|
| | mm | mm | mm | | MPa | MPa | MPa | MPa | | |
| CP01.45-P3 | 300 | 450 | 450 | Mortar 1:1 | 0.21 | 0.50 | 22.01 | 3.89 | P3 | low-pressure |
| CP02.45-V4 | | | | | | | | | V4 | low-pressure |
| CP03.45-V3 | | | | | | | | | V3 | low-pressure |
| CP04.45-P2 | | | | | | | | | P2 | low-pressure |
| CP05.45-P2 | | | | | | | | | P2 | pressureless |
| CP06.45 | | | | | | | | | - | - |
| CP07.45-K1 | 300 | 450 | 450 | | 0.16 | 0.48 | 22.01 | 3.83 | K1 | pressureless |
| CP08.45-V2 | | | | | | | | | V2 | low-pressure |
| CP09.45-K1 | | | | | | | | | K1 | low-pressure |
| CP10.45-V1 | | | | | | | | | V1 | low-pressure |
| CP11.45-P1 | | | | | | | | | P1 | low-pressure |
| CP12.45 | | | | | | | | | - | - |
| CP01.60-P3 | 300 | 600 | 450 | Mortar 1:1 | 0.20 | 0.46 | 22.01 | 3.8 | P3 | low-pressure |
| CP02.60-V4 | | | | | | | | | V4 | low-pressure |
| CP03.60-V3 | | | | | | | | | V3 | low-pressure |
| CP04.60-P2 | | | | | | | | | P2 | low-pressure |
| CP05.60-P2 | | | | | | | | | P2 | pressureless |
| CP06.6 | | | | | | | | | - | - |
| CP07.60-K1 | 300 | 600 | 450 | | 0.18 | 0.46 | 22.01 | 3.79 | K1 | pressureless |
| CP08.60-V2 | | | | | | | | | V2 | low-pressure |
| CP09.60-K1 | | | | | | | | | K1 | low-pressure |
| CP10.60-V1 | | | | | | | | | V1 | low-pressure |
| CP11.60-P1 | | | | | | | | | P1 | low-pressure |
| CP12.60 | | | | | | | | | - | - |

Note:

Mortar 1:1 – common lime mortar with 5% cement admixture diluted with sand in the 1:1 ratio, experimentally determined compressive strength 0,45 - 0,55 MPa

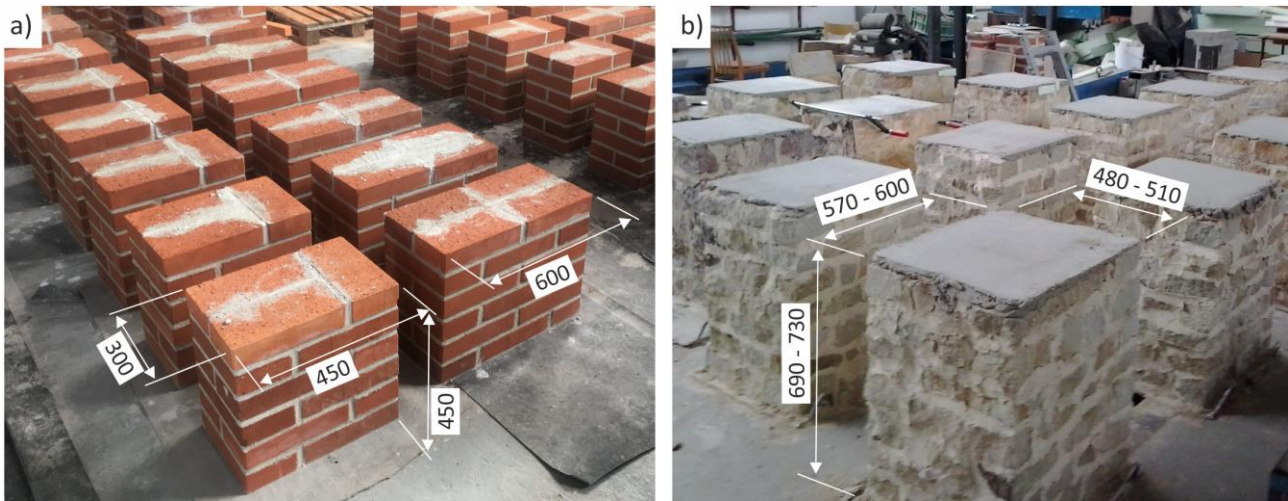


Fig. 1 - Experimental test pieces of brick masonry (a) and stone masonry (b)

Tab. 2 - Overview of test pieces – stone masonry

| Label | Dimensions width/thick./height | | | Mortar | $f_{tension, m}$ | $f_{compr, m}$ | $f_{compr, b}$ | $f_{k, masonry}$ accord. EC6 | grouting mixture | grouting method |
|------------|-----------------------------------|-----|-----|-----------------------|------------------|----------------|----------------|---------------------------------|---------------------|--------------------|
| | mm | mm | mm | | MPa | MPa | MPa | MPa | | |
| KP.ON01-V3 | 490 | 570 | 690 | lime mortar 1:3 | 0.20 | 0.80 | 15.17 | 0.35 | V3 | low-pressure |
| KP.ON02-K1 | 510 | 600 | 715 | | 0.20 | 0.80 | 15.17 | 0.35 | K1 | low-pressure |
| KP.ON03-P1 | 490 | 580 | 700 | | 0.20 | 0.80 | 15.17 | 0.35 | P1 | low-pressure |
| KP.ON04-V6 | 500 | 580 | 710 | | 0.32 | 0.83 | 15.17 | 0.34 | V6 | low-pressure |
| KP.ON05 | 500 | 595 | 710 | | 0.32 | 0.83 | 15.17 | 0.34 | - | - |
| KP.PN01-V3 | 495 | 590 | 700 | | 0.32 | 0.83 | 46.35 | 0.49 | V3 | low-pressure |
| KP.PN02-K1 | 505 | 585 | 705 | | 0.30 | 0.83 | 46.35 | 0.49 | K1 | low-pressure |
| KP.PN03-P1 | 475 | 600 | 720 | | 0.30 | 0.83 | 46.35 | 0.49 | P1 | low-pressure |
| KP.PN04-V7 | 490 | 600 | 730 | | 0.30 | 0.83 | 46.35 | 0.49 | V7 | low-pressure |
| KP.PN05 | 485 | 595 | 730 | | 0.32 | 1.01 | 46.35 | 0.52 | - | - |
| KP.TN01-K1 | 495 | 595 | 700 | | 0.32 | 1.01 | 63.58 | 0.56 | K1 | low-pressure |
| KP.TN02-P1 | 500 | 600 | 715 | | 0.32 | 1.01 | 63.58 | 0.56 | P1 | low-pressure |
| KP.TN03-V5 | 495 | 600 | 700 | | 0.32 | 0.79 | 63.58 | 0.52 | V5 | low-pressure |
| KP.TN04 | 480 | 595 | 695 | | 0.32 | 0.79 | 63.58 | 0.52 | - | - |
| KP.VN01-K1 | 480 | 590 | 740 | | 0.28 | 0.83 | 111.13 | 0.64 | K1 | low-pressure |
| KP.VN02-P1 | 480 | 590 | 710 | | 0.28 | 0.98 | 111.13 | 0.70 | P1 | low-pressure |
| KP.VN03 | 480 | 595 | 715 | | 0.28 | 0.98 | 111.13 | 0.70 | - | - |

Note:

Lime mortar 1:3 – lime mortar without cement, 5 years old slaked lime, diluted with sand in the 1:3 ratio, experimentally determined compressive strength 0,8 - 1,01 MPa



Fig. 2 - Experimental test pieces of brick (a) and stone (b) masonry during compressive tests

Experimentally verified grouting agents

According to the main base, the grouting agents were divided into 3 basic groups:

- Hydraulic lime-based grouts
- Resin-based grouts
- Silicate-based grouts

Within experimental research, a total of 11 different grouts were applied, of them 7 based on hydraulic lime, 3 based on resins and 1 grout based on silicates:

• Lime-based grouts

V1 Mixture of natural hydraulic lime and mineral admixtures without cement with good fluidity, filling ability and with no shrinkage after adding water, high resistance to water-soluble sulphates, bending strength at 28 days of ca 0.6 N/mm², compressive strength of ca 2.5 N/mm², dynamic modulus of elasticity of 2.5kN/mm². Filling and shaping joints, small cavities, cracks from 2 to 10 mm

V2 Two-component suspension from ultrafine hydraulic binder and a liquid grouting admixture resistant to sulphates, high initial strength (compressive strength at 7 days > 5 N/mm², at 28 days > 20 N/mm²), water impermeable. Filling cracks and cavities in concrete, mortar, brick and stone masonry, strengthening and increasing the load-bearing capacity of foundations

V3 Mixture based on hydraulic lime and mineral admixtures without cement, resistant to sulphates, with very low modulus of elasticity, low viscosity and good fluidity, mechanical characteristics at 28 days: bending strength of ca 3.3 N/mm², compressive strength of ca 16 N/mm², dynamic modulus of elasticity of 9.6 kN/mm². Filling and shaping joints, cavities, small

cracks, sealing, stabilization and strengthening of stone, mixed and multi-leaf masonry which is not exposed to permanent (long-term) loading with water (moisture)

V4 Trass-lime-based mixture resistant to sulphates, with very low modulus of elasticity, low viscosity, good fluidity and very low shrinkage, compressive strength at 28 days > 5 N/mm². Filling and shaping joints, cavities, small cracks, sealing, stabilization and strengthening of stone, mixed and multi-leaf masonry which is not exposed to permanent (long-term) loading with water (moisture)

V5 Calcium lime test portion was dispersed in ethanol and distilled water was added. The mixture was left in the magnetic stirrer for 24 hours. The resulting suspension was made by filling the reaction mix to a volume of 1 litre. The Ca(OH)₂ concentration is 5 g/l. Larger particles and lower viscosity than Ca₄. Strengthening, sealing concrete and brick, stone and mixed masonry

V6 Calcium methoxide test portion was dispersed in isopropyl alcohol and distilled water was added. The mixture was left in the magnetic stirrer for 24 hours. The resulting suspension was made by filling the reaction mix to a volume of 1 litre. The Ca(OH)₂ concentration is 5 g/l. Strengthening, sealing concrete and brick, stone and mixed masonry

V7 Test portions of calcium acetate Ca(OCOCH₃)₂ · H₂O and magnesium acetate Mg(OCOCH₃)₂ · 4H₂O, which were dissolved in distilled water. Strengthening, sealing concrete and brick, stone and mixed masonry

- **Resin-based grouts**

P1 Two-component epoxy resin with low viscosity of 100 mPa*s, mechanical characteristics at 7 days – tensile strength of 51 N/mm², bond strength of 7.4 N/mm², friction of 16.8 N/mm². Filling cracks and cavities in concrete

P2 Acrylate-based low-viscosity (ca 5 mPa*s) resin with very good penetration into fine-grained conglomerates, allowing grouting into dry, moist as well as water soaked environments, watertight, resistant to compression, compressive strength of 12.5 N/mm². Strengthening, sealing concrete and masonry, strengthening, sealing and improving cohesion of rocks and fine-grained soils

P3 Epoxy-based two-component duromer resin with high penetration activity, allowing grouting into moist environments as well, with fast increase in strength, hardening even under dynamic loading, tensile strength of ca 45.7 N/mm², compressive strength of ca 60 N/mm², modulus of elasticity of 2.6kN/mm². Strengthening, filling cracks, cavities, joints

- **Silicate-based grout**

K1 Based on silicic acid ethyl ester with no content of solvents with gel separated amounts greater than 40%, with deep penetration and high resistance to weathering and UV radiation, colourless to slightly yellowish. Strengthening of porous, moisture-absorbing, mineral building material (mainly sandstones, weathered bricks, mortar)

The grouts labelled V5, V6 a V7 based on nanoparticles were developed within the NAKI II DG16P02M055 research project in cooperation with The Centre of Polymer Systems, Tomas Bata University in Zlín [6], [7] and [8].

Table 3 presents the main characteristics of the grouting agents, including the spectrum and the particle proportion contained in the grout.

Tab. 3 - Main characteristics of grouting agents

| Label | Characteristic | Strength | Particle size (diameter) |
|-------|---|---|--------------------------|
| V1 | Mixture of natural hydraulic lime and mineral admixtures without cement | at 28 days bending strength ca 0.6 N/mm ² , compressive strength ca 2.5 N/mm ² | 1000 – 4000 nm |
| V2 | Two-component suspension from ultrafine hydraulic binder and a liquid grouting admixture | compressive strength at 7 days > 5 N/mm ² , at 28 days > 20 N/mm ² | 500 – 2500 nm |
| V3 | Mixture based on hydraulic lime and mineral admixtures without cement | at 28 days: bending strength ca 3.3 N/mm ² , compressive strength ca 16 N/mm ² | 160 – 2000 nm |
| V4 | Trass-lime-based mixture | compressive strength at 28 days > 5 N/mm ² | 1500 – 4000 nm |
| V5 | Calcium lime test portion dispersed in ethanol | n/a | 1330 – 1770 nm |
| V6 | Calcium methoxide test portion dispersed in isopropyl alcohol | n/a | 220 – 360 nm |
| V7 | Test portions of calcium acetate and magnesium acetate dissolved in distilled water | n/a | 35 – 835 nm |
| P1 | Two-component epoxy resin | at 7 days - tensile strength 51 N/mm ² , bond strength 7.4 N/mm ² , friction 16.8 N/mm ² | n/a |
| P2 | Acrylate-based low-viscosity resin | compressive strength 12.5 N/mm ² | n/a |
| P3 | Epoxy-based two-component duromer resin | tensile strength ca 45.7 N/mm ² , compressive strength ca 60 N/mm ² | n/a |
| K1 | Based on silicic acid ethyl ester with no content of solvents with gel separated amounts greater than 40% | n/a | n/a |

Laboratory research into porosity

The laboratory research into porosity was carried out in cooperation with the Institute of Rock Structure and Mechanics of the Academy of Sciences CR using the high-pressure mercury method on specimens of solid burnt bricks, sandy marlstone, sandstone, limestone, trachyte and lime mortar. The measurement was performed on specimen chippings sized 5 mm of the materials used in the test columns. The measurement was made on a set of Pascal 140 + 240 fir Thermo Electon – Porotec porosimeters. Based on the results of mercury porosimetry, the distribution and integral curves of the pore system of individual materials (masonry units) were drawn before and after grouting. The specimens of masonry units for porosity detection after grouting were sampled from the masonry columns after the load test from places in the vicinity of the grouting borehole (ca within a distance of 40 to 60 mm), from the grout hole and from places close to the masonry unit edge (ca 50 mm from the unit edge).

Table 4 and Table 5 list the characteristic values of the pore system of the masonry units and mortar detected by mercury porosimetry from the sampled specimens before and after the grout application. Figure 3 displays the time patterns of the distribution and integral curves illustrating the pore distribution in the selected materials from a radius of 0 to 10 nm up to a size of 30 000 to 50 000 nm.

Tab. 4 - Pore distribution in bricks and mortar

| Material – brick masonry | Total porosity (%) | Pore radius (nm) | | | | | | | |
|--------------------------|--------------------|------------------|---------|----------|-----------|------------|-------------|--------------|---------------|
| | | 0 - 10 | 10 - 25 | 25 - 150 | 150 - 600 | 600 - 2000 | 2000 - 7500 | 7500 - 30000 | 30000 - 50000 |
| brick P20 | 32.85 | 0.48 | 2.08 | 10.15 | 19.57 | 42.58 | 18.38 | 4.56 | 2.24 |
| brick P20 + V3 | 29.56 | 0.55 | 0.84 | 5.41 | 13.3 | 35.41 | 32.15 | 10.28 | 2.08 |
| brick P20 + K1 | 31.46 | 0.65 | 1.45 | 5.4 | 10.99 | 35.34 | 34.33 | 8.51 | 3.34 |
| brick P20 + V1 | 29.32 | 1.16 | 2.56 | 12.94 | 21.85 | 35.88 | 13.45 | 8.84 | 3.33 |
| mortar 1:1 | 32.35 | 0.32 | 2.46 | 6.8 | 7.22 | 14.11 | 17.97 | 28.79 | 22.32 |
| mortar 1:1 + V3 | 31.69 | 1.81 | 4.66 | 7.51 | 8 | 11.62 | 12.3 | 47.01 | 7.09 |
| mortar 1:1 + K1 | 31.25 | 2.46 | 3.76 | 8.62 | 10.25 | 14.23 | 22.29 | 29.14 | 9.24 |
| mortar 1:1 + V1 | 30.05 | 1.98 | 4.08 | 8.62 | 10.17 | 15.26 | 21.36 | 28.06 | 10.47 |

Note:

- dominant pores

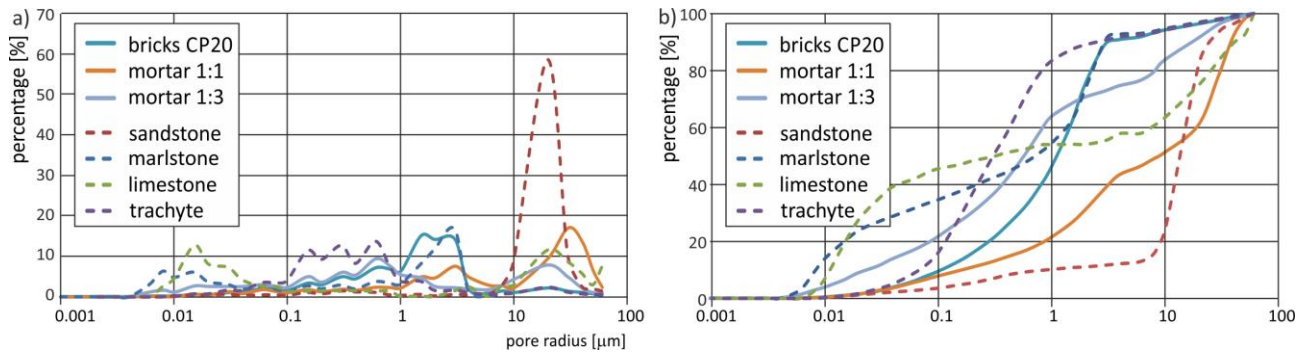


Fig. 3 - Distribution (a) and integral (b) curves of pore representation in bricks, mortar and stone units

Tab. 5 - Pore distribution in stone units and mortar

| Material – stone masonry | Total porosity (%) | Pore radius (nm) | | | | | | | |
|--------------------------|--------------------|------------------|---------|----------|-----------|------------|-------------|--------------|---------------|
| | | 0 - 10 | 10 - 25 | 25 - 150 | 150 - 600 | 600 - 2000 | 2000 - 7500 | 7500 - 30000 | 30000 - 50000 |
| marlstone + V3 | 21.47 | 20.13 | 10.44 | 6.85 | 8.97 | 22.77 | 25.28 | 3.79 | 1.79 |
| marlstone + K1 | 29 | 11.78 | 10.88 | 8.11 | 9.67 | 26.78 | 29.11 | 2.22 | 1.44 |
| marlstone + P1 | 26.53 | 14.35 | 11.1 | 9.08 | 9.98 | 24.77 | 23.64 | 4.71 | 2.35 |
| marlstone + V6 | 26.49 | 17.4 | 17.8 | 7.9 | 7.5 | 17.41 | 26.78 | 3.61 | 1.62 |
| marlstone | 26.4 | 14.11 | 12.94 | 10.35 | 10.7 | 26.35 | 19.41 | 4.36 | 1.77 |
| sandstone + V3 | 15.74 | 0 | 2.52 | 4.09 | 3.31 | 1.45 | 11.39 | 74.3 | 2.91 |
| sandstone + K1 | 15.83 | 0.28 | 2.82 | 2.82 | 2.54 | 2.53 | 9.59 | 71.56 | 7.89 |
| sandstone + P1 | 15.48 | 0.2 | 1.37 | 3.05 | 2.85 | 1.48 | 10.13 | 78.05 | 2.85 |
| sandstone + V7 | 15.18 | 0.17 | 2.55 | 4.76 | 5.61 | 1.19 | 10.19 | 70.29 | 5.27 |
| sandstone | 18.92 | 0.25 | 1.16 | 2.86 | 4.61 | 1.74 | 4.98 | 77.83 | 6.1 |
| trachyte + K1 | 6.79 | 0.48 | 10.2 | 16.47 | 29.35 | 19.58 | 11.7 | 8.59 | 3.81 |
| trachyte + P1 | 7.32 | 1.54 | 9.53 | 17.84 | 20 | 30.16 | 6.16 | 9.85 | 4.93 |
| trachyte | 11.76 | 0.26 | 3.3 | 24.31 | 44.18 | 17.11 | 4.17 | 4.6 | 2.08 |
| limestone + K1 | 1.17 | 4.93 | 18.52 | 11.1 | 6.16 | 9.88 | 14.81 | 22.22 | 12.34 |
| limestone + P1 | 1.50 | 1.47 | 27.93 | 16.17 | 7.35 | 1.47 | 8.82 | 26.47 | 10.29 |
| limestone | 2.1 | 7.15 | 28.11 | 11.65 | 5.65 | 1.55 | 6.7 | 23.19 | 15.95 |
| mortar 1:3 + V3 | 16.96 | 2.4 | 9.45 | 14.25 | 19.29 | 15.14 | 9.71 | 23.83 | 5.93 |
| mortar 1:3 + K1 | 20.97 | 4.17 | 7.22 | 11.72 | 19.95 | 13.19 | 7.1 | 27.06 | 9.59 |
| mortar 1:3 + P1 | 19.76 | 3.36 | 7.31 | 10.37 | 19.3 | 16.08 | 15.5 | 24.13 | 3.94 |
| mortar 1:3 + V7 | 19.45 | 4.57 | 7.53 | 14.29 | 21.93 | 15.18 | 12.79 | 20.04 | 3.37 |
| mortar 1:3 + V6 | 21.77 | 3.93 | 5.1 | 13.17 | 22.59 | 12.18 | 12.38 | 23.19 | 7.46 |
| mortar 1:3 | 26.23 | 3.82 | 6.32 | 13.37 | 25.11 | 23.49 | 11.16 | 14.24 | 2.49 |

Note:

 - dominant pores

Mechanical tests of masonry short columns

The load tests in concentric compression until failure were performed in an actuator with a digital central processing unit for reading compression manufactured by MFL – Germany (range of 0 to 10 000 kN, accuracy of 0.01 kN). The monotonously rising loading of the columns with concentric compression was performed in steps, amounting in the case of brick columns to 50 to 100 kN, and, in the case of stone columns to 30 to 60 kN, i.e. ca 10 to 15 % of the theoretically established ultimate load of column masonry pursuant to ČSN EN 1996 (EC6) in the case of brick columns and ČSN 731101 in the case of stone columns.

The results of the load tests of the masonry columns in concentric compression – strength in concentric compression, values of experimentally identified vertical and horizontal deformations, modulus of elasticity or lateral strain coefficient for individual sets of the test pieces after the grout application were summarized for subsequent analysis in a graphical form and in tables. Due to a large amount of these data, the section below presents partial results of this analysis focused on the assessment of the effectiveness of grouting on the compressive strength of the grouted masonry, on the effect of the grouting method, on the effect of the pore system and the grout particle size and on potential changes in the pore system of the grouted material as compared to ungrouted material. Table 6 and 7 present and Figure 4 to 7 graphically illustrate selected

experimentally obtained values, which are proportionally compared to the respective values of the ungrouted, so-called reference masonry test piece.

Tab. 6 - Results of experimental loading - brick masonry columns

| Label | Compressive strength | Hor. def. at 50% N _{um} | Vert. def. at 50% N _{um} | Hor. def. at 500 kN | Vert. def. at 500 kN | coefficient of lateral strain at 50% N _{um} | coefficient of lateral strain at 500kN |
|------------|----------------------|----------------------------------|-----------------------------------|------------------------|------------------------|--|--|
| | MPa | $\delta_{x, 1/2}$ (mm) | $\delta_{y, 50\%}$ (mm) | $\delta_{x, 500}$ (mm) | $\delta_{y, 500}$ (mm) | (-) | (-) |
| CP02.45-V4 | 5.65 | 0.98 | -3.50 | 2.33 | -5.13 | 0.34 | 0.55 |
| CP03.45-V3 | 4.79 | 0.94 | -3.42 | 4.56 | -6.35 | 0.33 | 0.87 |
| CP04.45-P2 | 5.45 | 1.03 | -3.86 | 2.89 | -5.48 | 0.32 | 0.64 |
| CP05.45-P2 | 6.00 | 0.51 | -4.14 | 1.06 | -5.21 | 0.15 | 0.25 |
| CP06.45 | 5.10 | 0.38 | -2.49 | 1.93 | -4.45 | 0.18 | 0.52 |
| CP02.60-V4 | 5.38 | X | -2.54 | X | -2.54 | X | 0.00 |
| CP03.60-V3 | 5.44 | 1.45 | -3.39 | 1.45 | -3.39 | 0.52 | 0.52 |
| CP04.60-P2 | 5.53 | 0.45 | -2.94 | 0.45 | -2.94 | 0.18 | 0.18 |
| CP05.60-P2 | 5.62 | 0.52 | -2.60 | 0.52 | -2.60 | 0.24 | 0.24 |
| CP06.60 | 4.92 | 0.95 | -2.10 | 0.95 | -2.60 | 0.55 | 0.44 |
| CP07.45-K1 | 5.09 | X | -2.76 | X | -4.80 | X | X |
| CP08.45-V2 | 4.95 | X | -2.90 | X | -4.79 | X | X |
| CP09.45-K1 | 4.71 | X | -2.36 | X | -4.97 | X | X |
| CP10.45-V1 | 4.70 | X | -2.90 | X | -6.10 | X | X |
| CP11.45-P1 | 4.44 | X | -2.26 | X | -5.40 | X | X |
| CP12.45 | 4.40 | X | -4.53 | X | -7.76 | X | X |
| CP07.60-K1 | 4.67 | X | -1.10 | X | -1.66 | X | X |
| CP08.60-V2 | 5.09 | X | -1.00 | X | -1.42 | X | X |
| CP09.60-K1 | 5.00 | X | -1.08 | X | -1.71 | X | X |
| CP10.60-V1 | 5.53 | X | -1.04 | X | -1.04 | X | X |
| CP11.60-P1 | 5.70 | X | -1.09 | X | -1.09 | X | X |
| CP12.60 | 5.76 | X | -1.31 | X | -1.31 | X | X |

Note:

X – values not measured

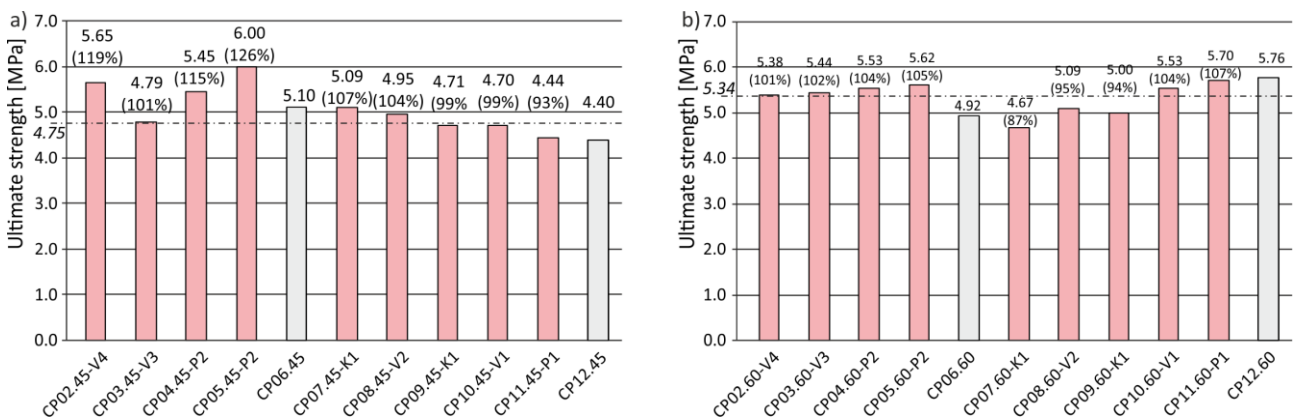


Fig. 4 - Experimentally obtained ultimate strengths of brick masonry columns

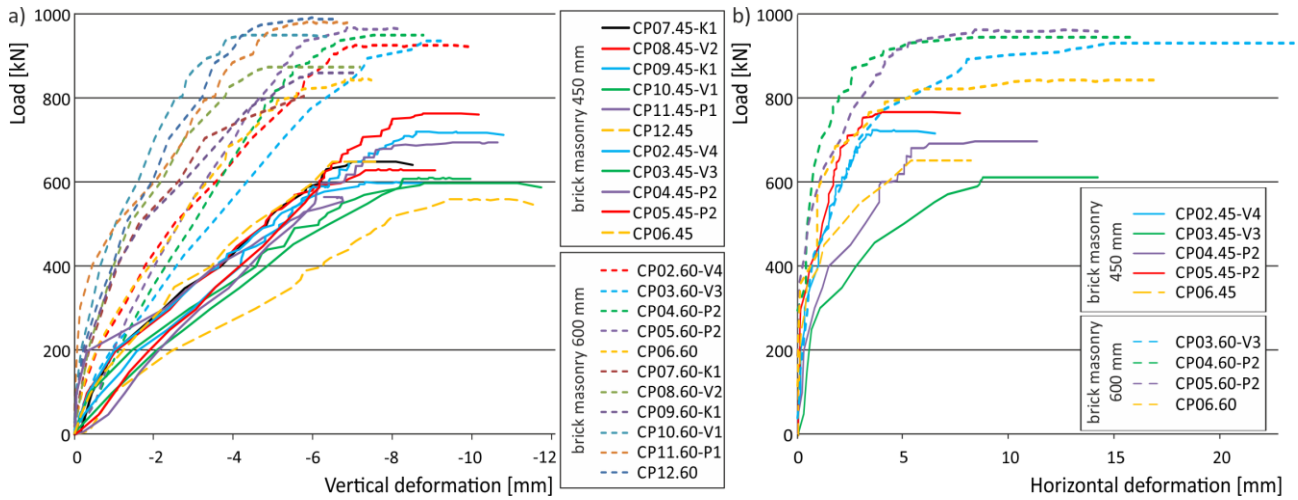


Fig. 5 - a) Vertical deformations of brick masonry with thickness of 450 mm and 600 mm, b) Horizontal deformations of brick masonry with thickness of 450 mm and 600 mm

Tab. 6 - Results of experimental loading – stone masonry columns

| Label | Compressive strength MPa | Vertical deformation δ_y (mm) | | | Horizontal deformation δ_x (mm) | | | Ratio ϵ_x/ϵ_y at 200 kN (-) | Ratio ϵ_x/ϵ_y at 50% N_{um} (-) | Ratio ϵ_x/ϵ_y at N_{um} (-) |
|------------|-----------------------------|--------------------------------------|--------------|------------|--|--------------|------------|---|---|---|
| | | ~ 200 kN* | 50% N_{um} | ultimate** | ~ 200 kN* | 50% N_{um} | ultimate** | | | |
| KP.ON01-V3 | 0.77 | -2.06 | -0.70 | -2.58 | 4.87 | 0.16 | 6.06 | 2.18 | 0.21 | 2.16 |
| KP.ON02-K1 | 0.82 | -1.24 | -0.48 | -2.36 | 2.05 | 0.89 | 3.90 | 1.60 | 1.79 | 1.60 |
| KP.ON03-P1 | 0.78 | -5.22 | -1.96 | -5.91 | 5.90 | 0.84 | 8.53 | 1.11 | 0.42 | 1.42 |
| KP.ON04-V6 | 0.86 | -1.36 | -0.60 | -2.32 | 3.71 | 1.55 | 6.75 | 2.67 | 2.52 | 2.83 |
| KP.ON05 | 0.96 | -0.81 | -0.44 | -2.16 | 3.68 | 1.49 | 10.70 | 4.43 | 3.34 | 4.84 |
| KP.PN01-V3 | 2.71 | -0.52 | -1.57 | -6.65 | 0.56 | 1.93 | 11.81 | 1.03 | 1.17 | 1.69 |
| KP.PN02-K1 | 3.29 | -0.24 | -1.62 | -8.03 | 0.54 | 0.98 | 9.23 | 2.23 | 0.59 | 1.12 |
| KP.PN03-P1 | 3.53 | -0.93 | -2.38 | -7.28 | 0.22 | 0.86 | 10.71 | 0.23 | 0.35 | 1.44 |
| KP.PN04-V7 | 2.15 | -0.55 | -1.57 | -6.26 | 0.89 | 1.73 | 7.68 | 1.61 | 1.08 | 1.21 |
| KP.PN05 | 2.89 | -0.76 | -2.05 | -6.60 | 0.50 | 1.72 | 10.08 | 0.68 | 0.86 | 1.56 |
| KP.TN01-K1 | 2.73 | -1.39 | -3.07 | -7.77 | 0.20 | 0.44 | 5.76 | 0.14 | 0.14 | 0.70 |
| KP.TN02-P1 | 2.35 | -0.91 | -1.76 | -8.54 | 0.23 | 1.64 | 19.93 | 0.24 | 0.90 | 2.25 |
| KP.TN04 | 2.33 | -0.73 | -1.68 | -7.08 | 1.08 | 1.68 | 13.32 | 1.45 | 0.97 | 1.84 |
| KP.VN01-K1 | 1.75 | -0.43 | -0.80 | -3.49 | 1.21 | 1.80 | 6.96 | 2.64 | 2.09 | 1.85 |
| KP.VN02-P1 | 1.71 | -0.96 | -1.29 | -6.85 | 1.31 | 1.71 | 12.11 | 1.19 | 1.16 | 1.54 |
| KP.VN03 | 2.31 | -1.41 | -2.59 | -8.35 | 1.05 | 1.83 | 13.46 | 0.66 | 0.63 | 1.43 |

Note:

* last measured value at 200 kN

** first measured value when reaching the ultimate load

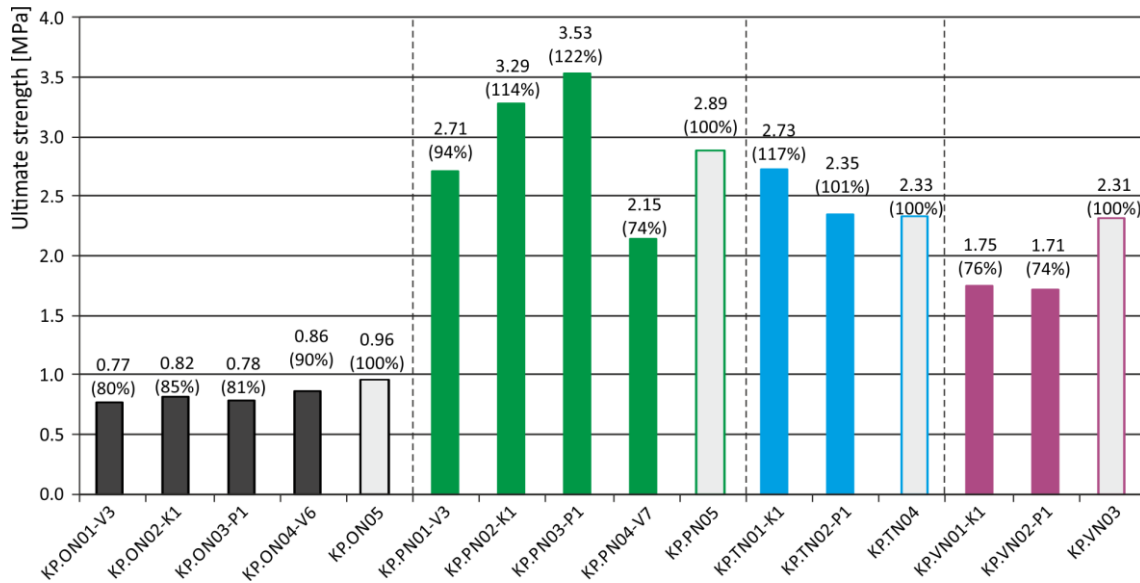


Fig. 6 - Experimentally obtained ultimate strengths of stone masonry columns

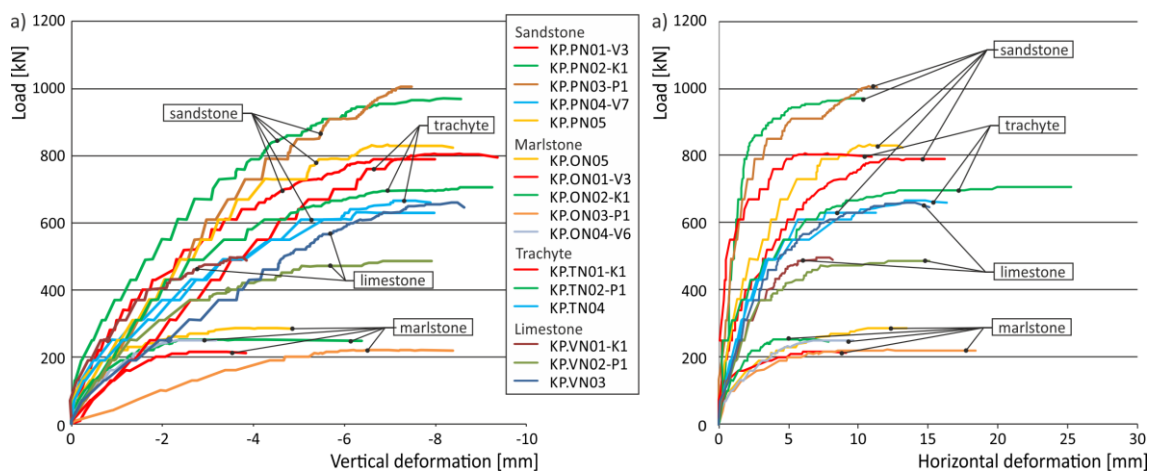


Fig. 7 - Vertical (a) and horizontal (b) deformations of stone masonry

DISCUSSION OVER THE RESULTS OF EXPERIMENTAL AND LABORATORY RESEARCH

Experimental verification of the effectiveness of low-pressure and pressureless grouting

The efficiency of the grouting method was verified for both the case of brick masonry – test pieces CP04.45 and CP05.45 for the resin-based grout P2, test pieces CP07.45 and CP09.45 for the silicate-based grout K1. In the case of stonework columns KP.PN02 and KP.VN01, for the silicate-based grout K1, and test pieces KP.PN03 and KP.VN02 for the resin-based grout P2.

The pressureless grouting was applied at an operating pressure range of 0.5 to 1 bar, while the low-pressure grouting was applied at a pressure range of 6 to 7 bars.

- **Assessment of the efficiency of grouting agents in terms of the implementation method (Figure 8)**
 - The experimentally identified ultimate strengths in concentric compression of the brick masonry 450 mm or 600 mm thick, using a resin-based grout applied by low-pressure grouting reached values $f_{exp} = 107\%$, or 112% respectively, and applied by pressureless grouting $f_{exp} = 118\%$, or 114% respectively, as compared to the experimentally identified ultimate compressive strength of the reference, i.e. ungrouted masonry of the corresponding group of test pieces ($f_{exp} = 100\%$). The highest ultimate strength value was reached in the case of the masonry grouted with the resin-based agent labelled P2.
 - The experimentally identified ultimate strengths in concentric compression of the brick masonry 450 mm or 600 mm thick, using a silicate-based grout applied by low-pressure grouting reached values $f_{exp} = 107\%$, or 87% respectively, and applied by pressureless grouting $f_{exp} = 116\%$, or 81% respectively, as compared to the experimentally identified ultimate compressive strength of the reference, i.e. ungrouted masonry of the corresponding group of test pieces ($f_{exp} = 100\%$). The highest ultimate strength value was reached in the case of the masonry grouted with the silicate-based agent labelled K1.

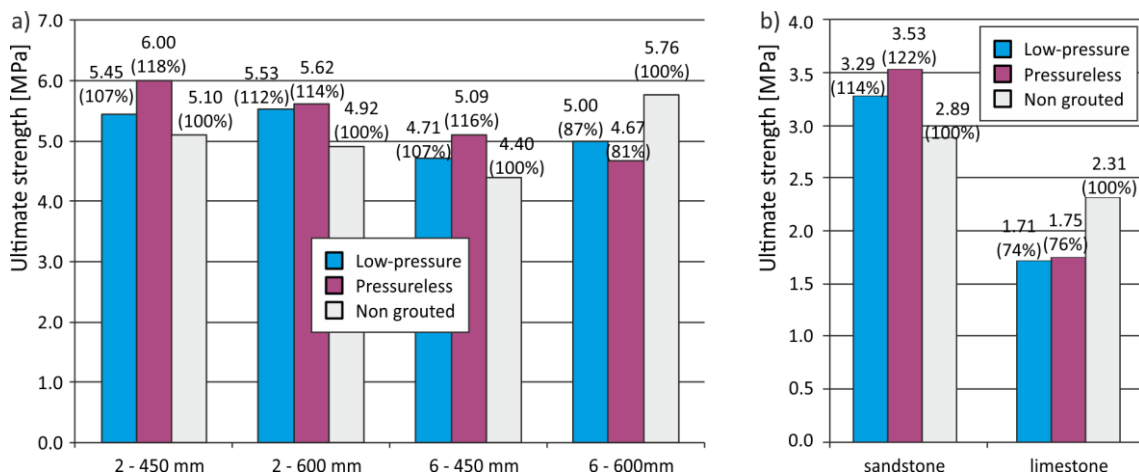


Fig. 8 - Comparison of ultimate strengths of brick (a) and stone (b) masonry grouted with pressureless and low-pressure technology

- The experimentally identified ultimate strengths in concentric compression of the limestone stonework using a resin-based grout applied by low-pressure grouting reached values $f_{exp} = 74\%$, and applied by pressureless grouting $f_{exp} = 122\%$ as compared to the experimentally identified ultimate compressive strength of the reference, i.e. ungrouted masonry of the corresponding group of test pieces ($f_{exp} = 100\%$). The highest ultimate strength value was reached in the case of pressureless masonry grouting with the resin-based agent labelled P2.
- The experimentally identified ultimate strengths in concentric compression of the sandstone stonework using a silicate-based grout applied by low-pressure grouting reached values $f_{exp} = 114\%$, and applied by pressureless grouting $f_{exp} = 76\%$ as compared to the experimentally identified ultimate compressive strength of the reference, i.e. ungrouted masonry of the corresponding group of test pieces ($f_{exp} = 100\%$). The highest ultimate strength value was reached in the case of pressureless masonry grouting with the silicate-based agent labelled K1.

Laboratory verification of porosity of masonry units and mortar

The objective of the investigation of porosity – distribution and integral curves and total porosity – was to obtain information allowing the assessment of the effect of the pore system – prevailing pore proportion – and the effect of the particle size of the grout on the grouting effectiveness. The proportion of prevailing pores of a certain size for individual types of the evaluated materials within the total porosity ranged ca from 25% to 80%.

- **Assessment of the effectiveness of grouting agents in terms of pore distribution** (Figure 9 to Figure 12)
 - The ultimate strength values of the brick masonry in concentric compression in relation to the particle (nanoparticle) size of the grout and the prevailing pore size of the bricks (600 to 2000 nm) and lime mortar (7500 to 30000 nm) ranged within $f_{exp} \in (94\%, 112\%)$ in the case of the brick masonry 450 mm thick grouted with the agents labelled V3, V2 and V4, and within $f_{exp} \in (88\%, 111\%)$ in the case of the grouting agents labelled V1 and V2 and the brick masonry thickness of 600 mm as compared to the ultimate strength of the ungrouted masonry. In the case of all the above grouts applied on the brick masonry, the particle size of the grouts was lower than the prevailing size of the pore radii $r \in (600 - 2000)$ nm of the bricks and mortar.

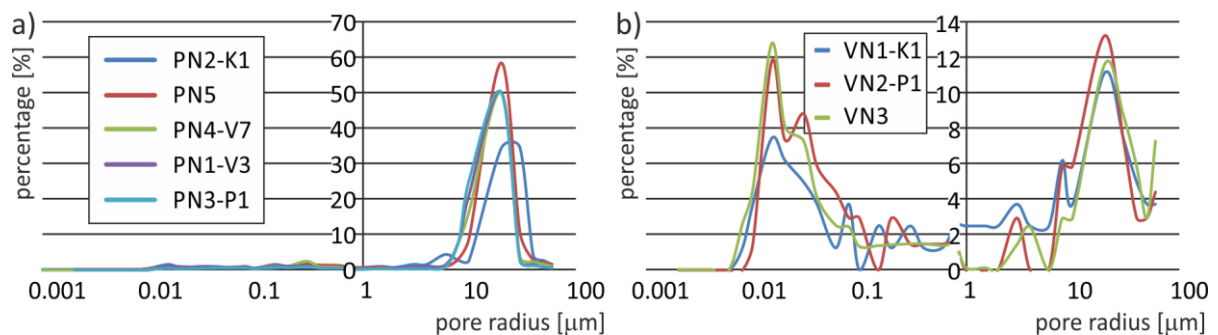


Fig. 9 Examples of distribution curves of the pore system of the masonry units before and after grouting – a) sandstone, b) limestone

- The ultimate strength values of the stone masonry in concentric compression in relation to the particle (nanoparticle) size of the grout and the prevailing pore size ranged within $f_{exp} \in (74\%, 147\%)$, in the case of the sandstone stonework grouted with the calcium-hydroxide-based agents labelled V7 and V3 within $f_{exp} \in (74\%, 94\%)$, in the case of the sandy marlstone stonework grouted with the calcium-hydroxide-based agents labelled V3 and V6 within $f_{exp} \in (80\%, 90\%)$, in the case of the limestone stonework grouted with the resin- and silicate-based agents labelled P1 and K1 within $f_{exp} \in (74\%, 147\%)$, in the case of the trachyte stonework grouted with the resin- and silicate-based agents labelled P1 and K1 within $f_{exp} \in (101\%, 117\%)$ as compared to the ultimate strength of the ungrouted reference masonry. In the case of all the grouting agents above applied on stone masonry, the particle size of the grouts was lower than the prevailing size of the pore radii of the masonry units and mortar.
- The experimental research into the effect of grouting on the total porosity pointed out a change in the total porosity due to grouting. In all the grouted materials used, the total porosity had decreased in a range of 1% - 9.5% of the total material volume and in a range of 20% - 50% of the total pore volume. In the case of the brick masonry, the porosity of the masonry units (bricks) decreased by 1% - 3% and of the binder (lime mortar 1:1) by 1% - 2% as compared to the ungrouted materials. In the case of the stone masonry, the total porosity of sandy marlstone decreased by 3% - 5%, sandstone by 3.5%, trachyte by 4% - 5%, limestone by 1%

and lime mortar by 5% - 9.5% as compared to the ungrouted materials. The greatest change in the overall pore volume was detected in the stone masonry units. In the case of the grouting agents based on lime and lime mortar, there was a drop by ca 40% and in sandy marlstone by ca 20%, in the case of the silicate-based grouts in limestone there was a drop by 50% and in trachyte by 45%. In the case of the resin-based grouts, the greatest drop in the total porosity recorded was in trachyte by 35% and in the lime mortar by 20%.

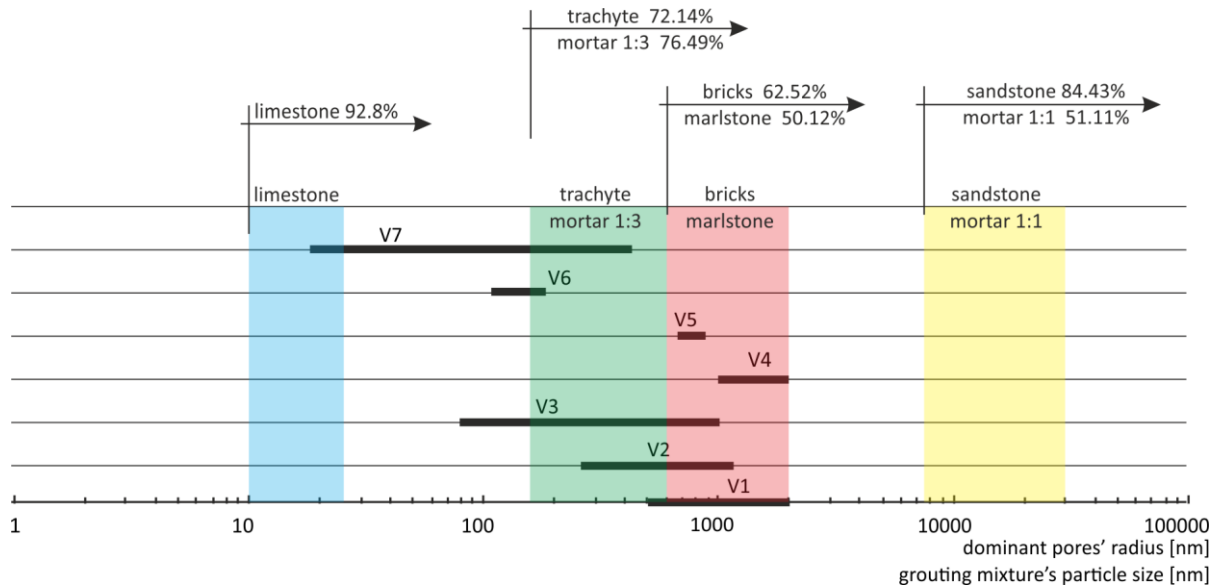


Fig. 10 - Comparison of the radius of the predominant pores of the masonry elements and mortar and particle size of the grouting materials

- A component part of the research was also the verification of the grout penetration into the pore system of the masonry units (sandstone). Partial results of the research that will need further attention in the next research phase are graphically presented in Figure 11 and Figure 12b, which display the total porosity of an ungrouted specimen and grouted specimens sampled from a distance of ca 1 cm and ca 15 cm from the grouting borehole. Figure 12b shows the little difference between the total porosity of the grouted specimens (sandstone) sampled from a distance of ca 15 cm (89% - 99%) as compared to the ungrouted specimen (100 %). Despite the small number of tests that cannot be subjected to statistical analysis, it is evident from the results that the penetration of the grout greatly depends on the mixture, as the K1 mixture shows better penetration (89% at 15 cm distance) than the V3 and V7 mixtures (96% - 99% at 15 cm distance).

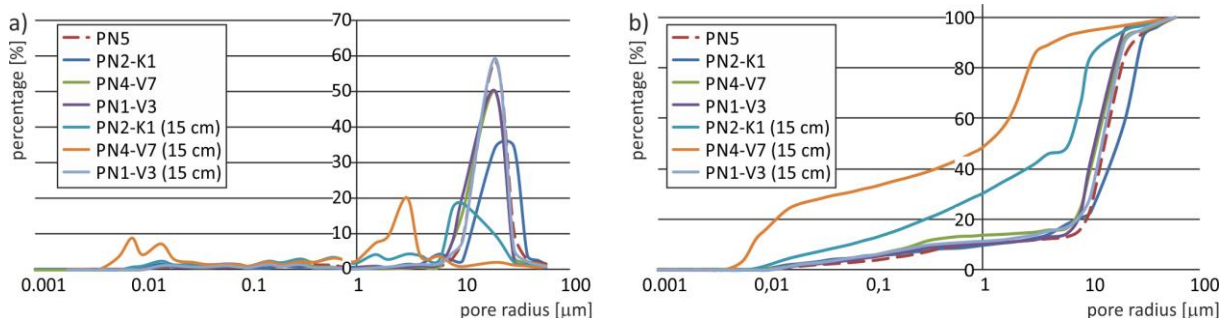


Fig. 11 - Comparison of distribution (a) and integral (b) curves of the pore system of the masonry units depending on the distance from grouting borehole.

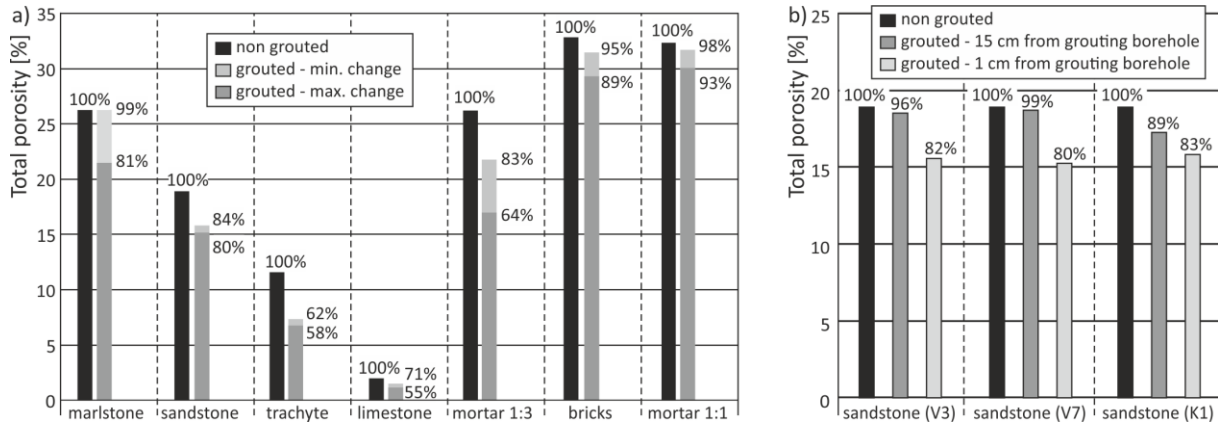


Fig. 12 - a) Comparison of the influence of grouting on the overall porosity of building materials, b) Comparison of the influence of distance from grouting borehole on the overall porosity

Experimental research into the effectiveness of grouting agents in terms of masonry strength in concentric compression

- **Assessment of the effectiveness of grouting agents in terms of brick masonry strength** (see Figure 4 and Figure 5)
 - Lime (mineral)-based grouts:

The experimentally identified ultimate strengths in concentric compression of the brick masonry grouted with a calcium-hydroxide-based mixture reached values within a range of $f_{exp} \in (88\%, 112\%)$ as compared to the experimentally identified ultimate strength in compression of the ungrouted masonry (100%). The highest ultimate strength value $f_{exp} \in (110\%, 112\%)$ was reached in the case of the masonry grouted with the calcium-hydroxide-based agents labelled V2, V3 and V4.
 - Low-viscosity-resin-based grouts:

The experimentally identified ultimate strengths in concentric compression of the brick masonry grouted with a low-viscosity-resin-based mixture reached values within a range of $f_{exp} \in (99\%, 118\%)$ as compared to the experimentally identified ultimate strength in compression of the ungrouted masonry (100%). The highest ultimate strength value $f_{exp} \in (112\%, 118\%)$ was reached in the case of the masonry grouted with the low-viscosity-resin-based agent labelled P2.
 - Silicate-based grouts:

The experimentally identified ultimate strengths in concentric compression of the brick masonry grouted with a silicate-based mixture reached values within a range of $f_{exp} \in (81\%, 116\%)$ as compared to the experimentally identified ultimate strength in compression of the ungrouted masonry (100%). The highest ultimate strength value $f_{exp} \in (107\%, 116\%)$ was reached in the case of the masonry grouted with the silicate-based agent labelled K1.

- **Assessment of the effectiveness of grouting agents in terms of stone masonry strength in concentric compression** (see Figure 6 and Figure 7)
 - Lime- (mineral-) based grouts:
The experimentally identified ultimate strengths in concentric compression of the stone masonry grouted with a lime-based mixture reached in the case of sandstone values $f_{exp} \in$ (74% of grout V7 to 94% of grout V3), in the case of sandy marlstone values $f_{exp} \in$ (80% of grout V3 to 90% of grout V6) as compared to the experimentally identified ultimate strength in concentric compression of the ungrouted masonry (100%). The highest ultimate strength value $f_{exp} = 94\%$ was reached in the case of sandstone and 90% in the case of sandy marlstone using the lime-based agents labelled V3 and V6.
 - Low-viscosity-resin-based grouts:
The experimentally identified ultimate strengths in concentric compression of the stone masonry grouted with a low-viscosity-resin-based mixture reached in the case of sandstone values $f_{exp} = 122\%$ of grout P1, in the case of trachyte 101% of grout P1, in the case of sandy marlstone 81% of grout P1 and in the case of limestone 74% of grout P1 as compared to the experimentally identified ultimate strength in concentric compression of the ungrouted masonry (100%). The highest ultimate strength value $f_{exp} = 122\%$ in the case of sandstone was reached using the low-viscosity-resin-based agent labelled P1.
 - Silicate-based grouts:
The experimentally identified ultimate strengths in concentric compression of the stone masonry grouted with a silicate-based mixture reached in the case of sandstone values $f_{exp} = 114\%$ of grout K1, in the case of sandy marlstone 86%, limestone 74%, trachyte 117% as compared to the experimentally identified ultimate strength in concentric compression of the ungrouted masonry (100%). The highest ultimate strength value $f_{exp} = 117\%$ was reached in the case of trachyte and 114% in the case of sandstone using the silicate-based agent labelled K1.

Probability assessment and statistical analysis of test results

The statistical analysis of the effectiveness of **brick masonry** grouting was based on the results of mechanical tests in concentric compression for 22 test pieces of brick masonry, ungrouted and grouted with the agents specified in previous parts. The average value of strength in concentric compression of the ungrouted (reference) brickwork test pieces was 5.04 MPa (100%) with a standard deviation of the set of values of the reference columns of 0.49 MPa (9.7%). The values of strength in concentric compression of the grouted masonry expressed in % lying within the scattering range of the strength values in concentric compression of the ungrouted brick masonry must be assessed as values that can be significantly affected by the strength scattering of the ungrouted masonry. The values whose percentage exceeds the scattering range limits of strength in concentric compression of the ungrouted masonry, on the other hand, can be more significantly affected by the grouting agent applied (Figure 13a).

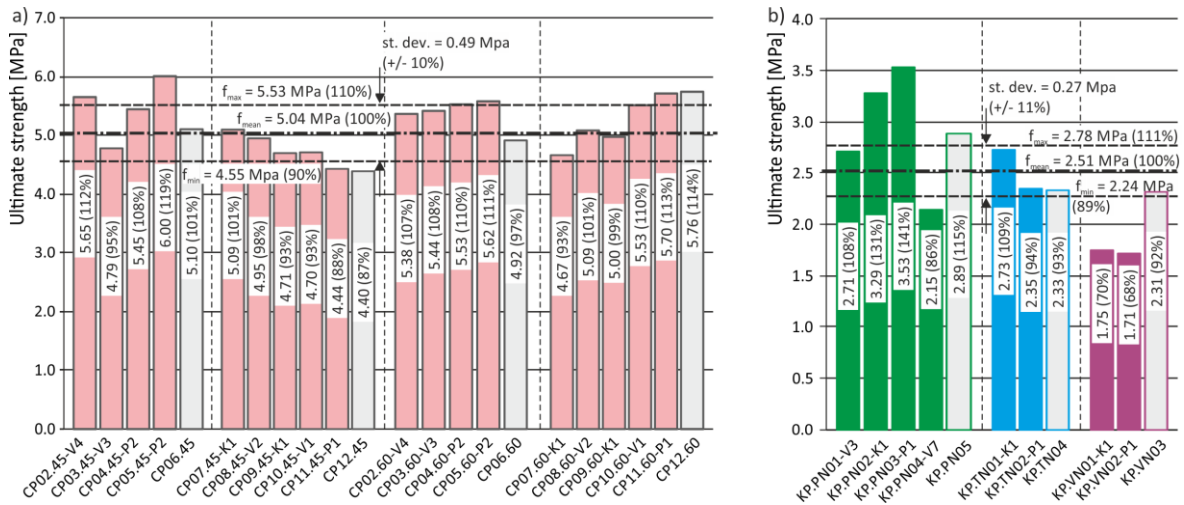


Fig. 13 - Evaluation of the grouting effectiveness of brick (a) and stone (b) masonry

From this perspective, more significant effects on the strength of brick masonry in concentric compression were reached by applying particularly the resin-based grouts labelled P1 and P2, and the lime-based grouts labelled V1 and V4. The probability assessment of the effect of grouting on the brick masonry strength is based on a set of four strength measurements of the ungrouted masonry, which shows an average of 5.04 MPa and a standard deviation of 0.49 MPa. The coefficient of variation is relatively low, 0.111. Figure 1 captures the strength probability density of the ungrouted masonry assuming the normal (red curve) and the lognormal (blue curve) distribution, together with marked values of the quantiles corresponding to probabilities of 5 and 95 %. The following pairs (or tetrads) of the identified strength values of the grouted masonry for different grouting agents indicate that the average value of these measurements is mostly slightly higher than the strength of the ungrouted masonry. It is, however, apparent that none of the measurements of the two (or four) strength values available of the grouted masonry is situated outside the quantile limits for probabilities of 5 and 95 % marked in Figure 14a. It may, therefore, be said that the average strength of the grouted masonry, for the most part, cannot be considered significantly greater than the average strength of the ungrouted masonry. The exception is grouting with agent P2 (Figure 14b), which significantly increases both the average and the characteristic strength (quantile with a probability of 5 %) of the grouted brick masonry.

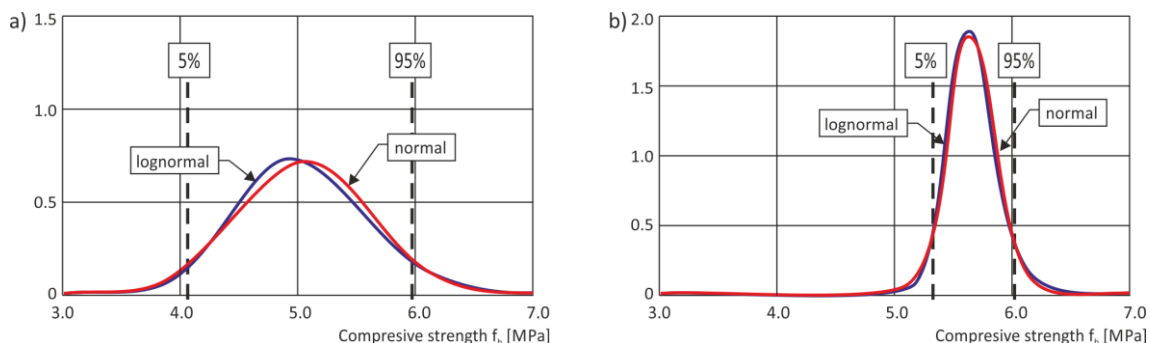


Fig 14 - a) Strength probability density of ungrouted brick masonry (a) and brick masonry grouted with agent P2 (b) assuming the normal and lognormal distribution with marked quantiles for probabilities of 5 and 95 %.

The statistical analysis of the effectiveness of **stone masonry** grouting was based on the results of mechanical tests in concentric compression for 11 test pieces of stone masonry, ungrouted and grouted with the agents specified in part 2. The average value of strength in concentric compression of the ungrouted (reference) stonework test pieces was 2.51 MPa (100%) with a standard deviation of the set of values of the reference columns of 0.27 MPa (11%). The values of strength in concentric compression of the grouted stone masonry expressed in % lying within the scattering range of the strength values in concentric compression of the ungrouted stone masonry must be assessed as values that can be significantly affected by the strength scattering of the ungrouted stone masonry. The values whose percentage exceeds the scattering range limits of strength in concentric compression of the ungrouted masonry, on the other hand, can be more significantly affected by the grouting agent applied (Figure 13b).

From this perspective, more significant effects on the strength of stone masonry in concentric compression were reached by applying particularly the resin-based grouting agent labelled P1 and the silicate-based agent labelled K1. The probability assessment of the effect of the grouting agents and the type of stone in stone masonry is less credible than the analysis of the masonry made up of bricks. It is based on a set of four strength values of stone masonry whose average value is 2.12 MPa and a standard deviation 0.8203 MPa. This is reflected by a high coefficient of variation of 0.39. The strength probability density of the ungrouted stone masonry assuming the normal and lognormal distribution with marked quantiles for probabilities of 5 and 95 % is presented in Figure 15.

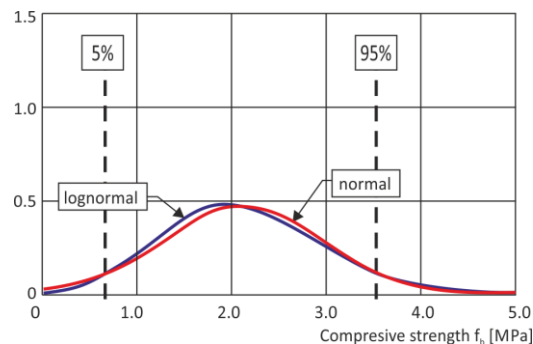


Fig. 15 - Strength probability density of ungrouted stone masonry assuming the normal and lognormal distribution with marked quantiles for probabilities of 5 and 95 %.

The experimental research into the strength of ungrouted stone masonry is followed by a limited number of strength measurements for different grouting agents and aggregate types. The high variability in the strength of the initial ungrouted stone masonry and the limited numbers of follow-up measurements do not allow sufficient confidence of the analysis of the effect of grouting agents and aggregate types. All the measurements available in both cases range within the quantile limits for probabilities of 5 and 95 % marked in Figure 14b. For this reason, it may be said again that (analogically to the brick masonry) the average strength of the ungrouted masonry in general cannot be considered significantly greater than the average strength of the ungrouted masonry. Despite this fact it seems that the grouting agents V7 and K1 provide slightly elevated masonry strengths, whereas the effect of the other grouting agents is highly uncertain. Figure 16a captures the probability density of the stone masonry grouted with agent K1. The lognormal distribution in this case differs considerably from the normal distribution due to the high variability of the grouted stone masonry. The analysis of the effect of the type of used aggregates indicates that the grouting has a positive effect in the case of sandstone and trachyte. The grouting of sandy marlstone masonry, on the other hand, seems to be the least favourable. Figure 16b captures the

probability density of the stone masonry of sandstone. Figure 15 and 16 clearly show that the effect of grouting on the strength of masonry made up of different materials is highly variable and requires further research. More accurate findings can only be obtained with a larger number of measurements for individual grouting agents and different types of materials.

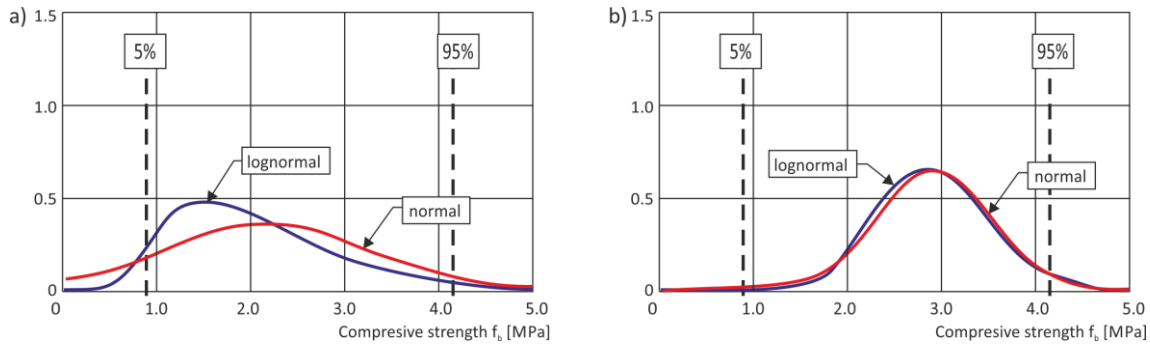


Fig. 16 - Strength probability density of stone masonry grouted with agent K1 (a) and V7 (b) assuming the normal and lognormal distribution with marked quantiles for probabilities of 5 and 95 %.

SUMMARY OF THE RESULTS OF EXPERIMENTAL AND LABORATORY RESEARCH

- Based on the values obtained by the experimental research into the effect of the grouting method we can say that in the case of brick masonry no significant effect of low-pressure grouting in terms of strength in concentric compression was manifested as compared to the strength in concentric compression of the brick masonry where the grout had been applied without grouting pressure. In the case of stone masonry, a demonstrably positive effect of a low-pressure application of the grout on the strength of the stone masonry in concentric compression was reached as compared to the strength of the stone masonry in concentric compression with a pressureless application of the grout.

The cause of the different result of the grouting method effect can primarily be seen in the difference in the pore system of the mortar used in the brickwork columns and the mortar used in the stonework columns. In the brickwork columns, the proportion of coarse pores sized 7500 to 30000 nm amounts to ca 30% of the total porosity, whereas the mortar of the stonework columns, which participates to a considerably greater extent in the strength of the stonework masonry of irregular quarried stone, has a prevailing proportion (ca 25%) of macropores sized 150 to 600 nm in which the low-pressure application of the grouts contributes to better “grouting through”.
- The experimentally identified values of the ultimate strength in concentric compression of the brick and stone masonry indicate a correlation between the grouting agents’ effectiveness in relation to the particle size (nanoparticles) of the grouting agent and the prevailing pore size. The experimental values of the ultimate strength identified also indicate that the assessment of the grouting agents’ penetration mechanism into the pore system is governed not only by the extent of the prevailing agreement of the pore size and the grouting agents’ nanoparticles, but also by other mechanisms like e.g. surface stress, the spectrum and nature of pores, viscosity and stability of the grouting agent, chemism, etc. The clarification of these mechanisms requires further experimental and theoretical research.
- Based on the values obtained through the experimental research into the effectiveness of grouting in terms of the strength of brick or stone masonry, based on the assessment and taking into account the strength scattering of the masonry itself (see Figure 13), we can say that a demonstrable increase in the load-bearing capacity of the masonry in concentric compression (exceeding the strength scattering of the ungrouted masonry) was reached in the

case of brick masonry by the application of the resin-based grouts labelled P1 and P2 and the lime-based grouts labelled V1 and V4, and in the case of stone masonry by the application of the resin-based grout labelled P1 and the silicate-based grout labelled K1. The identified values of an increased or decreased load-bearing capacity of the masonry in concentric compression reached by the application of the grouts labelled V2, V3, V5, V6 and P3 can be assessed as non-conclusive and unreliable, and, in general, they cannot be recommended as methods for the strengthening of undamaged masonry

CONCLUSION

The scattering of the monitored values of the physical and mechanical characteristics of grouted and ungrouted brick or stone masonry and the limited number of specimens do not allow statistical analysis as a basis for the formulation of unambiguous conclusions. The above assessment was performed on the basis of the results of the experimental research into the effect of grouting on the principal physical and mechanical characteristics of undamaged and compact brick and stone masonry, carried out as part of research phase 1. Phase 2 will include experimental research into the effect of grouting on the principal physical and mechanical characteristics of brick and stone masonry with increased void contents, damaged by an artificial crack and cavity. Based on the experimental research into the effectiveness of grouting on the physical and mechanical characteristics of undamaged masonry completed to-date, we may state that the effectiveness of individual types of grouting agents must be assessed in terms of the mutual relationship between the properties of the grouted masonry and the grouting agent. The grouting of undamaged brick masonry can be assessed as insufficiently effective in terms of increasing the ultimate strength in compression.

ACKNOWLEDGEMENTS

The article was written with support from the NAKI DG16P02M055 project "Development and Research into Materials, Procedures and Technologies for Restoration, Conservation and Strengthening of Historic Masonry Structures and Surfaces and Systems of Preventive Care of Historic and Heritage Buildings Threatened by Anthropogenic and Natural Risks".

REFERENCES

- [1] Kalagri, A., Miltiadou-Fezans, A., Vintzileou, E., 2010. Design and evaluation of hydraulic lime grouts for the strengthening of stone masonry historic structures. *Materials and Structures*, 43, pp. 1135-1146, DOI 10.1617/s11527-009-9572-1
- [2] Valuzzi, M. R., Porot da, F., Modena, C., 2004. Behavior and modeling of strengthened three-leaf stone masonry walls. *Materials and Structures*, 37, pp. 184-192, DOI: 10.1007/BF02481618
- [3] Vintzileou, E., Miltiadou-Fezans, A., 2008. Mechanical properties of three-leaf stone masonry grouted with ternary or hydraulic lime-based grouts. *Engineering Structures*, 30, pp. 2256-2276, DOI 10.1016/j.engstruct.2007.11.003
- [4] Maravelaki-Kalaitzaki, P., Bakolas, A., Karatasios, I., Kilikoglou, V., 2005. Hydraulic lime mortars for the restoration of historic masonry in Crete, *Cement and Concrete Research*, 35, pp. 1577-1586, DOI 10.1016/j.cemconres.2004.09.001
- [5] Papayianni, I., Pachta, V., 2015. Experimental study on the performance of lime-based grouts used in consolidating historic masonries. *Materials and Structures*, 48, pp. 2111-2121, DOI 10.1617/s11527-014-0296-5

- [6] Škoda, D., Kuřitka, I., Kroftová, K., Kubát, J., 2018. Technology of preparation of barium and magnesium hydroxide nanodispersion and possibilities of their use in monument care. Acta Polytechnica (in press)
- [7] Kroftová, K., Kuřitka, I., Škoda, D., Šmidtová, M., Masař, M., 2017. Synthesis of nanolime suspension and their potential use in cultural heritage preservation In. EASEC 15 – The Fifteenth East Asia – Pacific Conference on Structural Engineering and Construction.
- [8] Kroftová, K., Kubát, J., Škoda, D., 2018. Possibilities of Consolidation of Historical Materials with Selected Nanodispersions - Results of Experimental Research of the Strength Degree on Reference Formulas, In. NaNs: Moderní materiály a technologie ve stavebnictví

STUDY ON THE SEISMIC PERFORMANCE OF RECYCLED AGGREGATE CONCRETE-FILLED LIGHTWEIGHT STEEL TUBE FRAME WITH DIFFERENT ASSEMBLY JOINTS

Liu Wenchao^{1,2}, Cao Wanlin^{2}, Qiao Qiyun², Ren Lele², Wang Ruwei²*

1. Office of Postdoctoral Research, Beijing University of Technology, Beijing 100124, China; liuwenchao@bjut.edu.cn

2. Key Laboratory of Urban Security and Disaster Engineering, Beijing University of Technology, Beijing 100124, China; Email: wanlincao@bjut.edu.cn

ABSTRACT

In order to investigate the construction of column-to-beam joints and to understand the effect of recycled aggregate concrete (RAC) and cross-section of beams and columns on the seismic performance of recycled aggregate concrete-filled light steel tubular frame structure, four new types of assembly joints were proposed in this paper. A low cyclic loading test of six frame specimens was carried out. The failure characteristic, load bearing capacity, hysteresis property, ductility, strength and stiffness degradation, and energy dissipation were analysed. The damage process of the specimen was simulated using the ABAQUS software, and the results agreed well with those obtained from the experiments. The results showed that the construction pathway of the joints exhibited significant influence on the seismic performance of the frame. The proposed reinforced joint (using angle steel and stiffeners) significantly improved the bearing capacity, stiffness and energy dissipation capacity of the recycled aggregate concrete-filled steel tube frame. The seismic performance of the steel frame was improved, while the energy dissipation capacity increased by 635.7% using RAC filled in the steel tubes. Finally, by appropriately increasing the size of cross-section on the beams and columns can improve the bearing capacity, stiffness and ductility of the structure.

KEYWORDS

Recycled aggregate concrete-filled steel tube frame, Beam-column joints, Assembly structure, Seismic performance, Experimental research, Simulation

INTRODUCTION

Concrete-filled steel tubes (CFST) are widely used in high-rise and super high-rise structures due to the advantages of their high bearing capacity, good ductility, fatigue resistance, and impact resistance [1-4]. Accompanied by the continuous development of material science, as well as the continuous improvement of environmental awareness, recycled aggregate concrete (RAC) has been widely used in light steel frame structures [5-8]. At present, the research on the seismic behaviour of light steel frame structure is mainly focused on the specimens which consist of concrete-filled steel tubular columns and the steel I-beams [9-13]. Previous study [14] showed

that the seismic behaviour of the frame with square concrete-filled steel tube beam was better than that of the frame with steel I - beam. It can be seen that the rectangular concrete-filled steel tube frame structure has more advantages with regards to bearing capacity, seismic performance and material utilization. Therefore, it has the value of further research and application.

In this paper, four kinds of new types of prefabricated beam-column joints were proposed. The square recycled aggregate concrete-filled steel tubes were used as the beam and column of the frame. The beam and column were connected to each other by the bolts. Compared with the traditional steel frame, it has excellent fire resistance and good durability. The influence of joint structure forms, the RAC filling, and cross-section of beams and columns on the load-bearing capacity, stiffness, hysteresis characteristics, and seismic energy consumption of recycled aggregate concrete-filled light steel tubular frame structure were studied. Based on the experimental data, an ABAQUS finite element analysis of the lightweight steel frame was carried out, which provides a data reference for the practical application of the lightweight frames.

TESTS AND METHODS

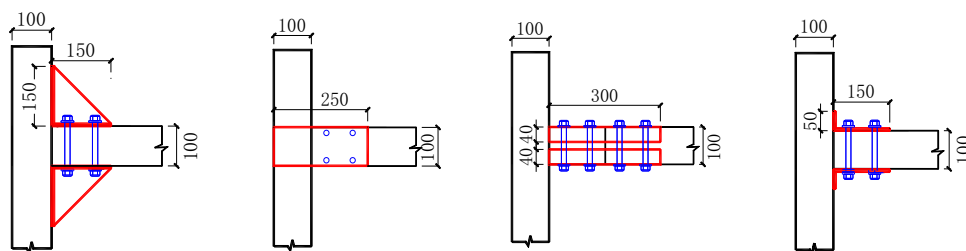
Design and construction of the specimen.

A single story - single span lightweight steel tube frame and five single story-single-span lightweight steel tube frames filled with recycled aggregate concrete were designed in this paper. The beams and columns of the frame were made of recycled aggregate concrete-filled square steel tube. Herein, the specimens are called FJ-1, FJ-2, FJ-3, FJ-4, FJ-5 and FJ-6, while the design parameters for the specimens are presented in Table 1.

Tab. 1 - Design parameters for the tested specimens

| No. | Size of column and beam /mm | Joint structural forms | Concrete strength /MPa |
|------|-----------------------------|--------------------------|------------------------|
| FJ-1 | 100×100 | Angle steel + stiffeners | -- |
| FJ-2 | 100×100 | Angle steel + stiffeners | C40 |
| FJ-3 | 100×100 | Straight steel plate | C40 |
| FJ-4 | 100×100 | U-steel plate | C40 |
| FJ-5 | 100×100 | Angle steel | C40 |
| FJ-6 | 120×120 | Angle steel + stiffeners | C40 |

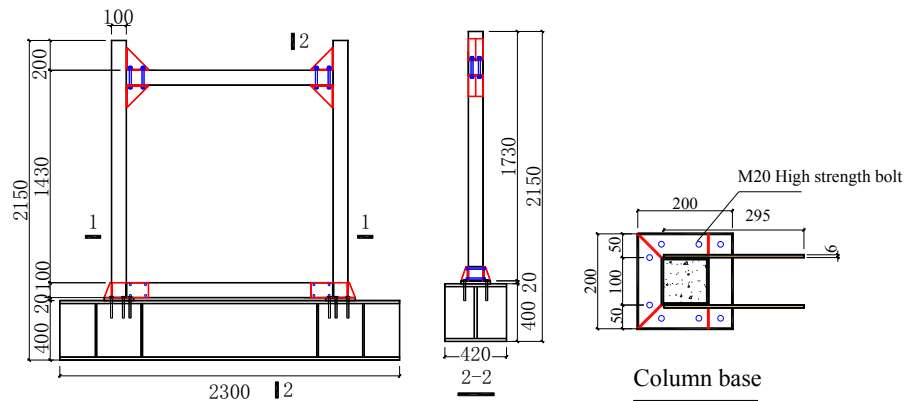
The joint structure of specimen FJ-1 is shown in Figure 1, and the production process of the specimens is shown in Figure 2.



a) FJ-1/FJ-2 Reinforced joint b) FJ-3 Straight joint c) FJ-4 U-steel joint d) FJ-5 Angle joint

(a) Design drawings of different joints

Fig. 1 - Details of the specimen FJ-1 – FJ-6



(b) Design drawings of the light steel frame FJ-2

Fig. 1 - Details of the specimen FJ-1 – FJ-6

Before pouring the concrete, the steel tube was fixed on the ground, and the concrete was poured from the top of the steel tube. The concrete was vibrated using a vibrator to ensure the uniformity of the recycled aggregate concrete. Then, the concrete at the top of the column was smoothed. The specimens were maintained under natural conditions for 28 days. Finally, the cover plate was welded at the end of the steel tube to ensure that the steel tube and the concrete worked together during loading. The construction of the specimens is shown in Figure 2.



(a) Fabrication of the steel tube



(b) Pouring RAC in the steel tubes

Fig. 2 - Preparation of the specimens

Material Properties

To ensure the welding quality and the assembly precision, the beams and columns were all made of Q345 steel with wall thickness of 4 mm. In addition, M12 bolts (nominal diameter of 12 mm) were used during the construction. The recycled aggregate concrete was made by mixing the recycled coarse aggregate (particle size of 5 - 10 mm), natural sand, ordinary Portland cement, water, mineral powder, fly ash and water reducer in a certain ratio. Necessary parameters of the recycled coarse aggregate were in accordance with the standard GB/T 25177-2010 [15]. The rate of replacement of the recycled coarse aggregate was 100%. Figure 3 shows the particle size distribution curve of the coarse aggregates in recycled concrete aggregate (RCA). On average, the compressive strength of the standard cubes [16] of the recycled aggregate concrete was 43.8 MPa. The mixing ratios of various components of the recycled aggregate concrete are presented in Table 2.

Tab. 2 - Mixing ratios of various components of the recycled aggregate concrete

| Strength Grade | Mix ratio of recycled aggregate concrete kg / m ³ | | | | | | |
|----------------|--|---------|----------------|------|-----------------|-------|---------------|
| | cement | fly ash | mineral powder | sand | recycled-pebble | water | water reducer |
| C40 | 369 | 79 | 79 | 841 | 841 | 181 | 3.5 |

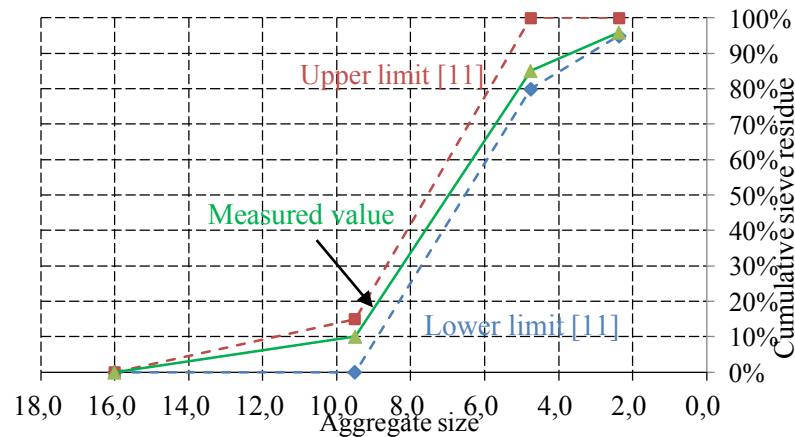


Fig. 3 - Aggregate gradation of the coarse aggregate in RCA

According to the Chinese standard GB/T 228-2002 [17], the mechanical properties of the steel plate used to construct the specimens are presented in Table 3.

Tab. 3 - Measured mechanical properties of the steel

| Base metal type | Yield strength /MPa | Ultimate strength /MPa | Modulus of elasticity /MPa |
|------------------|---------------------|------------------------|----------------------------|
| 4 mm steel plate | 375 | 477 | 2.18×10 ⁵ |

Test Set-Up and Loading

The experiments were carried out at the Integrated Earthquake Engineering Laboratory of the Institute of Engineering Mechanics, China Earthquake Administration, China. Figure 4 shows the scheme and photo of the loading device.

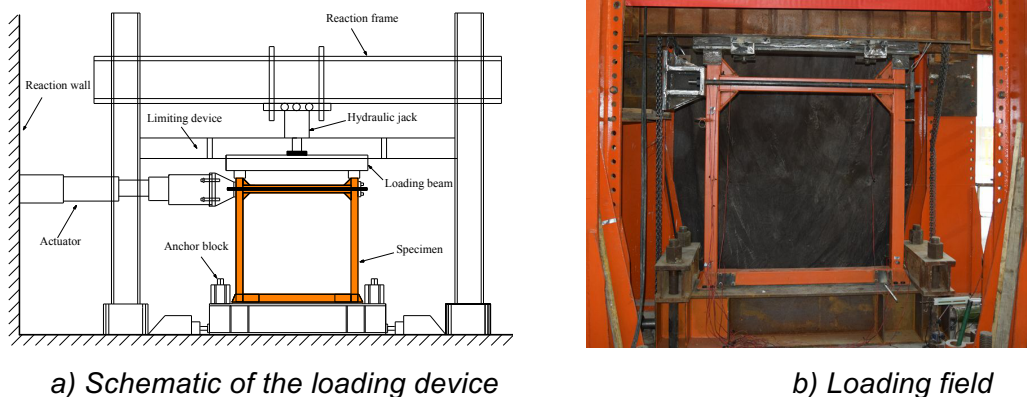


Fig. 4 - Schematic and photo of the experimental setup

The repeated low-cycle loading method was used in the experiments. The vertical axial force and the horizontal displacement were controlled by two vertical electro-hydraulic servo loading systems. The axial force was uniformly transmitted to the top of the column through distribution beam. Similarly, the lateral support beams were installed on the two flanks of the distribution beam to prevent the specimen from being out of plane. The column base of the specimen was connected to the I-shaped steel foundation through high strength friction grip bolt. The arrangement of the sensors on the setup is shown in Figure 5.

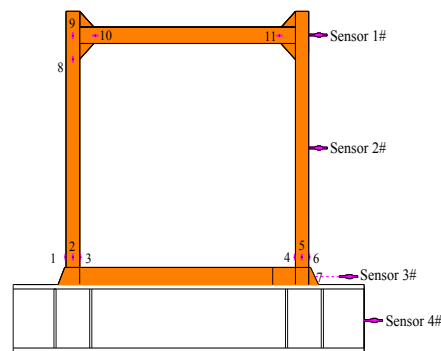


Fig. 5 - Displacement and the strain measuring points on the experimental setup

Loading Program

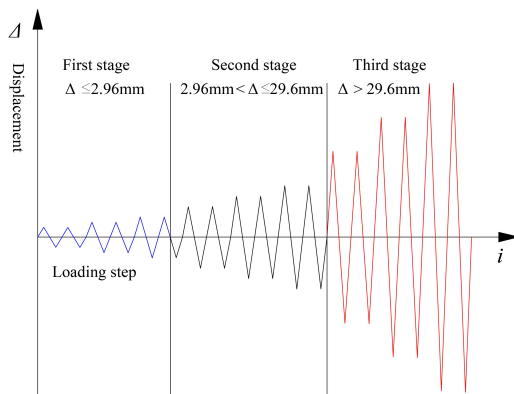


Fig. 6 - Loading protocol

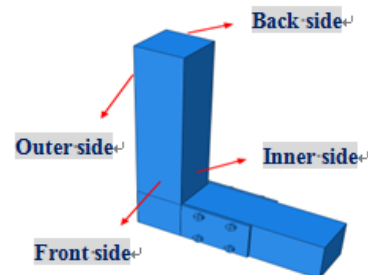


Fig. 7 - Definition of various sections of the column

In the experiment, the vertical load of 600 kN was applied on the loading beam of the specimens. The designed axial compression ratios of FJ-2 - FJ-5 specimens were 0.6, while the vertical axial force was kept constant during the experiments. The horizontal loading process was controlled by the displacement, which could be divided into three stages. (1) The displacement was applied in increments of 1/2500 displacement angle per cycle while the displacement angle was 0 - 1/500. (2) The displacement was applied in increments of 1/500 displacement angle per cycle while the displacement angle was 1/500 - 1/50. (3) The displacement was applied in increments of 1/25 displacement angle per cycle while the displacement angle was equal to 1/50. Each level of the loading displacement had two cycles. When the positive and negative horizontal loads dropped to 85% of the ultimate load of the specimen, the experiment was completed. During the experiment, the loading and unloading rates were same. The loading protocol is shown in Figure 6.

A vertical load of 600 kN was applied to FJ-1 and FJ-6 to ensure the consistency of loading conditions.

RESULTS AND DISCUSSION

Failure Characteristics

This paper defines four sides of the column, namely the front side, inner side, back side and the outer side, as shown in Figure 7. The failure mode of the light steel empty frame FJ-1 is different from the rest of specimens. For the specimen FJ-1, the middle part of the frame beam slightly warped upwards. When the displacement angle reached $1/500$, the paint of the column foot slightly wrinkled. When the displacement angle was $1/250$, the inner side of the proximal column slightly drummed up. The residual deformation of the proximal column foot occurred, and the steel plate of the column foot yielded when the displacement angle reached $1/83$. When the displacement angle was $1/71$, the deformation of the inner side of the column foot developed rapidly to about 5 mm. Additionally, the concave deformation of the front side was about 4 mm, while the horizontal load declined rapidly. When the displacement angle was $1/62$, the column base of the specimen yielded, and the horizontal load dropped below 85% of the ultimate load. At this point, the experiment was completed, as shown in Figure 8(a).

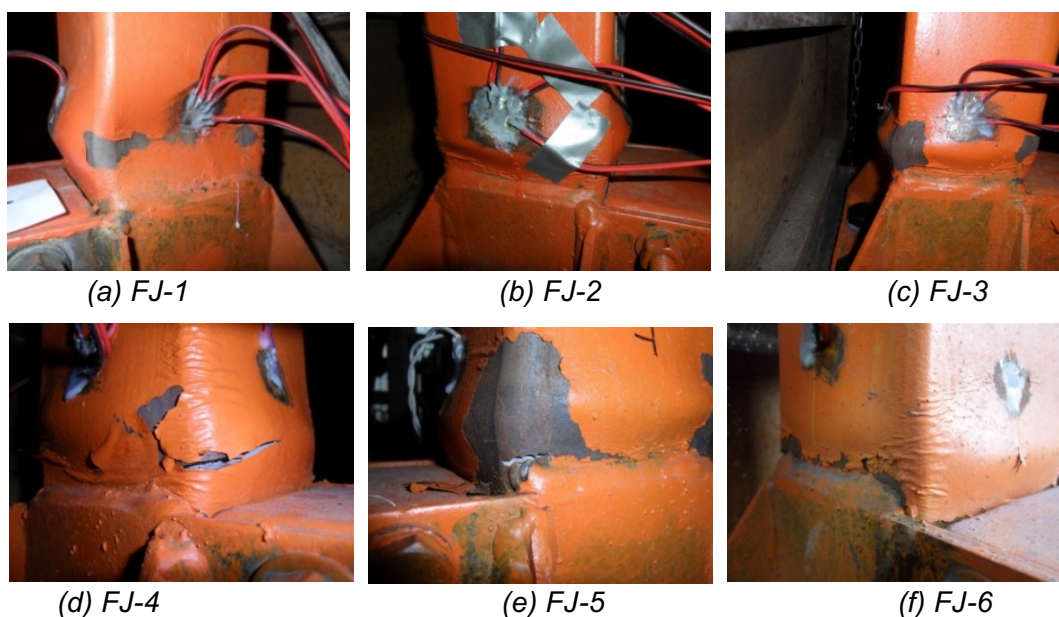


Fig. 8 - Failure modes of the column-base

The failure process of the RAC-filled steel tube frames (Figures 8(b) - 8(f)) was similar. During the loading process, part of the energy was dissipated through the fabricated joints, so that the damage of the frame beam was not significant. For the specimen FJ-3, when the displacement angle reached $1/83$, slight hollowing was observed at the beam end. Meanwhile, the recycled aggregate concrete was separated from the steel pipe. When the displacement angle was $1/71$, the paint of the bottom part of the column became slightly wrinkled. The bolts in the joint area slightly slid, and the joint plate showed a slight deformation. When the displacement angle was

1/62, the paint in the compression zone of the upper column folded. For the displacement angle of 1/38, the steel plate of the compression zone of the column foot drummed up by about 2 mm, while the fold range of the paint extended to the middle of the cross section of the column. At this moment, the recycled aggregate concrete inside the column was crushed. With the increase in displacement, the drum deformation appeared on both sides of the column foot. When the displacement angle reached 1/18, the steel plate at the bottom of the column tore, and the load dropped rapidly, as shown in Figure 8(c).

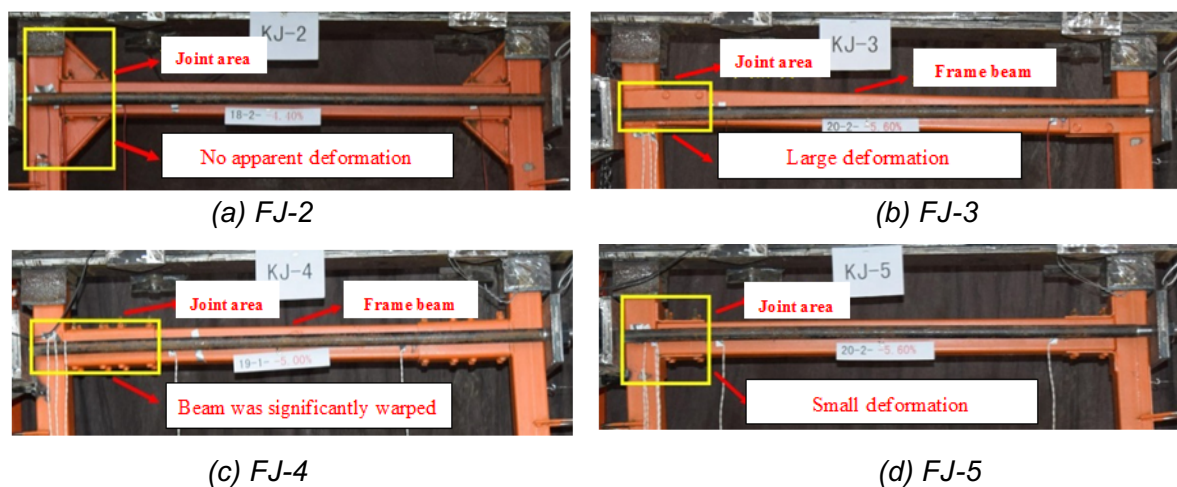


Fig. 9 - Deformation of beam and column

As seen in Figure 9 the specimens with different assembly joints exhibited different deformations in the joint domain when the specimens were finally destroyed. The specimen FJ-2 adopted the enhanced connection joint structure to expand the joint domain range, while the stiffness of the joint was huge. The joint domain did not show any obvious deformation. Because of the low flexural rigidity of the straight plate joint of FJ-3, the deformation of the joint area was large. The deformation of the frame beam was obvious. The assembly joint of FJ-4 was transferred to the beam end. The joint domain was deformed, and the beam was significantly warped. The joint domain deformation of FJ-5 was smaller in comparison to its large lateral rigidity.

Load-Displacement Response

Herein, F is the horizontal load (F_y is the yield load; F_u is the ultimate load; F_d is the destroyed load, $F_d=0.85F_u$), for which, the thrust load is positive, while the tensile load is negative. Additionally, Δ is the horizontal displacement (Δ_y is the yield displacement; Δ_u is the ultimate displacement; Δ_d is the destroyed displacement) corresponding to the horizontal load measured using the displacement meter #1. Figure 10 shows the comparison of the force–displacement ($F-\Delta$) skeleton curves of the specimens with different parameters.

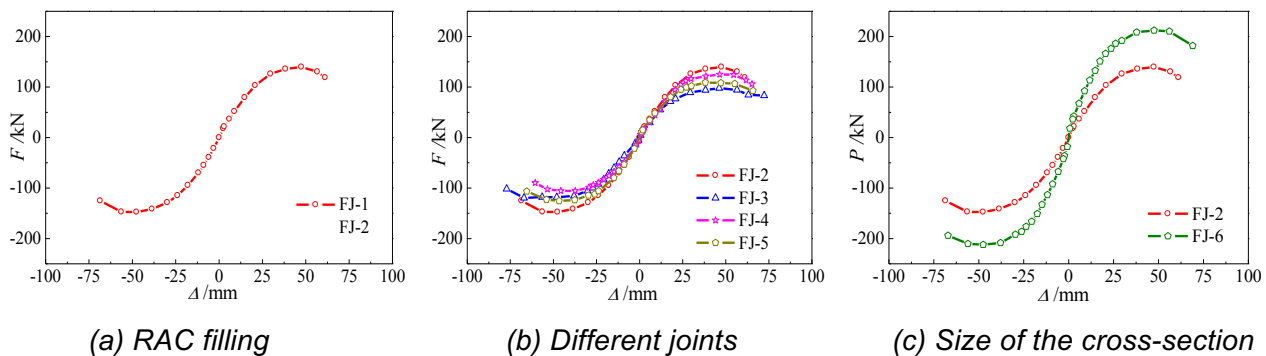


Fig. 10 - Skeleton curves of the hysteresis plots

As seen from Figure 11(a) that under the same joint form, the ultimate load of the FJ-2 specimen was 100% higher than that of the FJ-1. This is due to the reason that the recycled aggregate concrete slowed down the yield of the steel tube of the specimen, and improved the bearing capacity of FJ-2. As can be seen from Figure 11(b), the bearing capacity of FJ-2 was higher, while the degradation rate of the load was slightly faster than the other specimens in the failure stage. Although FJ-3 had the lowest bearing capacity, its bearing capacity did not decrease significantly after reaching the ultimate load. It shows that the specimen FJ-3 had a good ductility. The ultimate load of the specimen FJ-4 in positive and negative direction exhibited a larger difference, indicating that the specimen was seriously damaged during the loading process. Figure 11(c) shows that the cross-sectional dimensions of the beams and columns had a significant effect on the bearing capacity of the specimens. The downward trend of the bearing capacity of FJ-2 and FJ-6 were basically the same. In this paper, the energy equivalence method was used to determine the yield load and displacement of specimens (see results in Table 4).

Tab. 4 - Measured load and displacement of specimens at characteristic points

| No. | F_y /kN | Δ_y /mm | F_u /kN | Δ_u /mm | F_d /kN | Δ_d /mm |
|------|-----------|----------------|-----------|----------------|-----------|----------------|
| FJ-1 | 65.75 | 14.98 | 72.63 | 17.94 | 61.74 | 22.24 |
| FJ-2 | 120.74 | 26.83 | 143.56 | 47.54 | 122.03 | 64.89 |
| FJ-3 | 91.40 | 25.75 | 108.75 | 56.62 | 92.44 | 74.69 |
| FJ-4 | 98.77 | 24.40 | 115.01 | 46.07 | 97.75 | 62.91 |
| FJ-5 | 97.40 | 22.55 | 117.22 | 42.43 | 99.64 | 65.67 |
| FJ-6 | 184.62 | 21.07 | 221.14 | 47.51 | 187.96 | 68.10 |

Compared with FJ-1, the yield load and ultimate load of FJ-2 increased by 83.6% and 97.7%, respectively. This shows that the core-restrained recycled aggregate concrete can limit the yield of steel tube and increase the bearing capacity of the specimens. The yield loads of FJ-3, FJ-4 and FJ-5 were 24.3%, 18.2% and 19.3% lower than that of FJ-2, respectively. The ultimate loads of FJ-3, FJ-4 and FJ-5 were 24.2%, 19.9% and 18.3% lower than that of the FJ-2. This shows that the different types of assembly joints have a significant influence on the bearing capacity of the concrete-filled steel tube specimens.

Displacement and ductility

In this paper, Δ_d represents the plastic displacement of the specimen, which is the maximum displacement when the horizontal load drops to 85% of the ultimate load. In addition, Δ_y represents the yield displacement, while $\mu = \Delta_d/\Delta_y$ is used to define the displacement ductility coefficient of the specimen. Herein, θ is the displacement angle, $\theta = \Delta$ (horizontal displacement) / h (loading height), the loading height h is 1480mm. The results for these parameters are presented in Table 5.

Tab. 5 - Ductility coefficients of various specimens

| No. | Δ_y /mm | θ_y | Δ_u /mm | θ_u | Δ_d /mm | θ_d | μ |
|------|----------------|------------|----------------|------------|----------------|------------|-------|
| FJ-1 | 14.98 | 1/99 | 17.94 | 1/82 | 22.24 | 1/67 | 1.48 |
| FJ-2 | 26.83 | 1/55 | 47.54 | 1/31 | 64.89 | 1/23 | 2.42 |
| FJ-3 | 25.75 | 1/57 | 56.62 | 1/26 | 74.69 | 1/20 | 2.90 |
| FJ-4 | 24.40 | 1/61 | 46.07 | 1/32 | 62.91 | 1/24 | 2.58 |
| FJ-5 | 22.55 | 1/66 | 42.43 | 1/35 | 65.67 | 1/23 | 2.91 |
| FJ-6 | 21.07 | 1/72 | 47.51 | 1/32 | 68.10 | 1/22 | 3.23 |

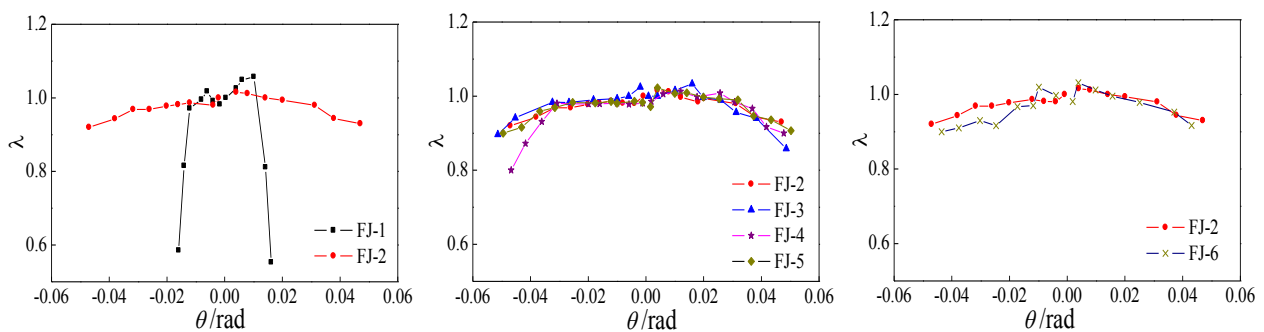
1) Compared with FJ-1, the displacement ductility coefficient of FJ-2 increased by 63.5%. It indicates that filling the recycled aggregate concrete in the steel tube can significantly increase the ductility of the structure. This may be due to the reason that the RAC delayed the yielding of the external pipe, and also the development of the plastic hinge of the specimen.

2) Compared with FJ-2, the ductility coefficients of FJ-3, FJ-4 and FJ-5 increased by 19.8%, 6.6% and 20.4%, respectively. This shows that the different types of assembly joints have a great influence on the ductility of the steel tube recycled aggregate concrete frame structure. In short, the ductility of these specimens with different types of joints was better than previously reported.

3) Compared with FJ-2, the ductility coefficient of FJ-6 increased by 33.5%, which shows that increasing the size of cross-section can improve the ductility of the RAC-filled steel tube frame.

3.4. Degradation of the strength

The loading process consists of two loops for each loading displacement. The degradation of the strength can be represented by the ratio of peak load of the second cycle (loop) to the peak load of the first cycle (loop) under the same loading displacement. The results for the degradation in strengths for various specimens are shown in Figure 11.



(a) Influence of the RAC filling (b) Influence of different joints (c) Influence of the size of cross-section

Fig. 11 - Strength degradation curves of various specimens

As can be seen from Figure 11, the strength of the empty steel frame degraded rapidly at the elastoplastic stage, which is mainly due to the buckling of the steel plate of the column base at the failure stage. Meanwhile, the plastic hinge was formed, while the bearing capacity of the frame decreased rapidly. The loading degradation of the RAC-filled light steel tube frames with different assembly joints was similar to each other. The strength under the same loading displacement remained basically unchanged, whereas the trend of the strength degradation after yielding was slow, indicating good ductility. The main reason is that the steel pipe can constrain the deformation of concrete after the concrete is crushed. However, the frame can still maintain high bearing capacity. The size of the cross-section showed little effect on the degradation of strength of various specimens.

Degradation of the stiffness

In this paper, the stiffness degradation feature is represented by the secant stiffness-displacement angle (K - θ) curve, which was obtained from the measured load and displacement at each stage of the specimen. The secant stiffness of each specimen was computed from the skeleton curve of the hysteresis plot using Equation (1).

$$K_i = \frac{|F_i^+| + |F_i^-|}{|\Delta_i^+| + |\Delta_i^-|} \quad (1)$$

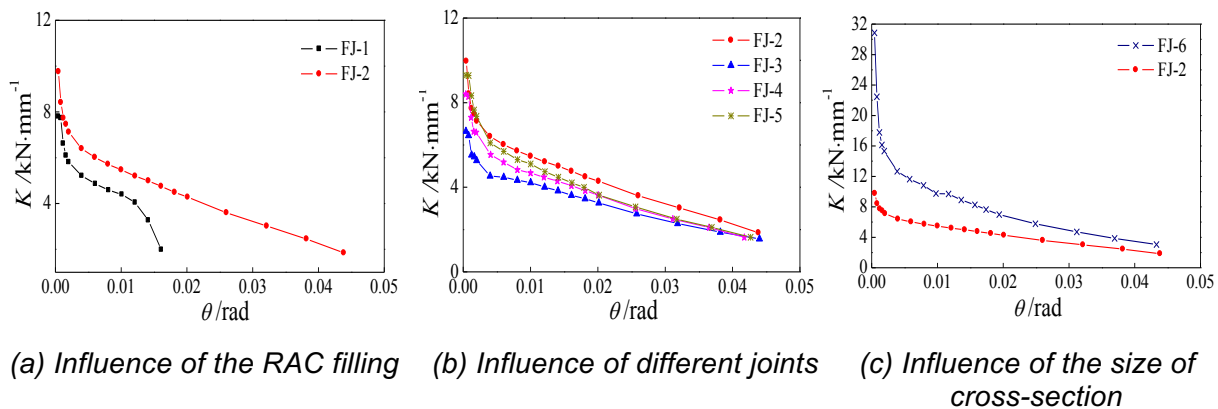


Fig. 12 - Stiffness degradation curves of various specimens.

Figure 12 shows that the stiffness degradations of the RAC-filled steel tube frames were similar to each other. FJ-2 experienced rapid stiffness degradation, while FJ-5 underwent slow stiffness degradation. The rate of degradation of stiffness was relatively fast in the elastic phase, whereas the stiffness degeneration tended to be slow in later stages. The steel tube and the confined concrete can work well in the elastic phase. With the increase in load, the concrete slipped and gradually separated from the steel tube, which degraded the specimen stiffness rapidly. FJ-1 experienced a rapid stiffness degradation process, followed by a slow degeneration process and then, an accelerated degradation process. The stiffness degradation of the steel frame FJ-1 is significantly faster than that of the RAC-filled frame FJ-2, especially in the elastoplastic stage. It shows that filling RAC in the steel tube can obviously slow down the stiffness degradation of specimens at the failure stage. Furthermore, different types of joints have a great influence on the initial stiffness of the RAC-filled steel tube frames. The initial stiffness of the specimen FJ-2 was the largest for the joint's high in-plane flexural rigidity. At the same displacement angle, the initial stiffness of the specimen with straight connection joint was the lowest. At the same displacement angle, increasing the size of beam's cross-section can significantly increase the stiffness of specimens. However, with a larger size of the cross-section of beam and column, the rate of degradation of stiffness of the specimens accelerated.

Energy Dissipation Capacity

The energy dissipation representative value E_p was considered to be the accumulated areas surrounded by the hysteretic curves of the specimens when the load dropped to 85% of the ultimate load. The corresponding results for the energy dissipation are presented in Table 6.

Tab. 6 - Experimental results for the energy dissipation capacities of various specimens

| No. | Energy dissipation value E_p (kN · m) | Relative value RV |
|------|---|-------------------|
| FJ-1 | 3.206 | 1.000 |
| FJ-2 | 23.584 | 7.357 |
| FJ-3 | 20.541 | 6.408 |
| FJ-4 | 17.101 | 5.335 |
| FJ-5 | 20.419 | 6.370 |
| FJ-6 | 25.728 | 8.026 |

The results show that, compared with the specimen FJ-1, the energy dissipation values of FJ-2, FJ-3, FJ-4 and FJ-5 increased by 635.7%, 540.8%, 433.5% and 537.0%, respectively. Filling RAC can obviously improve the energy dissipation of the steel frame. The energy-dissipation capacity of the specimens with different joints was different, and the energy dissipation of specimen FJ-2 was 15.5% higher than that of FJ-5. The stiffness of the FJ-2 increased the strength of the joint area of the specimen. The energy dissipation capacity of FJ-3 and FJ-5 was similar, while the influence of the two corresponding joint structures on the energy dissipation capacity of the specimen was small. The energy dissipation capacity of FJ-4 was 19.4%, 20.1% and 37.9% lower than those of the FJ-5, FJ-3 and FJ-2, respectively, indicating that the U-steel joint structure contributed less to the energy consumption of RAC-filled steel tube frame. The energy dissipation of FJ-6 was 9.1% higher than that of the FJ-2, which indicates that increasing the cross-sectional dimension of the column and beam can improve the energy dissipation capacity of the specimens.

THEORETICAL CALCULATION AND ANALYSIS

Material constitutive model

Under the confinement of steel tube, the constitutive relation of RAC is quite different from that of the general RAC. Considering the influence of the restraint effect coefficient, the Mander confined concrete model, revised by Yang[18], was used. In this paper, the coarse aggregate replacement rate is considered to be 100%.

In this paper, the elasticity enhancement model (double line model) was used to simulate the reinforcement law. The Mises yield and kinematic hardening criteria were used in the numerical simulation. The stress-strain relationship of the steel bar was simplified as an oblique line. In this study, $E_s=0.01E_s$ [19], and the Poisson's ratio was 0.3.

Finite Element Model

ABAQUS software provides a huge library of cells, including solid cells, beam cells, rigid body cells and shell cells [16]. The linear reduction integral 3D solid unit (C3D8R) was used in the modelling of the RAC. The pipe wall thickness was small in the experimental model, so that the shell element (S4R) was used in the modelling of the steel pipe. The model meshing is shown in Figure 13.

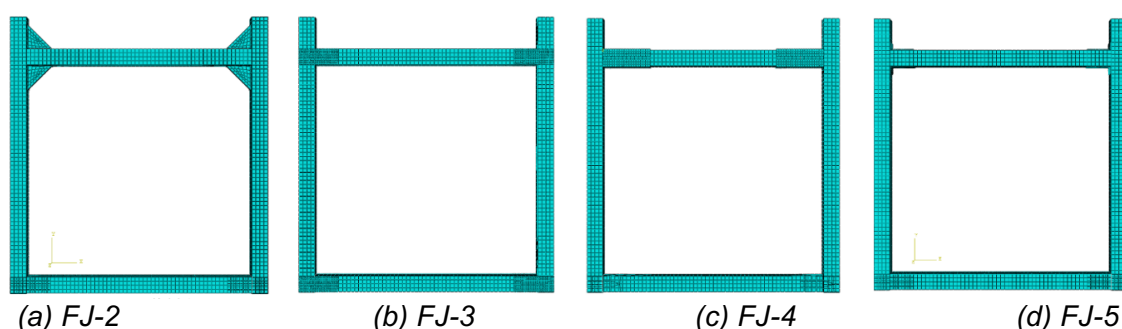


Fig. 13 - Element mesh of the model

Based on the experimental model, the bottom surface of the column was set as the fixed boundary condition. The vertical load was distributed to the top of the column through the rigid-body load beam with the upper end free. The horizontal displacement was transmitted by the loading beams to make the loading process clear and to improve the convergence of the analysis.

Finite element calculation results and analysis

Comparison of the skeleton curves

Figure 14 shows the comparison between the finite element analysis results and the experimental results of the specimens. It can be seen that the initial stiffness of the finite element simulation is higher than the measured stiffness, which is mainly due to the slight slip of the specimen during the loading test. Compared to the experimental results, the downward trend of the skeleton curves in the finite element analysis is not obvious. This is because the cumulative damage in the numerical analysis was not considered. In general, the calculated results are in good agreement with the experimental results.

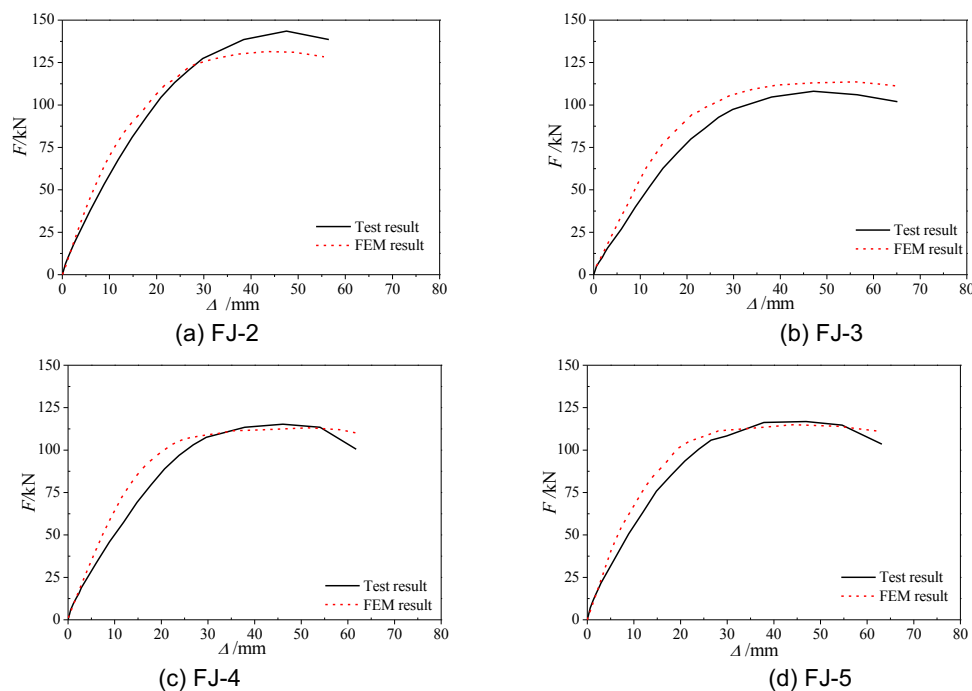


Fig. 14 - Comparison between the measured and calculated results for $F-\Delta$ curve

Analysis of stress and damage evolution

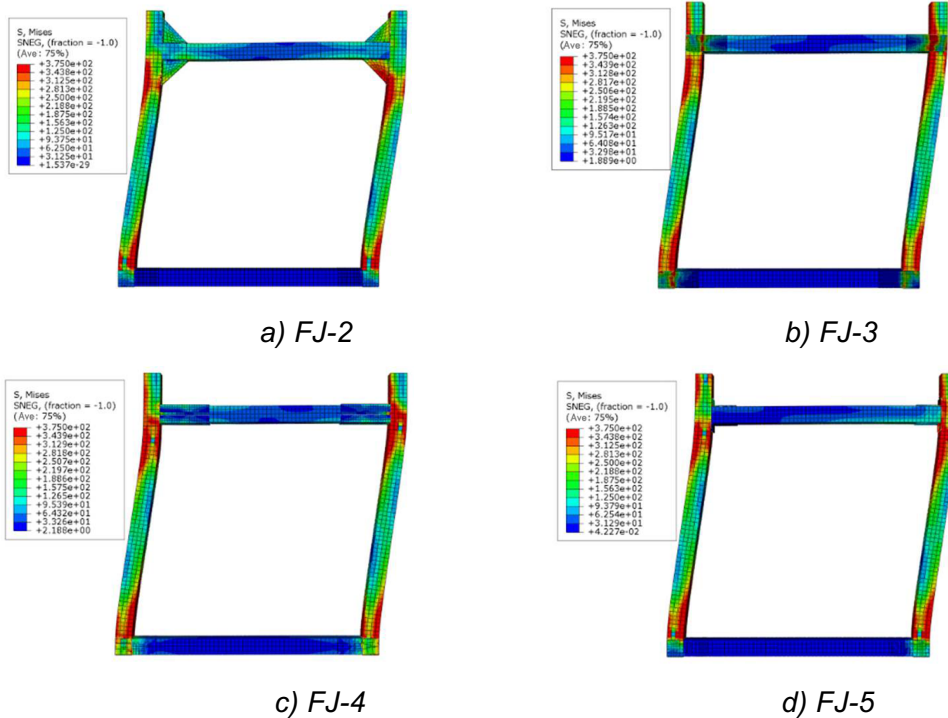


Fig. 15 - Stress cloud of the steel

Figure 15 shows the stress curves of the steel pipe of the four different types of joints when the specimens were damaged. The damage morphology of each specimen was basically similar. Under the action of horizontal loading, the steel pipe was damaged to yield at the top of the column and the column foot. It finally got destroyed. With the different types of joints, the final joint damage came out to be different. It can be seen that the damages of the joints of FJ-2 and FJ-3 were larger, and the damage of joints FJ-4 and FJ-5 were smaller. These results were found to be in accordance with those obtained from the experiments.

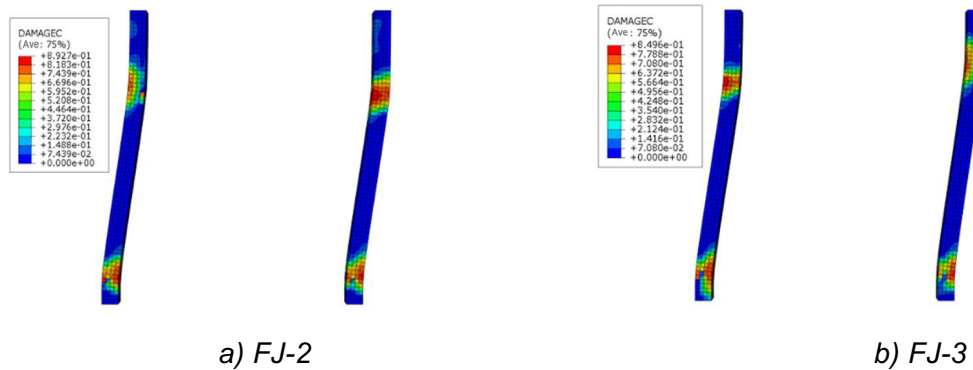


Fig. 16 - Compressional damage of the RCA

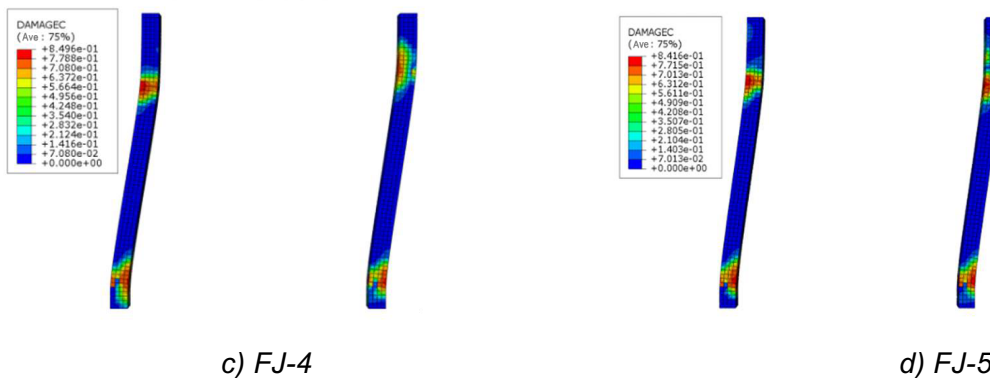


Fig. 16 - Compressive damage of the RCA

Figure 16 shows the plastic damage diagram of the concrete column of the specimens with four different types of joints. It can be seen that, under the action of horizontal load, the concrete in the column foot and joint area of the frame was greatly damaged, and finally crushed. The degree of damage of the concrete of the specimen with different joints was different. The damage of FJ-2 under the action of horizontal load was larger. This result was in accordance with the one obtained from experiments.

CONCLUSION

In this paper, the low cycle repeated load tests were carried out on six light recycled aggregate concrete-steel tube frames. The effect of various types of structures of fabricated joints, filled recycled aggregate concrete in the steel tube and sectional dimension of beam and column on the seismic behaviour of the lightweight recycled aggregate concrete (RAC) filled steel tube frame was studied.

(1) Under the same axial compression, filling RAC in the steel tube of the specimen can significantly improve the seismic performance of the steel frame. The ultimate bearing capacity, energy dissipation capacity and displacement ductility coefficient increased significantly.

(2) The failure displacement angles of the specimens with different assembly joints can reach the value of around 1/24, which shows a good structural ductility. The types of joint structures have a significant impact on the failure mode, bearing capacity, energy dissipation capacity and stiffness degradation of the RAC - filled steel tube frame. Among them, the strengthened joint frame has the strongest bearing capacity and the highest energy dissipation capacity. The ductility values of the angle connection joint frame and the straight connection joint frame were good.

(3) Increasing the cross-sectional dimension of the beam and column can significantly improve the bearing capacity, stiffness, ductility and energy dissipation capacity of the lightweight RAC - filled steel tube frame.

(4) Using ABAQUS, a finite element model was developed for the RAC - filled steel tubular frame with different types of the structures of joints. The evolution of the damage to the structure was analysed. The skeleton curve of the finite element model was in good agreement with the experimental results.

ACKNOWLEDGEMENTS

The authors would like to acknowledge the financial support from the Nation Key Research and Development Project (Grant NO. 2017YFC0703304), the China Postdoctoral Science Foundation (Grant NO. 71001015201705) and the Beijing Postdoctoral Science Foundation (Grant NO. Q6001015201702).

REFERENCES

- [1] Qiao Q, Wu H, Cao W, et al., 2017. Seismic behavior of bifurcated concrete filled steel tube columns with a multi-cavity structure. *Journal of Vibroengineering*, 19, 6222-6241.
- [2] Ekmekyapar T, Al-Eliwi B J M, Faraj R H, et al., 2017. Performance of lightweight aggregate and self compacted concrete filled steel tube columns. *Steel & Composite Structures*, 25, 299-314.
- [3] Koloo F A, Badakhshan A, Fallahnejad H, et al., 2017. Investigation of Proposed Concrete Filled Steel Tube Connections under Reversed Cyclic Loading. *International Journal of Steel Structures*, 17, 1-15.
- [4] Krishan A L, Chernyshova E P, Sabirov R R., 2018. The Bearing Capacity of the Pre-Compressed Concrete Filled Steel Tube Columns. *Defect and Diffusion Forum*.
- [5] Liu W.C., Cao W.L., Zhang J.W., et al., 2017. Mechanical Behavior of Recycled Aggregate Concrete-Filled Steel Tubular Columns before and after Fire. *Materials*, 10, 274.
- [6] Wang R.W., Cao W.L., Liu W.C., et al., 2017. Experimental study of joint work characteristic of assembly light steel tube frame with recycled concrete-thin wall. *Journal of Harbin Institute of Technology*, 12, 60-67.
- [7] Zheng J., Ozbakkaloglu T., 2017. Sustainable FRP recycled aggregate concrete steel composite columns: Behavior of circular and square columns under axial compression. *Thin-Walled Structures*, 120, 60-69.
- [8] Kadhim I. T., Güneş E. M., 2018. Code based assessment of load capacity of steel tubular columns infilled with recycled aggregate concrete under compression. *Construction and Building Materials*, 168, 715-731.
- [9] Zhang A. L., Zhang Z. Y., Jiang Z. Q., et al., 2017. Nonlinear Static Analysis of Repairable Prefabricated Steel Frame Beam-column Joint. *Journal of Architecture & Civil Engineering*, 4, 1-8.
- [10] Fanaie N., Tahriri M., 2017. Stability and stiffness analysis of a steel frame with an oblique beam using method of least work. *Journal of Constructional Steel Research*, 137, 342-357.
- [11] Kawaguchi J., Morino S., Sugimoto T., 1997. Elasto-Plastic Behavior of Concrete-Filled Steel Tubular Frames *American Society of Civil Engineers*, 272-281.
- [12] Rezvani F. H., Behnam B., Ronagh H. R., et al., 2017. Failure progression resistance of a generic steel moment-resisting frame under beam-removal scenarios. *International Journal of Structural Integrity*, 8, 308-325.
- [13] Zhang A. L., Guo Z. P., Liu X. C., et al., 2017. Experimental study on aseismic behavior of prefabricated steel-frame-joists with z-shaped cantilever-beam splicing. *Engineering Mechanics*, 8, 31-41.
- [14] Ricles J. M., Sause R., Peng S. W.; et al., 2002. Experimental Evaluation of Earthquake Resistant Posttensioned Steel Connections. *Journal of Structural Engineering*, 128, 850-859.

- [15] China Standards Publication, GB/T25177-2010, 2011. Recycled Coarse Aggregate for Concrete; Standard Press of China: Beijing, China.
- [16] China Standards Publication, GB 50010-2010, 2011. Code for Construction of Concrete Structures; Standard Press of China: Beijing, China.
- [17] China Standards Publication, GB/T 228-2002, 2003. Metallic Materials-Tensile Testing at Ambient Temperature;; Standard Press of China: Beijing, China.
- [18] Yang Y. F., Wen Z., Dai X. H., 2016. Finite element analysis and simple design calculation method for rectangular CFSTs under local bearing forces. *Thin-Walled Structures*, 106, 316-329.
- [19] Guo, Z.H., Shi, X.D., 2003. Reinforced Concrete Theory and Analyze; Press of Tsinghua University: Beijing, China.
- [20] Hibbitt, Karlsson, Sorensen., 2004. ABAQUS/Standard User's Manual, Version 6.4; Hibbitt, Karlsson, Sorensen Inc.: Rawtucket , RI, USA.

STUDY ON THE EFFECT OF THREE KINDS OF FILTER AID ON THE DEHYDRATION PERFORMANCE OF MICROCYSTIS AERUGINOSA

YANG Zong-zheng^{1*}, ZHANG Meng-yao², CAO Jing-guo¹, LIU Honglei³, HAN Chao-xi¹ TIAN Xin¹

1. College of Chemical Engineering and Materials Science, Tianjin University of Science & Technology, Tianjin 300457, China, 1373721662@qq.com
2. College of Marine and Environmental Science, Tianjin University of Science & Technology, Tianjin 300457, China;
3. Tianjin Academy of Environmental Sciences, Tianjin 300191, China

ABSTRACT

In recent years, algae bloom phenomenon outbreaks frequently in large-scale water bodies during summer. At present, mechanical method is used to collect cyanobacteria and reduce volume. However, the characteristics of algae, namely high viscosity, small particle size and high moisture content, lead to poor efficiency of dehydration. In order to improve the dehydration efficiency of algae and achieve the purpose of volume reduction and dehydration, the dehydration performance of *Microcystis aeruginosa* was studied in this paper. Three filter aid agent, including Poly Aluminium Chloride (PAC), Montmorillonite and Diatomite were added to the algae solution to improve filterability of *Microcystis aeruginosa*. The results showed that all of three filter aid agent have positive effect on the algae filtration rate, specific resistance, compression index and dehydration efficiency. Compared with the other two filter aid agents, the filtration rate of Diatomite is relatively faster. Meanwhile dehydration performance is better as well. When the dosage of Diatomite was 10.0g/L, the filtration rate increased from 0.108 L/h to 0.504 L/h. In addition, the compression index was reduced from 0.710 to 0.594. The specific resistance was reduced from $7.62 \times 10^{10} \text{ s}^2/\text{g}$ to $2.35 \times 10^8 \text{ s}^2/\text{g}$ while the water content was decreased from 86.5% to 66.4%.

KEYWORDS

Cyanobacteria dehydration, Filter aid agent, Filtration rate, Specific resistance, Compressible index, Water content

INTRODUCTION

In recent years, water eutrophication resulting in abnormal proliferation of algae, formed algae bloom phenomenon, and caused serious pollution of water, which led to internal ecosystem imbalances of water body [1]. The phenomenon is one of the major water environment problems of the world urgent need solving [2]. For the phenomenon of algae blooms, the salvage technology of original location is usually used to collect cyanobacteria in rivers and lakes, which can remove surface algae rapidly and efficiently. However, the salvaged cyanobacteria with high water content and large land area still needs volume reduction and dehydration. Zhang Qiang [3] carried out mechanical removal of water from cyanobacteria in Chao late (89 percent of water content) with sieve mesh filter. Xiong Hongbin et.al [4] adopted biosynthetic Polymerized ferrous sulphate (BPFS) coagulation - chamber filter press integration technology to remove the moisture from the cyanobacteria with water content of 89 percent. Wu Jun et al [5] studied the effect of Polymerized ferrous sulphate on the flocculation dehydration of cyanobacteria with water content around 90

percent. Even though physical methods and flocculation agents have positive effects on the dehydration, the water content remaining in cyanobacteria could be still relatively high, which may bring difficulties to the subsequent disposal' downstream processes. Therefore, a filter aid agent with lower cost should be chosen to improve the dehydration efficiency without introducing secondary pollution. Nevertheless, there have been few studies on influence of filter aid agent on cyanobacteria dehydration in China. In this paper, the dehydration performance of three filter aid agent, namely: Poly Aluminum Chloride (PAC), Diatomite and Montmorillonite was investigated. Four parameters, including filtration rate, filter cake specific resistance, compression index and moisture content are chosen as the parameters to study the effects of filter aid agent on the dehydration performance and filtration characteristics of cyanobacteria.

MATERIAL AND METHODS

Experimental Materials

Microcystis aeruginosa (FACHB-905) are provided by the Freshwater Algae Culture Collection at the Institute of Hydrobiology (FACHB-collection). Poly Aluminum Chloride (PAC), Diatomite and Montmorillonite are chosen as filter aid agent during the dehydration process of *Microcystis aeruginosa*.

RIC-250 Artificial climate incubator (Shanghai Bo Xun Industrial Co., Ltd.), UV-2700 ultraviolet visible photometer (Shimadzu Instruments Co., Ltd.), JSM6380LV scanning electron microscope (Hitachi Ltd.), Vacuum suction device (Sinopharm Chemical Reagent Co., Ltd.), High temperature upright microscope DM4000 (Germany Lycra Instruments), Electronic balance ME104E / 02 (METTLER TOLEDO Instrument Co., Ltd.), Blood count plate (Sinopharm Chemical Reagent Co., Ltd.).

Experimental Methods

(1) Cultivation of algae species

The *Microcystis aeruginosa* is cultured in BG11 medium located in the artificial climate incubator with constant temperature of 28°C and light/dark time ratio of 12h: 12h. The filtration experiment is started when its absorbance reaches 1.3 Abs. Table 1 presents the physical properties, namely algae solution organic content, particle size, viscosity and quantity of cyanobacteria and its culture medium. .

Tab. 1 - The basic physical properties of cyanobacteria culture medium

| Standard | Organics mg/L | Particle series μm | Viscosity m Pa·s | Concentration cell/L |
|----------|---------------|-------------------------------|------------------|----------------------|
| Value | 43600 | 2-5 | 15 | 1×10 ¹⁰ |

(2) Selection of filter aid agent

Two parallel algae solution samples are divided into four groups. One group is the original algal liquid. The other three groups are added different amounts of PAC, Montmorillonite and Diatomite. After well mixed, the filtration experiment is carried out at six different pressure levels (0.03, 0.04, 0.05, 0.06, 0.07 and 0.08 M Pa) in suction filtration device. When the filtrate volume V is increased 5 mL, a time (θ) needs to be recorded. Every θ - V data is respectively recorded. According to the experimental data recorded of different times θ and filtrate volume V , the specific resistance of the filter cake is measured. The specific resistance is calculated theoretically by the Equation 1 under constant pressure [6]:

$$r = \frac{2PA^2 b}{\mu C} \quad (1)$$

where P (Pa) is the filtration pressure, A (cm²) is the filtration area; μ (g/(cm·s)) is the dynamic viscosity of the filtrate; C (g/cm³) is the dry solid quality of the unit volume filtrate on the filter medium; b (s/cm⁶) is the slope of the linear relationship between t / V and V ; r (s²/g) is the specific resistance.

The filtration constant, K , is calculated as:

$$\Delta\theta/\Delta q = 2q/K + 2q_e / K \tag{2}$$

where K is the constant pressure filtration constant; $\Delta\theta$ (s) is the filter time of quantitative filtrate; Δq (mL/s) is the amount of filtrate filtering in the unit time of quantitative filtrate; q (mL/s) is the amount of filtrate filtering in unit time; q_e (m³/m²) is the equivalent filtrate volume of per unit filtration area.

After obtaining K under different pressures, compression indexes are calculated as:

$$\lg K = (1-s) \lg\Delta p + \lg(2K) \tag{3}$$

where s is the compression index; Δp (MPa) is the pressure difference.

RESULTS AND DISCUSSION

The filterability of algae liquor

The filtration rate and moisture content of filter cake under different pressure are shown in Figure 1:

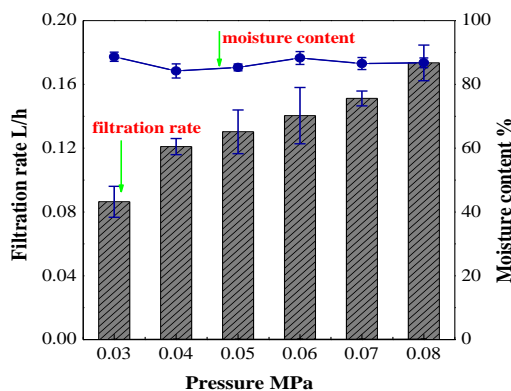


Fig.1 - Relationship between filtration rate and pressure in algae

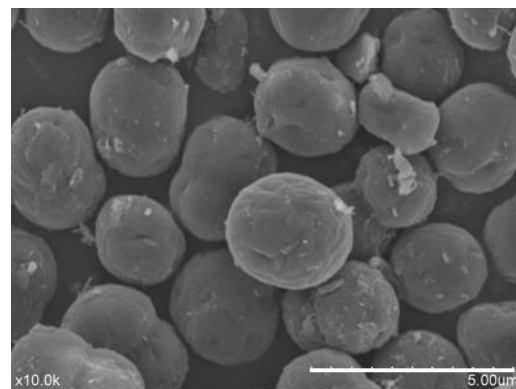


Fig.2 - SEM images of *Microcystis aeruginosa*

Figure 1 shows the influence of pressure on filtration rate and moisture of the filter cake. The filtration rate of algae solution increase from 0.0864 L / h to 0.174 L / h with the increasing pressure from 0.03 MPa to 0.08 MPa. Meanwhile, moisture content of the filter cake varies between 84.21% and 88.77% with an average value of 86.49%. *Microcystis aeruginosa* contains a large amount of organic substances, such as chlorophyll, algae proteins, enzymes, algae toxins and so on [7]. The organic matter can increase the viscosity of algae solution [8] thereby reducing the compression performance and permeability of algae solution [9]. In addition, elastic deformation caused by the compression of algae mud could reduce the filtration rate of algae solution, eventually leading to the decrease of dehydration efficiency. The scanning electron microscopy (SEM) image of *Microcystis aeruginosa* are shown in Figure 2. The average diameter of algae is around 2μm that is larger than microfiltration membrane (0.45μm). Therefore, *Microcystis aeruginosa* particles deposit on the membrane surface. At the beginning of filtration, the filter cake

forms gradually. The inside passage of the filter cake is more smooth, which makes the pass of liquid easier and leads to a faster filtration speed as well. With the increase of the amount of filtrate, the filter cake becomes more compact under the action of pressure. As a result, the permeability of the cake declines gradually. Furthermore, a larger number of ($\times 10^{10}$ cell/L) grained material with a certain level of viscosity may stick on the microfiltration membrane and then slow down the filtering speed.

In order to further study the filterability of algal liquid, the compression performance of the filter cake was calculated according to Equation 2 and 3. The results are shown in Figure 3.

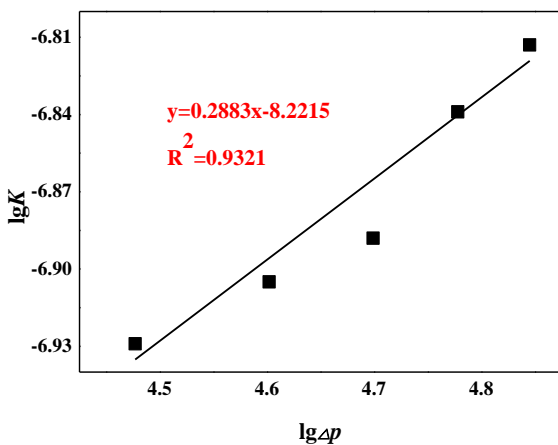


Fig.3 - Determination of Cyanobacteria Compression Index of Algae Water

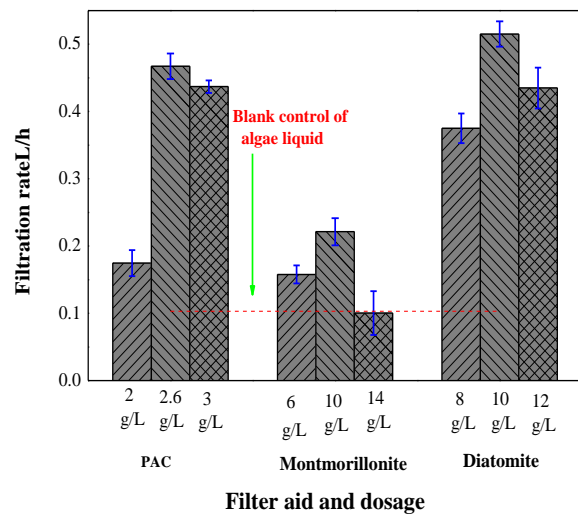


Fig.4 - Effect of Different Dipping Agents on Algae Water Filtration Rate

Figure 3 shows that the trend line of $y = 0.4809x - 9.016$, $R^2 = 0.9321$ has better linear relatedness. According to the slope of the trend line, the filter cake compression index of the algae solution is $0.71 > 0.3$, which is a high compressible material, indicating that the filtration performance of the algae solution is rather poor. The small particle size and viscosity of *Microcystis aeruginosa* results in slower algal filtration rate. Therefore, the filter aid can be added in the algae solution to speed up its filtration rate and improve its filtration performance.

The Effect of filter aid on filtration rate of algae solution

Three filter aids, including, Montmorillonite and Diatomite were tested to study the effect of filter aids on the filtration performance. The results are shown in Figure 4.

Figure 4 presents that the average filtration rate of algae solution is 0.108 L/h without filter aid agent. With an increasing filter aid dosage, the filtration rates with three filter aids shows similar trend which increase firstly and then decrease. The average filtration rate is 0.467 L / h with PAC dosage of 2.6 g / L. The average filtration rate is 0.221 L / h with Montmorillonite dosage of 10 g / L. The average filtration rate is 0.504 L / h with diatomite dosage of 10 g / L. The dosage of three filter aids had a certain improvement effect on the filtration rate of the algae solution, but the average filtration rate of the algae solution with Diatomite dosage was the highest among the three.

Optical images and cross-sectional SEM images of the filter cakes formed by the original algae solution and the solution with different filter aids are shown in Figure 5 and Figure 6 respectively.

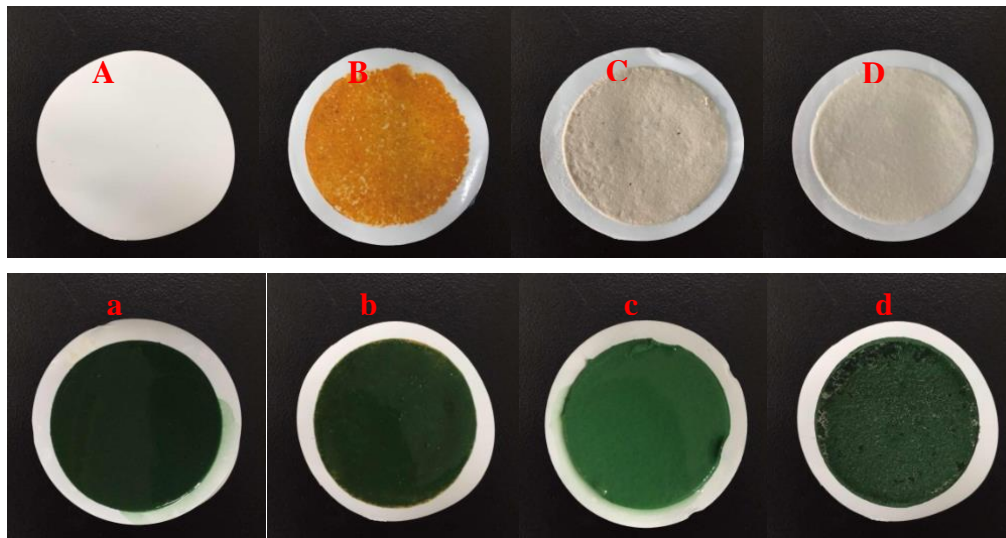


Fig.5 - Blank control (A) , PAC (B) , Montmorillonite (C) , Diatomite (D) Algae (a), Algae+PAC(b), Algae+ Montmorillonite (c) , Algae+ Diatomite (d)

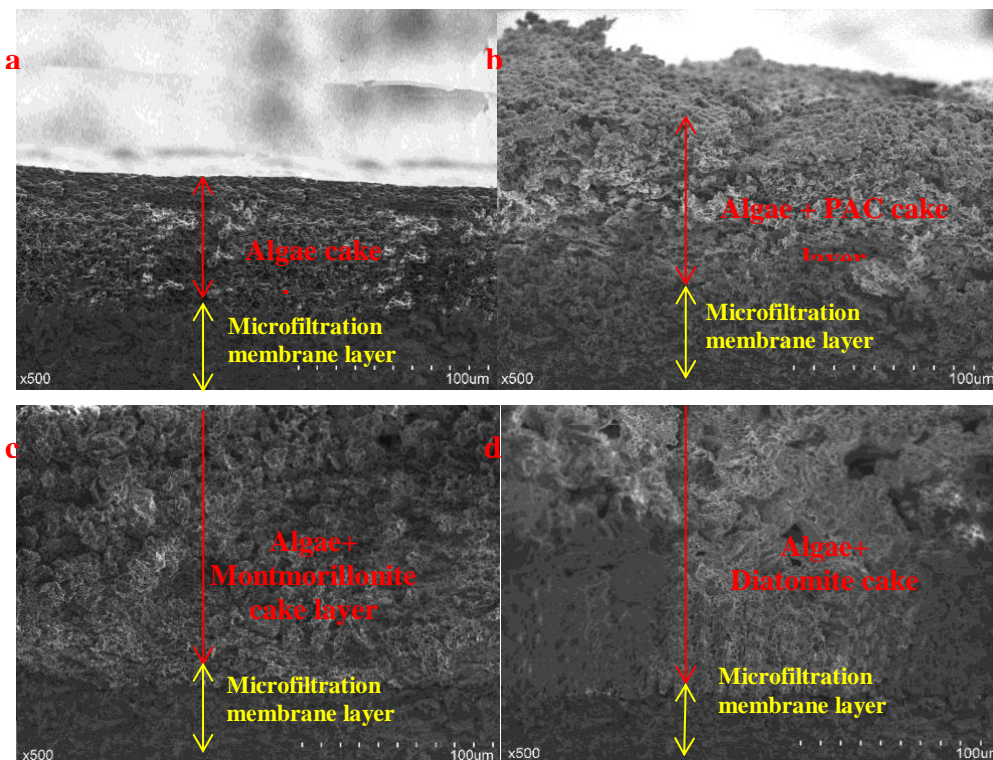


Fig.6 - Algae cake(a), Algae + PAC cake(b), Algae + Montmorillonite cake(c), Algae + Diatomite cake(d)

Compared with the original algae cake, the internal structure of the filter cake formed after adding the three filter aids change. The reasons are as follows:

- (1) PAC, as an inorganic polymer flocculant, has flocculation effect on *Microcystis aeruginosa*. The formed flocculant can gather the algae by the sedimentation trap. As a result, the filtration rate increases from 0.13 L / h to 0.467 L / h. Because *Microcystis aeruginosa* is negatively charged in the water. PAC hydrolyzes positively charged which can rapidly attract negatively charged *Microcystis aeruginosa* and accumulate to form larger flocculant through sediment mesh (Figure 7)

as well as help to flocculate. However, the positive charges could accumulate on the surface of *Microcystis aeruginosa* when the dosage of PAC is too high. In this case, electrostatic repulsion between *Microcystis aeruginosa* will occur, which restrains flocculation and sedimentation. The pores and internal structure of the filter cake formed during the constant pressure filtration are different from the original algal filter cake as shown in Figure 6b and 6a. After passing through the role of sediment mesh, the *Microcystis aeruginosa* in algae solution will aggregate from the fine-grained material into coarse-grained material. This procedure can increase the porosity of the filter cake thereby speeding up its filtration rate.

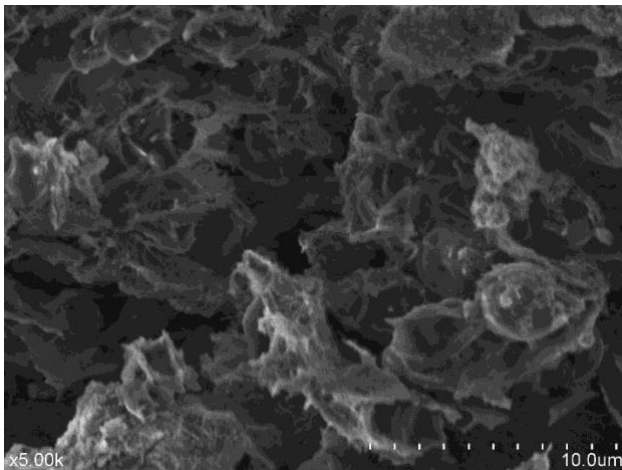


Fig.7 - SEM images of Algae + PAC on cyanobacteria flocculation

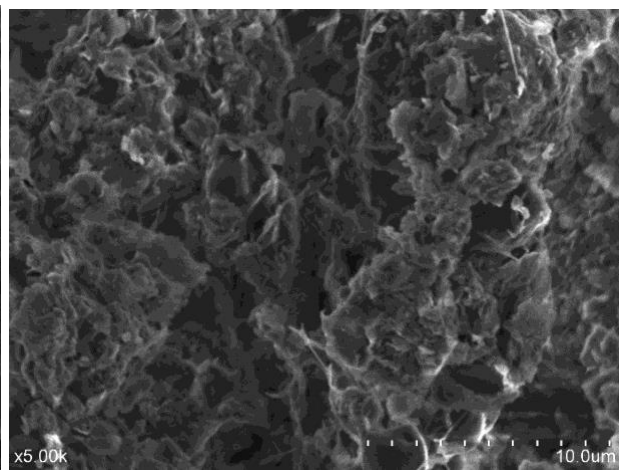


Fig.8 - SEM images of Algae + Montmorillonite

(2) Montmorillonite is a layered mineral silicate consisting of very finely particulate hydrous aluminum silicate. Wang et al [12] showed that the porosity and pore size of the filter cake are directly related to the particle size and composition of the material. The particle size distribution of the filter cake layer is the fundamental factor of the internal structure and filtration of the filter cake. The internal structure of the filter cake after adding Montmorillonite is shown in Figure 8. Montmorillonite is mainly inorganic particles. According to experimental measurement, its surface area is $744.66 \text{ m}^2/\text{g}$ while its porosity is 59.4%. A certain amount of Montmorillonite was added into the original algae solution and compared with the original algal filter cake (Figure 6a). The particle size of the filter cake added with Montmorillonite (Figure 6c) increased obviously which was equivalent to adding an inorganic coarse particle size material. It increased the size of the filter cake. Therefore, the filtration rate of algae solution increases from 0.13 L/h to 0.221 L/h after adding the Montmorillonite. When the amount of Montmorillonite exceeded to a certain limit (10g/L), the filter cake resistance increases with the thickness of filter cake, which slows down the filtration rate.

(3) Diatomite is a siliceous mineral soil with a pore volume of $0.45\text{-}0.98 \text{ cm}^3/\text{g}$ and a large specific surface area and porosity, which can be generally used as a filter aid [13,14]. Diatomaceous is based on inorganic particles with the specific surface area of $77.48\text{m}^2/\text{g}$ and a porosity of 73.28%. The compression deformation is very small. The filtration performance of different particle size is different. And the particle size of the material has certain influence on the filtration rate. In general, the water in the filter cake formed by fine-grained materials is difficult to get out with the slower the filtration rate and the larger the compression index. The porosity of filter cake formed by coarse-grained materials is larger. The probability of clogging the filter medium is smaller. And the filtration rate is relatively larger [15]. Adding diatomite to algae liquor with a certain viscosity is equivalent to add an inorganic coarse-grained material with a porous structure. After adding diatomite, the internal electron microscopy image of filter cake is shown in Figure 9. Compared with the original algal filter cake (Figure 6a), the porosity of filter cake after adding

diatomite (Figure 6d) increases, and the filtration rate is significantly faster than the original filter cake. Excessive dosage of diatomite could also increase the thickness of the filter cake and eventually lead to a decrease of the filtration rate.

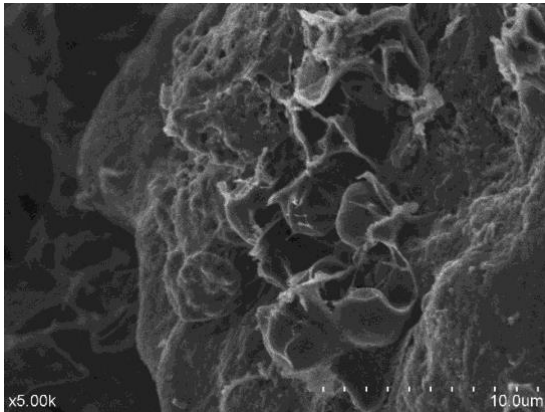


Fig.9 - SEM images of Algae + Diatomite

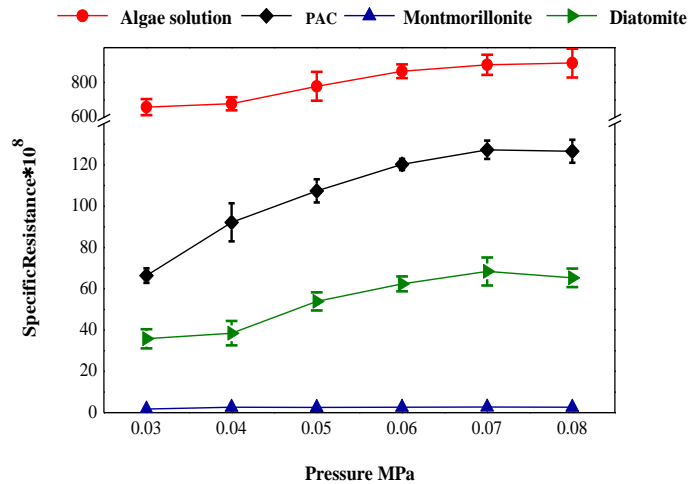


Fig.10 - Effect of Pressure on Specific Resistance of Algae Water

In order to improve the filtration performance of algal liquid, the effect of filter aid on specific resistance, compressibility index and moisture content of filter cake were studied under the optimum dosage condition.

Effect of filter aid on specific resistance

The effects of three filter aid on the specific resistance of the algae solution are shown in Figure 10.

Figure 10 presents that the specific resistance of the filter cake gradually increases with the increasing pressure. After adding filter aid into the algae solution, the specific resistance of the algae solution obviously decreases significantly. In general, a greater specific resistance leads to a worse dewatering efficiency. When the specific resistance is smaller than 0.4×10^9 s²/g, it is easier to perform the material dehydration. The material has a moderate dehydration efficiency with the resistance is between 0.5×10^9 s²/g and 0.9×10^9 s²/g. The material is difficult to dewater with the resistance between 1×10^9 and 1×10^{10} s²/g [6]. The average ratio of the original algal solution is 7.615×10^{10} s²/g, which is a difficult dehydrating material. The average specific resistance of algae solution with PAC is 9.32×10^9 s²/g which is even more difficult to dehydrate compared with the original algal solution. After adding Montmorillonite, the average specific resistance is 4.91×10^9 s²/g, indicating that the dehydration has a certain degree of improvement. After adding diatomite, the average specific resistance is 2.345×10^8 s²/g, indicating that the algal solution adding diatomite is relatively easy to dehydrate. The addition of three filter aids reduces the specific resistance of the filter cake, indicating that the filtration performance is improved after adding the filter aids. After adding the filter aids, the inner structure of the filter cake gradually changes as shown in Figure 9. Different particle size with different internal porosity of the filter cake lead to different filtering performance. Compared between coarse-grained material filter cake and the fine-grained material filter cake, the porosity of the former is larger, making it easier for the algae water pass and relatively smaller for the specific resistance. Compared with the three filter aids, the filtration performance of algae with diatomite is the best. Meanwhile, the specific resistance reduces from 7.615×10^{10} s²/g to 2.345×10^8 s²/g. The algae with diatomite is easy to dehydration material.

Effect of Filter Aid on the Compressibility Index and Dehydration Efficiency of Algae solution

The effect of different filter aids on the algae solution compressibility index and moisture content is shown in Figure 11:

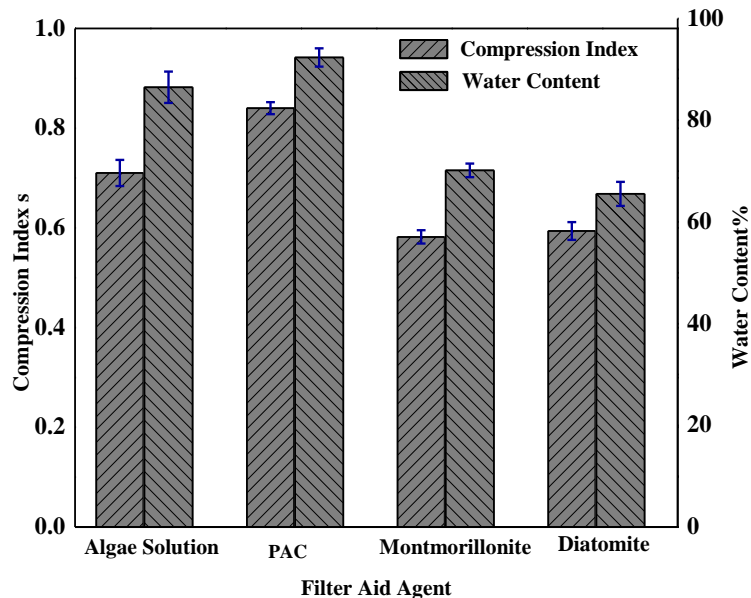


Fig. 11 - Effects of Different Aid Filter on Cyanobacteria Compression Index and Dehydration Efficiency

Figure 11 shows that both of the compression index and the cake moisture content have a certain change after adding filter aid. The original algae solution compressibility index is 0.71, while cake moisture content is 86.49%. After adding filter aid of PAC, the compression index increases to 0.84 while the filter cake moisture content increases to 92.28%. After adding filter aid Montmorillonite, the compressibility index was 0.582 and the cake moisture content was 69.94%. These were indicated that the compression index and the filter cake moisture content both decreased. After adding filter aid Diatomite, the compressibility index was 0.594 and the cake moisture content was 66.4%. These were indicated that the compression index and the filter cake moisture content both decreased. The poor compression performance and high water content of the filter cake are mainly caused by the small size and viscosity of *Microcystis aeruginosa* particle. After adding filter aid of PAC, the flocculation is formed by sedimentation mesh catching. But the structure of the filter cake layer is loose, which results in poor compressibility, higher compressibility index and higher moisture content. After adding filter aid of Montmorillonite or Diatomite, equivalent to adding an inorganic coarse-grained material, which can change the filter cake size and internal structure (Figure 12), increase the size and porosity of the filter cake as well as improve the filtration performance of the filter cake. Compared with the three filter aids, the compressibility index and moisture content of the filter cake adding Montmorillonite and Diatomaceous are relatively lower, indicating that the filterability is better.

In summary, the filtration rate of original algal liquid and algae solution adding PAC, Montmorillonite and are 0.108 L/h, 0.467 L/h, 0.221 L/h, 0.504 L/h, respectively. The average ratio of resistance are 7.615×10^{10} s²/g, 9.32×10^9 s²/g, 4.91×10^9 s²/g, 2.345×10^8 s²/g, respectively. Compression index are 0.71, 0.84, 0.582 and 0.594, respectively. The water contents are 86.49%, 92.28%, 69.94% and 66.4%, respectively. Diatomite has the greatest influence on the filtration rate, compression characteristics and dehydration effect of algae solution. Consequently, it can be used as filter aid for the dehydration experiment of algae solution.

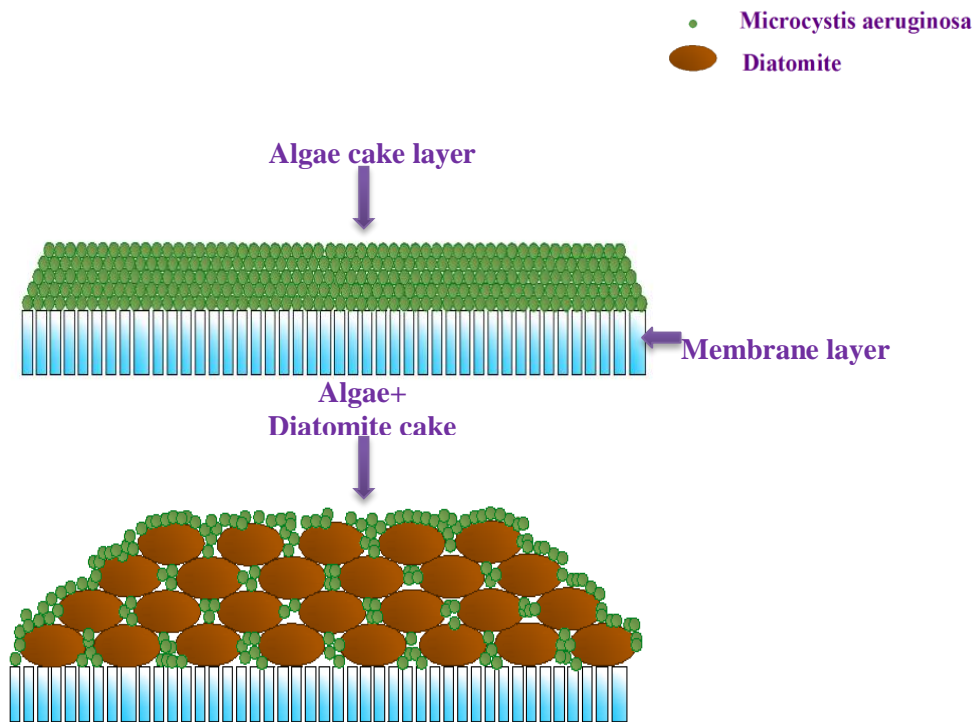


Fig.12 - The shape of the filter cake by two different filtering modes

CONCLUSION

(1) The experimental results of dehydration performance of *Microcystis aeruginosa* show that the dehydration efficiency is closely related to the compression index and specific resistance. The smaller the compression index of the cake is, the harder it is to be compressed. The larger the filtration rate is, the smaller the specific resistance is. The pore channels formed in the filter cake layer are relatively smooth. The dehydration efficiency is higher.

(2) *Microcystis aeruginosa* is a fine grain material in the algae solution. Adding inorganic coarse particle material to the algae solution can change the internal structure and porosity of the filter cake layer. According to the variations of filtration rate, filtration specific resistance, compression index, and moisture content of the cake layer, the filter cake filterability is significantly influenced by the particle size and porosity of the material. A larger specific surface area and porosity can lead to a smaller filtration resistance, a lower compression index and a smaller moisture content of the filter cake. The filtration properties can be strongly improved by adding an inorganic coarse-grained material with high porosity during the dehydration process.

The filtration properties of algal liquid are improved by adding PAC, Montmorillonite and Diatomite. Compared with the three kinds of filters, the filtration rate of algal fluid adding Diatomite increases from 0.108 L/h to 0.504 L/h. The specific resistance significantly decreases from $7.62 \times 10^{10} \text{ s}^2/\text{g}$ to $2.35 \times 10^8 \text{ s}^2/\text{g}$. The compression index decreases from 0.710 to 0.594. The dehydration efficiency of filter cake rises from 13.5% to 33.6%. Therefore, diatomite can be used as filter aid for the dehydration process of algal liquid.

(3) At present, there are few studies on the dehydration performance of *Microcystis aeruginosa* in China. Hence, dehydration of *Microcystis aeruginosa* has become a key technical issue. In this paper, it is proposed that the addition of Diatomite in algae solution can improve the dehydration efficiency of *Microcystis aeruginosa*. However, the dosage of Diatomite is relatively large. Taking

into account the economic costs, the future study will focus on the modification of the diatomite on an existing basis to reduce the dosage of filter aid and further improvement of the dehydration efficiency.

ACKNOWLEDGEMENTS

Our gratitude is also extended to reviewers for their efforts in reviewing the manuscript and their very encouraging, insightful and constructive comments.

REFERENCES

- [1] Shuwen Yan, Danny Zhang, Weihua Song. (2014). "Mechanistic considerations of photosensitized transformation of microcystin-LR (cyanobacterial toxin) in aqueous environments". *Environmental Pollution*, 193: 111-118.
- [2] Fotiou T, Triantis T M, Kaloudis T, et al.(2015). " Evaluation of the photocatalytic activity of TiO₂ based catalysts for the degradation and mineralization of cyanobacterial toxins and water off-odor compounds under UV-A, solar and visible light". *Chemical Engineering Journal*, 261: 17-26.
- [3] Hongbin Xiong, Yaoyao Li, Qiang Zhang.(2014). "Mechanical removal and dewatering of cyanobacteria blooms in Chaohu Lake". *Chinese Journal of Environmental Engineering*, 8 (2): 599-604.
- [4] Yun Ren, Xinping Yang, Dianzhan Wang, et al. (2011). "De watering blue-green algae slurry by filter press after combined coagulation with biosynthesis polymerized ferric sulfate and lime". *Chinese Journal of Environmental Engineering*, 5 (8): 1750-1754.
- [5] Junwei Wu, Xitao Cao.(2016). "Promotion of Polyferric Sulfate on Centrifugal Dehydration of *Microcystis Aeruginosa* in Taihu Lake". *Natural Sciences Journal of Harbin Normal University*, 32 (6): 63-66.
- [6] Shiyu Dai.(2017). *Study on Dewatering Efficiency and Mechanism of Water Purification Sludge*". Suzhou University of Science and Technology.
- [7] Lawton, L.A., Welgamage, A., Manage, P.M., et al. (2011) Novel bacterial strains for the removal of microcystins from drinking water. *Water Science. Technol.* 63 (6): 1137-1142.
- [8] Jinxiang Yi, Pei Wang, Fei Xue.(2016). "Study on Compression Characteristics of Municipal Sludge Solidified Landfill". *Journal of Basic Science and Engineering*, 1 (24): 139-147.
- [9] Yan Lu, Lei Er, Yan Xu, et al.(2011). "The Mechanism of Organic Matter Effect on Physical and Mechanical Properties of Turfy Soil". *Chinese Journal of Geotechnical Engineering*, 33 (4): 655-660.
- [10] Na Gu, Congqian Zhang, Jinlong Gao, et al. (2015). "Removal of the *Oscillatoria* Via the Compound Modified Montmorillonite". *Journal of Safety and Environment*, 4 (15): 250-256.
- [11] Hongxiao Tang.(2000). "Water particles and Refractory Organic Matter Characteristics and Control Technology Principles". Beijing: China Environmental Science Press, 356.
- [12] Xuwei Wang, Wenjun Zhang, Gewei Hu, et al. (2014). "Particle Size Distribution of Fine Coal Cake in Filtering Centrifuge and Press Filter and its Influences on Specific Filtering Resistance". *Journal of China Coal Society*, 10 (39): 2087-2091.
- [13] Yang Y, Zhang J, Yang W, Wu J et al.(2003). "Adsorption properties for Urokinase on local diatomite surface". *Applied Surface Science*, 206(1): 20-28.
- [14] Na Wang, Shuilin Zheng. (2012). "Effects of Different Calcining Process on Properties of Diatomite". *China Non-Metallic Minerals Industry*, (3): 16-20.
- [15] Changsheng Shi, Guangyuan Xie, Yueqiu Zhang. (2006). "Study of the Inner Structure of Fine Coal Filter Cake". *Journal of China University of Mining & Technology*, 35 (1): 99-103.

THE EFFECT OF GAMMA-RAY IRRADIATION ON MECHANICAL PROPERTIES OF EARLY-AGE CEMENT MORTAR

Yuliia Khmurovska¹, Petr Štemberk¹, Svyatoslav Sikorin², Yuliya Kaladkevich², Eryk Pavalanský² and Viktor Fatseyeu²

- 1. Czech Technical University in Prague, Faculty of Civil Engineering, Department of Concrete and Masonry Structures, Prague, Thákurova 7, Czech Republic; yuliia.khmurovska@fsv.cvut.cz, stemberk@fsv.cvut.cz*
- 2. The Joint Institute for Power and Nuclear Research - Sosny of the National Academy of Sciences of Belarus 47/22 Prilesye dist., Minsk dist., Belarus; sikorin@sosny.bas-net.by*

ABSTRACT

This study is focused on experimental investigation of the effect of gamma-ray irradiation on early-age cement mortar properties. Several working hypotheses were formulated based on the current research review. The results of the performed experiment in terms of the relative weight and the relative length change are described in detail in this study. Two observations could be made from comparison of the working hypotheses with the obtained experimental results. Firstly, the positive effect of gamma-ray irradiation in terms of the relative weight change was observed within the first 300 hours or within the equivalent absorbed irradiation dose of 450 kGy. Secondly, the shrinkage due to gamma-ray irradiation was smaller for the unsealed samples due to presence of carbon dioxide in the air, which is needed for the carbonation reaction. It is believed that the obtained experimental data themselves provide a platform for validation of related numerical models.

KEYWORDS

Carbonation, Hydration, Microstructure, Mortar, Shrinkage

INTRODUCTION

It can be stated that the influence of gamma-ray irradiation on the hydration reaction of cement-based mortar is poorly understood. According to the current research [1, 2], the early-age mortar samples subjected to gamma-ray irradiation have a significantly reduced amount of micropores and subsequently they show an increase in strength and shielding properties. However, the number and the form of the available results are not enough to comprehend fully the role of gamma-ray irradiation in the hydration and microstructural formation process. Due to the lack of this understanding, the current knowledge of the effect of gamma-ray irradiation on the hardened mortar may be analyzed and extrapolated to the early-age mortar studies.

Regarding the hardened mortar, the peroxide [3], which is formed by the ionization radiation radiolysis, reacts with calcium present in the pore solution while the peroxide octahydrate is produced and decomposed due to its metastability with simultaneous carbonation reaction [4]. From this follows that the gamma-ray irradiation enhances dissolution/precipitation reaction and may heal the cement crystal structure [5]. Furthermore, according to [6], gamma-ray irradiation causes accelerated carbonation and increases the sample carbonate rate, which contradicts [5], where the carbonate rate is not changed, but, in contrast to the normal carbonation, gamma-ray

irradiation can provoke formation of a significant amount of vaterite and aragonite instead of calcite, which under normal condition destruct CSH phases. The vaterite carbonation can be one of the key processes in the microstructure porosity decrease and the strength increase of the early-age mortar samples.

With consideration of the observations about the effect of gamma-ray irradiation on hardened cement mortar, five hypotheses related to early-age mortar behaviour were formulated. Then these hypotheses were tried to be confirmed with a new experiment aimed at the investigation of the effect of gamma-ray irradiation on the hydration reaction of the early-age mortar, which is described in detail in this paper.

OBJECTIVE AND WORKING HYPOTHESES

The assessment of the change in the hydration reaction process in terms of the weight and the length change of the early-age cement mortar samples under exposure to gamma-ray irradiation was the objective of the performed experimental investigation.

The following working hypotheses related to early-age mortar were assumed:

- (1) The influence of gamma-ray irradiation reduces the amount of micropores [1, 7].
- (2) The gamma-ray irradiation causes the peroxide formation and consequently accelerates the vaterite-carbonation reaction [5, 6].
- (3) The gamma-ray irradiation induced carbonation and the drop in the microstructure porosity cause an increase of strength [1, 5].
- (4) The dose of gamma-ray irradiation absorbed by the samples during the hydration process is too low to induce metamictization of minerals [8, 9].
- (5) The alkali-silica reaction is not accelerated by the gamma-ray irradiation dose absorbed during hydration [8, 10].

EXPERIMENT

Mixture composition

The used mortar consisted of Cement type CEM I 42.5R, siliceous aggregate with fraction of 0-4 mm, water-cement ratio of 0.38. The mortar and the cement composition are shown in Tables 1 and 2, respectively. All samples were cured in sealed conditions for eight hours after mixing.

Tab. 1 - Composition of mortar

| Component | Weight |
|--|---------|
| Cement (CEM I 42.5R Mokra, CZ) | 2 625 g |
| Water | 1 000 g |
| Siliceous aggregates with fraction of 0-4 mm | 4 200 g |

Tab. 2 - Composition of cement CEM I 42.5R Mokrá

| Component | % by weight |
|----------------------------|-------------|
| <i>Clinker composition</i> | |
| C ₃ S | 68.5 |
| C ₂ S | 11.6 |
| C ₃ A | 7.4 |
| C ₄ AF | 11.5 |
| C _{free} | 1.0 |
| <i>Cement components</i> | |
| Clinker | 95.0 |
| Gypsum | 3.5 |
| Fly ash | 1.3 |
| Slag | 0.2 |

Sample geometry

The shape of the sample with dimensions of 10x10x80 mm was selected so that the sample cross-section was small enough to ensure the gamma-heating dissipation.

Experimental sets

The insulated (sealed) and not insulated (unsealed) samples were considered in this experimental investigation so that the effect of drying on the hydration process could be assessed. The insulation was provided by a polyethylene foil. The following experimental sets were investigated:

- *Irln* – irradiated insulated sample
- *IrNi* – irradiated not insulated sample
- *Nrln* – not irradiated insulated sample (reference sample)
- *NrNi* – not irradiated not insulated sample (reference sample).

Irradiation facility

⁶⁰Co Irradiation Facility UGU-420 of The Joint Institute for Power and Nuclear Research - Sosny of the National Academy of Sciences of Belarus, Minsk with the following irradiator characteristics: the height of the active part is 50 cm; the generating dose rate is 0.1-10 Gy/s and the total number of sources is 768 with the total activity of 4.4·10¹⁵ Bq (120 kCi) was used in order to carry out the presented experimental investigation.

Irradiation

The sample irradiation started at the sample age of eight hours.

Measurements

The effect of gamma-ray irradiation was measured in terms of the weight and the length change of the samples. The insulation was removed from the samples for the dimension and the weight measurement. The environmental temperature and the relative humidity were also recorded. The radiation dose rate for the samples was equal to 3.72 kGy/h and 4.02 kGy/h for the experimental sets *Irln* and *IrNi*, respectively, with the corresponding total absorbed radiation dose of $2.3 \cdot 10^3$ kGy and $2.6 \cdot 10^3$ kGy at the end of the experiment. The average duration of irradiation per day was 13 hours.

RESULTS

The changes of the relative weight and the relative length of the early-age cement mortar samples over time are shown in Figures 1 and 2, respectively. The changes of the environmental relative humidity and the temperature are shown in Figure 3. These results represent the complete package of information about the gamma-ray irradiation induced volumetric and weight changes and together with the effect of environment they can be used for validation of related numerical models.

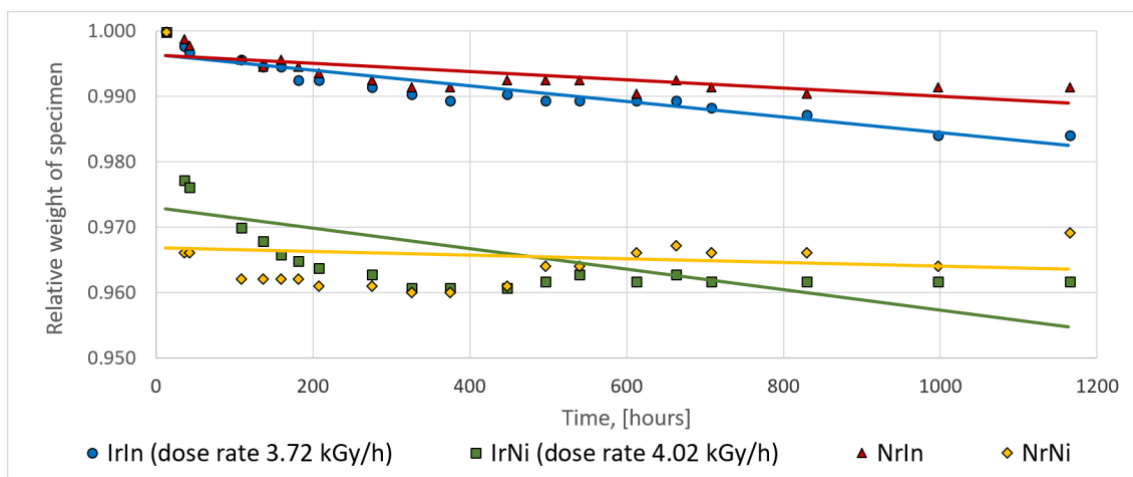


Fig. 1 – Change of relative weight of early-age cement mortar samples over time

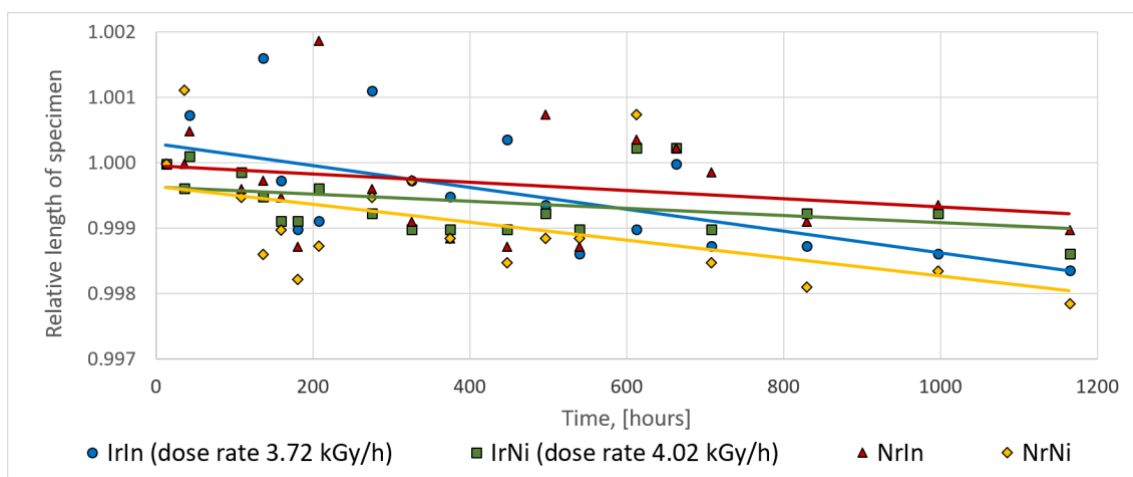


Fig. 2 – Change of relative length of samples over time

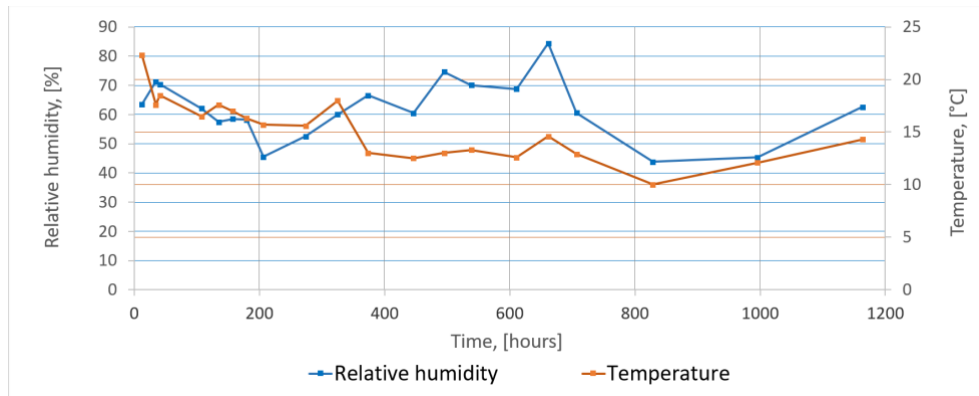


Fig. 3 – Environmental relative humidity and temperature

The weight of *IrNi* and *NrNi* samples decreased rapidly due to the drying, as can be seen in Figure 1. The slight increase of the weight of these samples after 500 and 1000 hours corresponded to the increase of the relative humidity in the laboratory, see Figure 3. The *IrNi* sample absorbed substantially less water than the *NrNi* sample. The decreased ability of the samples to absorb water from the environment is an indirect evidence of the drop in the microstructure porosity (working hypothesis (1)). A similar effect was observed in the relative length change, see Figure 2.

The higher weight of the *IrNi* sample during the first 300 hours (up to approximately 450 kGy in terms of the absorbed gamma-ray dose), see Figure 1, could be caused by the accelerated carbonation (working hypothesis (2)). After the first 300 hours, the *IrNi* sample had a higher weight loss than the *NrNi* sample, which means that the radiation-induced water decomposition with the subsequent gas evaporation became more important in terms of the weight loss. Presumably, the rate of carbonation reaction under the exposure to gamma-ray irradiation is much higher than the usual carbonation rate, but the reaction slows down after the absorption of a specific dose of radiation by the sample, which means that the difference in the carbonate rate of the irradiated and not irradiated samples decreases with time. This observation supplements the data presented in [5] and [6] without controversy.

The *IrNi* sample shrank less than the *NrNi* sample, see Figure 2, possibly due to the carbonation reaction, which reduced the shrinkage. However, the comparison of the *Irln* and the *Nrln* samples showed the opposite trend. The irradiated samples (*Irln* and *IrNi*) absorbed a different irradiation dose over time. However, the comparison of the relative length of these samples with dependence on the absorbed irradiation dose shown in Figure 4 had a similar trend with that shown in Figure 2. It means that the sample insulation affected negatively the irradiated early-age mortar due to the lack of carbon dioxide available for the carbonation reaction, which not only reduced the volumetric changes, but also could increase the strength of the samples (working hypothesis (3)).

The weight of the *Irln* and the *Nrln* samples decreased much slower than that of the *IrNi* and the *NrNi* samples, as can be seen in Figure 1, however, the weight loss of the *Nrln* sample is rather high. This loss was caused by an instant drop in the relative humidity from 100% to the ambient humidity due to the insulation removal, which was necessary in order to perform the measurements. Such a drop in the relative humidity caused the rapid free water evaporation.

The relative weight change of the *Irln* sample in the first 300 hours was similar to that of the *Nrln* sample, see Figure 1. After the first 300 hours, the relative weight of the *Irln* sample became smaller than that of the *Nrln* sample. This effect was similar to those in the *IrNi* and *NrNi* samples, but it was less pronounced. That confirmed both the accelerated carbonation during the first 300

hours (working hypothesis (2)) and the effect of the lack of carbon dioxide for the carbonation reaction due to the insulation.

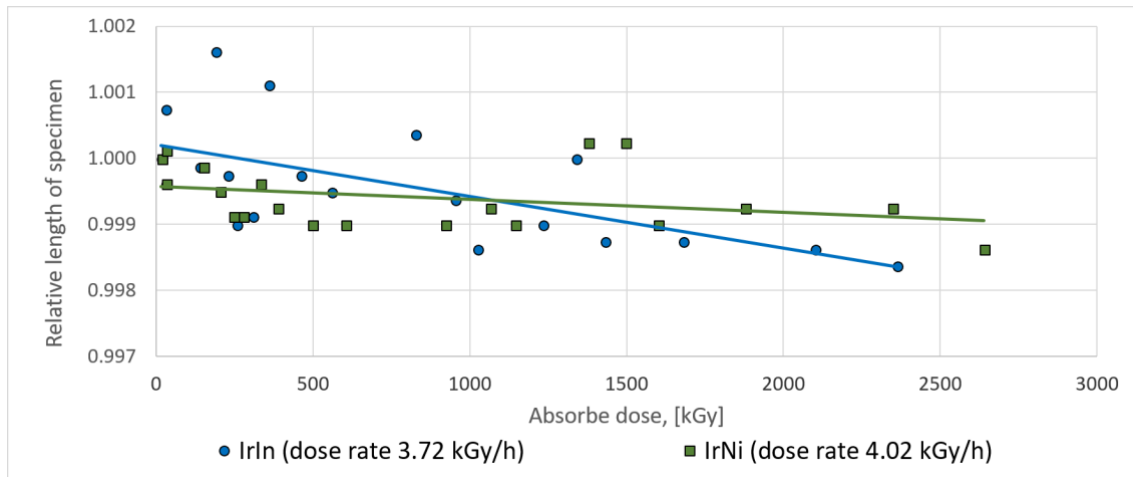


Fig. 4 – Change of relative length of samples with absorbed irradiation dose

The relative weight and the relative length of the *IrIn* sample reduced faster, see Figures 1 and 2, due to the summation the insulation removal effect and the radiation-induced water decomposition.

The *IrIn* and the *NrIn* samples swelled during the first several hours up to the several days, see Figure 2. This effect is common for concrete. The absence of the swelling of the irradiated samples after 28 days of the experiment is an indirect evidence that no metamictization or accelerated alkali-silica reaction started (working hypotheses (4) and (5), respectively).

CONCLUSION

The working hypotheses were confirmed indirectly, however the direct confirmations are still needed. Therefore, the experimental investigation of the sample microstructure, the chemical composition and the strength should be performed.

Two important observations have been made based on comparison of the working hypotheses and the experimental results. Firstly, the shrinkage due to gamma-ray irradiation was smaller for the unsealed samples. It is believed that this effect is associated with the unlimited source of carbon dioxide in the air, which is needed for the carbonation reaction. Secondly, the positive effect of the gamma-ray irradiation in terms of the reduced relative weight loss was observed within the first 300 hours, or within the equivalent absorbed radiation dose of 450 kGy.

It is believed that the obtained results along with the above discussion can provide a platform for validation of the numerical models which describe the effect of gamma-ray irradiation on the early-age cement properties.

ACKNOWLEDGEMENTS

This work was supported by Ministry of Education, Youth and Sports of Czech Republic, project 8F17002, the Czech Science Foundation, project 16-20008S, and the Czech Technical University in Prague, project SGS18/041/OHK1/1T/11, which are gratefully acknowledged. The Joint Institute

for Power and Nuclear Research - Sosny of the National Academy of Sciences of Belarus, Minsk is gratefully acknowledged for performing the irradiation.

REFERENCES

- [1] Rezaei-Ochbelagh D, Mosavinejad H G, Molaei M, Khodadoost M., 2010. Effect of low-dose gamma-radiation on concrete during solidification. *International Journal of Physical Sciences*, vol. 5: 1496-1500
- [2] Burnham S., Huang L., Jevremovic T., 2016. Examining the Effect of Gamma Radiation Exposure in Early Stage of Concrete Curing on its Strength and Long-Term Durability. In: *Proceedings of the 24th International Conference on Nuclear Engineering*, edited by American Society of Mechanical Engineers, V005T15A068-V005T15A068, doi: 10.1115/ICONE24-60924
- [3] Le Caër S., 2011. Water radiolysis: influence of oxide surfaces on H₂ production under ionizing radiation. *Water*, vol. 3: 235-253, doi: 10.3390/w3010235
- [4] Bouniol P, Aspart A., 1998. Disappearance of oxygen in concrete under irradiation: the role of peroxides in radiolysis. *Cement and concrete research*, vol. 28: 1669-1681, doi: 10.1016/S0008-8846(98)00138-0
- [5] Maruyama I, Kontani O, Takizawa M, Sawada S, Ishikawao S, Yasukouchi J, Sato O, Etoh J, Igari T., 2017. Development of soundness assessment procedure for concrete members affected by neutron and gamma-ray irradiation. *Journal of Advanced Concrete Technology*, vol. 15: 440-523, doi: 10.3151/jact.15.440
- [6] Vodák F, Trtík K, Sopko V, Kapičková O, Demo, P., 2005. Effect of γ -irradiation on strength of concrete for nuclear-safety structures. *Cement and concrete research*, vol. 35: 1447-1451, doi: 10.1016/j.cemconres.2004.10.016
- [7] Vodák F, Vydra V, Trtík K, Kapičková O., 2011. Effect of gamma irradiation on properties of hardened cement paste. *Materials and structures*, vol. 44: 101-107, doi: 10.1617/s11527-010-9612-x
- [8] Ichikawa T, Kimura T., 2007. Effect of nuclear radiation on alkali-silica reaction of concrete. *Journal of Nuclear Science and Technology*, vol. 44: 1281-1284, doi: 10.1080/18811248.2007.9711372
- [9] Maruyama I, Muto S., 2016. Change in relative density of natural rock minerals due to electron irradiation. *Journal of Advanced Concrete Technology*, vol. 14: 706-716, doi: 10.3151/jact.14.706
- [10] Pomaro B., 2016. A review on radiation damage in concrete for nuclear facilities: from experiments to modeling. *Modelling and Simulation in Engineering*, vol. 2016, doi: 10.1155/2016/4165746

STUDY ON A NEW DESIGN OF GROUTING PUMP FOR MANAGING WATER INRUSH IN KARST TUNNELS

Li Shucaij, Li Mengtian¹, Zhang Xiao and Zhang Qingsong¹

1. University of ShanDong, Research Center of Geotechnical and Structural Engineering, Jinan, 250061, China; 156207068@qq.com

ABSTRACT

The low flow rate and efficiency of existing grouting pumps such as piston pumps and diaphragm pumps result in difficulty in managing sudden water and slurry discharges. In this study, a new design for grouting pumps is proposed to improve the grouting flow rate and efficiency. A grouting model test scheme to manage the water inrush of a tubular karst is designed. The power consumption of this system is equivalent to that of a diaphragm grouting pump. Improved performance was also observed for the newly designed rotary piston pump in grouting plugging tests. The retention of slurry and changes in moving water flow are observed and recorded to examine the grouting effects of the pumps. In addition, the pressure and flow rate changes of the grouting slurry are used to gauge the performance parameters of the pumps. A rotary piston pump and a traditional piston pump were tested in single- and separate-hole grouting experiments in tunnel engineering sites. In the grouting model test, which manages the water inrush of a tubular karst, the newly designed rotary piston pump had a distinct advantage in terms of the slurry retention thickness and fracture sealing effect. In particular, the efficiency of the rotary piston pump increased by a factor of 10 over the diaphragm grouting pump. During the experiments in the engineering site, the grouting flow rate of the rotary piston pump showed significant increase when compared to the traditional piston pump. The construction time was halved. The proposed rotary piston grouting pump has shown obvious advantages over existing grouting pumps.

KEYWORDS

Karst water bursting, Grouting, Rotary piston pump, Grouting model test, Engineering field test

INTRODUCTION

In recent years, with the implementation of China's western development strategy, the construction of tunnels and underground infrastructure has gradually shifted to the southwest karst regions. When tunnels and underground works cross the karst areas, a sudden inrush of water often occurs. Such disasters endanger the personal safety of construction crews, delay the construction process, cause environmental hazards, and result in economic losses directly or indirectly [1-3]. The process of karst water bursting can be divided into five different types according to the karst's spatial characteristics. These are, fissure type, small vessel type, pipe type, cave type and underground river type. The research focus of this article is on the pipe type bursting process, as it has become one of the main influencing factors in the underground engineering works in karst areas. Such areas are characterised by high flow rate, strong recharge and strong difference [4]. Water bursting in the karst tunnel fissures is the result of a split in a fractured rock mass disturbed by the underground construction while under the continuous pressure of the karst water [5]. After the excavation of the fissure, the internal filling medium is continuously lost, resulting in a pipe gush of the filling material. The soil extrudes as a whole, and the underground river water, cavity water or surface water flows into the tunnel. Eventually, the lining fractures and

the water bursts into the tunnel [1]. To manage such disasters, comprehensive advanced geological forecasting should be carried out. In addition, optimised treatment schemes aimed at preventing water bursting should be designed dynamically. Ultimately, the management and governance plans need to be established [6]. Grouting is an effective method to control the flooding in underground engineering. With recent advancements in engineering applications, the idea of "draining" is gradually changing towards "blocking" [7,8].

In any grouting project, the core equipment is the grouting pump. The performance of this pump is critical to achieve higher quality and efficiency in the construction project. The main types of grouting pumps available to date are piston pumps, diaphragm pumps and various reciprocating pumps, with piston pumps being the primary choice [9]. The piston pump is driven by a rod mechanism that is operated by a crankshaft rotation, which completes the reciprocating motion of the piston inside a cylinder. Although the sealing system is relatively perfect and operates well under higher pressure, the reciprocating motion of the piston can cause imbalance of inertia moment and inertia force. This may lead to an overload of inertia in the piston pump structure and cause unstable vibration and noise [10-12]. Moreover, the low flow rate of the piston type grouting pump causes reduced grouting efficiency. Several high-pressure and large-flow-rate plunger pumps have been designed and tested on test benches [13]. However, these pumps merely improve the bore size, and do not solve the fundamental problem.

In order to achieve the benefits of a high-pressure and high-flow type pump, a rotary piston pump is designed, which takes the advantage of the high pressure of a reciprocating pump and the high flow rate of a centrifugal pump. This is operated in the way of rotary extrusion. The rotary piston pump can be classified as a rotor pump, which has many commonalities with a typical rotor pump structure. However, the volumetric efficiency of most rotor pumps is low due to poor chamber sealing [14-17]. This paper presents the operating principle of the new grouting pump and design of a karst pipeline grouting test procedure. The CN-0.5S model is used to test the newly designed pump and a typical piston pump. The collected data were analysed and processed. Finally, the test flow rate, pressure, efficiency and other performance parameters were calculated [18-20].

GROUTING CONTROL TEST ON PIPELINE WATER BURSTING IN KARST AREA

In the control treatment of sudden flooding in a karst area by grouting, the grouting pump injects the slurry into the stratum medium. The slurry blocks the groundwater runoff and influx mainly by filling the cave cavity, karst pipeline, fissure passage and other water storage structures. With a continuous pumping and curing of the slurry, the overcurrent cross-sectional area of the burst water gradually decreases. The diffusion resistance of the slurry gradually increases. In other words, the damping property of the injected formation medium gradually increases [21]. In order to test the performance of the proposed rotary piston pump in the above grouting process, a visual test system for grouting plugging of the karst pipe is designed. Grouting is performed in the visual test system, considering the impact of the pipe diameter, water velocity, grouting flow rate and other factors (affecting the slurry diffusion and sealing performance). The variation of the parameters was recorded by a real time data acquisition system. This allowed an investigation of the retention mode of the fluids under different moving water conditions. The results of this study have practical significance for slurry blocking and managing pipeline water inrush in karst areas.

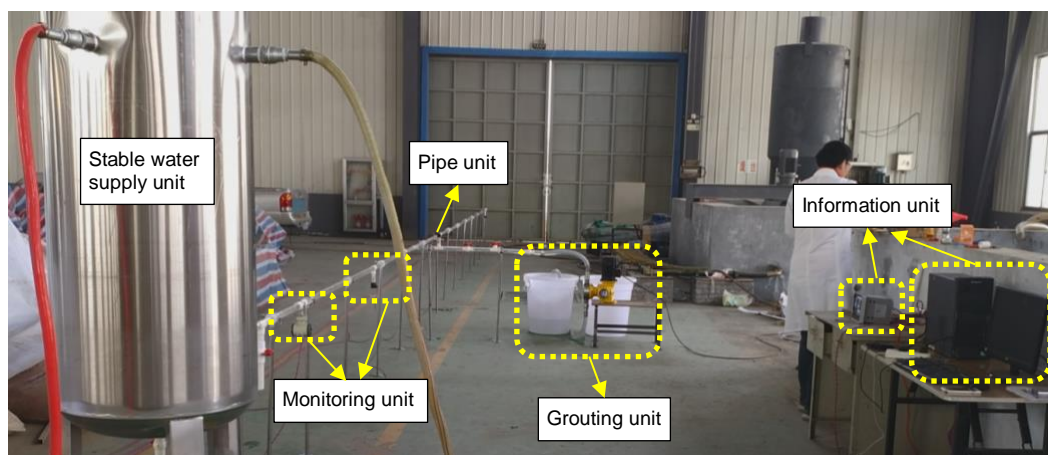
Test objectives

(1) Investigate the sealing ability of the piston grouting pump and the rotary piston grouting pump.

- (2) Investigate the sealing ability of the two grouting pumps in two different diameter pipe models.
- (3) Investigate the sealing capacity of the two grouting pumps at different water flow rates.
- (4) Investigate the maximum hydrodynamic retention rate of the slurry based on the theory of minimum deposition rate.
- (5) Study the precipitation and migration modes (layer displacement, slip type and suspended type) under the influence of different factors, and identify the criteria for determining the migration mode transition of the slurry.

Test System

The test system utilised in this work consisted of five parts. These are the pipe unit, the stable water supply unit, the monitoring unit, the information unit and the grouting unit. The size of the grouting test system was 5 m × 2 m × 1 m, as shown in Figure 1.



(a)

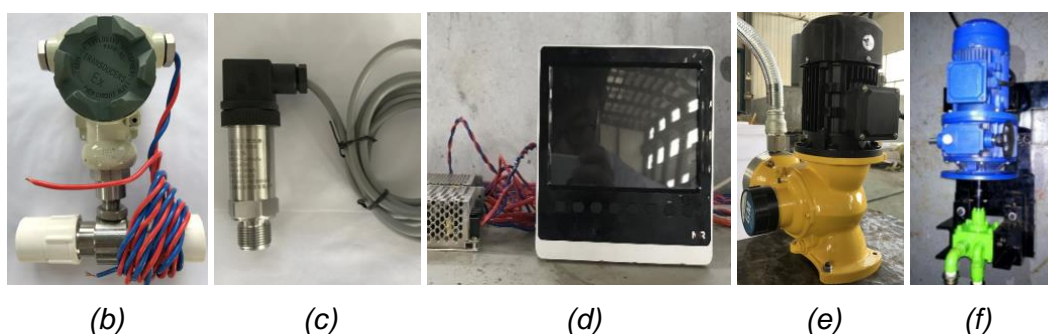


Fig. 1 – Test system of the grouting equipment; a) overall view of the test system, b) electromagnetic flowmeter, c) Pressure sensor, d) Paperless recorder, e) GM-500 diaphragm pump, f) CN-0.5S rotary piston pump

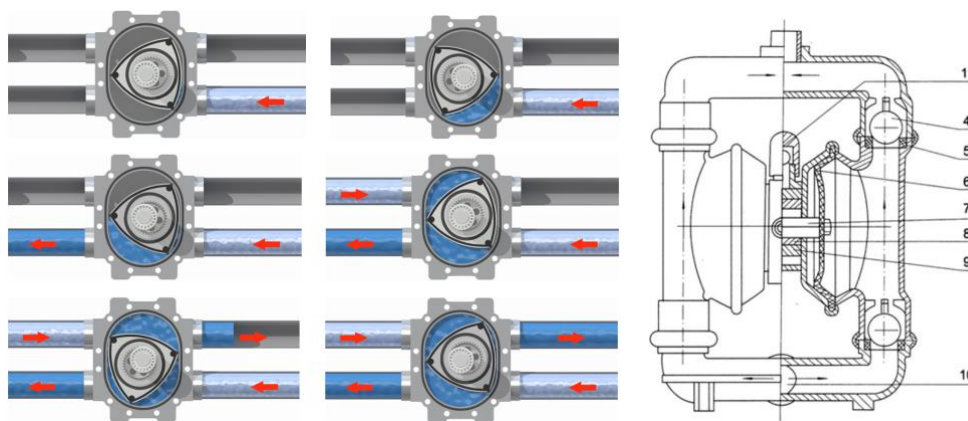
The pipe unit was equipped with two PMMA (Poly Methyl Methacrylate/methacrylic Acid) pipes (having diameters of 32 mm and 50 mm, respectively). The upstream end of the pipe was connected to the stable water supply unit, which consisted of a storage tank and a control valve.

To control the velocity of the flowing water steadily in the course of the experiment, the water tank was externally connected to the pressure-stabilising air pump. The downstream outlet of the pipeline was connected to the slurry collection container. The monitoring unit included a pressure sensor and an electromagnetic flowmeter. They were located at 6 and 4 m along the pipe, respectively. The variation rules of the pipeline flow and the pressure changes in the flowing water during the grouting process were recorded. The data from the sensors were collected by the information unit, which included an NHR-8100/8700 colour paperless recorder and a computer. The grouting unit included two grouting pumps and two slurry storage barrels.

The proposed CN-0.5S rotary piston grouting pump and the GM-500 mechanical diaphragm pump were used to test the grouting effect. Applying the principle of the triangular rotor engine, the newly developed rotary piston pump changes the cubage of the pump chamber to complete the slurry pumping process through the rotary motion. The rotary piston grouting pump has the advantages of the reciprocating motion of a piston pump. In addition, it relies on high-speed rotation akin to a centrifugal pump. As a result, it can produce both greater pressure and larger output flow. The working principle is shown in Figure 2(a). Each cylinder has two inlets and two outlets. The apex of the rotor divides the cylinder into three working chambers, each of which changes in volume to complete the suction and discharge operations.

The rotor movement is a complex process [22,23], which includes the rotation of the rotor cross-section centroid around the cylinder cross-section centroid. In addition, the rotor's self-rotation is centred on its cross-section centroid. When the power unit causes the main journal of the crankshaft to rotate, the connecting rod neck of the crankshaft drives the inner ring gear on the rotor into a mesh motion with the fixed gear. The rotor rotates around the connecting rod neck at the same time. Therefore, the compound motion of the rotor in the cylinder includes the self-rotation and the revolution of the rotor around the centre of the main journal of the crankshaft. The ratio of the rotor revolution speed to self-rotation speed is 3:1. Therefore, the crankshaft's main journal rotates three times, and three separate cavities accomplish inhalation and discharge twice. In other words, the crankshaft of the main journal rotates once, and a single cylinder completes suction and drainage of two cavities.

The structure of the diaphragm pump is shown in Figure 2(b). In the two symmetrical working chambers of the pump, each chamber is equipped with a flexible diaphragm. The two diaphragms are connected by a connecting rod. The synchronous reciprocating motion of the two diaphragms, driven by the coupling rod, results in cubage changes of the working chambers so as to continuously draw and discharge the liquid.



(a) Principle of the rotary piston pump

(b) Principle of a diaphragm pump

Fig. 2 – Operating principle of the pumps

The theoretical parameters of the CN-0.5S rotary piston grouting pump, and the rated parameters of the GM-500 mechanical diaphragm pump are shown in Table 1.

Tab. 1 - Comparison of parameters of different grouting pumps

| Type | Motor power (kW) | Grouting pressure (MPa) | Flow rate (L/min) | Maximum efficiency (%) |
|---------|------------------|-------------------------|-------------------|------------------------|
| CN-0.5S | 0.5 | 0-0.7 | 0-33.3 | 79.2 |
| GM-500 | 0.5 | 0-0.7 | 0-8.3 | 20.2 |

Test plan

As found from the previous studies, the management of high flow water inrush disaster in karst fissures is limited by the lack of availability of high flow rate grouting equipment. In most cases, methods such as increasing the water–cement ratio, aggregate filling, and chemical slurry were applied. Combined with the previous theoretical research, a grouting test scheme is designed as part of this work. In this test, the pipeline diameter, the moving water flow rate, and the grouting flow rate were focused upon. The thickness of the slurry retained at a fixed monitoring point and the reverse diffusion distance of the slurry were used as the evaluation indices to analyse the plugging effect of the karst pipeline. The role of the grouting flow rate in the karst pipelines was also studied. In this test:

- (1) A cement slurry with a water–cement ratio of 1:1 was used for grouting.
- (2) Three PMMA pipes with inner diameters of 26 mm (Pipe 1), 44 mm (Pipe 2) and 62 mm (Pipe 3) were used as different pore size karst pipelines.
- (3) Each of the PMMA pipes provided different flow velocities, which were 0.1 m/s, 0.2 m/s, 0.3 m/s, 0.4 m/s and 0.5 m/s (Table 2).
- (4) At different flow velocities, CN-0.5S was used to provide different grouting flow rates, which were 24 L/min, 26 L/min, 28 L/min, 30 L/min, and 32 L/min. GM-500 was used to provide different grouting flow rates, which were 2 L/min, 3.5 L/min, 5 L/min, and 6.5 L/min.
- (5) Grouting was started at 10 s after triggering the timer and was stopped at 85 s. The flow rate and the pressure were recorded at the monitoring points in the grouting process.

In order to ensure identical water flow velocity gradient inside the three pipes, different flow rates were designed (Table 2). The flow rates were controlled by the air pump of the water tank and the electromagnetic flowmeter. The error was controlled within 3%.

Tab. 2 - Flow rates at different flow velocity in each pipe

| | Pipe 1 | Pipe 2 | Pipe 3 |
|---------------------|-------------------|--------|--------|
| Flow velocity (m/s) | Flow rate (L/min) | | |
| 0.1 | 12.74 | 36.47 | 72.42 |
| 0.2 | 25.47 | 72.95 | 144.85 |
| 0.3 | 38.21 | 109.42 | 217.26 |
| 0.4 | 50.94 | 145.90 | 289.68 |
| 0.5 | 63.68 | 182.37 | 362.10 |

TEST RESULTS

Analysis of the slurry retention in pipe

When using GM-500 grouting, observation of the retention of the slurry under different grouting flow rates in Pipe 2 showed accumulated slurry at the bottom of the pipe. In addition, there were apparent upper and lower layers of flow water and accumulation. These are shown in Figure 3 (a)–(d). No slurry particles were observed in the upper flowing water. Additionally Figure 3 (a)–(d) shows that with the increase of water velocity, the thickness of the accumulated slurry decreases. In particular, Figure 3 (d) shows that the thickness is 0, indicating removal of the slurry by the flowing water (grouting flow rate: 2.0 L/min, and water velocity: 0.5 m/s).

Figures 3 (e) to (f) show the accumulation states of the slurry using CN-0.5S. The thickness of the accumulated slurry using CN-0.5S is significantly greater than the thickness using GM-500. When the velocity of the flowing water was low, the water in the upper layer was mixed with a large amount of cement granules, as shown in (e). With the increase of the velocity of the flowing water, the cement particles in the upper layer of the water decreased gradually. With the increase of the grouting rate, the thickness of the accumulated slurry increased gradually. Subsequently, the slurry formed many clumps, which rolled and accumulated along the flowing water until the pipe was blocked, as shown in Figures 3 (f) to (h).

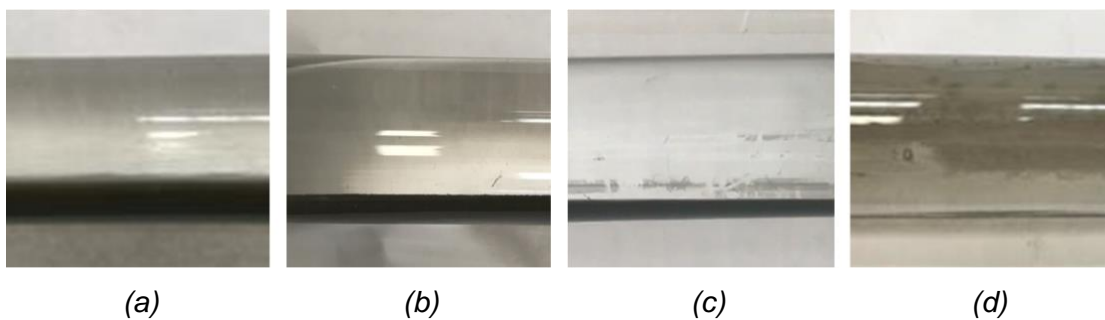


Fig. 3 – The accumulation of slurry in Pipe 2

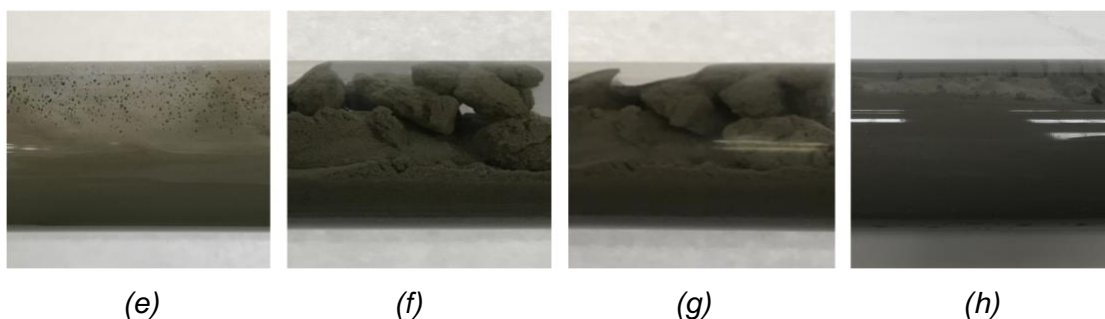
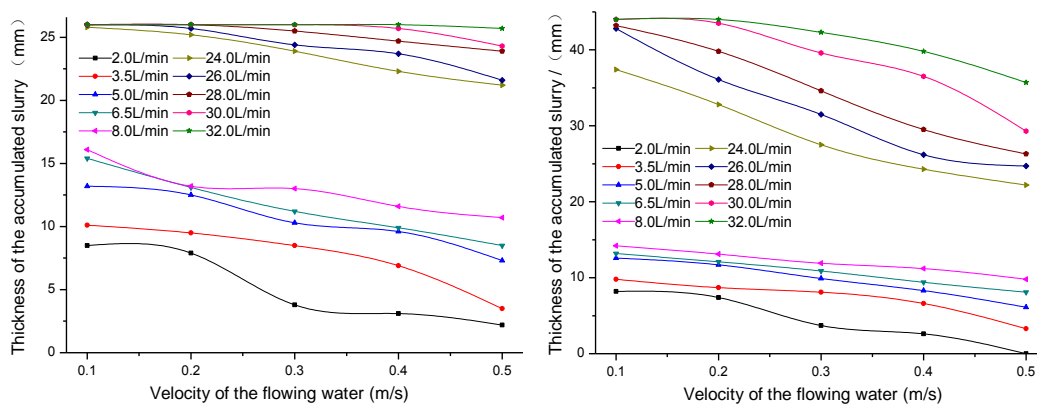


Fig. 3 – The accumulation of slurry in Pipe 2

The thickness of the accumulated slurry against the velocity of the flowing water is shown in Figure 4. It can also be seen from this figure that the thickness of the accumulated slurry using CN-0.5S was significantly greater than the thickness using GM-500. In Pipe 1, when the grouting rate using CN-0.5S was 32 L/min, the pipe was completely blocked at different water velocity. When the

grouting rate using CN-0.5S was 30 L/min, the pipe was completely blocked when the water velocity was lower than 0.4 m/s. The pipe was not completely blocked when the water velocity was 0.5 m/s, occurring a 1.7 mm top leak. When the grouting rate using CN-0.5S was 28 L/min, the pipe was completely blocked with a water velocity lower than 0.2 m/s. When the grouting rate using CN-0.5S was 26 L/min and 24 L/min, the pipe was completely blocked only when the water velocity was 0.1 m/s. In addition, when the grouting flow rate was 24 L/min, and the water velocity was 0.5 m/s, the maximum top leak appeared at 16 mm using CN-0.5S (about 1/5 of the total thickness). In general, the grouting sealing of CN-0.5S was very effective.

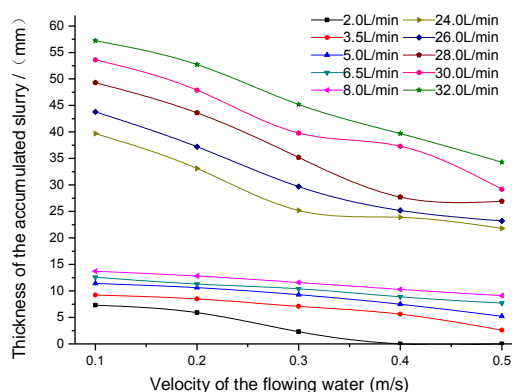
In Pipe 1, the maximum thickness of the accumulated slurry using GM-500 appeared when the grouting flow rate was 8 L/min, and the water velocity was 0.1 m/s, at 16.1 mm. In this case, a top leak of about 2/5 of the total thickness appeared. The accumulation of the slurry for other grouting rates and water velocities was worse, and GM-500 could not achieve effective sealing.



(a) Pipe 1

(b) Pipe 2

Fig. 4 – The thickness of the accumulated slurry with the velocity of the flowing water in three pipes



(c) Pipe 3

Fig. 4 – The thickness of the accumulated slurry with the velocity of the flowing water in three pipes

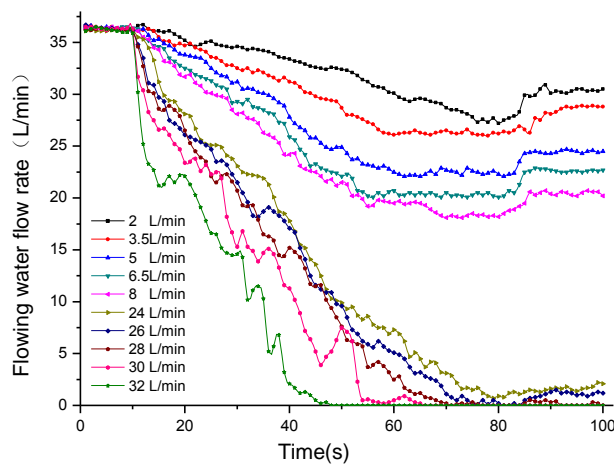
The grouting sealing effect using CN-0.5S was obviously better than GM-500 in Pipe 2 and Pipe 3. The pipe was completely blocked when the flowing water velocity was lower than 0.4 m/s. However, with the increase of the water velocity, the top leak occurred gradually. At the same time,

the top leak was larger using GM-500. This indicates a grouting pump with a larger flow rate is needed to solve the problem.

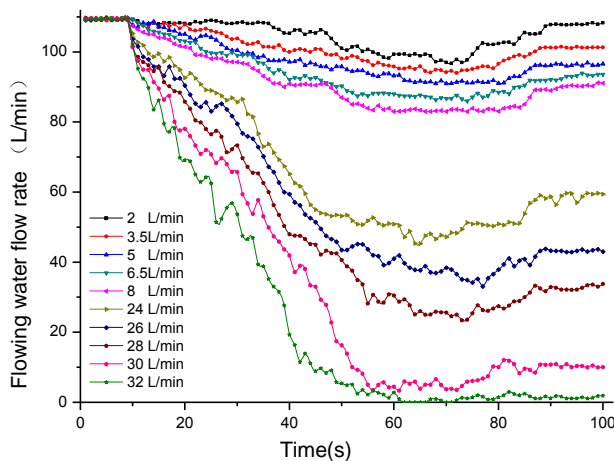
In general, grouting flow rate is an important factor affecting the sealing performance of the slurry. CN-0.5S indicated better grouting features than that of GM-500.

Analysis of the change of water flow rate under different grouting flow rate

Considering the grouting test in Pipe 2 as an example, different water flow velocities were analysed (at 0.1 m/s, 0.3 m/s and 0.5 m/s). Different grouting flow rates are shown against time in Figure 5.

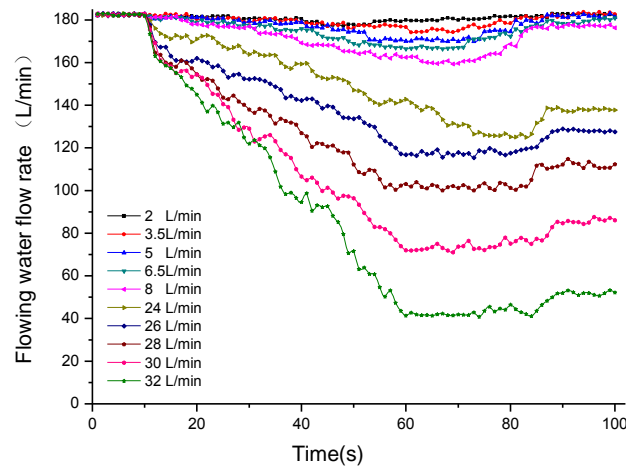


(a) initial flowing water velocity: 0.1 m/s



(b) initial flowing water velocity: 0.3 m/s

Fig. 5 – The curve of the flowing water flow rate over time



(c) initial flowing water velocity: 0.5 m/s

Fig. 5 – The curve of the flowing water flow rate over time

The following conclusions can be drawn from the above plots:

- (1) In case of an identical pipe and an identical initial water velocity, as the grouting flow rate increases, the water flow rate reduces.
- (2) In case of an identical pipe and an identical grouting flow rate, the larger the initial motive water flow, the smaller the amount of reduction. The slower the dynamic water flow changes, the greater the difficulty in sealing.
- (3) During the grouting process, as the flow rate of the grouting increases, the flow rate of the water decreases gradually. When the grouting is stopped, the water flow rate rebounds. When the grouting flow rate is too small compared with the initial water flow rate, the water flow rate is restored to the initial flow rate.
- (4) As shown in Figure 5(a), with an initial water flow velocity of 0.1 m/s and a grouting flow rate higher than 24 L/min (i.e., grouting using CN-0.5S), the flowing water could be sealed effectively. Figure 5(b) shows a case with an initial water flow velocity of 0.3 m/s and a grouting flow rate of 32 L/min, providing effective water sealing. Figure 5(c) shows a case where an initial water flow velocity of 0.5 m/s and a grouting flow rate of 32 L/min caused a reduced water flow rate, but could not seal it effectively. The grouting flow rate needed to be increased in this case.
- (5) From the above four points it can be deduced that the flow rate of the grouting pump plays a key role in the effective sealing of flowing water.

Analysis of the performance of CN-0.5S and GM-500

The monitored parameters of CN-0.5S and GM-500 in Pipe 2 were used to evaluate their performances. With a water flow rate of 0.5 m/s, and initial grouting flow rate of 32 L/min and 8 L/min (respectively for CN-0.5S and GM-500), the dynamic curves of the grouting flow rates for CN-0.5S (q_1) and GM-500 (q_2) with time (t), and the differential pressures between the inlet and outlet are shown in Figure 6.

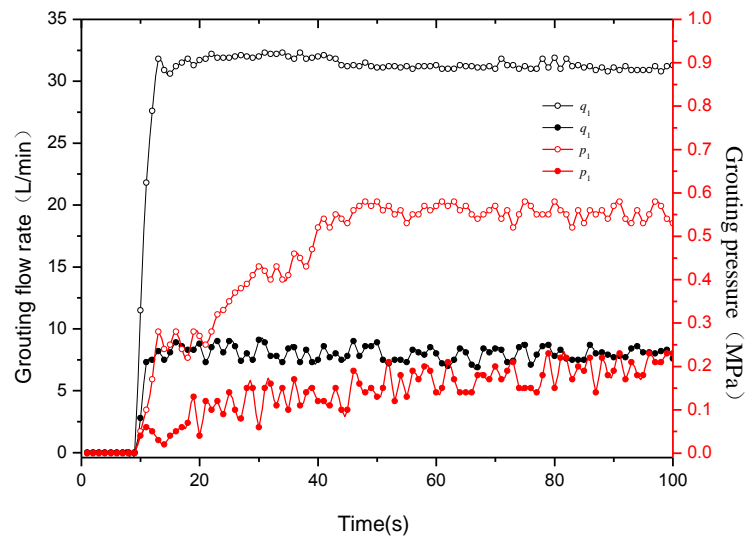


Fig. 6 – The flow and pressure changes over time

From the above flow rate and differential pressure curves, it can be observed that:

- (1) The flow rate and differential pressure of CN-0.5S were relatively stable with time, and the flow rate and differential pressure of GM-500 fluctuated significantly with time. The data after 8 s was selected to calculate the maximum flow rate (Q_{max}), the minimum flow rate (Q_{min}) and the average flow rate (Q_m) of CN-0.5S and GM-500. The results are as follows:

Tab. 3 - Flow characteristic value

| Pump | Q_m (L/min) | Q_{max} (L/min) | Q_{min} (L/min) |
|---------|---------------|-------------------|-------------------|
| CN-0.5S | 31.4 | 32.3 | 30.6 |
| GM-500 | 8 | 9.1 | 6.9 |

The fluctuation in the flow rate can be expressed by the non-uniform coefficient given by:

$$\delta Q = \frac{Q_{max} - Q_m}{Q_m} \times 100\% \quad (1)$$

Here, δQ is the non-uniform coefficient of the flow rate.

Using the data of Table 4 in Equation 1, the non-uniformity coefficients of the flow rate for CN-0.5S and GM-500 are found to be 2.9% and 13.8%, respectively. It can be seen that the stability of output for CN-0.5S is better than that of GM-500.

- (2) According to the differential pressure and flow rate, the expression of the head is given by:

$$H = \frac{p}{\rho g} + \frac{v_2 - v_1}{2g} \quad (2)$$

Here, H is the head of CN-0.5S, p is the differential pressure of the inlet and outlet; ρ is the density of the medium, g is the acceleration due to gravity, v_2 is the flow velocity at the outlet, and v_1 is the flow velocity at the inlet.

The flow velocity of the inlet and outlet can be obtained by the flow rate at these locations and the corresponding cross-sectional areas. The efficiency of the universal joint between the motor and the test pump shaft is 98%. The efficiency of CN-0.5S can be expressed as:

$$\eta = \frac{\rho g H_m Q_m}{0.98 P_0} \quad (3)$$

Here, η is the efficiency of the test pump, H_m is the average of the head of the test pump, and P_0 is the power of the motor.

The efficiency of CN-0.5S and GM-500 were obtained using the above expressions and were calculated at 51.27% and 4.08%, respectively. Evidently, the efficiency of CN-0.5S in the karst pipeline grouting test is significantly greater than that of GM-500.

ENGINEERING APPLICATION

Engineering background

The test area was located in a dam tunnel in Xiangxi Tujia and Miao Autonomous Prefecture in Hunan Province. The terrain of the tunnel was relatively high, the surrounding mountains were thick in vegetation, and the catchment area was large. The area has a subtropical monsoon humid climate zone with abundant, concentrated and high-intensity rainfall. The average annual rainfall is 1326.3–1468.4 mm. The maximum rainfall is 1992.7 mm. Separated by YK86+080 to YK86+200, the catchment area is large. After a precipitation, a large amount of surface water passes through the dissolution fractures and the fault fracture zones along the slopes into the tunnel. A large amount of groundwater infiltration causes the lining of this section to crumble and the floor moves up. The project safety was in question, and the construction progress was affected seriously. During a period when the first spray had been completed, but the second lining had not yet been constructed, a large amount of high-current water gushed in through the tunnel entrance right hole section (YK86+140–YK86+200). The maximum water flow rate reached 4.14 m³/s, and water inrush continued for 4-5 days, which gradually declined in subsequent. This event caused damages to some of the initial spray. The surrounding rock was partially floated up. Using a combination of high-density electrical profiling and drilling exploration, water infiltration diagrams at the tunnel vault, the right wall and the floor were developed. These are shown in Figure 7.

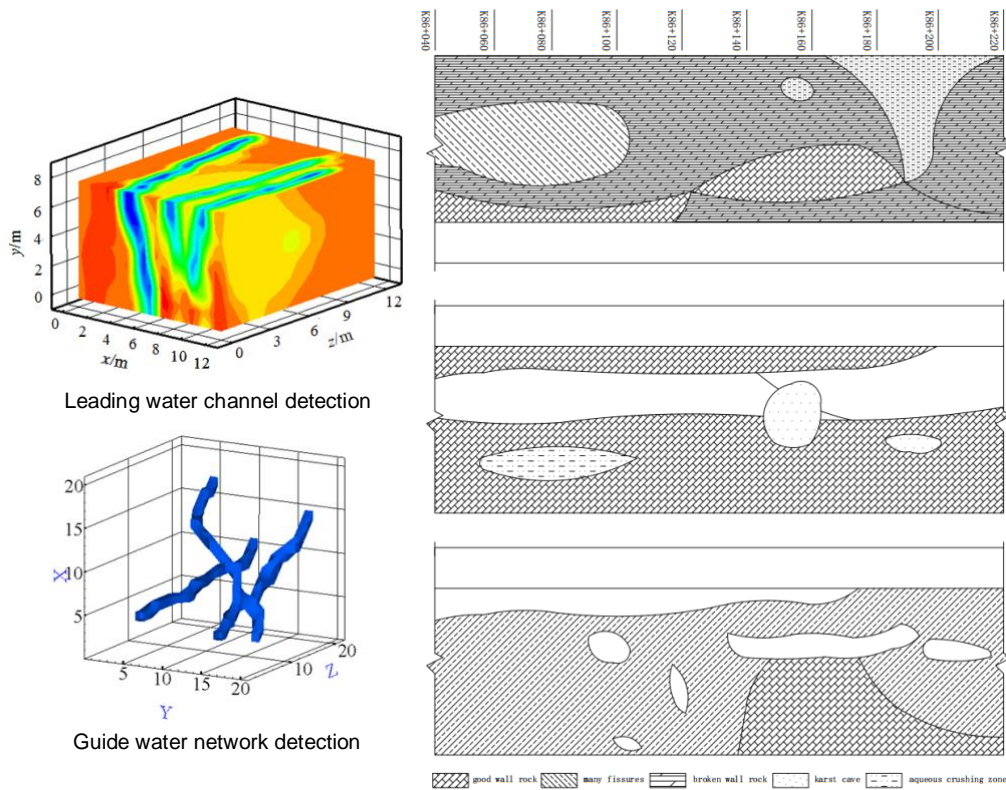


Fig. 7 – Tunnel surrounding rock environment detection

The affected section had two faults, F2 and F6. The F2 fault slanted to the southeast with an inclination of 35°–45°, and it chamfered the tunnel at YK86+130. The width of the crushed zone was 15–30 m. This affected the tumour-like limestone, created numerous karst fractures, caves and crushed rocks. The general fault orientation of F6 was toward the southeast with an inclination of 40°–45°. This fault caused disturbances along the slope and chamfered the tunnel at YK86+025. The width of the crushed zone was 15–20 m. The rocks of the two fault fractures and the affected zones went through slight silicification, mylonitisation and obvious chloritisation. The rock mass is mainly composed of fragmentation structures, influenced by tectonics, and karst, where jointed fractures develop. The presence of strong weathering shale in the limestone, make them fragile and prone to collapse during excavation. The stability of surrounding rock is poor.

In summary, this tunnel section is characterised by karst fissures and karst caves, close spatial relationships, strong hydraulic conductivity, diverse gushing water types, regionalisation and wide spatial distribution of inflow points. Strong surface precipitation and groundwater flow into the tunnel through the karst fissures and caves, thus constituting the main source of gushing water into the tunnel.

Grouting test on site

Using the results of the previous explorations, the centralised gushing channel and the large karst water storage structure area were chosen as the experimental sections. By using the traditional piston grouting pump 3NSA, and the newly designed grouting equipment CN-1.5S (discussed in this paper), the same-hole grouting and different-hole synchronous grouting tests were carried out. The performance parameters are listed in Table 4. In the process of grouting, single-liquid grout was mainly used. The dynamic grouting material was GT-1, and the single-grout

water–cement ratio was adjusted to 0.8:1–1:1 dynamically according to the thickness of the liquid leakage. As the first and the second lining of the tunnel had been completed, backwall grouting was adopted in order to prevent secondary damage to the lining structure caused by the grouting pressure, and the final grouting pressure was designed to be 2 MPa. During the process of grouting, the grouting pressure and grouting flow rates were collected in real time. A three-parameter logger was used to obtain the data during the whole grouting process using a common grouting pump and new rotary piston grouting pump. Finally, the grouting quantity of every drill hole and grouting time were analysed.



(a) Piston pump

(b) Rotary piston pump

Fig. 8 – Two types of grouting pumps

Tab. 4 - The parameters of the two grouting pumps

| Type | Motor power (kW) | Grouting pressure (MPa) | Grouting flow rate (L/min) |
|---------|------------------|-------------------------|----------------------------|
| CN-1.5S | 18.5 | 0-6 | 0-536.2 |
| 3SNSA | 18.5 | 0-10 | 0-207 |

Test results and analysis

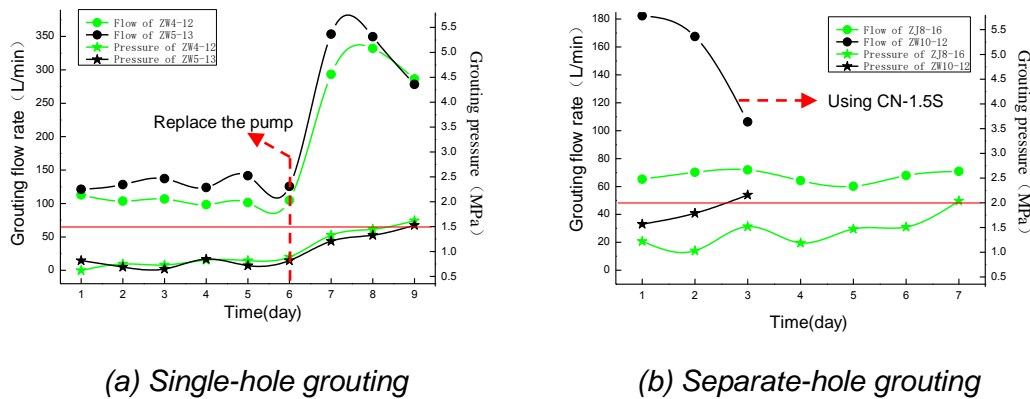
(1) Single-hole sequential grouting

A single liquid cement slurry was used to fill the cavity in the exposed single drilling hole ZW4-12 and ZW5-13, and the final pressure was 1.5 MPa. In the process of grouting, 3SNSA was used for grouting initially. After grouting for days, the amount of grouting did not decrease, and the grouting pressure did not increase. In this case, CN-1.5S was used for grouting and filling. The sealing of the cavity was completed in a short period of time. The total amount of grouting and grouting pressure is shown in Figure 13. For the ZW4-12 hole, 3SNSA was used for grouting during the first 6 days. The daily grouting volume did not change significantly, and the grouting pressure was consistently low. After using CN-1.5S, the daily grouting surged, and the grouting pressure reached the final designed pressure on the 3rd day.

(2) Separate-hole synchronous grouting test

The drilling hole ZJ8-16 and ZJ8-16 were exposed revealing the karst fissure pipeline and the water inflow was large. GT-1 double liquid cement slurry was used to seal the gushing water, and the final design pressure was 2 MPa. 3SNSA and CN-1.5S were used in ZJ10-12 and ZJ8-16, respectively, and grouting treatment was started at the same time. The daily grouting amount and

grouting pressure changes are shown in Figure 14. The daily grouting amount was significantly higher in the ZJ10-12 grouted by CN-1.5S than that of the ZJ8-16 grouted by 3SNSA. ZJ10-12 reached the designed final pressure in 3 days with CN-1.5S. The cumulative amount of grouting was 453 m³. The drilling of ZJ8-16 continued to reach the designed final pressure in 7 days, with a cumulative grouting volume of 470 m³.



(a) Single-hole grouting (b) Separate-hole grouting
 Fig. 9 – The changes of grouting flow rate and grouting pressure

Grouting effect

It can be observed from the grouting tests that the grouting flow rate of the new rotary piston pump is significantly higher than that of the existing grouting equipment, such as grouting filling in karst water storage structures or grouting sealing with low-pressure flowing water. The grouting efficiency is also considerably improved. After further adaptation of the newly developed grouting equipment in the overall test sites, the right hole of the tunnel reached the management requirement on October 15, 2015. The surrounding rock and lining were found to be intact. The entire right hole grouting project was 28 days ahead of the schedule, saving approximately 30% of the resources. A visual comparison of the test site before and after the grouting work can be seen in Figure 10.



(a) Before the grouting (b) After the grouting
 Fig. 10 – The comparison before and after the grouting engineering

CONCLUSION

In this study, a new type of grouting pump is proposed supported by a comparative grouting test carried out against existing grouting pumps. In the test, two kinds of PMMA pipes were chosen to simulate two kinds of karst pipes. CN-0.5S and GM-500 were used for grouting sealing tests at different grouting flow rates. The test results indicate that:

- (1) The thickness of the accumulated slurry using CN-0.5S is significantly greater than the thickness using GM-500 at the same monitoring points in each pipe.
- (2) In Pipe 1 and Pipe 2, CN-0.5S can realise the complete sealing of the flowing water.
- (3) With the same pipe diameter and the same initial flowing water velocity, an increase in the grouting flow rate causes significant reduction in the water velocity. The flow rate of the pump plays a key role in effectively blocking the flowing water.
- (4) By recording various parameters of the grouting pump, the mean value of the grouting pressure and grouting flow rate of CN-0.5S was found to be larger than that of GM-500. The operational efficiency of CN-0.5S is far greater than that of GM-500.

In a practical engineering application, the newly developed rotary piston pump CN-1.5S and a traditional piston pump 3SNSA were tested in single- and separate-hole grouting experiments. The following conclusions were drawn:

- (1) In the single-hole grouting, after changing CN-1.5S, the grouting flow rate increased greatly, and the target pressure of the design was quickly achieved.
- (2) In the separate-hole grouting, the hole using CN-1.5S achieved the design pressure within half the allocated time compared to the hole using 3SNSA.

In summary, it can be stated that the newly developed rotary piston grouting pump has a high flow rate and high efficiency, which allows the faster completion of grouting engineering tasks and the reduction of the associated costs.

ACKNOWLEDGEMENTS

This work is supported by the Natural Science Foundation of Shandong Province, China (ZR201702230205), the Key Project of Chinese National Programs for Fundamental Research and Development (973 Program) (2013CB036000).

REFERENCES

- [1] Xu Z. H., Li S. C., Li L. P., Chen J., Zhang Z. G. and Shi S. S., 2011. Cause, disaster prevention and controlling of a typical kind of water inrush and lining fracturing in karst tunnels. *Chinese Journal of Rock Mechanics and Engineering*, vol. 30, no. 7: 1396-1404.
- [2] Li S. C., Shi S. S., Li L. P., Chen J., Xu Z. H., Zhou Z. Q. and Yuan Y.C., 2014. Control of water inrush in typical karst tunnels in three gorges reservoir area and its application. *Chinese Journal of Rock Mechanics and Engineering*, vol. 33, no. 9: 1887-1895.
- [3] Li S. C., Li S. C., Zhang Q. S., Xue Y. G., Ding W. T., Zhong S. H., He F. L. And Liu Y. S., 2007. Forecast of karst-fractured groundwater and feffective geological conditions. *Chinese Journal of Rock Mechanics and Engineering*, vol. 26, no. 2: 217-225.
- [4] Sun Q., Zhu S. Y. and Zhang R., 2013. Analysis on Water Inrush Mechanism of Pipeline Conduction. *Chinese Journal of basic science and engineering*, vol. 21, no. 3: 463-470.
- [5] Li L. P., Li S. C. and Zhang Q. S., 2010. Study of mechanism of water inrush induced by hydraulic fracturing in karst tunnels. *Rock and Soil Mechanics*, vol. 31, no. 2: 523-528.
- [6] Xue Y. G., Li S. C., Su M. X., Li S. C., Zhang Q. S., Zhao Y. and Li W. T., 2011. Study of geological prediction implementation method in tunnel construction. *Rock and Soil Mechanics*, vol. 32, no. 8: 2416-2422.
- [7] Yuan J. Q., Chen W. Z., Huang S. W., Zhou X. S., Zhou Z. H., and Liu J. Q., 2016. Mechanism and synergetic treatment technology of water inrush disaster in completely and strongly weathered granite tunnels. *Chinese Journal of Rock Mechanics and Engineering*, vol. 35, supp. 2: 4164-4171.

- [8] Wang X. Y., Tan Z. S., Wang M. S., and Zhang M., 2008. Analysis of interaction between surrounding rock and lining in high water-level tunnels with controlled drainage. *Rock and Soil Mechanics*, vol. 29, no. 6: 1623-1628.
- [9] Liu S., Li X., Sun T., and Zhang H., 2016. Calculation of the Hydraulic Extension Limit of an Extended-Reach Well with Allowance for the Power Limitations of the Available Mud Pumps. *Chemistry and Technology of Fuels and Oils*, vol. 51, no. 6: 713-718.
- [10] Xia J. M., Liu H. B., Zhang Z. H., ZHU S. J. and YU X., 2016. Vibration Analysis of the Crank-link Mechanism of Reciprocating Bilge Pumps. *Noise and Vibration Control*, vol. 36, no. 3: 151-154.
- [11] Yan X. A., Zheng W., Zhang Q., and Lu B. X., 1999. Finite Element Analysis on the Structural Vibration of the Discharge Pipes for Reciprocating Pumps. *Chinese Journal of Mechanical Engineering*, vol. 35, no. 6: 74-76.
- [12] Wu H., Tong Z. W., Chen H. and Liang J. S., 2014. Dynamic simulation analysis on improved mud pump BW-280/12 using SolidWorks motion and ADAMS. *Manufacturing Automation*, vol. 19, no. 5: 65-66.
- [13] Zhang C., Feng S. B., Bai Q. P., and Ai Z. H., 2015. The Development of a Test Bench for Testing the Hydraulic Pump with High Pressure Large Flow. *Hydraulics Pneumatics & Seals*, no. 7: 82-84.
- [14] Song R. G., Zhang B. H. and Yang Y. X., 2007. Study on the meshing characteristic of a new cycloidal pump. *Powder Metallurgy Technology*, vol. 25, no. 2: 99-103.
- [15] Ren H. Y., Zhang S. C., Wang Z. H., Deng H. Y., Zhou S. B. and Xu Y. Y., 2011. Analysis of the Characteristics and Flow Rate of a New Eccentric and Squirmy Rotor pump for Cleaning Machine. *Light Industry Machinery*, vol. 29, no. 2: 14-17.
- [16] Li Y. L., Liu K. and Peng J. H., 2006. Research and Development on Integrative Parameterization Design with Its Solid Model for Cycloid Pump. *Transactions of the Chinese Society for Agricultural Machinery*, vol. 37, no. 12: 109-113.
- [17] Chen Z. B., Zou Y. Z., Jiang Z. and Dai M., 2017. Numerical Simulation of the Effect of the Gap between Rotor and Pump on the Performance of the Rotor Pump. *Noise and Vibration Control*, vol. 37, no. 2: 62-66.
- [18] Xu B., Hu M., Zhang J. H. and Su Q., 2016. Characteristics of volumetric losses and efficiency of axial piston pump with respect to displacement conditions. *Journal of Zhejiang University SCIENCE A*, vol. 17, no. 3: 186-201.
- [19] Yan P., Li S. Y., Yang S., Wu P. and Wu D. Z., 2017. Effect of stacking conditions on performance of a centrifugal pump. *Journal of Mechanical Science and Technology*, vol. 31, no. 2: 689-696.
- [20] Wen D., Chen F., Zhen X. S., Chai W. C., Wang J. and Zhou C., 2016. Analysis of Leakage and Volumetric Efficiency for Cam-Rotor Double-Stator Vane Pump. *Journal of Xi'an Jiaotong University*, vol. 50, no. 9: 20-24.
- [21] HU W., 2013. Grout diffusion and plugging mechanism in rockmass channel and fissures under hydrodynamic condition[Ph. D. Thesis]. China University of Mining and Technology.
- [22] LI S. C., Li M. T., Zhang X., Zhang Q. S., Hao P. S. and Wang Z. A., 2018. Investigation on Performance of Triangular Rotor Pump Based on Numerical Simulation and Experiment. *Transactions of the Chinese Society for Agricultural Machinery*, vol. 49, no. 9: 389-396.
- [23] LI M. T., LI S. C., Zang X. and Zhang Q. S., 2018. Experimental investigations on extrusive eccentric rotary pump. *Journal of Harbin Institute of Technology*, 2018-03-26.

EVALUATION OF FLEXURAL CAPACITY AND DUCTILITY ON HIGH-STRENGTH CONCRETE BEAMS REINFORCED WITH FRP REBAR AND STEEL FIBER

Jinzhong Li^{1,2}

1. *University of Tongji, Faculty of Civil Engineering, Department of Geotechnical Engineering, Siping Road 1239, Shanghai, China*
2. *University of Tongji, Key Laboratory of Geotechnical and Underground Engineering of Ministry of Education, Siping Road 1239, Shanghai, China; 1310300@tongji.edu.cn*

ABSTRACT

C60 class of concrete is produced with addition of hooked-end steel fibres at dosages of 0kg/m³, 39kg/m³, 78kg/m³, 117kg/m³, and its compressive strength and split tensile strength are measured. The flexural behaviour of high-strength concrete beams containing basalt fibre reinforced polymer (BFRP) rebars and steel fibres is investigated in the present study. An experimental program was set up and seven reinforced concrete beams have been tested, including one series with steel fibres content of 0%, 0.5%, 1.0%, and 1.5% in volume, and one series with ratio of BFRP rebars from 0.38%, 0.57% to 0.76%, 0.95% and tested under four-point flexural loading condition. The result revealed that with the addition of steel fibre, crucial properties of working performance, ductility, and bearing capacity is improved. By increasing BFRP rebar reinforcement ratio, desired ultimate strength is anticipated. Considering the deformability and energy dissipation, a synthesis ductility index for FRP and steel fibre reinforced beams was proposed; while a synthesis ductility index for FRP reinforced flexural structure was also advised. The model of the synthetic ductility index coefficient is verified by relevant experimental data, and was expected to give an insight into the problem of deformability and ductility for the FRP rebar (and steel fibre) reinforced flexural concrete member.

KEYWORDS

BFRP rebar, Steel fibre, High-strength concrete, Flexural capacity; Ductility

INTRODUCTION

The application of fibre reinforced polymer (FRP) bars on reinforced concrete structure has been restricted by its specific characteristics of the lower elastic modulus which is the ratio of elastic stress to strain, linear elastic response and bond performance with concrete. In order to reduce crack width, deflection and mitigate contradiction between durability and workability of FRP structural member, several engineering measures such as mixed reinforcement, pre-stressing technique and fibre concrete has been advised by many scholars to improve the bearing capacity of normal service limit state and ductility. Review of literature shows that limited number of studies were undertaken to investigate the behaviour of concrete beams reinforced with FRP rebar and steel fibre. This paper deals with the flexural capacity of high-strength concrete beams reinforced with BFRP bars and steel fibres, ratio of FRP bars and steel fibre volume fraction is the main study parameter. The variation in steel fibre volume fraction and ratio of FRP bars that affect the working performance, failure mode and ductility of the specimens was studied and discussed. Furthermore, a synthetic ductility index to evaluate and analyse the ductility of FRP and steel fibre reinforced

concrete beam was presented, which can provide a new method to estimate relative ductility of FRP (and steel fibre) reinforced concrete flexural member.

THE WORKABILITY AND DUCTILITY OF STEEL FIBER REINFORCED FLEXURAL CONCRETE MEMBER

For the purpose of getting ideal workability and ultimate bearing capacity and limiting deflection and crack width of FRP reinforced concrete structure, some scholars have suggested several engineering measures as follows: improving the property of concrete, adopting hybrid fibre reinforced plastic rebar, applying pre-stressing force on FRP, configuring different modulus of FRP or steel rebar et al. Alsayed and Alhozaimy [1] found that the ductility index increase as much as 100% with the addition of 1% volume steel fibres. Wang and Belarbi [2] tested flexural beams reinforced with fibre-reinforced-concrete. The detailed results showed that addition of fibre improve the flexural properties by increasing the ductility level more than 30% compared with companion specimen. The ductility indices for all the beams were above the minimum requirement of 4. Harris et al. [3] found that the ductility capacity of beams reinforced with hybrid FRP bar were close to that of beams reinforced with steel. Wierschem and Andrawes [4] studied the property of damping and dynamics about SMA-FRP bars. According to test of cantilever beams reinforced with SMA-FRP rebar, the components have good performance of energy dissipate and ductility. SMA-FRP will give a well application foreground when structures applied with dynamic load.

APPRAISAL INDEX ON DUCTILITY OF FRP REINFORCED CONCRETE STRUCTURE

The workability and bearing capacity of FRP reinforced concrete flexural member is limited by some disadvantages such as more wider crack width and larger deflection. Furthermore, ultimate bearing capacity of flexural structure was dominated by FRP strain, bond-anchor property, concrete performance and reinforcement ratio and so on. Through analysis of theory and experiment, scholars proposed three main ductility index and calculation method named energy criterion, deformation and energy-deformation criterion to evaluate the performance of deformation and ductility for FRP reinforced concrete structure.

(1) Energy criterion

Spadea et al. [5] studied several flexural beams designed to failure by FRP rupture. The results are given of theoretical and experimental investigation, which failure mould release large amount of energy. The ductility appraisal index which is the ratio of total energy to elastic energy was advised. The calculation formula was that:

$$\mu_E = \frac{E_{\text{tot}}}{E_{0.75u}} \quad (1)$$

Where E_{tot} is the total energy, equivalent to the total area under the load-deflection curve up to the failure load, $E_{0.75u}$, the elastic energy, can be estimated from the load-deflection curve of 75% ultimate load.

Naaman and Jeong [6] proposed a ductility index, μ_E , based on the conventional ductility definition, and expressed in terms of a ratio of energies, Equation 2. The total energy, E_{tot} , can be computed as the area under the load deflection curve up to the failure load such as maximum load, failure load, and 80% maximum load so on. E_{ela} , can be estimated from unloading test.

$$\mu_E = \frac{1}{2} \left(\frac{E_{\text{tot}}}{E_{\text{ela}}} + 1 \right) \quad (2)$$

If the unloading data are not available, E_{ela} can be calculated as the area of the triangle formed at the failure load by a line with slope S computed by Equation 3.

$$S = \frac{P_1 S_1 + (P_2 - P_1) S_2}{P_2} \quad (3)$$

Where P_1 is the cracking load, and P_2 is the yielding load, S is the slope of the unloading branch, S_1 , the first line slope, S_2 , the second line slope.

(2) Deformability criterion

Jaeger et al. [7] proposed that the ductility could be measured by the ratio of deformation at ultimate and service limit. The ductility index μ_D must take into account of strength and deflection (or curvature), produced by the strength factor C_s and deflection factor C_d (or curvature factor C_c), the strength (or deflection curvature) factor expressed as the product of moment (or deflection, curvature) at ultimate, M_u (or Δ_u, ψ_u), to the moment (or deflection, curvature) at service limit state, $M_{0.001}$ (or $\Delta_{0.001}, \psi_{0.001}$) respectively. Also, the service limit state refers to a concrete strain at the compression marginal zone of 0.001. Detailed formula was shown in Equation 4.

$$\mu_D = C_s \cdot C_d \quad (\text{or } C_c) \quad (4)$$

$$C_s = \frac{M_u}{M_{\varepsilon=0.001}}; \quad C_d = \frac{\Delta_u}{\Delta_{\varepsilon=0.001}}; \quad C_c = \frac{\psi_u}{\psi_{\varepsilon=0.001}}$$

(3) Energy-deformation criterion

Oudah and El-Hacha [8] developed a new ductility model that relates to the deformability of reinforced concrete structure strengthened by using FRP. Through dividing the applied loading into static and monotonic, relevant ductility calculation model was established based on the tri-linear load-deflection response and a bi-linear trend. The ductility can be expressed as the product of the deformability ratio and a compatibility factor defined in Equation 5.

$$\mu_{E-D} = \frac{E_{tot}}{E_{ela}} \cdot \frac{\Delta_u}{\Delta_y} \cdot \frac{\Delta_y}{\Delta_u} = \mu_d \beta; \quad \mu_d = \frac{\Delta_u}{\Delta_y}; \quad \beta = \frac{E_{tot}}{E_{ela}} \cdot \frac{\Delta_y}{\Delta_u} \quad (5)$$

$$\beta = \begin{cases} \frac{S \Delta_y [P_y (\Delta_u - \Delta_c) + P_u (\Delta_u - \Delta_y) + P_c - \Delta_y]}{P_u^2 \Delta_u}; & S = \frac{P_y - \Delta_c}{\Delta_y - \Delta_c} \\ \frac{S \Delta_y [P_y \Delta_u + P_u (\Delta_u - \Delta_y)]}{P_u^2 \Delta_u}; & S = \frac{P_y}{\Delta_y} \end{cases}$$

Where Δ_u is the ultimate deflection, Δ_c is the cracking deflection, Δ_y is the yield deflection, P_u is the ultimate capacity, P_y is the yield capacity, μ_d is the traditional ductility index of deflection, S is the slope of the unloading branch that can be obtained from experimental test or use approximate formula, μ_{E-D} is the ductility index, β is the optimum ductility. More information refers to the relevant literature.

As different evaluation indexes of ductility were adopted, the value of ductility index of FRP reinforced concrete flexural member differ considerably. So, the existing problem urges us to understand and evaluate deeply the ductility performance of FRP reinforced structure, forming a relative unified formula of ductility index.

METHODS

Beams specifications

In this research, seven high-strength concrete beams reinforced with BFRP bar and steel fibre were tested monotonically under four point bending. All the beams had a constant cross-

section of 150x300 mm and length of 2100 mm. The distance between supports was 1800 mm, and the shear span 600 mm, so the distance between loads was 600 mm shown in Figure 1. The shear span was reinforced with steel stirrups ($\phi 6\text{mm}/75\text{mm}$) in order to avoid shear failure and minimize shear effects. In the pure bending zone no stirrups and reinforcement were provided. As a top reinforcement, $2\phi 6$ steel rebars were used to hold stirrups in the shear span zone.

The variables of FRP bar ratio and volume fraction of steel fibre were studied by using four different amounts of longitudinal reinforcement and three steel fibre content. One reinforced beam B0 without steel fibre were used for comparison. The geometric and reinforcement details of the beam are shown in Figure 1 and Table 1.

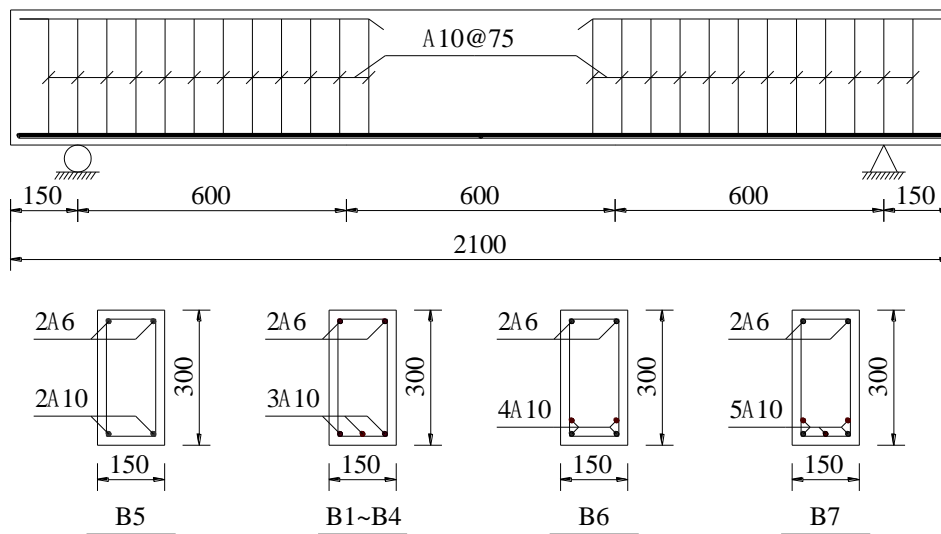


Fig. 1 - Geometric and reinforcement details

Tab. 1 - Geometric characteristics of sections and properties of concrete

| Beam ID | B (mm) | H (mm) | Volume Fraction of Steel Fiber (%) | Main Rebar | Compressive Strength f_c (MPa) | Splitting Tensile Strength (MPa) |
|---------|--------|--------|------------------------------------|------------|----------------------------------|----------------------------------|
| B1 | 150 | 300 | - | $3\phi 10$ | 68.0 | 3.0 |
| B2 | 150 | 300 | 0.5 | $3\phi 10$ | 76.2 | 6.7 |
| B3 | 150 | 300 | 1.0 | $3\phi 10$ | 81.6 | 8.9 |
| B4 | 150 | 300 | 1.5 | $3\phi 10$ | 80.4 | 10.8 |
| B5 | 150 | 300 | 1.0 | $2\phi 10$ | 79.6 | 7.6 |
| B6 | 150 | 300 | 1.0 | $4\phi 10$ | 80.0 | 8.0 |
| B7 | 150 | 300 | 1.0 | $5\phi 10$ | 81.7 | 8.2 |

Materials property

High-strength concrete reinforced with steel fibres with 60MPa compressive cubic strength at 28 days were utilized to cast the concrete beams. Table 2 shows the concrete's adopted composition. Cubic specimen having dimensions of 150 mm×150 mm×150mm were also in-situ casted for each beam to perform compressive and splitting tests. The hooked-end steel fibres used in the study were 30 mm in length and 0.55 mm in diameter, aspect ratio 65, and they were known as "Dramix ZP305", whose tensile strength is greater than 1345 MPa, and elastic modulus 200 GPa. BFRP rebars were used as flexural reinforcement. Plain round steel rebars HRB400 were used as top reinforcement and stirrups. The mechanical properties of these rebars were obtained by a uniaxial tension test and are shown in Table 3.

Tab. 2 - Mix proportion of high-strength concrete reinforced with steel fibre

| Concrete Strength | Water (kg/m ³) | Cement (kg/m ³) | Sand (kg/m ³) | Gravel (kg/m ³) | Steel Fiber (kg/m ³) | Superplasticizer (kg/m ³) |
|-------------------|----------------------------|-----------------------------|---------------------------|-----------------------------|----------------------------------|---------------------------------------|
| C60 | 146 | 487 | 618 | 1199 | – | 7.3 |
| CF60 | 156 | 520 | 710 | 1064 | 39 | 7.8 |
| CF60 | 164 | 547 | 696 | 1043 | 78 | 8.2 |
| CF60 | 164 | 547 | 696 | 1043 | 117 | 8.2 |
| CF60 | 172 | 573 | 720 | 985 | 156 | 8.6 |

Tab.3 - Mechanical properties of BFRP and steel rebar

| Material | Diameter (mm) | Elastic Modulus(MPa) | Yield Strength(MPa) | Tensile Strength(MPa) | Elongation (%) |
|----------|---------------|-----------------------|---------------------|-----------------------|----------------|
| BFRP | 10 | 4.408×10 ⁴ | – | 951.9 | – |
| HRB400 | 6 | 2.020×10 ⁵ | 512.2 | 465 | 0.21 |

Experimental setup and instrumentation

Each beam was simply supported by reaction frame shown in Figure 2. A hydraulic jack transmitted the load to the test beam by a spreader beam. The load was applied in displacement control mode, and all data was collected by a data acquisition system. Every 5 kN of applied load before beam cracking and 10 kN after cracking, the load applier was paused 10 minutes for the purpose of measure and take note of crack width.

Seven transducers (LVDT and strain gauge based transducers) were used: one at each support, one in the mid-span section, two at 600 mm and two at 800 mm distance from the supports. The mid-span section was instrumented with five concrete strain gauges at side surface of the beam (distributed evenly with 75 mm) to verify the theory of plane-section hypothesis. An instrument of concrete crack width observation was used to measure the development of crack width. Strain gauges were also adopted on the surface of BFRP rebar. These strain gauges were distributed over the shear span length and concentrated in the mid-span zone. All data were automatically measured and stored in the data-acquisition system. The details of test beams and test set-up were shown in Figure 2.

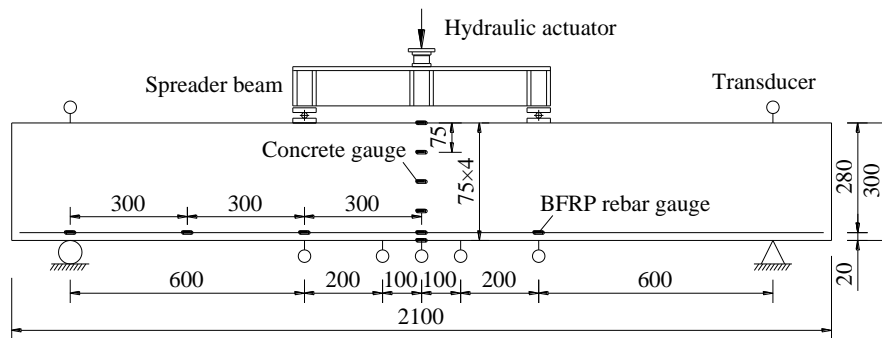


Fig. 2 - Details of test beam and setup

RESULTS

Failure mode analysis

Because of BFRP bars do not exhibit yielding, flexural failure of high-strength concrete beams reinforced with FRP rebar and steel fibre is characterized by either concrete crushing (over-reinforced case) or FRP bar rupture (under-reinforced case).

Under-reinforced failure case B2 ~ B6, BFRB reinforced beams with reinforcement ratio less than balanced reinforcement ratio, their failure started due to increasing of deflection followed by BFRP rupturing. On the other hand, the beam B8 was over-reinforced section which failure mode was duo to concrete crushing, with deflections reaching values more than 50 mm. Tensile rupture of the reinforcing BFRP and concrete crush were depicted in Figure 3.



(a) B2~B6 BFRP rupture



(b) B7 concrete crush

Fig. 3 - Typical failure mode of beams tested

The flexural capacity with different steel fibre volume fraction

An experimental load–deflection relation derived from the measurement of midspan transducer is shown in Figure 4 and Table 4, indicates the comparison of high–strength concrete beams with steel fibre and plain concrete beam. With the addition of steel fibre, concrete beams show steeper slope in the ascending part of the load-displacement, which means the beams

possess higher flexural rigidity. When increase steel fibre volume fraction with 0.5%, 1.0% and 1.5%, the series of B2 ~ B4 revealed that percentage increase in flexural capacity of the high-strength concrete beams reinforced with BFRP rebars and steel fibre are 2.1%, 23.6% and 16.8%, percentage increase in servicing capacity is 75%, 100% and 125%, and percentage increase in cracking load is 25%~50%, through contrast with plain concrete reinforced beam B1 respectively.

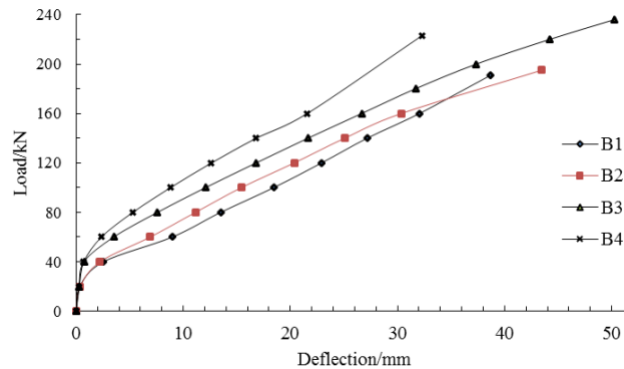


Fig. 4 - Load-deflection relationship for different dosages of steel fibre

Tab. 4 - Cracking load, servicing load and flexural ultimate strength

| Beam ID | Dosage of Steel Fibre(kg/m ³) | Main Rebar | Cracking load (kN) | load refer to crack width 0.7mm (kN) | Ultimate strength (kN) |
|---------|---|------------|--------------------|--------------------------------------|------------------------|
| B1 | - | 3φ10 | 20 | 40 | 191 |
| B2 | 39 | 3φ10 | 30 | 70 | 195 |
| B3 | 78 | 3φ10 | 30 | 80 | 236 |
| B4 | 117 | 3φ10 | 25 | 90 | 223 |
| B5 | 78 | 2φ10 | 25 | 60 | 167 |
| B6 | 78 | 4φ10 | 30 | 83 | 260 |
| B7 | 78 | 5φ10 | 25 | 105 | 310 |

The flexural capacity with different reinforcement ratio of FRP bars

As shown in Figure 5 and Table 4, with the increase of BFRP reinforcement ratio 0.38%, 0.57%, 0.76% and 0.95%, the ultimate loads of the high-strength concrete beams reinforced with BFRP rebar and steel fibre increase from 167 kN to 195 kN, 260 kN and 310 kN respectively, while the servicing loads increase from 60 kN to 70 kN, 83 kN and 105kN, respectively.

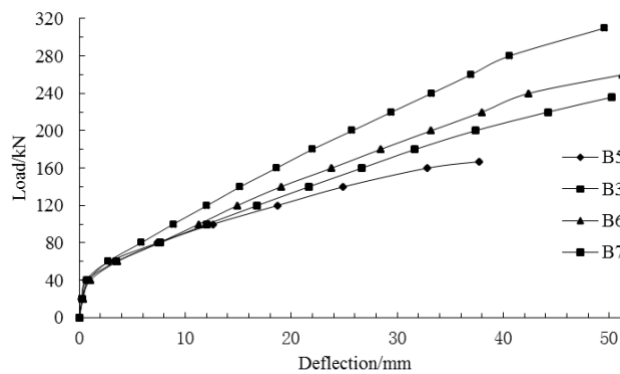


Fig. 5 - Load-deflection relationship for different reinforcement ratio of BFRP bars

SYNTHESIS DUCTILITY COEFFICIENT

Analysis on deformity and ductility of FRP reinforced flexural concrete member

From the viewpoint of mechanics, FRP bars and concrete bear the applied loading together before cracking. After cracking, the stress shifts from the concrete to FRP bar rapidly. There is a sudden change on the stress of FRP bar. The deformability and bearing capacity of FRP structure is mainly controlled by the strain of FRP. Accompanying with load-deflection curve appears inflection point, the deformation rate grows steadily. Before failure, the performance of structure on bond and anchor gradually degraded. Deformation rate of structure become larger and tend to presents unsteady growth. The ultimate bearing capacity mainly depended on the properties of concrete and FRP bar. In addition, FRP bar has a weak shear capacity and bond stress, implying less influence on the circumference concrete. The fatigue is interior fabricate-dependent. So, the influence factor mentioned above increases the complexity of ductility analysis.

From the viewpoint of bond performance, the property of deformation and ductility for FRP reinforced structure substantially depend on the bond behaviour between FRP and concrete. Cosenza and Manfredi et. al. [9-10] put forward that bond stress was transferred by means of the mechanical interlocking of the concrete and steel, and the bond action depending on the coefficient of friction. Bi [11] explored anchorage length, type and diameter of FRP bar, and concrete strength grade upon the bond performance and degrade trend for FRP reinforced concrete structure. The result reveals that these factors mentioned above can influence parameter of deformability and ductility for flexural member relatively. Belarbi [12] discovered that fiber reinforced concrete could improve the degrading trend of FRP bar and concrete remarkably. Especially bond property closely related to the tensile strength of FRP.

From the viewpoint of failure model, brittle fracture was found when different loading applied on FRP reinforced structure. It was obvious that the failure model of FRP reinforced structure which will dissipate large elastic energy. The failure process was dramatic. The bearing capacity of structure lost rapidly, it cannot provide sufficient warning. The other failure model of concrete crushing, due to the concrete property of elastic-plastic, proportional energy was dissipated gradually present preferable ductility. Large deformation of FRP reinforced structure does not imply better performance of ductility contrast to conventional steel reinforced concrete beam. Conventional evaluation model cannot be applied to FRP reinforced flexural member. Consequently, Taniguchi [13] proposed that the failure model of concrete crushing gained a better ductility, which provided apparent sufficient warning compared to FRP fracture.

Synthesis ductility coefficient for FRP and steel fibre reinforced beams

Research showed that the steel fibre substantially enhances the flexural property, toughness and crack resistance in the service limit state. Some tensile loads can be transferred across the cracks by the bridging function of fibre, which make the process of stress transferring from concrete to FRP bar more smoothly, so it is beneficial to gain better workability and ideal failure model of concrete crushing.

The synthetic ductility model for FRP and steel fibre reinforced beams is based on full analysis of research achievements and expressed as the product of deformability factor μ_{Δ} , the ratio of deflection at ultimate, Δ_u , to the deflection at service limit state, $\Delta_w=0.7$ mm, and energy factor and the ratio of total energy, E_{tot} , can be calculated as the area under the load-deflection curve up to the load defined as the failure load, while the elastic energy, E_{ela} , can be estimated from unloading test. The service limit state corresponds to crack width at the tensile marginal zone for concrete was defined as 0.7mm.

Typical load-deflection curve for FRP rebar and steel fibre reinforced flexural concrete member was adopted, shown in Figure 6. The synthetic ductility index for FRP rebars and steel fibre reinforced beams defined as follows:

$$\left\{ \begin{array}{l} \mu_s = \mu_{\Delta} \cdot \mu_e \\ \mu_{\Delta} = \frac{\Delta_u}{\Delta_{w=0.7}}; \quad \mu_e = \frac{E_{ela}}{E_{tot}} \\ E_{tot} = \frac{1}{2} [P_c \cdot \Delta_c + (P_c + P_u) \cdot (\Delta_u - \Delta_c)] \\ E_{ela} = \frac{1}{2} \cdot \frac{P_u^2}{S}; \quad S = \frac{P_{w=0.7} S_1 + (P_u - P_{w=0.7}) S_2}{P_u} \end{array} \right. \quad (6)$$

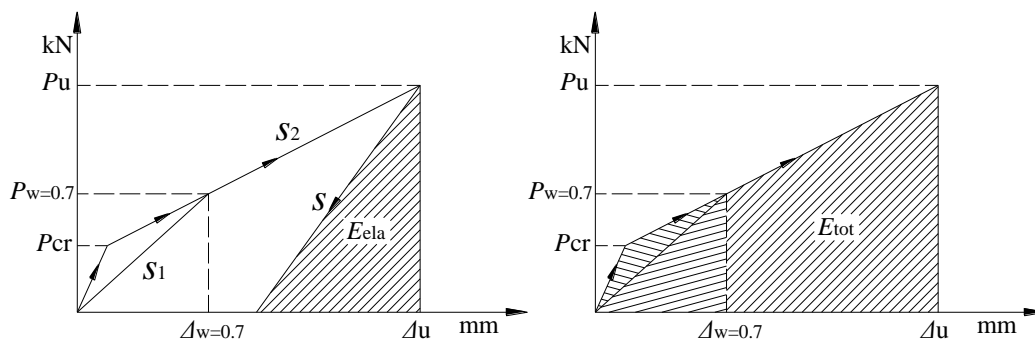


Fig. 6 - Typical load-deflection curve for FRP rebar reinforced flexural concrete member

Where μ_s is the synthetic ductility index, μ_{Δ} is the deformability factor, μ_e is the energy factor, Δ_u is the deflection of ultimate load (mm), Δ_c is the deflection for cracking load (mm), $P_{w=0.7}$ is the load for service limit state corresponds to mid-span crack width at the tensile marginal zone for concrete was defined as 0.7 mm (kN), P_u is the ultimate bearing capacity (kN), E_{ela} is the dissipated elastic energy of FRP, obtained from unloading experiment (kN·mm), E_{tot} is the total energy (kN·mm), virtually the area of load-deflection curve, S is the slope of the unloading branch, S_1 is the first line slope, S_2 is the second line slope.

Experimental data of load-deformation was gathered and analysed, which revealed the different influence factors of steel fibre volume fraction and ratio of FRP rebar. Based on data

collected, the synthetic ductility index of high-strength concrete beams reinforced with BFRP rebars and steel fibre was communicated and presented respectively. Detailed results were shown in Table 5.

Tab. 5 - The synthetic ductility index for BFRP rebars and steel fibre reinforced beams

| Beam ID | $P_{w=0.7}$ (kN) | P_u (kN) | $\Delta_{w=0.7}$ (mm) | Δ_u (mm) | μ_Δ | S | E_{tot} (kN.mm) | E_{ela} (kN.mm) | μ_e | μ_s | Failure model |
|---------|------------------|------------|-----------------------|-----------------|--------------|------|-------------------|-------------------|---------|---------|---------------|
| B2 | 70 | 195 | 9.02 | 43.45 | 4.82 | 5.11 | 3712.4 | 4128.3 | 0.90 | 4.34 | FR |
| B3 | 80 | 236 | 7.59 | 50.26 | 6.62 | 5.99 | 5235.8 | 5879.2 | 0.79 | 5.24 | -- |
| B4 | 90 | 223 | 7.04 | 32.28 | 4.59 | 8.30 | 3242.6 | 3557.6 | 0.84 | 3.86 | -- |
| B6 | 83 | 260 | 8.69 | 51.25 | 5.90 | 5.88 | 5978.3 | 6587.8 | 0.87 | 5.15 | -- |
| B7 | 105 | 310 | 9.66 | 49.57 | 5.13 | 7.08 | 7107.1 | 7643.5 | 0.89 | 4.56 | CC |

Note: CC: concrete crushing, FR: FRP rupture.

The reasons of improving ductility for high-strength concrete beams reinforced with BFRP and different dosage of steel fibre could be explained exactly that: the steel fibre can take proportional stress, which delayed the development trend of crack width, remarkably improved the service capacity. For BFRP reinforced beams which contain constant 1% volume ratio of steel fibre, the ductility improved through increase the ratio of FRP reinforcement. After balanced reinforcement, BFRP-reinforced beams have the trend to degrade ductility, because fail model is controlled by the property of steel fibre reinforced concrete.

Synthesis ductility coefficient for FRP reinforced beams

The synthetic ductility factor takes into account the factor of nonlinear characteristics of concrete and FRP rebar, state of stress delivery from FRP to concrete and potential ultimate bearing etc. The energy factor is related to the storage of elastic energy, the tendency of bond deterioration and nonlinear property of the compression zone. Essentially, the deformability and ductility for FRP reinforced concrete beams highly depends on the property of FRP, elastic-plastic property for concrete and bond performance between them. While such factor of failure mode of concrete crushing and reasonable FRP ultimate strain is help for the better deformability and ductility of FRP reinforced concrete flexural member. Thus, the synthetic ductility index model relates to the deformability and the energy dissipated more reasonably.

The formula of synthetic ductility index for FRP reinforced concrete beams is similar to Equation 6, only two parameters $P_{w=0.7}$ and $\Delta_{w=0.7}$ are changed with $P_{\epsilon=0.001}$ and $\Delta_{\epsilon=0.001}$, which defined as the load and deflection at service limit state. The service limit state corresponds to concrete strain at marginal tensile zone was defined as 0.001 mm. If relevant data are not available, for normal concrete, $P_{\epsilon=0.001}$ can be estimated in the following Equation 7, Where f_{cu} is the cubic concrete compressive strength, based on the test of compressive strength.

$$P_{\epsilon=0.001} = 1.9f_{cu}^{3/4} \quad P_{\epsilon=0.001} = 3.0f_{cu}^{2/3} \quad P_{\epsilon=0.001} = 4.1f_{cu}^{2/3} \quad (7)$$

When the value of $P_{\epsilon=0.001}$ is got, then calculate the values of Δ_c and $\Delta_{\epsilon=0.001}$ respectively. Detailed procedures refer to the Equation 8 and current code ACI 440.

$$\begin{cases} \Delta_{\epsilon=0.001} = \frac{Pa}{24E_c I_e} (3L^2 - 4a^2) + \frac{Ph^2 a}{10GI_e} \\ I_e = I_g \quad \text{when } M_\alpha \leq M_{cr} \\ I_e = \left(\frac{M_{cr}}{M_\alpha}\right)^3 \beta_d I_g + \left[1 - \left(\frac{M_{cr}}{M_\alpha}\right)^3\right] I_{cr} \leq I_g \quad \text{when } M_\alpha > M_{cr} \end{cases} \quad (8)$$

Also E_{tot} can be calculated as the area of the bi-linear curve formed by the failure load. Where $\Delta_{\epsilon=0.001}$, the deflection for service limit state corresponds to the strain 0.001 of marginal compression concrete fibre (mm). More information is shown in Figure 7 and Equation 9.

$$E_{tot} = \frac{1}{2} [P_{\epsilon=0.001} \cdot \Delta_{\epsilon=0.001} + (P_{\epsilon=0.001} + P_u) \cdot (\Delta_u - \Delta_{\epsilon=0.001})] \quad (9)$$

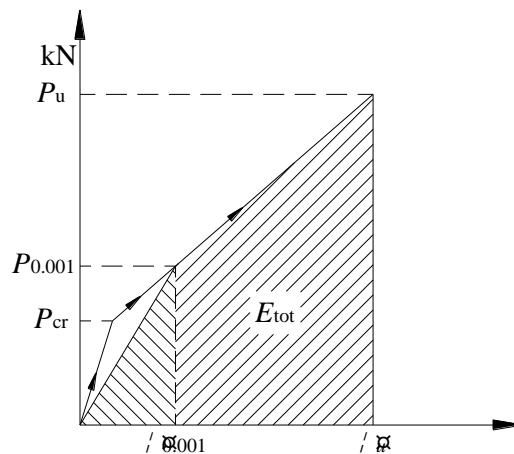


Fig. 7 - The graph of approximate formula on E_{tot}

In order to reduce crack width, deflection and mitigate contradiction between durability and workability of FRP reinforced flexural member, several engineering measures such as mixed reinforcement, pre-stressing technique were proposed by many scholars to improve the capacity of deformation and ductility on FRP reinforced concrete beams. Based on data gathered, the synthetic ductility index for FRP rebars reinforced flexural concrete member was communicated and analysed respectively. Detailed results were shown in Table 6.

Tab. 6 - The synthetic ductility index for FRP rebars reinforced flexural concrete member*

| Beam ID | $P_{\epsilon=0.001}$ (kN) | P_u (kN) | $\Delta_{\epsilon=0.001}$ (mm)* | Δ_u (mm) | μ_{Δ} | S | E_{tot} (kN.mm) | E_{ela} (kN.mm) | μ_e | μ_s | Failure model |
|---------------------------|--|---------------|------------------------------------|--------------------|----------------|------|----------------------|----------------------|---------|---------|---------------|
| | $\mu_{\Delta} = \Delta_u / \Delta_{\epsilon=0.001}; \mu_e = E_{ela} / E_{tot}; \mu_s = \mu_{\Delta} \cdot \mu_e$ | | | | | | | | | | |
| GL-2-0 ^[14] | 22.4 | 66.1 | 8.9 | 50.0 | 5.62 | 1.56 | 1918.4 | 1404.1 | 0.73 | 4.11 | CC |
| GL-3-0 ^[14] | 39.8 | 88.4 | 12.8 | 42.9 | 3.35 | 2.29 | 2184.1 | 1708.0 | 0.78 | 2.62 | |
| GL-3-2 ^[14] | 31.4 | 72.0 | 12.3 | 45.0 | 3.66 | 1.81 | 1883.7 | 1429.3 | 0.76 | 2.78 | |
| LGL-2-2 ^[14] | 29.0 | 67.5 | 7.4 | 35.7 | 4.82 | 2.46 | 1472.8 | 926.2 | 0.63 | 3.03 | |
| LGL-2-4 ^[14] | 27.7 | 76.0 | 6.0 | 27.2 | 4.62 | 3.13 | 1182.3 | 922.5 | 0.78 | 3.60 | |
| LGL-3-3 ^[14] | 41.5 | 79.2 | 11.6 | 39.1 | 3.37 | 2.53 | 1900.3 | 1241.0 | 0.65 | 2.20 | |
| YRGL-1 ^[15] | 70 | 90 | 14.5 | 37.4 | 2.58 | 3.95 | 2339.5 | 1025.6 | 0.44 | 1.13 | CC |
| YRGL-2 ^[15] | 90 | 110 | 13.3 | 28.7 | 2.16 | 5.77 | 2138.5 | 1048.0 | 0.49 | 1.06 | FR |
| YRCL-1 ^[15] | 80 | 100 | 11.5 | 27.6 | 2.40 | 5.81 | 2125.0 | 860.0 | 0.40 | 0.97 | CC |
| YRCL-2 ^[15] | 80 | 140 | 6.0 | 23.1 | 3.85 | 9.12 | 2121.0 | 1074.2 | 0.51 | 1.95 | |
| CFRP+GFRP ^[16] | 70 | 120 | 20 | 63 | 3.15 | 2.53 | 6535.0 | 2850.2 | 0.44 | 1.37 | CC |

CC: concrete crushing, FR: FRP rupture.

GFRP bar reinforced beams [14] with failure model of concrete crushing have better ductility. More FRP bar and reinforcement embed in compressed area is contributed to the improvement of FRP structure on the synthetic ductility index, especially for continuous beam. By increasing the amount of steel at tensile zone and compression region simultaneously, the value of ductility index declined obviously.

Pre-stressed FRP reinforced flexural member [15] could remarkably increase the cracking load, reduce crack width and deflection at the service limit state. The more degree of pre-stressing force means better effect. The synthetic ductility index of pre-stressed FRP reinforced flexural member is closely related to the modulus and pre-stressing force degree of FRP. Pre-stressed CFRP reinforced beams have worse ductility. Fabricated FRP (different modulus) reinforced beams have better synthetic ductility [16] contrast with Pre-stressed FRP reinforced flexural member.

CONCLUSION

Mechanical behaviours of high-strength concrete beams reinforced with steel fibre and BFRP rebar are investigated in this study. By analysing working performance, ultimate bearing capacity and synthetic ductility index, the following conclusions may be drawn from the present work.

The compressive strength and splitting tensile strength of high-strength concrete improved with additions of steel fibre at various volume fractions. Increase steel fibre volume content from 0.5% to 1.5%. The compressive strength grows from 12.1% to 18.7% and 18.2% contrast with plain concrete. While, splitting tensile strength grows from 61.6% to 173.3% and 260% with the same steel fibre volume.

For high-strength concrete beams reinforced with BFRP rebar and steel fibre, there is an increase of 2.1%, 23.6% and 16.8% higher than beams without steel fibre was observed in flexural

capacities when fibre content is increased from 0.5% to 1.5% by volume. Meanwhile, the serving load increase with range from 75%, 100% and 125% and the cracking load increase from 25% to 50%.

Reinforcement ratio of BFRP rebar is a key factor influence bearing capacity and failure mode of high-strength concrete beams reinforced with steel fibre. When keep the addition of 1% in volume steel fibre constant, increase reinforcement ratio of BFRP rebar 0.57%, 0.76% and 0.95%, the ultimate strength is improved by about 16.8, 55.7 and 85.6% and the servicing load is increased by 33.3%, 38.3% and 75% compared with contrast specimen.

Improving the property of concrete regarded as an effective measure to get the desired ductility capacity for flexural member. Under the condition of appropriate reinforcement ratio and steel fibre volume, the synthetic ductility indices of steel fibre reinforced concrete reinforced with FRP rebar are above the minimum requirement of $\mu_c \geq 4$. The synthetic ductility of double reinforced beam possess better capacity of deformation and ductility. Pre-stressed FRP bar reinforced concrete beam and hybrid FRP reinforced flexural member have poor synthetic ductility performance due to the deteriorate capacity of ultimate bearing.

Due to ignoring the factor of load types and insufficient data, the analysis of statistical and uncertainty are not done. Therefore, we need to conduct additional analytical, structural innovation and experimental research to optimize the deformability and ductility of FRP reinforced structure. Furthermore, based on the demand bearing capacity, deflection and crack width, we need to develop various types of FRP strengthening systems to ensure desired adequate ductility and deformability at different situation.

ACKNOWLEDGEMENTS

The investigation of this paper was supported by the National Natural Science Foundation of China (Grant No. 41572285 and No. 51178433).

REFERENCES

- [1] Alsayed S H, Alhozaimy A M. Ductility of concrete beams reinforced with FRP bars and steel fibers. *Journal of composite materials* 1999; 33(19):1792-1806.
- [2] Wang H, Belarbi A. Ductility characteristics of fiber-reinforced-concrete beams reinforced with FRP rebars. *Construction and Building Materials* 2011; 25(5): 2391-2401.
- [3] Harris H G, Somboonsong W, Ko F K. New ductile hybrid FRP reinforcing bar for concrete structures. *Journal of composites for construction* 1998; 2(1): 28-37.
- [4] Wierschem N, Andrawes B. Super-elastic SMA-FRP composite reinforcement for concrete structures. *Smart Materials and Structures* 2010; 19(2): 025011.
- [5] Spadea, G., Bencardino, F. And Swamy, R.N. Strengthening and upgrading structures with bonded CFRP sheets. *Design Aspects for Structural Integrity, Proceeding of the 3rd International RILEM Non-Metallic (FRP) for Concrete Structures*. Sapporo, Japan; 1997. p. 379-386.
- [6] Naaman AE, Jeong SM. Structural ductility of concrete beams prestressed with FRP tendons. In: *Proceedings of the second international RILEM symposium (FRPRCS-2): Non-metallic (FRP) for concrete structures*. Ghent, Belgium; 1995. P. 379-86.
- [7] Jaeger L G, Mufti A A, Tadros G. The concept of the overall performance factor in rectangular-section reinforced concrete members. *Proceedings of the 3rd International Symposium on Non-Metallic (FRP) Reinforcement for Concrete Structures*, Sapporo, Japan; 1997. 2: 551-559.

- [8] Oudah F, El-Hacha R. A new ductility model of reinforced concrete beams strengthened using fiber reinforced polymer reinforcement. *Composites Part B: Engineering* 2012; 43(8): 3338-3347.
- [9] Cosenza. E, Manfredi. G. and Realfonzo. R. Behaviour and modeling of bond of FRP rebars to concrete, *Compos. For Constr.*, ASCE, 1997; 1(2):40-51.
- [10] Cosenza E, Manfredi G, Realfonzo R. Analytical modeling of bond between FRP reinforcing bars and concrete. *Proc. 2nd Int. RILEM Symp. (FRPRCS-2)*, L. Taerwe, ed; 1995.
- [11] Bi Q W. Experimental Research on the Micro-structure of Basalt Fiber Reinforced Concrete and the Oblique Section Bearing Capacity of the BFRP bars Reinforced fiber Concrete Beams. D.E. thesis, Dalian University, Dalian; 2012. (in chinese)
- [12] Belarbi A, Wang H. Bond durability of FRP bars embedded in fiber-reinforced concrete. *Journal of Composites for Construction* 2011; 16(4): 371-380.
- [13] Thniguchi. Grace. Response of continuous CFRP Pre-stressed concrete bridges under static and repeated loadings. *PCI Journal* 2000; 45(6): 84-102.
- [14] Qi A, Weng C.G. Experimental Study on Ductility Behavior of Concrete Beams Reinforced with FRP rebars. *Earthquake Resistant Engineering and Retrofitting*, 2008, 29(5): 63-67. (in chinese)
- [15] Yuan J F. Analysis on Flexural Behavior of Concrete Beam Reinforced with FRP bars. M.E. thesis, Southeast University, Nanjing; 2007. (in chinese)
- [16] Yang J. Experimental Study and Theoretical Analysis on Concrete Beams Reinforced with Different FRP Bars Blended. M.E. thesis, Chongqing University, Chongqing; 2013. (in chinese)

PARALOID B72 NANODISPERSION PREPARATION TECHNOLOGY AND ITS POSSIBILITIES FOR USE IN THE MONUMENT CARE

David Škoda¹, Renata Pučalíková¹, Ivo Kuřitka¹ and Klára Kroftová²

1. *Centre of Polymer Systems, Tomáš Baťa University Zlín, Tř. Tomáše Baři 5678, Zlín, CZ-76001, Czech Republic; dskoda@utb.cz*
2. *Czech Technical University in Prague, Faculty of Civil Engineering, Department of Architecture, Thákurova 7, Prague 6, CZ-162 00, Czech Republic; Klara.Kroftova@seznam.cz*

ABSTRACT

The paper summarizes the results of laboratory research on acrylate polymer Paraloid B72, the use of which is widespread in the consolidation and protection of historical materials. The aim of laboratory research was primarily to analyse the possibilities of modifying particle sizes, given that this material characteristic plays an important role in the penetration process and hence the effectiveness of the consolidator. The contribution shows and compares the basic properties of the tested dispersions of Paraloid B72. The tested polymer system has a smaller particle size and it is possible to assume the possibility of proper use in monument care.

KEYWORDS

Paraloid B72, Nanodispersion, Ethanol, Cultural heritage, Consolidation

INTRODUCTION

Many materials used for plastering reinforcement have been based on acrylic copolymer dispersion in recent decades [1]. Acrylic polymers are macromolecular reinforcing agents derived from acrylic acid, methacrylic acid and their esters (e.g. Paraloid B72, Primal AC33, Hydro-Grund 750, Veropal UV40 and others). Acrylates are applied in the form of dispersions in organic solvents and are currently used in the consolidation of plasters, wall paintings and sgraffittos or to protect the substrate against UV radiation (e.g. Paraloid B72, Veropal UV40, Solakryl BMT, Disapol M 1-40 and others). In general, the main advantages of these devices include high efficiency and variability, i.e. usability in many phases of technology, low cost, easy accessibility and user experience. The acrylates can also be characterized by their high bonding ability, high photooxidation and hydrolytic stability and, in particular, sufficient penetration capacity. Among the disadvantages of the application of acrylates can be the introduction of foreign material into historical matters and especially irreversibility (especially in penetration), high diffusion resistance, surface film formation and last but not least negative impact on the optical properties of the treated material (especially when massive use) [2].

Paraloid B72 Acrylic Resin is one of the most widely used means used since the 1960s to strengthen natural stone, plaster, wood, etc. [3]. Paraloid B72 is especially known as consolidation and impregnation agent of mural paintings and oil paintings, as a picture varnish or as a fixative for charcoal and chalk drawings, pastels, as well as for the consolidation of wood. It is also recommended as an adhesive for glass and ceramics. Its positive features include easy

processing, UV resistance, non-stickiness and resistance to acid rains and biological attack. The matured material is transparent and has good optical properties.

For the purpose of restoration and conservation practice, Paraloid B72 granules are dissolved in organic solvents, the choice of which affects the properties and the way of use. Since Paraloid B72 is widely used in restoration praxis as mentioned, its particle size plays important role in a penetration process and final consolidation [4, 5]. In the case of use of a too concentrated solution, the risk of over-absorbing surface of the treated material, the formation of a sealable film and the appearance of shine may occur. Particle size study can be realized in case of Paraloid B72 dispersions. These studies involve a use of good and bad solvents which enable to tune the size of particles and dispersion characteristics. Moreover, the use of various surfactants within these experiments was found beneficial as well [6].

METHODS

In this work we studied dispersions of Paraloid B72 by means of its particle size. We have chosen different solvents system based on good solvents such as ethanol and acetone. Contrary, water was used as a bad solvent to achieve precipitation of Paraloid B72 particles [7]. The aim of this work is to find an optimal solvent combination to achieve different particle size of Paraloid B72.

Chemicals

Paraloid B72 was supplied from Krusta shop. Ethanol (technical) and acetone (p.a.) were purchased from Mikrochem (Slovakia). Tween 20 sufractant was supplied from Sigma-Aldrich.

Instrumentation

Particle size distributions were analysed on a Malvern Zetasizer ZS instrument by dynamic light scattering technique (DLS) [8]. Refractive index of Paraloid B72 was set to 1.48. The samples for DLS measurement were used as prepared.

Experimental part

10 wt% dispersion of Paraloid B72 was prepared as follows: Paraloid B72 (4.0 g) was dissolved in ethanol (44.0 ml) to produce clear dispersion. The second dispersion was obtained by the addition of 10 ml of acetone into the first dispersion of EtOH and Paraloid B72. The concentration of Paraloid B72 in ethanol + acetone is 8.6 wt%. Then, 10 ml of each dispersion was used for water addition. To modify the particle size, the aliquots of water was added into 10 ml of both dispersions.

Tab. 1 - Prepared dispersions of Paraloid B72

| Paraloid B72 [g] | Solvent 1 | [ml] | Solvent 2 | [ml] | Wt % |
|------------------|-----------|------|-----------|------|------|
| 4.0 | EtOH | 44.0 | | | 10.0 |
| 4.0 | EtOH | 44.0 | Acetone | 10.0 | 8.6 |

RESULTS

Paraloid B72 is copolymer consisted from ethyl methacrylate (EMA) and methyl methacrylate (MA) with weight average molecular weight 65128 M_w . This number represents the total weight of polymer divided by the number of polymer molecules. The weight fractions of EMA and MA are 70 % and 30 %, respectively. A number average molecular weight is 11397 M_n . This value is determined by measuring the molecular mass of n polymer molecules, summing the masses, and dividing by n (Figure 1).

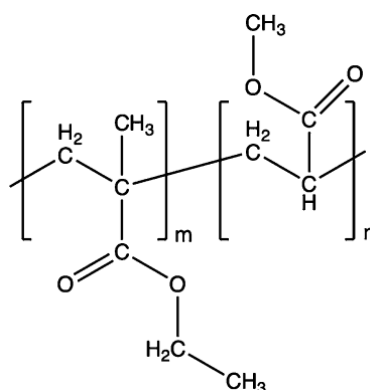


Fig.1 - Structure of Paraloid B72 ($m = 70$, $n = 30$).

Based on the knowledge of Paraloid B72 structure, the gyration radius of Paraloid B72 polymer chain can be derived. This number gives us information about the size of polymer particle in dispersion.

Polymer chain length (L) can be calculated from Equation 1.

$$L = \sin \alpha * d * P, \quad (1)$$

Where α is bond angle in polymer chain, d is C-C bond length and P is degree of polymerization. Then, the gyration radius is calculated from Equation 2.

$$S = \sqrt{\left(\frac{M_o * 2 \left(\frac{L}{2}\right)^2}{M_o}\right)}, \quad (2)$$

Where M_o is the molecular weight of monomer unit formed by 0.7 EMA and 0.3 MA. The gyration radius calculated from presented equations (Equations 1 and 2) is ca. 7.6 nm. From this we can conclude that the diameter of Paraloid polymer particle is ca. 15.2 nm.

We have studied two model systems of Paraloid B72 in different solvents. Ethanol and acetone were chosen as good solvents,. It was found that these solvents dissolve Paraloid B72 resulting in clear dispersions. In case of EtOH and EtOH + acetone solvents, the concentration of Paraloid B72 was 10 and 8.6 wt%, respectively. The volumes of studied samples were 10 ml. To evaluate the size of Paraloid B72 particles in prepared solvents, a dynamic light scattering (DLS) method was employed. This method provides the information about hydrodynamic diameter of analyzed particles. The values of particle sizes and Pdl indexes are given in Table 1. As illustrated, particle size is changing with the addition of water.

Dispersion of Paraloid B72 in ethanol was clear and according to DLS measurement the particle size of Paraloid is 26 nm (Fig. 2). After addition of 1 ml of water the size remained the same. However, after addition of 2 ml of water the size was increased to 58 nm while the dispersion was still clear. Addition of 4 ml resulted in colour change and milky dispersion was

observed. According to DLS analysis the size of Paraloid B72 is about 797 nm. With the addition of 6 and 8 ml of water the precipitation of bigger white bulky solid was observed. This behaviour is connected to shift of equilibrium to precipitation of Paraloid B72. The dispersion above the precipitate was analysed by DLS and the sizes were about 683 and 416 nm. This decrease is caused by the precipitation of bigger particles of Paraloid B72 after water addition whereas smaller particles were preserved in the suspension.

In the case of dispersions based on ethanol and acetone, smaller size of Paraloid B72 was evidenced (Fig. 3). This observation can be assigned to supporting effect of acetone. Acetone works as a good solvent for Paraloid B72 and we assume that its presence allows better solubility of Paraloid in this system of solvents. The size of 11 nm is smaller than the gyration diameter calculated above (15 nm). This difference can be caused by specific orientation of polymer in this solvent system. DLS measurements of dispersions exhibit big increase of size when 4 ml of water were added. In this case the precipitation of Paraloid was evidenced and milky colour of dispersion was observed as well as in the previous case. The size after addition of 4 ml is about 383 nm. However, after the addition of 6 and 8 ml of water, the particle size is almost similar. From this we can conclude that the particles in residual dispersion are stable with the sizes about 360 nm.

DLS distribution curves of Paraloid B72 in EtOH and EtOH with acetone are displayed in Figures 2 and 3, respectively. Fig. 2 illustrates Paraloid B72 in EtOH solvent with water additions. Distribution peaks revealed almost monomodal distribution except the sample with the addition of 6 ml of water. In this case the peak is very broad indicating wide particle size distribution. As mentioned above, this behaviour is attributed to precipitation of Paraloid in the dispersion. Fig. 3 shows DLS curves of Paraloid B72 in EtOH and acetone solvents. Similarly to previous dispersion, broad size distribution is observed after addition of 6 ml of water.

Polydispersity index values (Pdl) of prepared dispersions are between 0.14 and 0.36 indicating moderately polydisperse distribution type (Table 2).

Tab. 2 - DLS results of Paraloid B72 dispersions.

| Solvent | DLS results | Water addition | | | | | |
|--------------|----------------|----------------|------|-------|------|------|------|
| | | 0 ml | 1 ml | 2 ml* | 4 ml | 6 ml | 8 ml |
| EtOH | Z-Ave [nm] | 26 | 25 | 58 | 797 | 683 | 416 |
| | Main peak [nm] | 29 | 23 | 74 | 964 | 686 | 519 |
| | Pdl | 0.25 | 0.34 | 0.23 | 0.17 | 0.36 | 0.19 |
| EtOH+Acetone | Z-Ave [nm] | 11 | 14 | 48 | 383 | 365 | 359 |
| | Main peak [nm] | 12 | 14 | 61 | 418 | 641 | 417 |
| | Pdl | 0.20 | 0.33 | 0.20 | 0.22 | 0.29 | 0.14 |

*dispersion used for Tween 20 addition

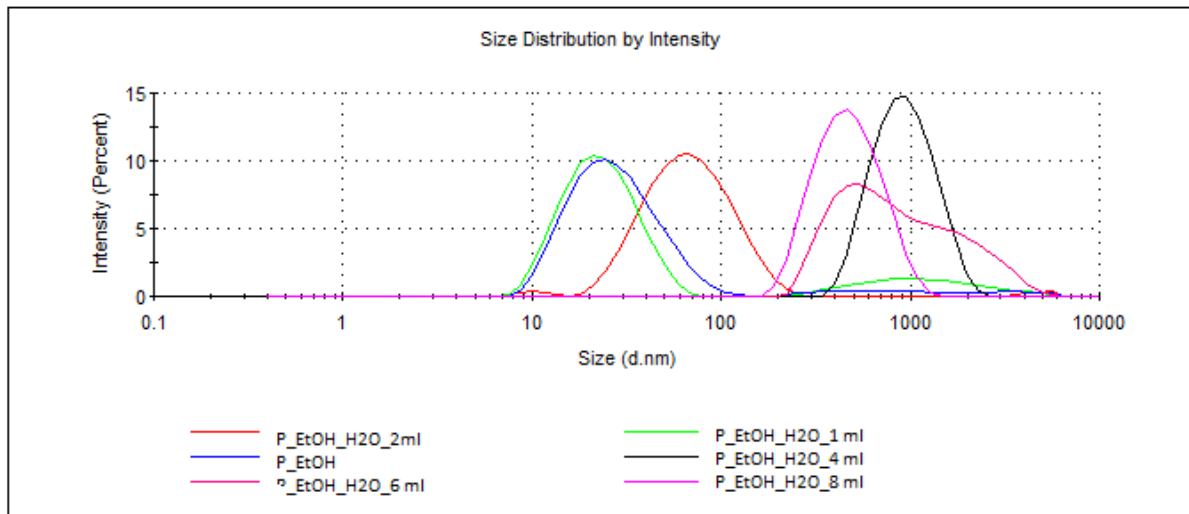


Fig. 2 - DLS size distribution curves of Paraloid B72 dispersion in EtOH with water additions.

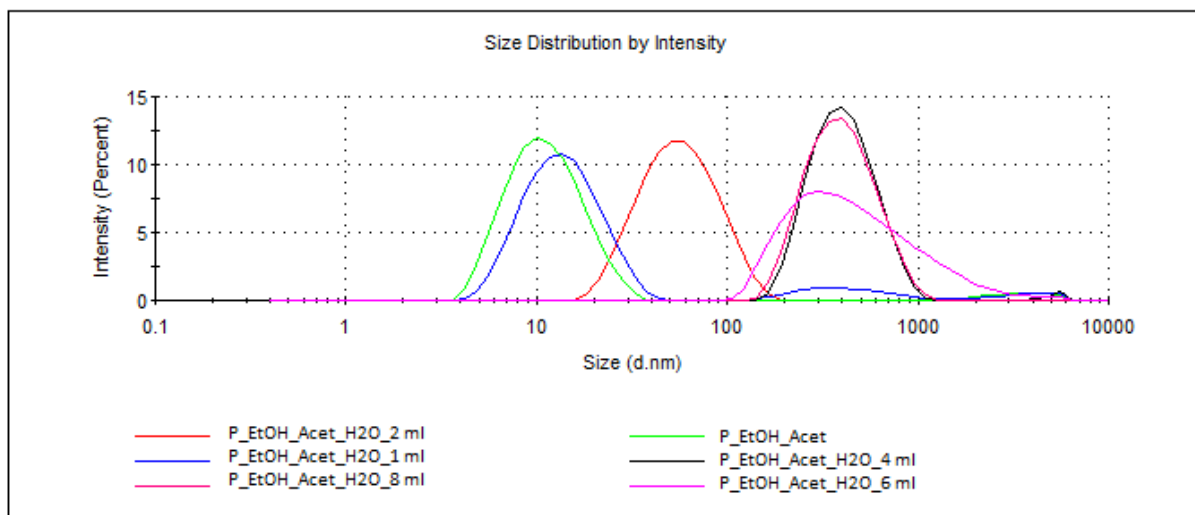


Fig. 3 - DLS size distribution curves of Paraloid B72 dispersion in EtOH + acetone solvents mixture with water additions.

From the obtained data we can conclude, that EtOH and EtOH + acetone solvent systems can be used for dispersions of Paraloid B72. Moreover, the additions of water portions modified particle size of polymer.

Effect of Tween 20 surfactant addition on the size of Paraloid B72 particles was studied in case of dispersions in EtOH solvent with 2 ml of water addition. As displayed in Table 3, the addition of 0.3 ml of Tween 20 led to particle size increase up to 97 nm. This change is caused most probably due to agglomeration of Paraloid particles and their coating with the Tween 20 surfactant.

Tab. 3 - DLS results of Paraloid B72 dispersion after Tween 20 addition.

| solvent | DLS results | without Tween 20 | Tween 20 (0.3 ml) |
|----------------------------|----------------|------------------|-------------------|
| EtOH + 2 ml water addition | Z-Ave [nm] | 58 | 97 |
| | Main peak [nm] | 74 | 121 |
| | Pdl | 0.23 | 0.26 |

CONCLUSION

In this work particle size distribution of Paraloid B72 copolymer was studied. Paraloid B72 was dispersed in ethanol and ethanol + acetone solvent mixture and its size was about 26 and 11 nm, respectively. After water addition, the particle size was significantly increased due to precipitation of Paraloid B72 particles. With the use of acetone as a co-solvent we achieved smaller particles of Paraloid B72. Based on the obtained data we can conclude, that the system of ethanol and acetone with 2 ml water addition can be found as an optimal mixture for following applications in restoration. Moreover, the tuning of particle size is beneficial for utilization of Paraloid in different morphologies of consolidated materials. In other words, different porosity of consolidated materials requires different particles of consolidant. From this point of view, the particle size modification brings important data for further use of Paraloid B72. We believe that these data can be useful for application of Paraloid B72 in restoration praxis.

ACKNOWLEDGEMENTS

This article was written as part of the NAKI DG16P02M055 research project "Development and Research of Materials, Methods and Technologies for the Restoration, Preservation and Strengthening of Historic Masonry Constructions and Surfaces and Systems of Preventive Conservation of Cultural Heritage Buildings Threatened by Anthropogenic and Natural Hazards (2016 – 2022, MK0/DG)".

REFERENCES

- [1] Bárta, J., Rathouský, J. Z historie českých organokřemičitých konzervantů, Sborník konference: Organokřemičitany v české památkové péči, NPÚ Praha, 2008, str. 21-27
- [2] Tichý, M., Zpevňování omítek vápennou vodou – metoda a související aspekty, dostupné online: www.studioaxis.cz/images/pamatky/tichymarek.doc
- [3] Paraloid B72 – technický list, <http://www.imesta.com/dokumenty/paraloid-b72.pdf>
- [4] Čejka, T.; Zigler, R.; Kroftová, K.; Šmidtová, M. Grouting methods for the rehabilitation and reinforcement of masonry structures damaged by cracks [online]. The Civil Engineering Journal. 2016, 0(3), ISSN 1805-2576. Available from: http://www.civilengineeringjournal.cz/archive/issues/2016/2016_3/3-2016-0015-Final.pdf
- [5] Witzany J., Zigler R., Kroftová K., Čejka T., Kubát J., Holický M., Karas J. The effect of pore distribution in historic masonry on the grouting method and grouting mix selection (in press). The Civil Engineering Journal. ISSN 1805-2576
- [6] Baglioni, M., Montis, C., Chelazzi, D., Giorgi, R., Berti, D., Baglioni, P., Polymer Film Dewetting by Water/Surfactant/Good-Solvent Mixtures: A Mechanistic Insight and Its Implications for the Conservation of Cultural Heritage. Angew. Chem. Int. Ed. 2018, 57;57(25):7355-7359. doi: 10.1002/anie.201710930.



- [7] Lebouille, J.G.J.L., Stepanyan, R., Slot, J.J.M., Cohen Stuart, M.A., Tuinier, R., Nanoprecipitation of polymers in a bad solvent, *Colloids and Surfaces A: Physicochemical and Engineering Aspects*, Volume 460, 2014, Pages 225-235, ISSN 0927-7757, <https://doi.org/10.1016/j.colsurfa.2013.11.045>.
- [8] Nobbmann, U., Morfesis, A., Light scattering and nanoparticles, *Materials Today*, Volume 12, Issue 5, 2009, Pages 52-54, ISSN 1369-7021, [https://doi.org/10.1016/S1369-7021\(09\)70164-6](https://doi.org/10.1016/S1369-7021(09)70164-6)

RANKING OF MAJOR HAZARDS SUITABLE FOR THE GOVERNMENT SUPERVISION

Hao Yu ¹, Sun Chaolun ^{2*}

1. School of Emergency Management, Henan Polytechnic University, Jiaozuo, Henan, China; 761799439@qq.com
2. College of Safety and Engineering, Henan Polytechnic University, Jiaozuo, Henan, China

ABSTRACT

Based on the basic theory of risk, we add the sensitivity factor in the process of design the risk classification model of the major hazard sources, and establish the quantitative classification model and the qualitative classification three-dimensional model of the major hazard source. According to the risk status of the major hazard sources in the production site, the system of risk evaluation index is determined from the three dimensions of probability, severity and sensitivity. (AHP) was used to calculate the weights of each index, and established the mathematical model of risk classification of major hazard sources in production sites. Besides, there are more than 30 enterprises in Taiwan that were selected for empirical research. The empirical research shows that the risk classification model of the major hazard source which is established in this paper has good practicability and convenience. It is suitable for the government safety supervision department to carry out the hierarchical supervision work, and can systematically and conveniently realize the government's scientific safety supervision and the effective safety management of the enterprise.

KEYWORDS

Production site, Major hazard, Sensitivity, Risk classification

INTRODUCTION

With the development of social economy, China has paid more and more attention to safety production, and the rate of each dangerous industry accident has been decreasing year by year. The situation of national safety production is stable and showing a better trend. This shows that China's safety work has made great progress, but the number of casualties is still much higher than the developed countries. As the focal point of safety production and emergency management work, China's security work of major dangerous sources still have many problems, for example inherently safe technology is not in place, security education is not in place, security management is not in place and so on. In recent years, many major accidents occurred, due to the management major dangerous source is not very well. Among them, the major hazard of production is an important part of the work of major hazard management, and we can also ignore the danger result from it and its supervision work [1]. Risk assessment is the most basal work of Security management work in major hazard sources, and it is also the key link of accident prevention [2]. Therefore, to strengthen the risk management of major hazard sources, through risk identification and assessment and clear safety supervision purposes, in order to improve the level of safety management of major dangerous sources [3].

Although there are many major hazard classification methods at home and abroad, the author found through reading a lot of literature that the existing classification methods still have the following problems:

(1) Single grading index and lack of integrity. Many of the existing classification methods at present only considered dangerous chemicals critical mass, to critical mass classification standard for single, often ignored the environment of dangerous chemical storage conditions, for enterprise's management level and other important factors, they did not consider other necessary conditions for the existence of hidden dangers, not overall and systematic consideration of major hazard installation.

(2) The multi-dimensional risk factors were not taken into account and the system was not considered. Most of the existing major hazard classification methods in China only consider the severity of major hazard accident, take single consequence factors such as the number of deaths as the index of classification, and do not consider the possibility of major hazard accident and the time and space sensitivity of the accident. The multi-dimensional risk factors were not taken into account and the system was not considered.

(3) Evaluation procedures are numerous and complicated, and they are not suitable for government supervision. The existing classification and evaluation methods of hazardous chemicals have complex evaluation process, numerous steps, difficult calculation, high professional level required, and are applicable to professional safety evaluation, not applicable to government graded safety supervision.

By selecting risk evaluation indexes in three-dimensions, this paper evaluates the risk level of various major hazard sources, classifies major hazard sources and applies them to government supervision, making it more scientific and convenient for the government to manage major hazard sources, so as to formulate more effective safety measures and effectively reduce the accident rate.

THREE-DIMENSIONAL HIERARCHICAL MODEL OF MAJOR HAZARD RISK

The bring up of question

Major hazards are divided into two parts, there are the major hazard source in production site and the major hazard source in storage area [4]. Major hazard source in production site is the facilities or places where the number of production or use of civil explosives, Pyrotechnic compound, fireworks and firecrackers, flammable liquids, combustible gases, toxic substances etc., can reach or exceed the critical number. Safety [5] management of major hazards in production site is an important content in safety production, it has important significance to improve the level and effect of safety production management. Our government and relevant departments have always pay attention to the risk classification of major hazards [6], the existing classification methods of major hazards include: "death radii-method", "flammable, explosive, toxic and significant risk source evaluation" ext. [7]. Through the existing evaluation and grading methods of major hazards, we can see that the classification of major hazards has been mature. However, these evaluation indicators are too single. Most only consider the serious of the major hazard accident consequences, use death tolls and other single consequences factors as the grading indicators, not taking into account the possibility of major hazards and the sensitivity of time and space of accident [8]. The classification method of major hazard installations in metal and nonmetal underground mines and tailings dam, drafted by China Academy of Safety Science and Technology, is comprehensive and detailed, suitable for safety evaluation, but it is not suitable for government regulation. Therefore, combined with the needs of government safety supervision, to study the model and method of major hazards in production site, classify major hazard sources, for government regulation, make the government more scientific and more convenient to manage major hazards, so as to develop more effective safety measures to reduce the accident rate.

Quantitative classification model of major risk sources

In the area of security, risk generally refers to the combination of the likelihood of a particular hazard event and its consequences [9]. A large number of accident investigation studies have shown that the severity of accidents at different times or locations is different, that is, time and space have a sensitive effect on the accident [10]. Therefore, based on the risk function, taking into account the sensitivity of the accident, adding the sensitivity factor, and add the three influencing factors influencing the major hazard source to the mathematical model, according to factor index and score of Possibility influencing factors of risk source, the score of sensitivity influencing factors index and the weight of each index, establish the quantitative grading model of major risk source, as shown below.

$$R = P \times L \times S = \sum_{i=1}^n d_i \omega_i \cdot \sum_{j=1}^m d_j \omega_j \cdot \sum_{k=1}^l d_k \omega_k \quad (1)$$

In the formula: R is the risk value of the major hazard; P, L, S, respectively represent the possibility, severity, sensitivity.

Possibility P represents the possibility influencing factors, that is, select the risk factors that affect the likelihood of occurrence of major hazard sources, to reflect the different possibilities of the accident, such as the storage of dangerous chemicals.

Severity L represents the consequences of the consequences of the consequences, that is, select the risk factors that affect the consequences of major hazards, to reflect the severity of the loss after the accident, such as population density.

Sensitivity S represents the sensitivity of factors, that is, special time or special location, the consequences of the accident occurred in different degrees, this time and place is divided into sensitive factors such as the equipment in which the environmental function area.

D_i , d_j , d_k are the actual scores of the i , j , k indicators, respectively; ω_i , ω_j , and ω_k are the weights of the i , j and k indices relative to the primary index respectively; n , m , l represent respectively, Severity, sensitivity evaluation index number;

According to the above quantitative grading model, a single index according to the degree of danger is divided into four grades, respectively, assigned 1,2,3,4 points, as shown in Table 1. According to the actual situation, select the actual risk level of each index, the index risk value and the index weight multiplied to calculate the final risk value of the risk source. According to the overall risk level of local risk sources, according to the principle of ALARP to extract the corresponding proportion of major hazard sources, risk classification. For example, a major hazard risk value in the top 20% in a city is divided into level one major hazard source. The risk value in the middle 20-50% is divided into level two major hazard sources. The risk value in the back 50% - 80 % is divided into level three major hazard sources; the risk value in the last 20% is divided into level four major hazard sources, represent the risk is acceptable. And finally according to the classification standards, the development of appropriate risk improvement measures to take different levels, different strength of the safety supervision measures [11].

Three-dimensional model of qualitative classification of major hazard sources

The risk factor of the major hazard sources is based on the two-dimensional elements of the risk function - the likelihood of the occurrence of the accident and the seriousness of the consequences. Adding the sensitivity factor, from the serious consequences of the accident (in order of ABCD to indicate the severity), the possibility A、b、c、d in turn express the possibility of size) and sensitivity (1234 in order to indicate the degree of sensitivity) three dimensions to consider the relative dynamic risk of various types of risk, comprehensive consideration of personnel, equipment, environment, management and other factors and the relationship between

time and space. Establish a qualitative three-dimensional model of hazard risk assessment, as shown in Figure 1. According to the ALARP principle, the unacceptable range of risk is expressed in red. The ALARP area is divided into orange and yellow. The acceptable Range of risk is indicated by blue, see Table 1.

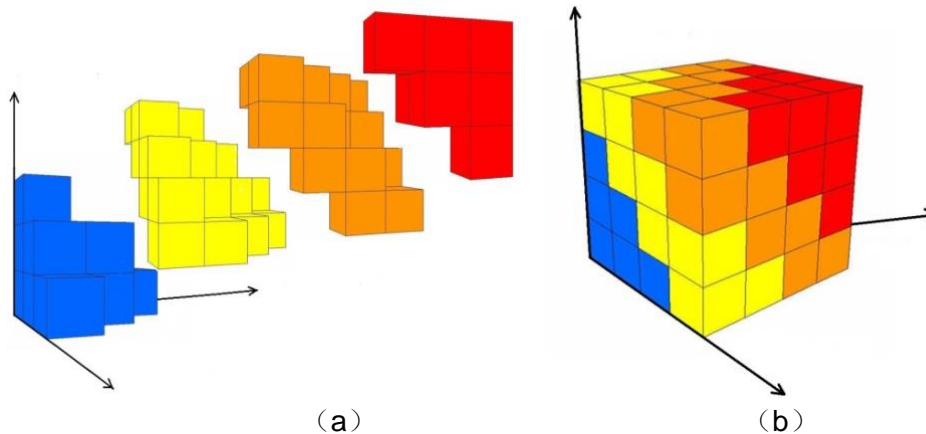


Fig. 1 - Three dimensional model of qualitative classification for risk assessment of major hazard sources as a whole (a) and grading (b)

Tab. 1 - Risk combination table of three-dimensional model elements for risk assessment of major risk sources

| Risk level | Factor risk combination |
|----------------|---|
| Level IV risk | Aa1, Aa2, Aa3, Ab1, Ab2, Ab3, Ba1, Ba2, Bb1, Bb2, Ca1 |
| Level III risk | Aa4, Ab3, Ab4, Ac2, Ac3, Ad1, Ad2, Ba3, Ba4, Bb3, Bc1, Bc2, Bd1, Ca2, Ca3, Cb1, Cb2, Cc1, Da1, Da2, Db1 |
| Level II risk | Ac3, Ad3, Ad4, Bb4, Bc3, Bc4, Bd2, Bd3, Ca4, Cb3, Cb4, Cc2, Cd1, Cd2, Da3, Da4, Db2, Db3, Dc1, Dc2, Dd1 |
| Level I risk | Bd4, Cc3, Cc4, Cd3, Cd4, Cb4, Cc3, Dc4, Dd2, Dd3, Dd4 |

METHOD OF RISK CLASSIFICATION FOR MAJOR HAZARD SOURCES IN PRODUCTION SITES

Selection of risk assessment index for major hazard sources in production sites

Through the combing of major safety accidents in production sites in recent years and the investigation of accidents in production sites, it is found that the main types of safety accidents in the production sites are the ones to focus on. Therefore, the author from the three aspects of the possibility of occurrence, severity and sensitivity to consider the design of risk-based, for the needs of government safety supervision of the production site of the major risk of risk assessment index system. Including a total of eight factors affecting the occurrence of accidents in production sites, four severity influencing factors and two sensitivity influencing factors. And take the questionnaire survey method, the index is preferred. A total of 35 risk assessment indexes for major hazard areas were collected, 10 of which were filled out by government safety supervisors, 15 were filled by technical staff and 10 were filled by researchers. After three rounds of Delphi method and expert meeting method, part of the repeated and non-critical indicators, through the index

screening, and ultimately determine the production site risk assessment index system and a single index grading standards as shown in Table 2 below.

Tab. 2 - Workplace major hazards risk assessment index system tables

| Level 1 indicators | Level 2 indicators | Level 3 indicators | Index classification | | | | |
|---------------------------------|-----------------------------|--|--|--|--|---|---------------------|
| | | | Level 4 | Level 3 | Level 2 | Level 1 | |
| Possibility Factors P | Technical factors P1 | Storage material quality critical value P11 | Amount of substance/ critical quantity ≤ 1 | Amount of substance / critical quantity = (1,5] | Amount of substance / critical quantity = (5,10] | Amount of substance / critical quantity > 10 | |
| | | Production substance hazard P12 | 1.6 Insensitive substances and other substances | 1.4 items, 1.5explosives, 2.2 gas, 4.3 solid meet one | 1.2,1.3 explosives, 2.3 gas, 4.2 solid,5.2 substances, 9 categories of hazardous substances, to meet one | 1.1 explosives, 2.1 gases, flammable liquids, 4.1 solids, 5.1 substances, toxic, infectious, radioactive, and corrosive substances, to meet one | |
| | | Production technology Mechanization degree P13 | Mechanization degree $\geq 95\%$ | Mechanization degree [75%,95%) | Mechanization degree [50%,75%) | Mechanization degree $< 50\%$ | |
| | | Safety alarm and control system P14 | Have and can be used normally | have, some parts fail, does not affect the alarm | have, some parts fail, cannot alarm | no, or the overall failure, cannot alarm | |
| | | Management factors P2 | Safety production standardization grade P21 | Level 1 | Level 2 | Level 3 | No review or grade. |
| | Use factor P3 | Safety precautions of Production device P31 | have security measures and personal protective equipment for workers | have security measures ,not have personal protective equipment for workers | Not have security measures ,have personal protective equipment for workers | Not have security measures and personal protective equipment for workers | |
| | | Years of use P32 | < 5 years | [5,10) years | [10,1) years | ≥ 15 years | |
| | | Total number of accidents in recent years P33 | Nearly 10 years without casualties | no casualties in the past five years | no casualties in the past five years | no casualties in the past five years | |
| | Severity affecting factor L | Personnel influence L1 | Population density L11 | < 10 people | [30,50) people | [50,100) people | ≥ 100 people |
| | | Property impact L2 | Dangerous distance L21 | ≥ 500 m | [100,500) m | [50,100) m | $d < 50$ m |
| Environmental impact L3 | | Without firewalls L31 | yes | -- | -- | no | |
| Sensitivity affecting factors S | Space factor S1 | Environmental function area S11 | industrial area | Agricultural area, business district | Residential area, administrative office area traffic hub area | Science and technology culture area ,and so on | |

Damage risk of major hazard sources in production sites

After determining the risk evaluation index of the production site, use the analytic hierarchy process to determine the index weight. Through the questionnaire, we can calculate the importance of each index as shown in Table 3 below:

Tab. 3 - Important degree of workplace major hazards risk assessment indicators

| Level 3 indicators | Indicator importance RI |
|--|-------------------------|
| Storage material quality / critical value P11 | 9.60 |
| Storage substance hazard P12 | 8.80 |
| Production technology mechanization degree P13 | 7.21 |
| Safety alarm and control system P14 | 9.03 |
| Standardization of Safety Production Standard for Industrial Employees P21 | 8.4 |
| Safety of production equipment P31 | 9.20 |
| Number of years of production equipment P32 | 9.30 |
| In recent years the number of accidents P33 | 8.40 |
| Population density L11 | 8.66 |
| Dangerous distance L21 | 8.29 |
| Whether the firewall L31 | 8.15 |
| The environmental function area S11 | 8.34 |

According to the importance of the above indicators and finally find the index comparison between the two scales, the contrast scale is entered into the AHP software, construct judgment matrix, probability influencing factor indicators need to construct the first level of the judgment matrix A1 and the second level of the judgment matrix (B1, B2). The severity influence factor index only needs to construct a judgment matrix A2.

Probability influencing factor index judgment matrix $A_1 = \begin{bmatrix} 1 & 2 & 3 \\ 1/2 & 1 & 2 \\ 1/3 & 1/2 & 1 \end{bmatrix}$. Technical factor

index judgment matrix $B_1 = \begin{bmatrix} 1 & 2 & 3 & 2 \\ 1/2 & 1 & 2 & 1/2 \\ 1/3 & 1/2 & 1 & 1/3 \\ 1/2 & 2 & 3 & 1 \end{bmatrix}$. Use factor index judgment matrix

$B_2 = \begin{bmatrix} 1 & 2 & 1/2 \\ 1/2 & 1 & 1/2 \\ 2 & 2 & 1 \end{bmatrix}$. Severity Factor Affect Judgment Matrix $A_2 = \begin{bmatrix} 1 & 2 & 2 \\ 1/2 & 1 & 2 \\ 1/2 & 1/2 & 1 \end{bmatrix}$.

The consistency of the judgment matrix is obtained by calculating the influence factors $CR=0.0089 < 0.10$. Technical factors index judgment matrix consistency $CR=0.0266 < 0.10$; Judgment of matrix consistency using factor index $CR=0.0517 < 0.10$; Severity influencing factor index judgment matrix consistency $CR=0.0517 < 0.10$, Consistency is acceptable. Therefore, the

calculation of the three indicators for the primary index weight: Possible Impact Factor Index Weight $\omega_p = (0.2220, 0.1009, 0.0582, 0.1579, 0.2973, 0.0511, 0.0803, 0.0324)$, Severity Impact Factor Index Weight $\omega_l = (0.4934, 0.3108, 0.1958)$, Sensitivity Impact Factor Index Weight $\omega_s = (1)$.

Production site risk classification model

Based on the above theoretical model and weight of risk assessment, the risk assessment model of production site can be obtained:

$$R = \sum_{i=1}^n d_i \omega_i \cdot \sum_{j=1}^m d_j \omega_j \cdot \sum_{k=1}^l d_k \omega_k = r_p \times r_L \times r_s$$

$$= [d_{p11}, d_{p12}, d_{p13}, d_{p14}, d_{p21}, d_{p31}, d_{p32}, d_{p33}] \begin{bmatrix} 0.0220 \\ 0.1009 \\ 0.0582 \\ 0.1579 \\ 0.2973 \\ 0.0511 \\ 0.0803 \\ 0.0324 \end{bmatrix} \cdot [d_{L11}, d_{L21}, d_{L31}] \begin{bmatrix} 0.4934 \\ 0.3108 \\ 0.1958 \end{bmatrix} \cdot [d_{s11}] [1] \quad (2)$$

According to the risk classification model, combined with the production site risk assessment indicators of the actual data information, calculate the production site risk value.

AN EMPIRICAL STUDY ON THE RISK OF PRODUCTION

Empirical analysis of production sites

In order to verify the scientific and validity of the above-mentioned risk classification model, we selected about 30 production facilities in Taiwan City, Shandong Province, Taiyuan Biotechnology Co., Ltd., Ningana County Hali Chemical Co., Ltd., Taiwan Sheng Chemical Co., Ltd. District for the empirical analysis of the object. Through the issuance of production site risk assessment empirical data questionnaire, the index system to collect the actual data of the indicators of information, the establishment of production sites risk assessment index database, Calculate the risk value of the production site (plant area). According to the production site risk assessment data, calculate the production site (installation area) risk value from small to large as shown in Table 4 below.

Tab. 4 - Workplace major hazards risk data tables

| Serial number | Production site name | Risk value | Serial number | Production site name | Risk value |
|---------------|--|------------|---------------|---|------------|
| 1 | Acetylene gas workshop | 1.68 | 16 | Oxygen workshop | 4.84 |
| 2 | Acetaldehyde oxide production workshop | 2.15 | 17 | Acetaldehyde oxide production workshop | 4.96 |
| 3 | Synthesize a workshop | 2.64 | 18 | Pesticide six plants | 5.14 |
| 4 | Synthesis of two workshops | 2.94 | 19 | Pesticide three plants | 5.25 |
| 5 | Insoluble sulfur production workshop | 2.96 | 20 | Sulfur dioxide station | 5.34 |
| 6 | Air separation workshop | 3.02 | 21 | Cyclohexylamine plant area | 5.37 |
| 7 | 106 workshop | 3.03 | 22 | waste acid enrichment device area | 5.37 |
| 8 | Nitric acid production plant area | 3.11 | 23 | Phosphorus dichloride production workshop | 5.45 |
| 9 | Propane storage filling device area | 3.36 | 24 | Argon workshop | 5.49 |
| 10 | Fine chemical plant | 3.39 | 25 | Nitrobenzene, aniline plant area | 5.63 |
| 11 | Dimethyl ether production plant area | 3.44 | 26 | Carbon dioxide production plant area | 6.54 |
| 12 | Sodium dichloroisocyanurate production of a workshop | 3.84 | 27 | Chloe-alkali plant | 6.85 |
| 13 | Barium chloride workshop | 3.99 | 28 | Optoelectronic plant | 7.08 |
| 14 | Phenolic resin production plant (place) | 4.09 | 29 | Synthesis of three workshops | 9.64 |
| 15 | Potassium nitrate production plant | 4.20 | 30 | Synthetic ammonia production area | 9.76 |

According to the risk data table, the risk of production sites can be calculated as shown in Figure 2.

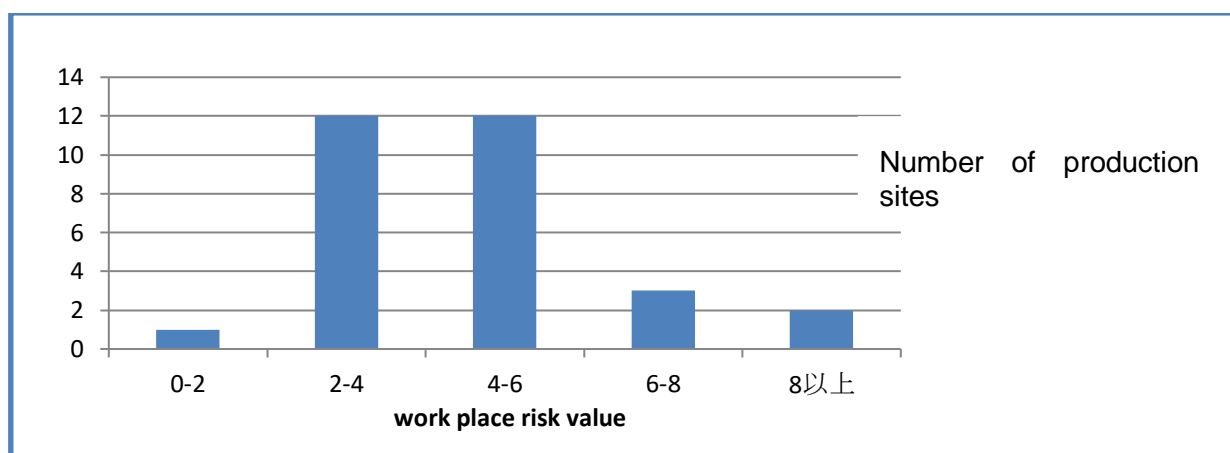


Fig. 2 - Workplace major hazard value distribution

From the figure of Figure 5-1, the risk value of the production site is also normal distribution. According to the risk index of the major hazard risk index developed earlier, the risk of production sites in the top 20% of the classified as a major hazard; the risk value in the middle 20-50%, divided into two major risk sources; risk value in the 50% -80%, divided into three major hazard;

The risk value is at the last 20%, divided into four major hazard sources, A source of danger that is acceptable. The specific grading standards are shown in Table 5 below.

Tab. 5: Workplace major hazards risk grade division standard

| Risk level | IV (Acceptable risk) | III | II | I (Unacceptable risk) |
|------------|----------------------|-----|-----|-----------------------|
| Risk R | 0~2 | 2~5 | 5~8 | ≥8 |
| proportion | 20% | 30% | 30% | 20% |

CONCLUSION AND PROSPECT

Based on the basic theory of risk, this paper adds the sensitivity influencing factors to the risk evaluation factors, constructs the classification model of the major hazard based on the risk three-dimensional model. This paper chooses the grading index of the risk assessment of the major hazard sources in the production sites, which is applicable to the government supervision, and establishes the three-dimensional model classification method for the risk of the major hazard sources in the production sites. And it carried out empirical research. The specific conclusions are as follows.

This paper takes two factors of risk: the probability of accident and the consequences of the accident, adding the sensitivity influence factor, considering the risk of the major hazard from three dimensions, and establishing the three - dimensional risk assessment model of the major hazard. And comprehensively and systematically evaluate the risk level of the major hazard sources from the three aspects of the influencing factors, the influencing factors and the influencing factors of the sensitivity.

In this paper, the production of major hazards as an example, the risk assessment index system of major hazard sources in production sites was established, and the risk evaluation index system of major hazard sources in production sites was constructed by Delphi method and questionnaire survey method. The model and grading method is a quick grading method for government regulation, it does not need complex data and calculation process, simple and practical, to meet the needs of government regulation.

In this paper, the author makes an empirical research on all kinds of major hazard data provided by Taiwan City. Collecting local actual data, statistical analysis, calculate the actual risk of various types of dangerous sources. According to the region's major risk of the overall risk level will be a major hazard into four levels, to achieve a major hazard classification, to verify the model's simplicity and practicality, and also more suitable for Taiwan City Safety Production Supervision and Administration of the city The scope of the production site of major hazard classification supervision work. However, due to limited data in Taiwan City, it is necessary to collect more representative data in more areas, so as to continuously improve the classification standards, and further ensure the classification method and model of practicality.

ACKNOWLEDGEMENTS

This study is financially supported by the project of the humanities and social science fund project of the Ministry of Education of China (No. 16YJCZH026), by the project of philosophy and Social Sciences in Henan Province of China (No.2015CZH007), by the project of the Subject of Henan provincial government decision making of China (No.2016B290) and by the project of the Education Department of Henan Province of China (No.2017-ZZJH-188). Our gratitude is also extended to reviewers for their efforts in reviewing the manuscript and their very encouraging, insightful and constructive comments.

REFERENCES

- [1] WU Yan. "Research on method of major hazard assessment on production operations area". Journal of Safety Science and Technology, vol. 8, pp. 158-164, 2012.
- [2] SHAO Hui, YANG Li-dan, LI Jing. "The Study on Major Hazards Ranking for Chemical Industrial Park". Industrial Safety and Environmental Protection, vol. 37, pp.12-16,2011.
- [3] HAO Yuan-fei, ZHANG Jian. "Analysis the risk assessment techniques of dangerous chemicals Major hazard in China". Journal of Safety Science and Technology, vol. 8, pp.52-56,2012.
- [4] 《Notice on Regulating the Supervision and Administration of Major Dangerous Sources》 (Safety Supervision Coordinator [2005] No. 62.
- [5] LIU Jingo Jian-Ming, GUAN Lei, YU Li Jian. "Probe into the Grading Method for Major Hazard Installation". China Safety Science Journal, vol. 18, pp.162-165,2008.
- [6] Wu Zongzhi. "Discussion on Control of Major Hazards and of Major Accident Potential". China Safety Science Journal, vol. 13, pp.20-23,2003.
- [7] SUN Jin-Feng, CHEN Goodhue. "Research on pre-warning technology for accidents risk of major hazards ".Journal of safety science and technology, vol. 9, pp.44-46,2010.
- [8] H. Taubenböck, J. Post, A. Roth,E. "Taltar conceptual vulnerability and risk framework as outline to identify capabilities of remote sensing". Natural Hazards and Earth System Sciences, vol. 8, pp.409-420,2008.
- [9] Mao Xiaojie et al. "Research on Safety Supervision of Major Hazardous Source in Chemical Industry Park". Shenyang: Northeastern University, 6.2008.
- [10] LUO Ying-qint, et al. "Statistical analysis on dust explosion accidents occurring in China during 2009-2013". Journal of Safety Science and Technology, vol. 11, pp.186-190,2012.
- [11] Luo Yun.. "Introduction to safety science". Beijing: China quality press, 7.2013.

RELIABILITY EVALUATION IN CONSTRUCTION QUALITY BASED ON COMPLEX VAGUE SOFT EXPERT SET METHOD

Xiaoping Bai¹, Hongyue Zhao²

Xi'an University of Architecture & Technology, School of Management, Xi'an 710055, China; xxpp88@126.com (Bai), 371639195@qq.com (Zhao)

ABSTRACT

The control of the construction quality is very important in the construction industry. In this paper, the fuzzy reliability and construction quality are linked together to establish a specific quantitative evaluation model, which not only can help to make up for the lack of the traditional reliability qualitative evaluation methods, but also can avoid the inaccuracy of fuzzy quantitative evaluation of construction quality to a certain extent. This paper firstly selects some influencing factors of construction quality, and then makes use of complex vague soft expert set theory to study the construction quality and reliability. By the operational relationship and quantitative evaluation index, the membership functions of each subset are obtained, and different evaluation intervals are divided, it is helpful to draw the quantitative evaluation results of quality within a reasonable range and improve the accuracy of the quality and reliability. The presented hybrid method and detailed steps can provide some references for the reliability evaluation of construction quality.

KEYWORDS

Engineering, Vague soft expert set, Membership function, Reliability, Construction, Quality

INTRODUCTION

Under the changeable market competition environment, for the sustainable development of the construction industry, quality control is a crucial process. Since the construction phase is an important part of the whole process, the quality of this phase will directly affect the entire process. To ensure the quality of this stage, the construction industry can better achieve high quality goals. As the construction quality of construction projects affects the economic development and social harmony, it is necessary to evaluate the quality of the construction process. Construction quality is often affected by staff, materials, technical means and other multi-dimensional interference factors. Among the many factors that affect construction quality, some of them have a certain direct or indirect impact on the construction quality assessment results due to their own certain ambiguity, even have the loss of "reliability and validity" of the evaluation work, these factors are also known as fuzzy factors. In reality, because there are some objectively ambiguous factors in each project, the application of these factors in construction quality evaluation standards will affect quality supervision and evaluation. Therefore, it is necessary to deal with interval partitioning of the construction quality from the perspective of fuzzy reliability.

DEFINITIONS OF SOME CONCEPTS AND COMPARATIVE ANALYSIS OF RELATED LITERATURES

The connotation definition and literature analysis about construction or engineering reliability

As a comprehensive discipline involving many fields such as aerospace, nuclear energy, communications, and civilian industry, the reliability theory has achieved fruitful influence not only in electronics, instruments, but also in strengthening the defence forces, and this theory is also widely used in management science in recent years.

In the field of construction or engineering field, more and more scholars apply reliability theory to the construction and make a concrete study. Zhang [1] proposed a comprehensive system identification and reliability assessment framework for stochastic building structures. Through the combination of system identification method based on statistical moment and reliability assessment method based on the probability density evolution equation to respectively evaluate random component reliability and system reliability of a structure. Skrzypczak [2] adopted the methods of simulation FORM and SORM and Monte Carlo simulation to calculate the structural reliability index and the probability of failure so as to ensure the rules and requirements of structural safety, practicability and durability. Lehky [3] solved the problem of reliability design by using artificial neural networks and two-cycle optimization methods, then used the method in steel structures and steel plates. With the development of structural reliability, construction reliability has drawn increasing attention in recent years. Simanaviciene [4] supplemented the previously proposed multi-attribute decision-making synthesis method with the sensitivity analysis of decision making and improved the reliability of the method to determine the reliability of construction decision-making, thus improving the structure, technology and safety of the building Decision-making level. Saputra [5] measured the reliability of a project with time and cost by considering the uncertainty of resource availability, and used the Monte Carlo model to provide a technical solution to this type of problem. Bernardino [6] presented a computational tool that aims to help practitioners to design material-efficient structures for multi-storey buildings frames. The tool is based on an optimization framework, which – given a small set of input parameters defining the overall frame geometry and the system of loadings – seeks for optimized cross-sections for each structural member, based on a finite set of commercially available section profiles.

Professor Cong [7] first conducted a series of collations on the research results of engineering structural reliability and summarized them. Until now, the research and application of reliability in the field of project construction management are still under exploration, and the definition of the reliability of construction system in China is also very vague. Although the construction reliability has not yet come to a clear concept, along with numerous engineering quality problems, technical problems of construction and production and management problems in the construction process, the focus of construction reliability has gradually been paid attention by many scholars.

Reliability engineering and theory have been popularized and applied in many fields. However, based on the system reliability, there are only some research results on the reliability of the construction system of construction project. The theory and research on the reliability of the construction system in engineering project are relatively new topic.

Reliability means the ability to perform a specific function under a limited set of conditions [8]. Therefore, Yufang [9] defined the reliability of construction system. Ning [10] proposed that the construction system reliability is the reliability of the total construction system formed by the combination of duration reliability, quality reliability, cost reliability and safety reliability. As the three major objectives of project management are the duration, cost, quality. People use time to measure the duration, use cost money to measure cost, but there is no effective measure of quality. In the current literature, there are many papers studying engineering projects and reliability issues

from a single point of view, such as quality and duration [11, 12]. For example, Shijing [11] regarded a construction project as a complex construction network system and used a network system optimization theory to optimize the project duration cost. From a double perspective, there are also literatures on engineering projects and reliability studies [13, 14]. By establishing a multi-objective genetic algorithm model, Yongbo [14] made a series of optimization on the duration and cost objectives and obtained the optimal Decision-making program. In addition, Wei [15] used ant colony algorithm based on the three major goals of project management to optimize the project's system reliability.

Simanaviciene [16] offered a new method for multiple attribute decision synthesis, SyMAD-3, which helps to choose an effective construction project alternative from multiple alternatives by assessing various construction, technological and occupational safety solutions, based on a set of quantitative attributes; and supplemented the SyMAD-3 method with decision sensitivity analysis (SyMAD-3 with SA) to improve the reliability of the SyMAD-3 method and assess the reliability of the obtained decision. Nosenko [17] carried out the forecast based on the known regularities of change in the reliability of analogs and prototypes of the investigated modules and their elements. The units and parts of modules limiting reliability are used for the assessment of reliability. Alfred [18] developed a method to determine the influence of time-independent variables on the development of failure probability over time. This method can be also used to evaluate target reliability indices of other civil and geotechnical structures.

The definition and literatures of construction quality and reliability

Because of there are many uncertain factors in quality risk, and the complexity of the risk theory, analysis far exceeds schedule and cost risk, this paper focuses on the study of quality reliability. Evaluating the reliability of construction quality of the project is the coordination between reliability and quality. There is relatively little literature on reliability issues from a single quality objective.

Tao [19] established SRO model of system reliability optimization, first determine the reliability of structural functions, and then use Levenberg-Marquard global optimization method to optimize project construction quality and improve the quality of project performance; Tiejun [20] defined the reliability of construction quality and pointed out that the quality reliability is the degree of reliability of the construction system in achieving its quality objectives. Ning [21] established the construction process reliability model using entropy method, and finally calculated the quality, reliability of each subsystem, the construction process of the three goals can be quantitatively managed. Liqiong [22] continued to propose the OBDD method and applies it to the assessment system of construction quality reliability. It is concluded that this method is suitable for the conclusion of large-scale construction projects. Acikara [23] determined the attitudes of construction project participants towards quality management. For this purpose, a questionnaire was administered to 120 participants of construction projects in Turkey. Rekleiti [24] focused on studying the validity and reliability of the Greek edition of DQOL-BCI. DQOL-BCI includes 15 questions-elements that are evaluated on a 5-grade scale like Likert and two general form-shapes. Bright [25] evaluated the usefulness of OpenStreetMap [OSM] data for researching the spatial availability of alcohol, a field which has been hampered by data access difficulties; they showed how OSM quality metrics can be used to select areas with more complete alcohol data. The ease of access and use may create opportunities for analysts and researchers seeking to understand broad patterns of alcohol availability.

THE EVALUATION INDEX SYSTEMS ON THE CONSTRUCTION QUALITY

In this paper, we refer to 124 engineering quality accidents related to the Ministry of Housing and Urban-Rural Development, reference [26, 27], online materials and media materials from 2012 to the first half of 2017. Based on the experts' opinions in the quality field and considering the

scientific nature of each factor, the accident statistics and classified data analysis. After analysing, according to the construction staff experience, construction technology, structural design and analysis, reasonable degree of material selection, construction accuracy and the quality of inspectors and other fuzzy factors, accidents are divided into the following categories: collapse, cracking, settlement, leakage, hollowing, shedding, elevator failures and accidents, construction electricity failures and accidents, bearing capacity decline and others, a total of 43 kinds of influencing factors.

The construction quality evaluation model

These factors are interrelated. In order to accurately grasp the fuzzy factors that affect the construction quality of the project, made on-site investigation of 12 construction projects under Shanjian, Zhongtian, Guangsha, Changfeng and Changye, obtained 43 kinds of factors weight situation, identified and processed the data to obtain the quality evaluation model. Each project had 20 quality questionnaires, the questionnaire was issued for more than three years relevant work experience of the construction workers, technicians and supervisors, the questionnaire method is to use Likert5 scale fuzzy evaluation method. A total of 178 valid questionnaires were collected, with an effective rate of 74.2%. The study used SPSS17.0 to test the overall reliability of the sample.

Screening key influencing factors

Genetic algorithms (GA) are used to screen the fuzzy factors that affect construction quality because of the large amount of data that can be processed by this method. By the questionnaire method, 43 scores of influencing factors were collected. The chromosome length was set as 43, the gene on each chromosome was set as 0 or 1, and the gene was 1 if the gene was involved in construction and 0 otherwise. When running GA, select the fitness function:

$$f(x) = \frac{1}{\sum_{i=1}^n (t'_i - t_i)^2} \quad (1)$$

Where: $T = \{t_1, t_2, \dots, t_n\}$ is the true value of the data; $T' = \{t'_1, t'_2, \dots, t'_n\}$ is the predicted value of the collected data; "n" is the number of samples. Select the proportion operator as:

$$P_k = \frac{f(x_k)}{\sum_{k=1}^n f(x_k)} \quad (2)$$

Where P_k is the various factors that affect the proportion of fitness; $f(x_k)$ is the various factors of fitness. After using Matlab to run the program, get blurred fuzzy influencing factors as Table 1:

Tab. 1 - The project quality accident classification and statistics

| Target layer | Phenomenon layer | Factor layer | Frequency |
|-------------------------------------|---|--|-----------|
| Construction Quality Evaluation (A) | Collapse (B ₁) | Formwork support system (C ₁), Earthwork, foundation pit and fence (C ₂), Steel truss (C ₃), Scaffolding (C ₄) | 33.9% |
| | Cracking (B ₂) | Wall (C ₅), Body Structure (C ₆), Floor and Foundation (C ₇) | 43.5% |
| | Settlement (B ₃) | Wall cracks (C ₈), Wall water seepage and perfusion (C ₉), Ground subsidence and Slide (C ₁₀), Building inclination (C ₁₁) | 22.6% |
| | Leakage (B ₄) | Wall seepage (C ₁₂), Roof seepage (C ₁₃), Ground seepage (C ₁₄), Pipeline seepage (C ₁₅) | 9.7% |
| | Emptying (B ₅) | Wall hollowing (C ₁₆), Ground and ceiling decoration hollowing (C ₁₇) | 8.9% |
| | Lost (B ₆) | Beam column structure, shedding (C ₁₈), Inside and outside the wall off (C ₁₉) | 6.5% |
| | Elevator Accident (B ₇) | Steel cord breakage (C ₂₀), Improper use and maintenance (C ₂₁) | 9.7% |
| | Construction Electricity Accident (B ₈) | Electrical Equipment (C ₂₂), Fault Line Leakage (C ₂₃), Improper Use and Maintenance (C ₂₄) | 7.2% |
| | | | |
| | Bearing Capacity Decrease (B ₉) | Column bearing capacity decreased (C ₂₅), Beam capacity decreased (C ₂₆) | 8.6% |
| Others (B ₁₀) | Fire (C ₂₇), Explosion (C ₂₈) | 6.8% | |

Equalized and normalized the probability distribution of each kind of accident phenomenon [28], using the formula:

$$y_k = g(x_k) = \sum_{i=0}^k \frac{n_i}{N} = \sum_{i=0}^k h_i, k = 0, 1, \dots, L-1 \quad (3)$$

The new probability is:

Tab. 2 - Project quality accident (B) statistical table

| Accident | Phenomenon layer B | | | | | | | | | |
|-----------|--------------------|----------------|----------------|----------------|----------------|----------------|----------------|----------------|----------------|-----------------|
| | B ₁ | B ₂ | B ₃ | B ₄ | B ₅ | B ₆ | B ₇ | B ₈ | B ₉ | B ₁₀ |
| Frequency | 21.5% | 27.6% | 14.3% | 6.2% | 5.7% | 4.1% | 6.2% | 4.6% | 5.4% | 4.4% |

It can be seen from the Table 2 that the collapsing, cracking and settling caused by the fuzzy factors is frequent quality accidents with the probability of 21.5%, 27.6% and 14.3% respectively.

The above accidents not only affect the quality and appearance of buildings, but also affect the personal and property safety. Therefore, the construction quality of construction projects has become a particularly important issue. Controlling the quality of construction not only can reduce the number of casualties of construction workers, but also can reduce the economic losses caused by construction quality problems.

THE PROPOSED HYBRID METHOD

The evaluation interval based on vague soft expert set hybrid method for quality reliability

As the previous methods evaluating the construction quality are more subtle and subjective, the quality is judged based on the management experience of the management staff, so there is a lack of objectivity. The introduction of quality and reliability can effectively solve this problem. Using fuzzy linguistic variables as a measure to measure the degree of quality, reliability and calling it "degree", we use fuzzy language operators to make a scientific assessment of construction quality management and make a reasonable division of construction quality reliability, then come to its evaluation interval, make a more scientific and accurate project quality conditions.

The language operator is used to divide the construction quality, reliability into different basic fuzzy subsets, and combine these subsets with vague soft expert sets. By using the Vague set evaluation index system, different membership functions of vague soft expert sets about construction quality, reliability are established, and can solve the membership function to get the range of different subsets. Vague soft expert sets represent a certain extent, so calculated results are more intuitive and accurate.

The fuzzy language variables

Professor Zadeh proposed fuzzy set theory in 1965 and marked the birth of fuzzy mathematics [29]. From then on, fuzzy set theory was promoted in many fields. Fuzzy theory uses the single-valued membership function to represent "a certain degree of belonging", but this theory cannot represent neutral evidence and therefore has obvious drawbacks [30]. Gaussian and Burchere [31] proposed the vague soft expert sets in 1993 and used this fuzzy theory to deal with fuzzy information. Bustince [32] recapitulate the definition given by Atanassov (1983) of intuitionist fuzzy sets as well as the definition of vague sets given by Gau and Byehrer (1993) and see that both definitions coincide.

Javier Gutiérrez_García [33] demonstrates two meta-mathematical propositions concerning the increasingly popular "intuitionistic" (= vague) approaches to fuzzy sets and fuzzy topology, as well as the closely related interval-valued (= grey) sets and interval-valued "intuitionistic" sets: (1) the term "intuitionistic" in these contexts is historically inappropriate given the standard mathematical usage of "intuitionistic"; and (2), at every level of existence—powerset level, topo-logical fibre level,

categorical level—interval-valued sets, interval-valued "intuitionistic" sets, and "intuitionistic" fuzzy sets and fuzzy topologies are redundant and represent unnecessarily complicated, strictly special subcases of standard fixed-basis set theory and topology. This theory applies the membership function to solve the traditional fuzzy set of defects. The degree of subordination is used by the expression method of interval, so it expresses the relation of "belonging to within a certain interval", and can deal with the fuzzy information that Fuzzy Sets cannot achieve. In this paper, the fuzzy mathematical theory is used to study the reliability of construction quality. Vague soft expert sets and language operators are used to determine the membership functions, and finally the evaluation interval is divided.

As a new subject, fuzzy mathematics has achieved good results in many fields, such as fault diagnosis and decision-making. In real life, many things cannot be described in precise language, which requires using vague language in fuzzy mathematics. Fuzzy mathematics has broad prospects of economic development, business management and so on. For example, customers evaluate a service, can use the "good service", "poor service" and other vague terms, and cannot use accurate values to express the value of this service. In the quality evaluation process, you cannot use the exact value to evaluate the quality of good, but instead of fuzzy language variable assessment instead of accurate evaluation.

A vague linguistic variable is represented by a five-tuple^[34] $(X, T(X), U, G, M)$. "X" is the language variable name. " $T(X)$ " is a collection of X's language values. "U" is the domain. "G" is the grammars' rule that produces "X". "M" is a semantic rule.

The division evaluation interval of Fuzzy language operator

In natural language, there are still some words that play a role in modification. For example, "very", "slightly".... putting these words in front of a word changes the affirmation of the meaning of the word and turns the original word into a new word. Therefore, we regard these kinds of words as an operator, respectively, as a language operator.

The language operator is defined as a mapping $H_\lambda: F(U) \rightarrow F(U)$ ($\lambda > 0$). H_λ transforms the fuzzy set "on U" into a fuzzy set $H_\lambda A$. The relationship between the two is: $(H_\lambda A)(U) = [A(u)]^\lambda$.

When $\lambda > 1$, H_λ is called the centralization operator; when $\lambda < 1$, is called a diffusive operator and can be properly named, for example: $H_2 =$ "Very", $H_{\frac{1}{2}} =$ "Pole", $H_{\frac{1}{4}} =$ "micro"^[34].

Here we use the language operator to evaluate the construction quality, reliability and divide it into six basic fuzzy subsets: V_1 is very reliable, V_2 is reliable, V_3 is slightly reliable, V_4 is slightly unreliable, V_5 is unreliable, and V_6 is very unreliable.

Vague soft expert sets and membership function

Vague soft expert sets

Definition ^[35]: Let the domain $X = \{x_1, x_2, \dots, x_n\}$ and x_1, x_2, \dots, x_n belong to "X". A vague set "A" in "X" is described by the true membership function t_A , and the pseudo membership function f_A , which are denoted by $t_A: X \rightarrow [0,1]$ and $f_A: X \rightarrow [0,1]$ respectively. For $x \in X$, $t_A(x)$ is the lower bound of the affirmative membership of "x" determined by support, $f_A(x)$ is the lower bound of the negative membership of "x" determined by the opposition "x", and $1 - f_A$ represents the upper bound, and $t_A(x) + f_A(x) \leq 1$. Then the solution of the membership function of "x" with respect to A is denoted $[t_A(x), 1 - f_A(x)]$, expresses this interval as the vague value of "x" in "A", denoted as $v_A(x)$.
 "x" unknown degree of "A": $0 \leq \pi_A(x) = 1 - t_A(x) - f_A(x) \leq 1$.

When $\pi_A(x) = 1 - t_A(x) - f_A(x) = 0$, "A" degenerates into a general fuzzy set of "X". Therefore, vague soft expert sets can be regarded as a complement to Fuzzy sets. For example: if $[t_A(x), 1 - f_A(x)] = [0.1, 0.9]$. This result can be interpreted as follows: "U" belongs to the Vague set "A" is 0.1, not to "A" is 0.1, hesitation is 0.8.

When "X" is a continuous set, the Vague set "A" in "X" can be written as $A = \int_X [t_A(x), 1 - f_A(x)] / x$. When "X" is a discrete set, recorded as $A = \sum_{i=1}^n [t_A(x_i), 1 - f_A(x_i)] / x_i$

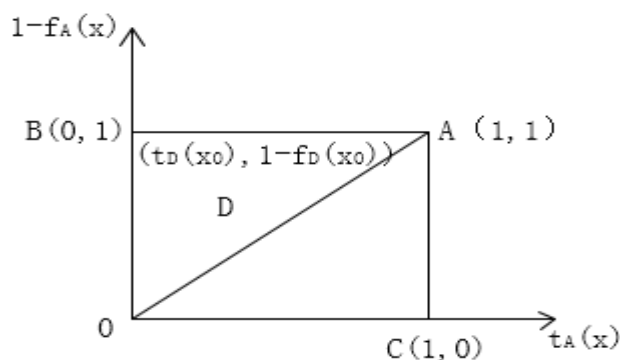


Fig. 1 - The geometric meaning of vague set

Determine the membership function

Before making a comprehensive evaluation, determine the value of each parameter "X" evaluation, that membership. The fuzzy set of membership degree is expressed by membership function.

The steps to determine the membership function are shown as below:

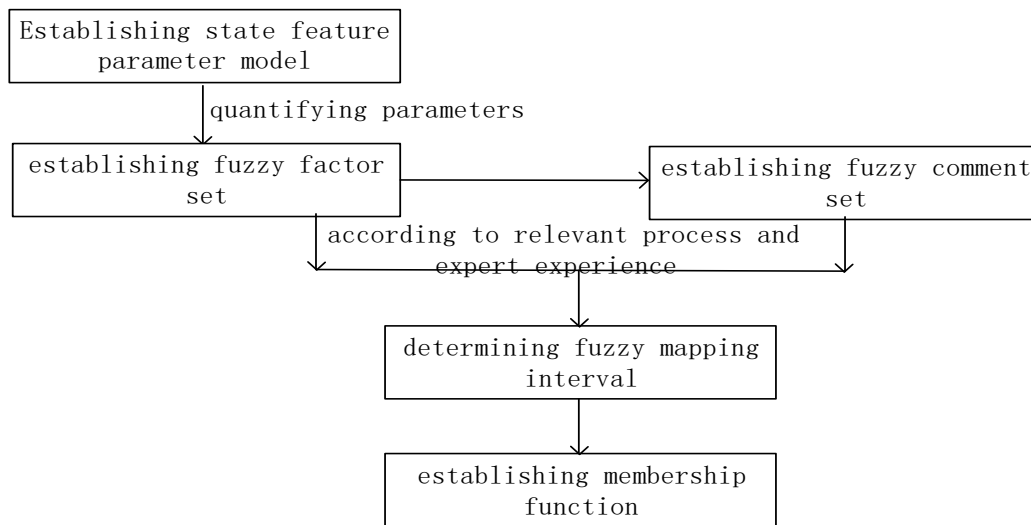


Fig. 2 - Membership functions determination model

This article evaluates the reliability of construction quality in a construction project and adopts such vague language as "very reliable", "reliable", "slightly reliable", "slightly unreliable", "unreliable", "very unreliable", and so on. As can be seen from the above vague language, the higher the reliability of the better, so the use of the larger the more excellent evaluation index; the lower the degree of unreliability is better, so the smaller the more superior type evaluation index ^[36].

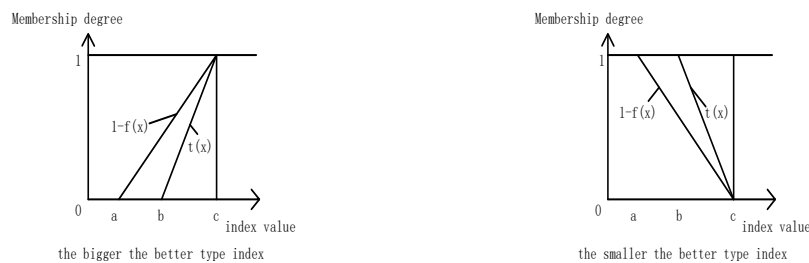


Fig 3 - Vague soft expert set membership function graph

For the bigger and better evaluation index, the Vague set membership function can be expressed as:

$$V = [t(x), 1 - f(x)] = \begin{cases} [0, 0] & x < a \\ [0, \frac{x-a}{c-a}] & a \leq x < b \\ [\frac{x-b}{c-b}, \frac{x-a}{c-a}] & b \leq x < c \\ [1, 1] & c \leq x \end{cases} \quad (4)$$

Contrary to the above evaluation index, the smaller the more superior evaluation index, Vague set membership function can be expressed as:

$$V = [t(x), 1 - f(x)] = \begin{cases} [1, 1] & x < a \\ \left[\frac{c-x}{c-a}, 1\right] & a \leq x < b \\ \left[\frac{c-x}{c-a}, \frac{c-x}{c-b}\right] & b \leq x < c \\ [0, 0] & c \leq x \end{cases} \quad (5)$$

The membership functions of the defined six vague soft expert sets are expressed respectively by $V_1(X)$, $V_2(X)$, $V_3(X)$, $V_4(X)$, $V_5(X)$, $V_6(X)$. The definition of fuzzy language operator can be respectively derived membership function of six vague soft expert sets:

$$[\text{Very reliable}]V_1(x) = \begin{cases} [0, 0] & x < a \\ \left[0, \frac{2(x-a)}{1-a}\right] & a \leq x < \frac{1+a}{2} \\ [1, 1] & \frac{1+a}{2} \leq x \end{cases} \quad (6)$$

$$[\text{Reliable}]V_2(x) = \begin{cases} [0, 0] & x < a \\ \left[0, \frac{x-a}{0.563-0.563a}\right] & a \leq x < \frac{1+a}{2} \\ \left[\frac{x-0.5(1+a)}{0.063-0.063a}, \frac{x-a}{0.563-0.563a}\right] & \frac{1+a}{2} \leq x < 0.563+0.437a \\ [1, 1] & 0.563+0.437a \leq x \end{cases} \quad (7)$$

$$[\text{Slightly reliable}]V_3(x) = \begin{cases} [0, 0] & x < a \\ \left[0, \frac{2(x-a)}{1-a}\right] & a \leq x < 0.437+0.563a \\ \left[\frac{x-0.437-0.563a}{0.063-0.063a}, \frac{2(x-a)}{1-a}\right] & 0.437+0.563a \leq x < \frac{1+a}{2} \\ [1, 1] & \frac{1+a}{2} \leq x \end{cases} \quad (8)$$

$$[\text{Slightly unreliable}]V_4(x) = \begin{cases} [1, 1] & x < \frac{1-a}{2} \\ \left[\frac{2(1-x-a)}{1-a}, 1\right] & \frac{1-a}{2} \leq x < 0.563(1-a) \\ \left[\frac{2(1-x-a)}{1-a}, \frac{1-x-a}{0.437-0.437a}\right] & 0.563(1-a) \leq x < 1-a \\ [0, 0] & 1-a \leq x \end{cases} \quad (9)$$

$$[Unreliable]V_5(x) = \begin{cases} [1,1] & x < 0.437(1-a) \\ \left[\frac{1-x-a}{0.563-0.563a}, 1\right] & 0.437(1-a) \leq x < \frac{1-a}{2} \\ \left[\frac{1-x-a}{0.563-0.563a}, \frac{2(1-x-a)}{1-a}\right] & \frac{1-a}{2} \leq x < 1-a \\ [0,0] & 1-a \leq x \end{cases} \quad (10)$$

$$[Very\ unreliable]V_6(x) = \begin{cases} [1,1] & x < \frac{1-a}{2} \\ \left[\frac{2(1-x-a)}{1-a}, 1\right] & \frac{1-a}{2} \leq x < 1-a \\ [0,0] & 1-a \leq x \end{cases} \quad (11)$$

According to the above six Vague set membership function, using Matlab to make interval map, as shown below.

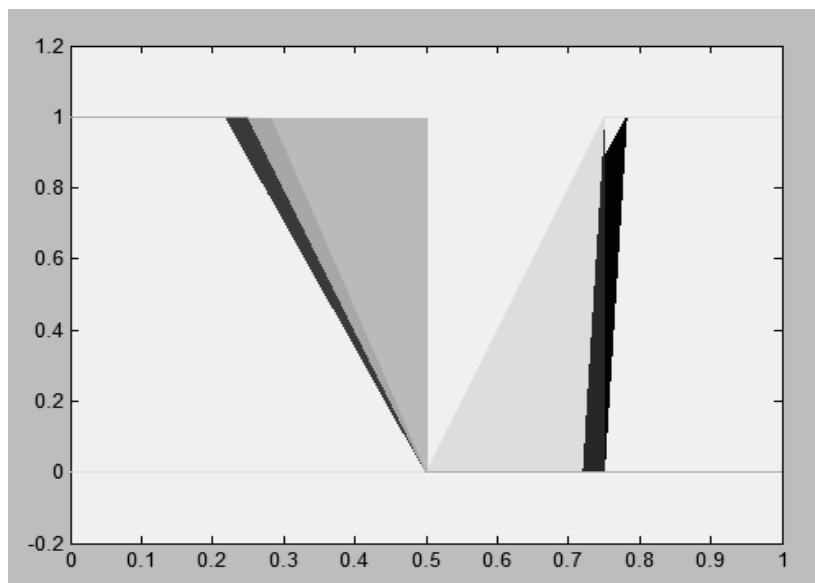


Fig 4 - Membership function interval diagram

The range of reliability is between [0, 1], and each membership function corresponds to one graph. According to the principle of maximum membership, the value range corresponding to the x-axis can be judged as the reliability value of each fuzzy language.

The solution of the membership function interval

Because each membership function is a piecewise function, and for each function, the interval is not the same according to the range of values of “x”, so each function is expressed in terms of surface. As can be seen from the functional formula, the value of the parameter “a” determines the division of the evaluation interval. Different items, “a” value is different. Therefore, when using this model in actual projects in different regions, we should make statistics on the projects in the area in advance and select the representative projects to determine the reasonable value of “a”.

CASE ANALYSIS

Project background

Taking Galaxy Center 1 # building project as an example, it is located south of the junction of Chaoyang Road and Shengli Road in Bengbu City, south of China Life Insurance Building. Design from the ground floor and underground space development. The project covers an area of 10683.63 square meters. 27 floors above ground, 1 underground, with a total construction area of 43489.43 square meters, of which construction area of 37,950 square meters on the ground floor, underground building area of 5539.43. On the ground 1-4 for commercial development, 5-27 layers for the office area, the ground floor of the parking lot.

The reliability rating of construction quality

Due to the technical complexity of the project, large scale and long construction period, developers hope that the data quality can be used to judge the construction quality of the project. Therefore, the interval value of the reliability of construction quality is calculated to ensure the successful completion of the project. Through the statistical analysis of the most representative engineering data in the city, the value of “a” is determined to be 0.5.

Tab.3: Construction quality, reliability evaluation interval

| Vague language | Grade | Range | Degree of hesitation |
|---------------------|-------|---------------|----------------------|
| Very reliable | VG | [0.75,1] | 0.25 |
| reliable | G | [0.7186,0.75] | 0.0314 |
| Slightly reliable | FG | [0.5,0.7186] | 0.2186 |
| Medium reliable | M | [0.5,0.5] | 0 |
| Slightly unreliable | FP | [0.2814,0.5] | 0.2186 |
| Unreliable | P | [0.25,0.2814] | 0.0314 |
| Very unreliable | VP | [0,0.25] | 0.25 |

In this paper, the Fuzzy set calculation method is used in the previous literature ^[29], and a new interval evaluation method based on vague soft expert sets is proposed. The difference between the two is that fuzzy membership is represented by a single value, and the six membership functions are respectively calculated to obtain the final degree of membership. The vague membership is expressed in intervals, and each membership function corresponds to an interval, the range belongs to [0, 1], the result is more intuitive. Vague set theory can use the support degree, opposition degree, the hesitation degree to represent the work information of the object; fuzzy set cannot express hesitation degree information. In contrast, vague soft expert sets are simpler and the expression of fuzzy information is more accurate.

CONCLUSIONS

In order to make up for the drawback of traditional construction, reliability methods, this paper established a quantitative evaluation model of quality, reliability based on Vague set and fuzzy language operator, and reached the following conclusions:

(1) With the appearance of numerous quality accidents every year, quality problems has become a problem that cannot be ignored. Therefore, the reliability of single index quality is studied from construction reliability.

(2) This paper made the interval partitioning of reliability of construction quality based on the fuzzy language operator. The membership functions of the six vague subsets are derived based on the relations among the language operators, as well as the larger and more superior indexes and the smaller one. The result of the final evaluation interval is affected by the value of “a”, because of different projects, “a” value is also different, so the quality of different projects reliability evaluation interval is different

ACKNOWLEDGEMENTS

This work was supported in part by National Natural Science Foundation of China (NSFC)(E042205), Shanxi Province Education Department Research Project (15JK1414) and Shanxi Province Natural Science Basic Foundation (2016JM5088).

REFERENCES

- [1] Zhang J, Xu Y L, Li J. Integrated system identification and reliability evaluation of stochastic building structures. *Probabilistic Engineering Mechanics*, 2011, 26(4):528-538.
- [2] Skrzypczak I, Słowik M, Buda-Ożóg L. The Application of Reliability Analysis in Engineering Practice – Reinforced Concrete Foundation. *Procedia Engineering*, 2017, 193:144-151.
- [3] D. Lehky, O. Slowik, D. Novak. Reliability-based design: Artificial neural networks and double-loop reliability-based optimization approaches. *Advances in Engineering Software*, 2017:136-147.
- [4] Simanaviciene R, Liaudanskiene R, Ustinovichius L. Assessing reliability of design, construction, and safety related decisions. *Automation in Construction*, 2014, 39(4):47-58.
- [5] Saputra Y A, Latiffianti E. Project Reliability Model Considering Time – Cost – Resource Relationship under Uncertainty. *Procedia Computer Science*, 2015, 72:561-568.
- [6] Bernardino D’Amico , F Pomponi. Accuracy and reliability: A computational tool to minimise steel mass and carbon emissions at early-stage structural design. *Energy & Buildings*, 2018:236–250
- [7] Dong Cong. System structure, reliability theory: progress and review. *Engineering Mechanics*, 2001, (04): 79-88 + 59.
- [8] Mei Qizhi, Liao Jiongsheng, Sun Huizhong. *System Reliability Engineering Foundation*. Beijing: Science Press, 1992.
- [9] Shi Yufang, Li Huimin, Lu Ning. Research on construction system reliability and calculation method of engineering project. *Journal of Xi'an University of Architecture & Technology*, 2011, (01):125-130.
- [10] Lu Ning, Feng Yanping, Wang Fang. Integrated Reliability Control of Four Objectives of Unit Engineering. *Journal of Xi'an University of Architecture & Technology*, 2007, 39(5):652-656.
- [11] Zhou Shijing, Zhao Dan, Li Yongji. Cost Optimization of Construction Project Based on Ant Colony Algorithm. *Construction Technology*, 2015, (18):86-89.
- [12] Shi Yufang, Xie Yanping, Lu Lu. Research on reliability prediction of construction period of mining engineering. *Journal of Xi'an University of Science and Technology*, 2011, (05):593-597.
- [13] Li Xusheng, Shi Chaofeng, Chen Xin. Optimization framework of urbanization construction project investment under risk perspective. *World Science and Technology Research and*

Development,2013,(05):644-646 + 655.

- [14] Yuan Yongbo,Ruan Hongbo,Wang Xingkai.Comprehensive optimization of project construction cost based on genetic algorithm.Journal of Sichuan Building Science Research, 2008,(03):227-230.
- [15] Tian Wei,Liu Wenhan.Construction cost control based on system reliability optimization.Liaoning Building Materials,2009,(04):56-58.
- [16] Ruta Simanaviciene, Rita Liaudanskiene, Leonas Ustinovichius. Assessing reliability of design, construction, and safety related decisions. Automation in construction, 2014, 39(1): 47-58.
- [17] A. Nosenko, A. Domnitskiy, E. Shemshura. Predictive Reliability Assessment of Loading and Transport Modules of Tunneling Equipment during Construction of Road Tunnels. Procedia Engineering, 2017, 206:1661-1666
- [18] Roubos A A, Steenbergen R D J M, Schweckendiek T, et al. Risk-based target reliability indices for quay walls[J]. Structural Safety, 2018, 75:89-109.
- [19] Tao R, Tam C M. System reliability optimization model for construction projects via system reliability theory[J]. Automation in Construction, 2012, 22(4):340-347.
- [20] Deng Tiejun.Structural engineering construction system reliability theory and its application.Changsha: Hunan University, 2007.
- [21] Lu Ning,Shi Yufang, Gao Xiangqiang, Li Weihong, Liao Xianghui.A Method to Determine the Reliability of Construction Process Subsystem.Journal of Xi'an University of Architecture & Technology (Natural Science Edition),2006,(03):311-315 +320.
- [22] Yang Liqiong,LI Shirong,XU Bo.Establishment of construction system in large-scale engineering projects.Journal of Chongqing University (Social Sciences Edition),2012,(05): 64-69.
- [23] Turgut Acikara, Aynur Kazaz, Serdar Ulubeyli. Evaluations of Construction Project Participants' Attitudes toward Quality Management in Turkey. rocedia Engineering, 2017, 196: 203-210.
- [24] Maria Rekleiti, Kyriakos Souliotis, Pavlos Sarafis, Ioannis Kyriazis, Maria Tsironi. Measuring the reliability and validity of the Greek edition of the Diabetes Quality of Life Brief Clinical Inventory. Diabetes Research and Clinical Practice, 2018, 140:61-71.
- [25] Jonathan Bright, Stefano De Sabbata, Sumin Lee, Bharath Ganesh. OpenStreetMap data for alcohol research: Reliability assessment and quality indicators Health & Place, 2018,50:130-136.
- [26] Pan Wei. Status and causes of construction quality accidents based on case analysis. Engineering Quality, 2012, 30 (04): 28-31.
- [27] Sun Huifen. Analysis of China's housing construction quality of the causes and countermeasures. Manager, 2015, (20): 314.
- [28] Liang Guangming, Tang Yupeng, Sun Shixiang. Normalization Algorithm based on probability distribution equalization and its application in pattern recognition. Signal Processing, 2009, 25 (04): 636-638.
- [29] Zadch L A.Fuzzy sets.Internation and control,1965,8(3):338-353.
- [30] Lin Zhigui, Xu Li, Liu Yingping.Vague set theory and its application in fuzzy information processing.Journal of Information and Control,2005,(01):54-59.
- [31] Gau W L,Buehrer D J.Vague sets. IEEE Transactions on Systems, Man, and Cybernetics, 1993, 23 (2): 610-614.
- [32] Bustince, Burillo. Vague sets are intuitionistic fuzzy sets. Fuzzy Sets & Systems, 1996, 79(3):403-405.
- [33] J. Gutiérrez García, S.E. Rodabaugh. Order-theoretic, topological, categorical redundancies of interval-valued sets, grey sets, vague sets, interval-valued "intuitionistic" sets, "intuitionistic" fuzzy sets and topologies. Fuzzy Sets & Systems, 2005, 156(3):445-484.
- [34] Li Qian,Mu Mu, JI Xiaoning.Risk Decision Analysis of Aviation Project Development Based on Fuzzy Linguistic Variables.Aviation Science and Technology, 2009, (02):10-13.
- [35] Liu Lin,Cao Yanping,Wang Ting,Li Juanfei.Fuzzy Mathematics.Second Edition.Shanxi: Shanxi Science and Technology Press,2008:156-157.
- [36] Shi Yufang,Wang Xiufen,Kang X.Evaluation of Construction Project Reliability Based on Fuzzy Language Operators.Journal of Xi'an University of Architecture & Technology,2015,47 (05):740-744 .

HISTORICAL ORTHOPHOTOS CREATED ON BASE OF SINGLE PHOTOS - SPECIFICS OF PROCESSING

Jindřich Hodač, Anna Zemánková

*Czech Technical University in Prague, Faculty of Civil Engineering, Department of Geomatics, Prague, Thákurova 7, Prague 6 - Dejvice, Czech Republic;
hodac@fsv.cvut.cz*

ABSTRACT

This article focuses on problematics of creating digital orthophotos using historical aerial photos. The project is part of a grant project that deals with change in rural architecture over the last two centuries. The orthophotos are one of the outputs created in the grant project and illustratively represent development of the selected villages over the last 80 years. In addition to orthophotos other outputs such as analytical map data (development of selected villages since the years around 1830 till present) are created. The article describes the current state of orthophoto creation and also difficulties that might be encountered at processing of historical photos. The specificity of this project is in small areas (primarily built-up areas of selected villages) that are processed. Such an area is usually captured only in one or two photos, which significantly affects the way of the photogrammetric processing. The project involves three preselected villages. Orthophotos are created for each of them in three terms (approximately 1938 + 1970 + 1985) and this chronological order is amended with purchased data for the year 1953 and the present. The time series of orthophotos, together with other inputs, bring better understanding to the development of rural settlements in the context of socio-historical events – e.g. Second World War, socialist expropriation, collectivization, agricultural large-scale production, changes in ownership after 1989 etc.

KEYWORDS

Historical aerial photo, Historical orthophoto, Photogrammetric technologies, Rural transformations, Multitemporal analysis

INTRODUCTION

Orthophotos have been a major product of aerial photogrammetry for many years and they are widely used not only in GIS applications. The speed of their processing and the quality of the outputs have increased with the arrival of digital cameras, as well as the availability of orthophotos capturing the most current state of a particular area.

Historical aerial photos - sources

In addition to current image data, historical aerial photos (HAP) can also be used for various purposes. In the former Czechoslovakia, the systematic aerial photography began in 1935 on the territory of Slovakia, as Nociarová mentions in [1]. The HAP for the Czech Republic has been managed by the Military Geographic and Hydrometeorological Authority (in Czech: Vojenský geografický a hydrometeorologický úřad - VGHMU) in Dobruška. Their archive contains about

900,000 photos which have been stored since 1936, as reported by Stehlík [2]. The gradual digitization of the archive is currently being carried out in cooperation of the VGHMUr and the Land Survey Office. For viewing, searching for HAP information and ordering, an application Archive of aerial survey photos (in Czech: Archiv leteckých měřických snímků) is available at [3].

This archive is a main source of HAP in the Czech territory. Photos from foreign archives are used only in extraordinary cases. An example of that are archive military reconnaissance aerial photos of Prague taken at the end of the Second World War. With accessing and using these photos for various purposes deals e.g. [4].

The development of aerial photography for reconnaissance purposes, which occurred during the First World War, certainly had an impact in our country. However, the oldest currently known report on aerial photography for measuring purposes is related to the year 1927. At that time the Technical Squadron was established at the 2nd Aviation Regiment in Olomouc and within it the Photographic Section, as stated by Prokeš [5] and Fidler [6]. Former Military Geographic Institute had permanently available one airplane and a trained pilot for aerial photography since 1927, supplemented in 1929 with the equipment for serial photography, as mentioned by Jalůvka [7]. In the spring 1927, a photogrammetric aerial photography of Adamov forestry farm was carried out for the University of Forestry in Brno. This set of photos was retained and recently was processed into an orthophoto by Skoupý [8]. Another valuable ensemble was purchased in that year for the Olomouc municipality by the same provider. These photos were transformed in the form of photoplan by Prokeš [5]. The first documented aerial photography of several archaeological sites dates back to 1929, see Böhm [9]. However, except of the above mentioned valuable findings, most of photos of an older date are difficult to trace, precisely data on them have not been stored in the archive of VGHMUr.

Historical orthophotos and HAP - utilization

The historical orthophotos can be used in many areas. In most of the works mentioned below, they are brought into context with other map and image resources. Thus they form one of the layers of multitemporal analysis.

Observation of landscape changes is one of the areas where historical photos and outputs created from them are applied. Applications in forest management are reported by Skoupý [8] - who describes a creation of thematic forest maps. Other examples are mentioned by Nociarová [1] - she deals, among others, with the issue of property restitution of forest grounds and by Kardoš [10] - who also describes a creation of relevant resources for complex land consolidation projects. With issues in the monitoring of development of the landscape structure in particular cadastral districts deals Jiskrová [11] and a similar topic in a larger territory has been solved by Prchalová [12].

An example of the use of historical photos in geographic research is the work of Chmelová [13], who deals with changes in land use in a given territory, and Stoupa [14] solves also a similar theme.

In built-up areas, historical orthophotos can be used, for example, to explore urban development from various perspectives. This issue is addressed, e.g. by Sádovská [15] in Olomouc city, she uses also the above mentioned HAP from 1927. Most of the large cities in the Czech Republic also publish historical orthophotos from several time periods on their public map servers. The institute of urban planning and development of Prague, among other documents, has published foreign HAP by 1945 (mentioned above) within the project of Two Pragues [16].

Archaeology is another area where HAP finds its use. Šmejda [17] deals with such applicability, for example. An interesting application is also the use of HAP in mapping of poorly

documented drainages constructed in the past, see Šafář [18]. A project that is in scope of the environmental protection was introduced by the Czech Environmental Information Agency [19]. The historical orthophoto of the entire Czech Republic has been created as a basis for the inventory of contaminated sites (orthophoto CENIA – photos primarily from year 1953). For more information about this project see Sukup [20]. The topic of searching for old ecological burdens or localization of unexploded war ammunition using HAP is reported in foreign resources e.g. in [4].

The use of historical aerial photos as one of the resources for exploration and design works is also recommended by methodical publications such as [21], [22] and [23]. Surely we can find other areas where this type of image data finds its use. The user community is also constantly expanding with an improving availability of the image data.

Rural transformations – project objectives

The historical orthophotos are used together with other documents in our project for an art-historical research of the urban development of selected villages. One of the project objectives is to point out neglected historical and art values of rural architecture. These values are often not taken into account when planning urban development. Thirty-nine smaller villages, which are far from the main interest of historical-urban research, have been chosen for the project. These villages are homogeneously distributed throughout the Czech Republic.

Village development analyses are based, besides the historical orthophotos, mainly on the analytical map data (maps of urban changes) and also on 3D digital models and simplified ground plans of rural architecture. The art-historical assessment has been carried out for the whole set of selected villages. However maps and models are created for a third of them only and finally just three villages have been selected for the creation of historical orthophotos. For these villages two orthophotos has already existed - current and historical (see CENIA). Our task was to create three more orthophotos approximately for periods around years: 1938 + 1970 + 1985, with the main emphasis on a built-up area of the villages, and required orthophoto accuracy within 3 m.

The next part of the article deals with creation of historical orthophotos. The data used, the technological process and the achieved outputs are described in more detail. Attention is also paid to the specifics of the approach we used and the difficulties we encountered. It needs to be emphasized that the described project is still in process and also other ways to improve the project outputs will be sought after.

METHODS

Although the general procedure of photogrammetric processing of HAP is more or less standardized, the specific process of a particular project is always strongly influenced by a number of factors. These include e.g. – the quality and number of photos and a knowledge of calibration data; size of the area to be processed and a possibility of finding suitable ground control points in them; the availability of the digital terrain model etc. Features of the processing software need to be mentioned, too. Possible variants of the technological process of a historical orthophoto creation in the context of the input conditions are summarized, for example, by Šafář [18].

Various authors choose a variety of ways of the photogrammetric processing according to the type of assignment, the parameters of required outputs and their technical equipment. In some cases, HAP is used directly, i.e. the HAP is interpreted without further processing. This is used in archaeological applications see Šmejda [17], for example. Simplified processing of HAP into photoplanes using various types of planar geometric transformations is also quite common. This procedure was used by Prokeš [5] or Dědková who took advantage of affine transformation [24].

Sádovská and Stoupa used polynomial transformations of various degrees, see [15], [14]. However, the outputs obtained in these ways have limited geometrical accuracy only (i.e. dozens of meters), as the authors report in their projects. The goal of our project is to obtain outputs with much higher precision. The subsequent text deals with this topic.

Processed territories - basic characteristics

Detailed analysis of the processed area for the photogrammetric processing of HAP is not necessary. However, it is usually advisable to be familiar with its basic parameters. Three selected villages - Hostouň u Prahy (pilot project), Ropice and Držkov have been gradually processed in the project. The basic characteristics of the mentioned villages, which influence the processing, are summarized in Table 1.

Tab. 1 - Processed territories - basic characteristics

| <i>village</i> | Hostouň | Ropice | Držkov |
|--|--------------------|----------------------|--------------------|
| <i>region</i> | Central Bohemia | Moravian-Silesian | Liberec |
| <i>acreage of Cadastral District - CD [km²]</i> | 10,3 | 10,1 | 5,9 |
| <i>average altitude [m]</i> | 341 | 310 | 597 |
| <i>type of relief</i> | flattened | slightly wavy | wavy |
| <i>distribution of forest land in CD [%] *</i> | up to 5 | up to 20 | up to 50 |
| <i>building structure</i> | constricted | diffused | constricted |
| <i>number of houses **</i> | 471 | 488 | 260 |
| <i>development of build up area 1938-2018</i> | dynamic | gradual | little |
| <i>urban area in CD [%] *</i> | up to 20 | up to 60 | up to 20 |
| * author's estimate based on orthophoto 2018 | | | |
| ** data source - Registry of census circuits and buildings .. http://apl.czso.cz/irso4 .. validity to 5.9. 2018 | | | |

Regarding the used technology of processing, the following parameters are of particular importance - the type of the terrain relief, the afforestation of the area, the extent of the built-up area and its development in the monitored periods. The first one is related to the knowledge of the elements of interior orientation (mainly the lens distortion) and the other mentioned are foremost related to the availability of sufficient number of appropriately positioned ground control points.

Input data

The following input data were acquired in order to elaborate our project of creating historical orthophotos of the selected villages in three time periods: HAP, current digital terrain model, current cadastral map, current orthophoto and historical orthophoto CENIA.

Historical aerial photos

Key data for further processing are HAP from the archive of VGHMUr. These photos were selected within an application [3]. The pilot part of the project was the processing of the village of Hostouň, where stereo pairs were ordered from the archive for testing of the technological process. Regarding the results obtained (see below), the demand for stereo pairs was not further applied. Altogether fourteen photos were finally ordered and their basic parameters are reported in Table 2.

Tab. 2 - Historical aerial photos - basic parameters

| village | YOR | NOI | f [mm] | FS [cm] | h [km] | S | DAOV [°] | NFM |
|---------|------|-----|--------|---------|--------|--------|----------|-----|
| Hostouň | 1938 | 2 | 211,59 | 18 x 18 | 4,2 | 19 900 | 52,6 | 4 |
| | 1969 | 2* | 115,21 | 18 x 18 | 3,2 | 24 500 | 94,8 | 4 |
| | 1983 | 1 | 151,99 | 23 x 23 | 2,8 | 18 300 | 92,1 | 4 |
| Ropice | 1937 | 2 | 211,31 | 18 X 18 | 4,3 | 20 500 | 53,2 | 4 |
| | 1972 | 2 | 114,36 | 18 x 18 | 2,7 | 23 400 | 90,7 | 4 |
| | 1986 | 2* | 152,00 | 23 x 23 | 4,5 | 29 600 | 90,2 | 4 |
| Držkov | 1938 | 1 | 211,09 | 18 x 18 | 4,2 | 19 700 | 59,0 | 4 |
| | 1971 | 1 | 209,87 | 18 x 18 | 2,9 | 13 700 | 57,6 | 4 |
| | 1988 | 1 | 152,27 | 23 x 23 | 2,1 | 13 700 | 91,0 | 8 |

legend: YOR - year of recording; NOI - number of photos; f - focal length; FS - frame size; h - flight height; S - scale; DAOV - diagonal angle of view; NFM - number od fiducial marks
 * used only one of them

Following values were known for photos - the focal length (shown in the photo) and the scan resolution value (VGHMUr denotes 14/15 μm). Other values were derived also from the knowledge of the extent of the area displayed on particular HAP, see Figure 1. The values show relatively large variability of the used scales and the use of cameras with normal and wide-angle lenses.

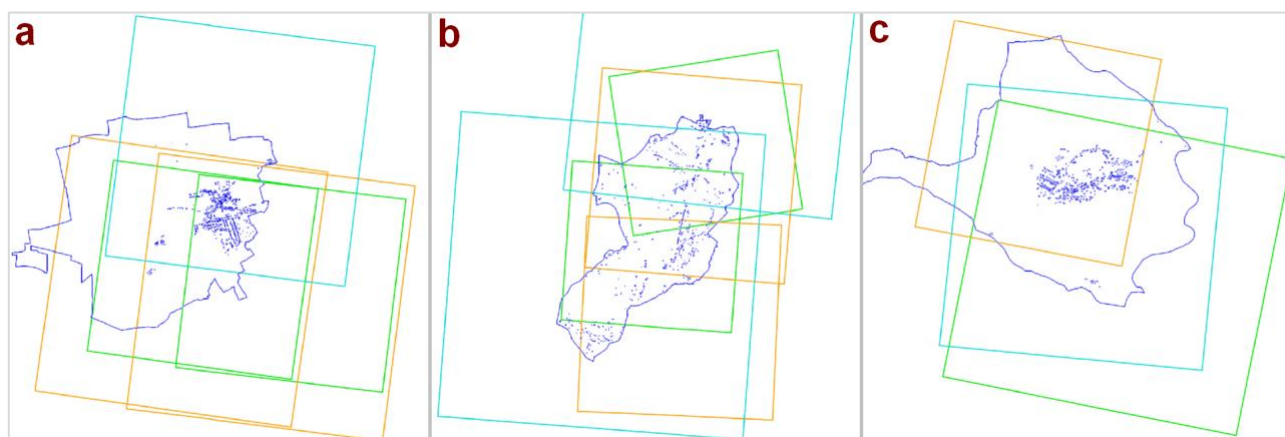


Fig. 1 – Covering of cadastral districts by HAP – a)Hostouň, b)Ropice, c)Držkov.
 Years – green = 1938+37+38, orange = 1969+72+71, blue = 1983+86+88

Digital terrain model and map data

The digital terrain model (DTM) is an essential resource for creation of an orthophoto. The specificity of HAP processing is in the fact that the model should relate to the historical state of the area. Most authors, such as Šafář [18] and Sukup [20], state that one of the ways to deal with this is to use the current DTM as a basis and provide its local editing. In case of its locally non-updated areas for a given timeframe, they recommend to use the HAP and edit DTM, by using stereoplotting, for example. The extent of possible mismatches depends, among other things, on the size of the territory and the way of its development since the acquisition of HAP, which can be determined from various sources.

In our project we process three relatively small cadastral districts, where large changes are not expected. In the pilot project Hostouň (1969) stereo pairs of photos were acquired for purposes of testing. We wanted to verify the possibility of using HAP for automated DTM creation by image correlation method. The progress and results in our case have shown that DTM in satisfactory quality cannot be expected, see below. That is why the digital terrain model based on the data of aerial laser scanning - DMR 5G was purchased from the Land Survey Office.

The current orthophoto, the historical orthophoto CENIA and the current cadastral map are other resources available to all localities. This type of resources is mainly used to find suitable ground control points for orthophoto and to verify the accuracy of the results.

Processing – image orientation

The process of image orientation is always influenced by the number of the photos, by their layout and also by our knowledge of their parameters. In our case, we worked with single photos only, where the elements of interior orientation were not known. We used the PhoTopoL Digital Photogrammetry Workstation v.9 and 9.5 for photogrammetric processing.

Interior orientation

A calibration protocol, which contains all the essential information for the photogrammetric processing, is usually not available for historical photos. Therefore, the elements of interior orientation (IO) are to be determined in another way.

The approximate value of the focal length can be determined directly on the HAP, where it is part of the frame data. If scanning resolution is known, then it is also possible to determine the actual dimensions of the photo at the time of scanning and image coordinates of the fiducial marks (FM). In our case four fiducial marks were designated on all photos. Their pixel coordinates were deducted twice from the digital image, and the real values in mm were acquired from the average values using resolution knowledge. For the purposes of comparison, the coordinates were transformed by the congruent transformation so that the origin is in the centre of the image and the x-axis in the horizontal link of FM. Other elements of IO (the position of the principal point + the course of distortion) could not be easily detected at that moment.

It is commonly reported that unknown IO values can be determined by using the bundle block adjustment, with knowledge of at least approximate values, see Šafář [18], Prchalová [12] at al. However, this procedure can only be used if we process multiple photos, which is not the case of our project. Other authors neglect image distortion and principal point shift, see Skoupý [8], which certainly affects the accuracy of the outputs. It depends on the required accuracy, the type (plane / rugged) and size of the area, the type of lens used (angle of view vs. distortion), etc. whether the outputs will be still suitable for use (see also Table 3).

With regard to the technical and time conditions (e.g. the need to produce at least preliminary outputs), a simplified solution was chosen for the current stage of our project. The focal length and the FM image coordinates were considered only. Finding suitable process and technical solution for acquiring other elements of IO is priority topic for the second part of project works.

Exterior orientation

Ground control points (GCP) are of a key significance in calculation of elements of exterior orientation of HAP. Their optimal number and spacing is determined by the calculation method (block of photos vs. a single photo). Considering GCP are primarily sought out on historical photos, their image quality is of a great importance. This quality, as shown in Figure 2, can be very variable. It is not a rule that photos of older data are of lower quality.



*Fig. 2 – Image quality of HAP – Ropice village (selected part of photos)
Historical aerial photos © VGHMUR*

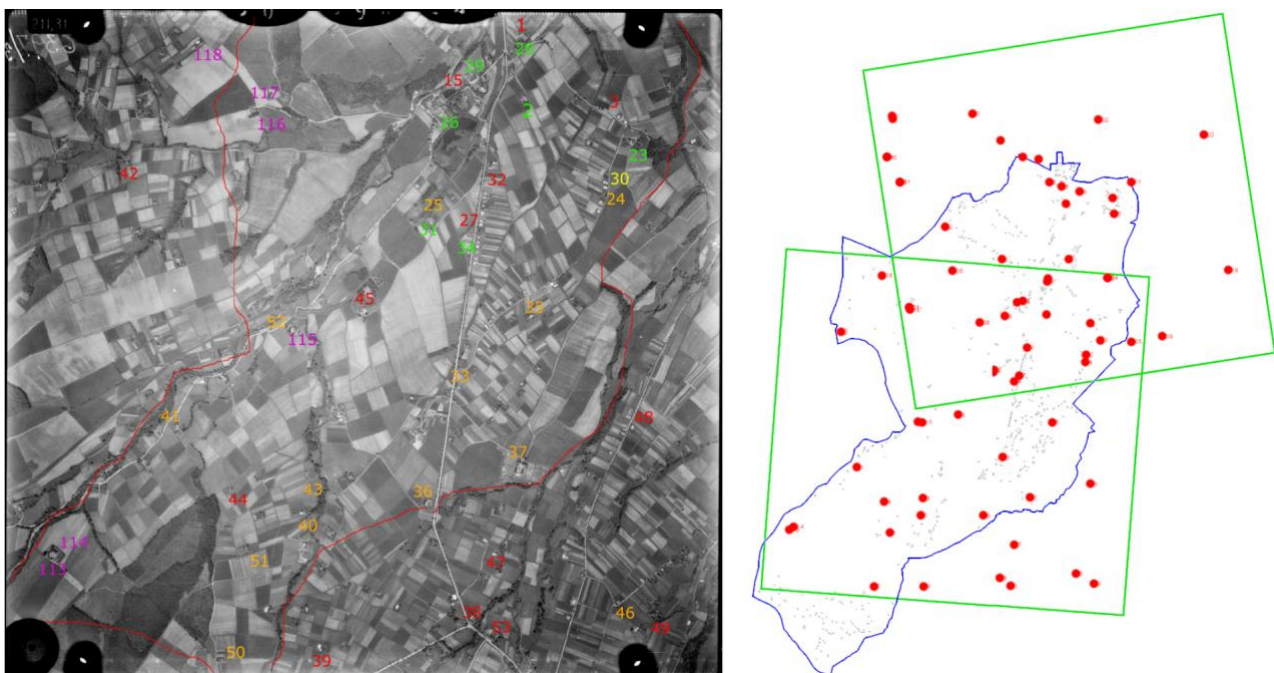


*Fig. 3 – Distribution of GCP – layout (left) and scheme (right), Ropice village – 1937
Historical aerial photos © VGHMUR*

When searching for GCP, all of the above mentioned map resources were used as a reference. Our goal was to cover the particular photos homogeneously if possible with sufficient density, also in context of the next calculation of other unknown IO. When selecting the points, special emphasis was placed on covering the urban areas of the villages, because they are in our focus primarily. Natural points were selected (corners of buildings, crossing roads, etc.). In some cases, identifying the same point on particular photos was very difficult. This was especially true in areas with more significant changes – e.g. a continuous new building development or in the forest or fields areas. The coordinates of the GCP were determined primarily from the cadastral map and the current orthophoto. In case of small number of the ancillary points orthophoto CENIA was also used. Thus differences in coordinates (acquired from various resources) were obtained for each point. These differences, together with information of point identification, indicate credibility of the point, which was color-coded in our sketch. A set of 20-30 points was obtained in this way for each photo, see Figure 3. The heights of all points were acquired using the purchased digital model, see also the Hypsography Analysis application [25].

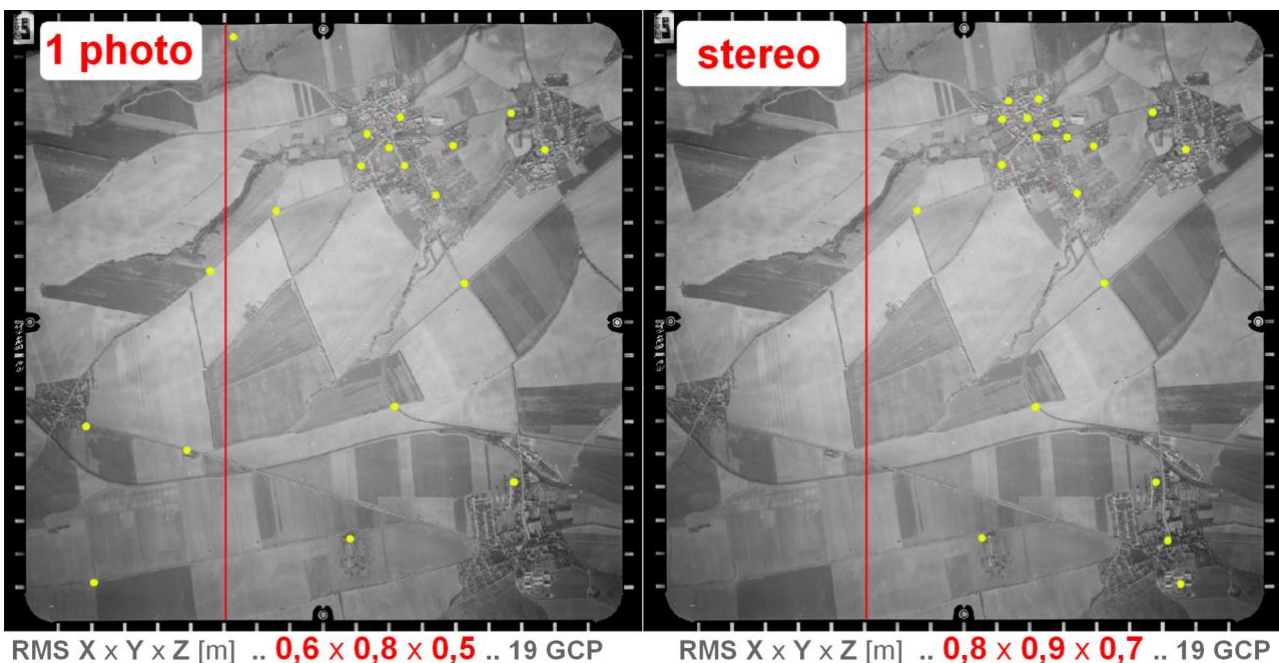


Fig. 4 – Distribution of GCP and EO precision, Hostouň village – 1969
Historical aerial photos © VGHMUR

In the pilot part of the project a suitable procedure for calculating the elements of exterior orientation of photos (EO) has been sought out. Photos from the Hostouň village acquired in 1969 were processed. The calculation of EO for both stereo pair and single photo was tested. To calculate EO and unknown IO values AeroSYS computing system was planned to be utilized, however this intention has not been fulfilled. The calculation failed - the results achieved even after a number of experiments did not match with the assumptions and the source of the problem has not been detected. It is possible that in our case there was a hidden incompatibility between the two used computing systems in terms of import / export of data or other defect difficult to detect. Thus, the calculation of EO has been performed in the PhoTopoL system, which in our version did not allow us to determine unknown IO values. Figure 4 illustrates an example of the resulting GCP layout for EO calculations for both test cases and achieved accuracy of the calculation. In total,

eleven variants of the GCP layout have been verified, with an emphasis on a particular parameter – e.g. homogeneous distribution, emphasised build-up area, the build-up area only, etc.

Interpretation of the results achieved should be treated with certain circumspection. As indicated in results at Držkov village, see Table 3, the results may be of lower quality under other conditions. The calculation also showed an unexplained instability when changing some adjustable parameters - for example prior GCP accuracy. On the other hand, it has to be mentioned that verification of the accuracy of the outputs within the pilot project yielded in results that fulfilled the original assignment, see below. In the light of the lessons learned, the simpler way of processing was chosen for other locations. Only one photo with homogeneous coverage of points was used, also in context of the results obtained in the DTM creation, which is described below.

Tab. 3 - Exterior orientation – summary of results

| | rms X [m] | rms Y [m] | rms Z [m] | MDZ [m] | IQ | S | DAOV [°] |
|---|------------|------------|-----------|---------|-----------|--------|----------|
| Ropice | | | | | | | |
| 1937_PH2 | 0,5 | 0,5 | 0,3 | 100 | good | 20 500 | 53 |
| 1972_PH2 | 0,5 | 0,6 | 0,5 | | weak | 23 400 | 91 |
| 1986_PH1 | 0,7 | 0,9 | 0,8 | | very good | 29 600 | 91 |
| Držkov | | | | | | | |
| 1938_PH1 | 1,0 | 1,7 | 0,7 | 150 | very good | 19 700 | 59 |
| 1971_PH1 | 1,8 | 1,4 | 0,8 | | very good | 13 700 | 58 |
| 1988_PH1 | 1,9 | 3,5 | 2,0 | | very good | 13 700 | 91 |
| Hostouň | | | | | | | |
| 1969_PH1 | 0,6 | 0,8 | 0,4 | 50 | good | 24 500 | 95 |
| <i>legend:</i> 1937_PH2 - year of recording + photo number; S - scale; DAOV - diagonal angle of view; MDZ - maximum difference of Z coordinate of used GCP; IQ - image quality | | | | | | | |
| <i>initial assumptions:</i> <ul style="list-style-type: none"> - distribution of GCP is equable on each used HAP - one typical result of EO is presented for each year - number of used GCP is 15-25 per photo | | | | | | | |

The issue of fine-tuning the EO calculation is not completely closed in our project. Some questions remain opened and search for relevant answers and procedures is currently being performed.

Processing - testing of DTM creation

The pilot project also tested possibility of obtaining a historical DTM directly on the basis of HAP. The stereo pair from 1969 with quite good image quality was used. The DTM was created with the automated image correlation method in the PhoTopoL system and the objective of testing was to find appropriate parameters of model creation. In this way, a number of model variants have been gradually created. Their common feature was a relatively high amount of incorrectly determined points. This reduced accuracy of output can be attributed to various influences. The nature of the territory (primarily built-up area) and limited image quality of the HAP belonged to the important ones. Achieving usable results required a large amount of manual editing – i.e. operator intervention. The factual result of the test was a model, which served as a basis for creation of one of the orthophoto variants. The accuracy of this output is shown in Table 4.

Based on the testing, the plan to use HAP for automated DTM creation was rejected. Reasons which had led to this were: large error rate of the automated processing, the need for

extensive operator intervention and variability of HAP quality, see Figure 2. The purchased DTM was used for the further processing of the orthophoto in the project. Possible local deformations due to its out-of-date nature would be in accordance with the recommendations of other authors, see above, solved individually by using of a stereoplotting of HAP, for example. However, this case has not occurred in our project yet.

Processing - orthophoto creation

The orthophoto has been created in three variants for the pilot project. These variants vary by - EO result used (one photo vs. stereo pair) and also by the type of DTM used (created in the project vs. purchased). The combination of EO from a single photo and the purchased DTM was used for the other projects based on the results of testing in the pilot project.

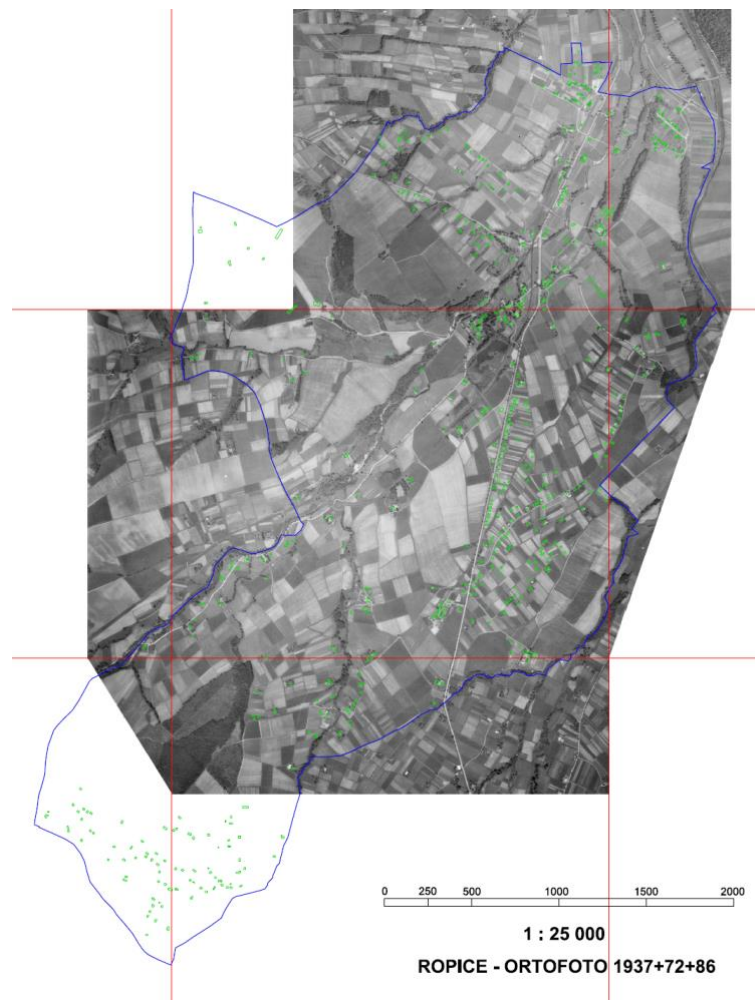


Fig. 5 – Ropice village – orthophoto 1937

Orthophoto creation was performed in a standard way. In case of more photos to choose from, the image quality was the key criterion. With regard to the size of the areas of interest and their coverage by HAP, see Figure 1, two neighbouring photos have to be used only at Ropice. Masking (manual mode) and mosaic operations were performed at two time levels (1937+72) in this case. The overlap of photos was not large, and achieved accuracy of matching corresponded to our expectations. Tie area of photos took place in rural areas and the dissonance there reached

up to several meters (about 5 m). This inaccuracy can be explained, among other things, that the tie areas were mainly at the edges of the photos, where the influence of the neglecting of the distortion of the photos is the most obvious. This is another reason for seeking a suitable procedure for finding out all unknown IO, see above.

The resulting orthophoto was parted into 1: 5000 scale map sheets at the end of the processing and cartographic outputs were created, as reported in Figure 5.

Accuracy verification

Within the framework of the pilot project, a quality verification of the orthophotos (the three variants mentioned above) was performed. There were two types of the verification.

The first type was a visual verification at exposed sites of the area (both in the built-up area and in the rural area). Current orthophoto served as a reference. There were no significant inconsistencies in both types of data found in this type of verification. This shows, among other things, that there were no major changes in the terrain in the given territory during the reference period (i.e. 1969-2017). The set of images capturing tie areas was the result of the verification, see Figure 6 on the left. A similar type of verification was carried out in all other projects, and the results were generally analogical. A significant mismatch was not detected in built-up areas by this way. Slightly worse results have shown up in several rural areas, which may be attributed to above mentioned simplification in processing.



Fig. 6 - Verification of accuracy - visual in urban area (left) and CP distribution (right) Hostouň village – 1969

The use of control points (CP) was the second type of verification. These points were sought out only in a built-up area of a village. The points were easy to identify in both types of data – i.e. on the 1969 orthophoto and the reference orthophoto 2017. Placement of the CP depicts Figure 6 on the right. The CP coordinates were obtained by using these two types of resources. The results of comparison of coordinates are summarized in Table 4. The table shows that the maximal differences in variants using the purchased DTM are almost identical. The maximal differences, in the variant using the DTM created, are twice higher. This finding is consistent with the assumption, that the quality of the purchased DTM is more homogeneous. Noteworthy values of average differences are at the third project. The systematic effect has occurred at the most in the case of single photo variant. Although all variants match the original requirements for

orthophoto accuracy, they show possible future directions of our project development - dealing with systematic influences, for example.

We plan a more detailed accuracy analysis of all outputs with a larger CP set after modifying the technological process (including the exact determination of unknown IO values and the stabilization of the EO calculation).

Tab. 4 - Verification of accuracy – with use of CP

| method | 1 photo | | stereo v1 | | stereo v2 | |
|--------|----------------|----------------|----------------|----------------|----------------|----------------|
| CPN | $\Delta Y [m]$ | $\Delta X [m]$ | $\Delta Y [m]$ | $\Delta X [m]$ | $\Delta Y [m]$ | $\Delta X [m]$ |
| 1 | -1,30 | -0,58 | -0,48 | -0,31 | 4,12 | -1,18 |
| 2 | -0,08 | -0,40 | -0,51 | -0,23 | -0,36 | 1,03 |
| 3 | 1,52 | -1,75 | -0,55 | 2,17 | 0,35 | 0,53 |
| 4 | 0,84 | 1,34 | 0,56 | 1,99 | 0,01 | 3,45 |
| 5 | 2,23 | -0,65 | 2,08 | 0,23 | 1,82 | 0,55 |
| 6 | -0,02 | -2,28 | 0,38 | -0,67 | -1,13 | -2,68 |
| 7 | -0,01 | -0,84 | -0,14 | -0,07 | -0,70 | 0,38 |
| 8 | 0,35 | -1,51 | -0,03 | -0,98 | -1,12 | -1,29 |
| 9 | -0,63 | -0,04 | -0,88 | 0,11 | -1,21 | 0,69 |
| 10 | 1,74 | -0,69 | 1,80 | 0,43 | -0,01 | -2,17 |
| Ø | 0,46 | -0,74 | 0,22 | 0,27 | 0,18 | -0,07 |

legend: CPN - control point number
1 photo - exterior ori. calculated on base of 1 photo only
stereo v1 - exterior ori. calculated on base of stereo + purchased DMR
stereo v2 - exterior ori. calculated on base of stereo + DMR created by us

CONCLUSION

The article describes the process of creating orthophotos on the basis of HAP. This type of output data will, together with other data, serve for assessment of the cultural - historical aspects of the transformation and development of rural architecture over the past two centuries. Historical orthophotos have been created for three selected villages at three time levels.

The technology used for orthophotos is quite standard. The main specificity of the project is that the areas of interest are of a small size (built-up areas of selected villages) and therefore only a single HAP was used for processing. Therefore, in context of the recommendations of various authors mentioned above, the bundle block adjustment method could not be used to calculate the unknown IO and EO values. With regard to the organizational progress of the project, the simplified version of outputs creation was used in the first half of the project. The missing elements of interior orientation have been neglected. Even such a procedure is consistent with the examples cited in the literature, see above.

A pilot project was performed. The use of HAP for automated DTM production was tested. Testing of various EO calculations was done too. On the basis of knowledge learnt in the pilot project, only a single photo (not a stereo pair) was used for the calculation of EO in the other projects and only the purchased DTM was used because of an excessive elaborateness when creating own DTM from HAP. The quality of the pilot project outputs has been verified in two procedures. The results obtained match with our expectations and intensions how the output data

will be utilized. The results of the calculations and the accuracy verification also correspond to the values mentioned in the literature, see for example Šafář [18].

In the second half of the project, we will address issues that have gradually emerged during the processing. First of all - finding the right process and tools for detecting unknown IO, if we only process single photo, will be done. We will deal with certain instability of EO calculation when changing the parameters of the calculation also. Finally, greater attention will be paid to verifying of the accuracy of all outputs by using a larger set of CP to detect possible systematic errors. Our ultimate objective is, besides the further improvement of the outputs, the completion and stabilization of the used technology. It is important to emphasize that our outputs even in the current form are already well usable for cultural - historical research.

ACKNOWLEDGEMENTS

The project is supported by the Ministry of Culture of the Czech Republic as a part of the Program for the Support of Applied Research and Development of National and Cultural Identity for the Years 2016-2022 (NAKI II), Grant "Change of Rural Architecture with Emphasis on Developments in the 19th and 20th Century" DG16P02H023. More information about the project can be found on the project's website venkov.fsv.cvut.cz/projekt.

REFERENCES

- [1] NOCIAROVÁ, Petra. Archívne letecké snímky a ich uplatnenie pri identifikácii lesných pozemkov. In: Symposium GIS Ostrava 2013 - Geoinformatika pro společnost. Ostrava: VŠB - Technická univerzita Ostrava 2013. ISBN 978-80-248-2951-7.
- [2] STEHLÍK, Petr. Taking Plane Images. *Vojenský geografický obzor / Military Geographic Review*, 2004, 1, 32–37, ISSN 1214-3707.
- [3] LAND SURVEY OFFICE. Archive of aerial survey photos [online]. 2018 [cit. 2018-09-30]. Available from: <http://lms.cuzk.cz/lms/>
- [4] LUFTBILDDATENBANK. Acquisition, archiving and analysis of historical air-photos and files [online]. 2018 [cit. 2018-09-30]. Available from: <https://www.luftbilddatenbank.de/>
- [5] PROKEŠ, Jiří. Fotografický plán hlavního města Olomouce z roku 1927 [online]. 2010 [cit. 2018-09-30]. Available from: <http://www.aviatik-cs.cz/projekty.html>
- [6] FIDLER, Jiří a Václav SLUKA. *Encyklopedie branné moci Republiky československé 1920-1938*. 1. vyd. Praha: Libri, 2006, 767. ISBN 80-7277-256-2.
- [7] JALŮVKA, Igor. The Rivals in Photogrammetry. The background of competing between Czechoslovak photogrammetric aeroplane Praga E-51 and German Focke-Wulf Fw 189 before the Great War (WW1). *Vojenský geografický obzor / Military Geographic Review*, 2004, 1, 23–31, ISSN 1214-3707.
- [8] SKOUPÝ, Ondřej. Processing remote sensing data for land change analysis. Brno: 2013. Disertační práce. Mendelova univerzita v Brně, Lesnická a dřevařská fakulta.
- [9] BÖHM, Jaroslav. Letecká fotografie ve službách archeologie. *Zprávy památkové péče*, 1939, III, 63-65.
- [10] KARDOŠ, Miroslav, Ján TUČEK, Zuzana SLATKOVSKÁ a Julián TOMAŠTÍK. The historical orthophotomap of Slovakia – analysis of the positional accuracy and its application in identification of parcels. *Kartografické listy / Cartographic letters*, 2017, 25 (1), 37-47, ISSN 1336-5274.
- [11] JISKROVÁ, Petra. Hodnocení vývoje krajiny pomocí geoinformačních technologií v katastru Kamenická Stráň. Ústí nad Labem: 2012. Diplomová práce. UJEP v Ústí nad Labem, Fakulta životního prostředí.
- [12] PRCHALOVÁ, Jitka. Proměny kulturní krajiny – aplikace archivních snímků v socioekonomickém výzkumu. *Arc REVUE*, 2005, 14 (4), 30-35, ISSN 1211-2135.
- [13] PAVELKOVÁ CHMELOVÁ, Renata a Patrik NETOPIIL. Historical Aerial Images in Geographical Research – Processing Problems and Possible Solutions. In: *Miscellanea Geographica* 13. Plzeň: ZČU v Plzni, Fakulta pedagogická, 2007, 129-136.

- [14] STOUPA, Svatopluk. Analysis of landscape changes by means of GIS and RS in the upper Chomutovka River catchment. Praha: 2011. Bakalářská práce. UK v Praze, Přírodovědecká fakulta.
- [15] SÁDOVSKÁ, Petra. Vývoj urbanizovaného území na základě leteckých snímků. Olomouc: 2011. Diplomová práce. UP v Olomouci, Přírodovědecká fakulta.
- [16] IPR - Prague Institute of Planning and Development. Two Pragues application [online]. 2018 [cit. 2018-09-30]. Available from: <http://www.dveprahy.cz/>
- [17] ŠMEJDA, Ladislav. Možnosti využití kolmých leteckých a družicových dat v archeologii. Plzeň: 2008. Disertační práce. ZČU v Plzni, Fakulta filozofická.
- [18] ŠAFÁŘ, Václav a Lenka TLAPÁKOVÁ. Alternative Methods of the Processing of Archival Aerial Photos. Geodetický a kartografický obzor / Geodetic and Cartographic Review, 2016, 62 (12), 253-257, ISSN 1805-7446.
- [19] CENIA - Czech Environmental Information Agency. Contaminated sites application [online]. 2018 [cit. 2018-09-30]. Available from: <https://kontaminace.cenia.cz/>
- [20] SUKUP, Karel. Tvorba ortofotomap z historických leteckých snímků území ČR. In: Seminář - Podpora a propagace oblasti podpory 4.2 - Odstraňování starých ekologických zátěží. Praha: Ministerstvo životního prostředí, 2012, 99-103.
- [21] ROZMANOVÁ, Naděžda a Zuzana POKORNÁ. Charakter a struktura zástavby venkovských sídel v územních plánech. Praha: Ministerstvo pro místní rozvoj ČR - Ústav územního rozvoje, 2017. Metodiky a pomůcky, ISBN 978-80-7538-153-8.
- [22] KREJČÍŘÍK, Přemysl a Miloš PEJCHAL. Architektonicko-historický průzkum památky krajinářské architektury. Lednice: Zahradnická fakulta Mendelovy univerzity v Brně, 2015. Metodiky.
- [23] BERÁNEK, Jan, Lucie BERÁNKOVÁ, Jana ČEVONOVÁ, Petr MACEK, Michal PATRNÝ, Jindřich ZÁHORKA a Pavel Zahradník. Metodika stavebněhistorického průzkumu. Praha: Národní památkový ústav, generální ředitelství, 2015. Metodiky, Dokumentace památek (Národní památkový ústav). ISBN 978-80-7480-037-5.
- [24] DĚDKOVÁ, Pavla. 3D visualization of extinct village and its evaluation in term of user cognition. Olomouc: 2012. Bakalářská práce. UP v Olomouci, Přírodovědecká fakulta.
- [25] LAND SURVEY OFFICE. Hypsography Analysis application [online]. 2018 [cit. 2018-09-30]. Available from: <http://ags.cuzk.cz/dmr/>

THE EFFECT OF AXIAL COMPRESSION RATIO ON SEISMIC BEHAVIOR OF INFILLED REINFORCED CONCRETE FRAMES WITH PROFILED STEEL SHEET BRACING

FENG Ningning¹, WU Changsheng², MA Junyue¹, MAO Xiaotian¹

1. Changzhou Institute of Technology, Faculty of Civil Engineering, Civil Engineering & Architecture, Changzhou Jiangsu, No.666 Liaohe Road, China; fengningning1104@163.com
2. Southeast University, Institute of Geotechnical Engineering, Sipailou 2#, Nanjing Jiangsu, China; shengchangwu@126.com

ABSTRACT

Seven infilled reinforced concrete (RC) frames strengthening with profiled steel sheet bracing are researched on the effect of axial compression ratio (0.3~0.9). Hysteretic curves, envelope curves, stiffness degradation curves, ductility and energy dissipation capacity are analysed in the finite element. The results show that profiled steel sheet bracing plays a good role in reinforcing infilled RC frames and the hysteretic curves express plump relatively. With the increase of axial compression ratio, the bearing capacity is improved significantly. The axial compression ratio has little effect on the lateral stiffness of the structure, and the initial stiffness increases slightly with the increase of axial compression ratio. The structure has good ductility when the axial compression ratio is less than 0.6. The ductility is declined with the increase of axial compression ratio. As the displacement increases, the energy dissipation capacity of the specimens increases. However, the energy dissipation capacity is reduced as the increase of axial compression ratio.

KEYWORDS

Axial compression ratio, Profiled steel sheet bracing, RC frame, Seismic behaviour, Hysteretic curve

INTRODUCTION

Steel bracing is the anti-lateral force member, which is used in reinforced concrete (RC) frame structures widely. Some scholars [1-4] have studied and proved the efficiency of steel bracing. The seismic performance of the structure has improved greatly. Tahamouli Roudsari et al. [5] adopted five different types including V-shaped, X-shaped, K-shaped, eccentrically braced and Y-shaped to reinforce RC frames. The damage characteristics and mechanical properties of RC frame were studied in the test. The experimental results showed that eccentrically braced had better ductility and less strength reduction factor than other braces. At the same time, X-shaped brace showed the good performance in improving the strength, stiffness and crack control in the process of strengthening. Guo and Fan [6] conducted dynamic characteristics and elastic seismic responses analysis on different reinforced concrete frames (5 floor, 8 floor and 12 floor) and RC frame with X-shaped central brace respectively. The results showed that X-shaped brace improved the lateral stiffness and reduced natural vibration period of the structure. In the action of horizontal earthquake, lateral displacement and storey drift angle were decreased. Yang et al. [7] based elastic analysis and elastic-plastic Pushover analysis on three RC frames, which had different

quantity of braces. The key research is the concept of RC frame with less steel brace. The research results indicated that collapse resistant capacity had enhanced with less steel brace. Fan et al. [8] studied eight layer framework strengthened with X-shaped brace. Pushover analysis was operated under the earthquake action. The research results showed that reasonable support increased the lateral stiffness of the structure effectively. At the same time, it decreased story drift and improved the seismic performance of the structure.

The above results show that steel braces can work with RC frame to obtain good seismic performance. On the basis of existing research, Cao and Feng [9] proposed RC frames strengthening with profiled steel sheet bracing which takes the influence of infill walls into consideration. Through the experimental study, the feasibility of infilled RC frame reinforcing with profiled steel sheet bracing had been verified. With the advantage of greater out-of-plane stiffness than ordinary plane, the profiled steel sheeting was adopted. The results showed that the strength is enhanced by 225%, the stiffness is increased by 108%, ductility is increased by 26.85%, cumulative energy is improved by 202.63%, respectively.

The seismic performances of multi-storey reinforced concrete frame structure reinforcing by profiled steel sheet bracing are different under different axial compression ratio. However, there are few studies on the seismic performance of infilled RC frame structures with axial compression ratio. Wang et al. [10] researched multi-storey and high-rise RC frame reinforcing by Y-shaped brace under different axial compression ratio. A nonlinear finite elements analysis was carried out to investigate the failure modes and the ultimate strength of structures. The results indicated that the bearing capacity and initial stiffness increased with the increase of axial compression ratio. Wang et al. [11] established square steel tube concrete frame model to analyse the influences of axial compression ratio. The results showed that the ductility of the frame decreased as the axial compression ratio increased.

Therefore, the objectives of this research was to reveal that the seismic performance of structures with different axial compression ratios and the influence on performance of structural reinforcement. On the basis of experimental study, finite element model of infilled RC frames with profiled steel sheet bracing are studied on the effect of different axial compression ratio. Structure seismic performances are investigated under axial compression ratio of frame column.

Experimental model and finite element model

Experimental model

The experimental model was completed in the structural engineering laboratory of Hohai University. Two-layer, one-span test specimen was carried under the low cyclic loading. Longitudinal bar and stirrup were HRB400. The diameter of longitudinal bar was 10 mm and the average yield strength was 382.11 MPa. The diameter of transversal tie was 8 mm and the average yield strength was 390.36 MPa. The average compressive strength of concrete was 38.23 MPa. The specimen design is shown in Figure 1. The steel type of profiled steel sheeting was Q235 and the model was YX35-250-1000. The thickness of profiled steel sheeting was 0.4 mm. The section of profiled steel sheeting is shown in Figure 2.

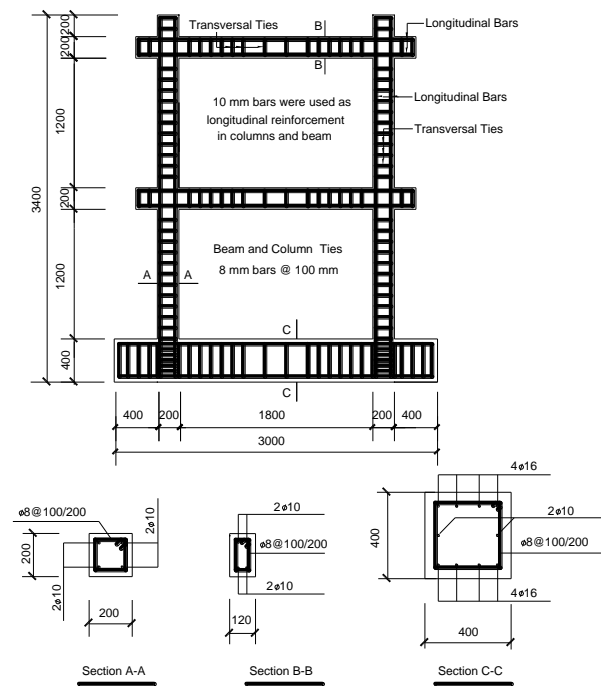


Fig. 1 – Specimen design

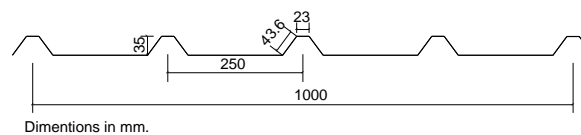


Fig. 2 – Sectional dimension of profiled steel sheet

Finite element model

It was complicated when finite element models established the actual reinforced concrete structure. Hence, integral modelling was adopted in finite element modelling, which dispersed the longitudinal bar and stirrup into concrete. The software was adopted ANSYS and the unit of reinforced concrete used solid element SOLID 65. The reason was that the element can define concrete materials and three kinds of reinforcement materials. In other words, there were three kinds of reinforcement in different direction, and the selection of finite element model reinforcement was based on the Specimen design (Figure 1). According to the above material properties, the material constitutive model [12] was defined. The test model was arranged with infill walls inside RC frame. The two sides of infill walls were supported by profiled steel sheet bracing. The two faces were X-shaped and the test model is shown in Figure 3. It can be seen that test model was installed with steel plates and steel rods on beams and columns. And the channel steel was welded with steel plates inside RC frame. Infill walls were built in the channel steel, and tapping screws were used to connect profiled steel sheet bracing and channel steel. On the basis of test model, finite element modelling was simplified appropriately. The first simplification was that infill walls were equivalent to the diagonal pressure bar [12] (Figure 4 (a)). Simplification principle was basic on the main cracks of infill walls in the test developed along the diagonal line. The cracks were called as shear fracture. The test phenomenon accorded with equivalent diagonal brace model, which was proposed by Polyakov [13]. Polyakov showed that the infill walls in the frame were considered as a diagonal brace, which could bear pression but not tension; the second simplification was that profiled steel sheet bracing connected with RC frame directly. The common

nodes method was adopted to insure reliable connection. Namely, the common nodes method replaced steel plates and steel rods on beams and columns. Profiled steel sheet bracing was connected with beams and columns directly (Figure 4 (b)).

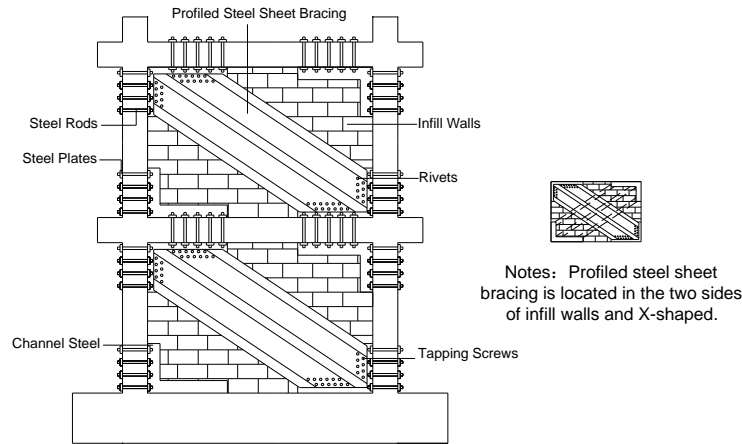


Fig. 3 – Test model

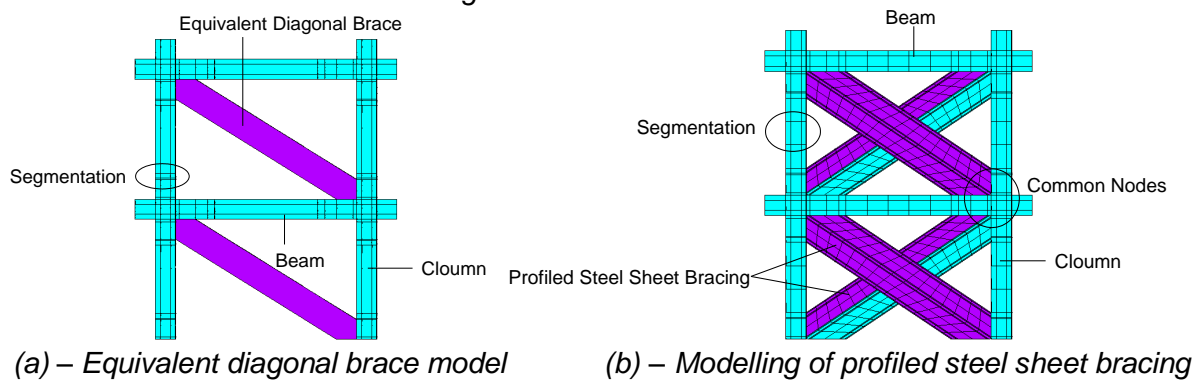


Fig.4 – Finite element model

Validation of the finite element model

Hysteretic curves and skeleton curves in the test and finite element are shown in Figure 5. The experimental data came from the test [9] and the finite element analysis came from literature [12]. By comparing the two results, it can be seen that finite element analysis curve trend were similar with the test. It got gain access to the good plump curves. The maximum horizontal loads were 142.2 kN and 130.35 kN in the test and finite element and the deviation is 8.3 %. The compared results showed that effectiveness of profiled steel sheet bracing reinforcement. Profiled steel sheet bracing worked well with RC frame structure.

Because of the experimental conditions and fund assistance, it was impossible to pour more specimens in an experiment. However, axial compression ratio was an important factor affecting the seismic capacity of the frame. As a result, it was necessary to study axial compression ratio particularly. Based on the above research results, this paper focused on the research of seismic capacity of infilled walls RC frame with different axial compression ratio.

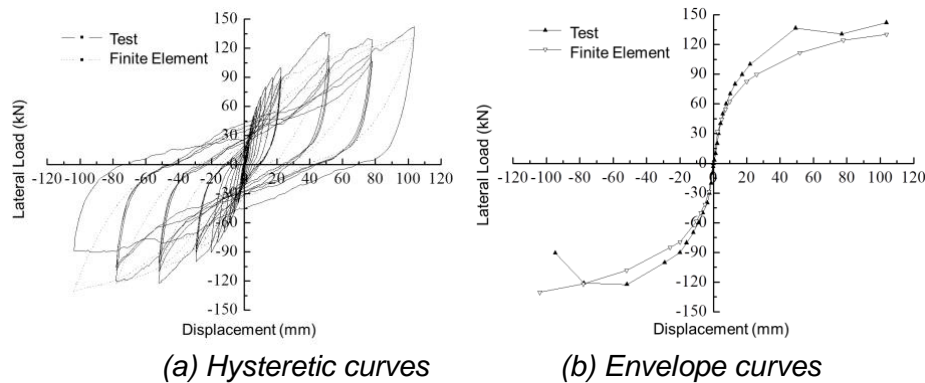


Fig.5 – Comparison of hysteretic curves and Envelope curves

Selection of axial compression ratio

Axial compression ratio is one of the important factors in affecting the seismic capacity of frames. Enough ductility can be gained by limiting axial compression ratio of reinforced concrete frame structures in the earthquake. Structures or components can avoid brittle damage and meet the requirement of earthquake resistance as per Chinese Standard Design Code (2010). As a result, it is important to study the influence of different axial compression ratio on infilled RC frame structure. Controlling axial compression ratio is one of the important measures to ensure the necessary ductility of the structure. After Wenchuan Earthquake (China) in 2008, more attention is paid on structures with the design of axial compression ratio.

Axial compression ratio n is introduced as per Chinese Standard (2010), which can be expressed by axial pressure design value N , column section area A and concrete axial compressive strength design value f_c . The calculation can be expressed by Equation (1).

$$n = \frac{N}{f_c A} \tag{1}$$

In the test, the measured strength grade of concrete was C38 and corresponding design value of concrete axial compressive strength f_c is 18.1 N/mm² as per Chinese Standard (2010). Column cross-sectional area was denoted by $A = 200 \times 200 = 40000 \text{ mm}^2$ and axial compression ratio was 0.27.

According to the axial compression ratio of common concrete column design, axial compression ratio is selected 0.3, 0.4, 0.5, 0.6, 0.7, 0.8 and 0.9. The values accord with the limit of axial compression ratio as per Chinese Standard (2010). The selected values are shown in Table 1.

Tab.1 - Axial compression ratio

| Specimen | KJ1 | KJ2 | KJ3 | KJ4 | KJ5 | KJ6 | KJ7 |
|-------------------------|-------|-------|-----|-------|-------|-------|-------|
| Axial Pressure/kN | 217.2 | 289.6 | 362 | 434.4 | 506.8 | 579.2 | 651.6 |
| Axial Compression Ratio | 0.3 | 0.4 | 0.5 | 0.6 | 0.7 | 0.8 | 0.9 |

Hysteretic curves

Hysteretic curves of Specimens KJ1-KJ7 are shown in Figure 6. In the finite element analysis, the load steps were set up to control the incremental loading of the specimen. And finite element program realized the load steps. In order to facilitate analysis and comparison, different loads under the same displacement were selected for comparison. As can be seen from the figures, the residual deformation was very small and the horizontal load - displacement curves were close to the linear change. Specimens were in the initial stage of loading, which called elastic phase. There were small cracks in concrete with increasing lateral loads and horizontal displacements. The compression cracks could close and the structure deformation was small. The formed areas of

hysteresis loops by the addition and unloading were not big. After the displacement was loaded to 25.95 mm, the area of the hysteretic loops increased gradually. The frame entered into the elastic-plastic stage. Profiled steel sheet bracing supported the tensile force and the wall bear pressure. As a result, profiled steel sheet bracing and the wall worked together to improve the structural bearing capacity. Due to the concrete spalled and the compression zone of the column bottom destroyed, the hysteresis curves were difficult to simulate. Therefore, it considered that the test reached the limit state and the bearing capacity was the largest when the displacement reached to 103.8 mm. Finally, infilled RC frame structure strengthening by profiled steel sheet bracing gained plump hysteresis loop under the action of different axial compression ratio.

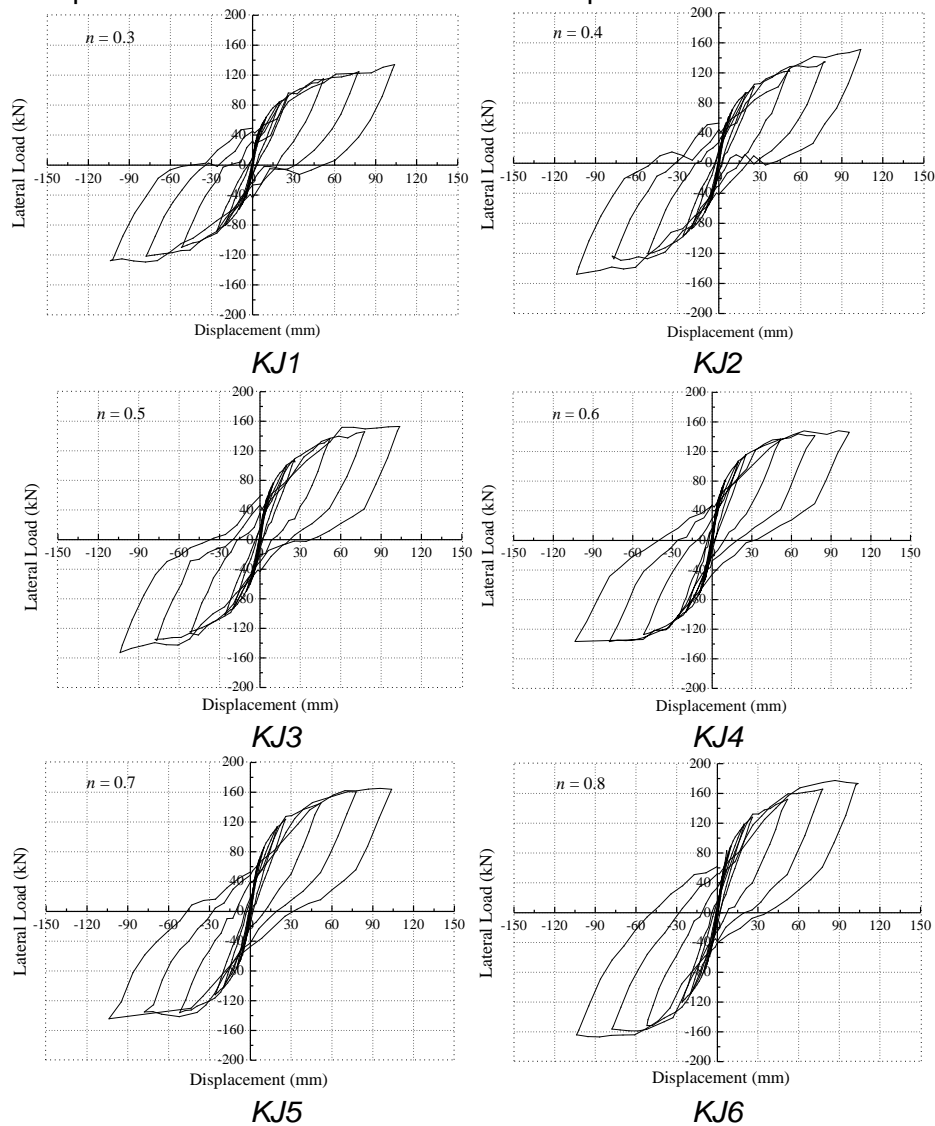


Fig.6 – Hysteretic curves

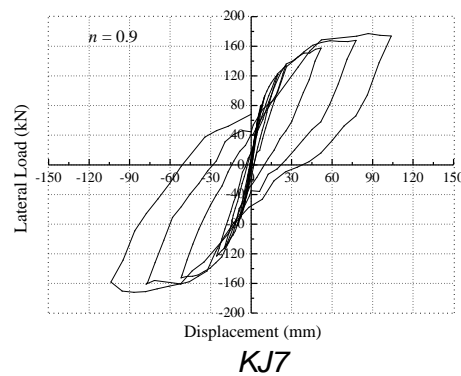


Fig.6 – Hysteretic curves

Skeleton curves

Skeleton curves of Specimens KJ1-KJ7 are shown in Figure 7. Load values at each stage are shown in Table 2. The skeleton curve reflected bearing force and deformation characteristics of the structure. It was an important basis for the study of the inelastic seismic response. The results showed that the maximum carrying capacity of Specimens KJ1, Specimens KJ2, Specimens KJ3 and Specimens KJ4 is 134.24 kN, 151.37 kN, 152.92 kN and 146.08 kN respectively. It can be seen from the results that Specimens KJ1 reached the minimum carrying capacity when the axial compression ratio was 0.3. The carrying capacity was similar when the axial compression ratio was 0.4 and 0.5. The bearing capacity of Specimens KJ3 is 1.02 % higher than that of Specimens KJ2. When the axial compression ratio reached 0.7, the maximum bearing capacity of the KJ5 was increased to 163.99kN. When the axial compression ratio was 0.8 and 0.9, the maximum bearing capacity of KJ6 and KJ7 were 173.34 kN and 173.99 kN respectively. With the increase of axial compression ratio, the bearing capacity increased when axial compression ratio was between 0.3 and 0.6 in the same displacement. When the axial compression ratio was 0.6, the bearing capacity decreased slightly. When the axial compression ratio was between 0.7 and 0.9, bearing capacity improved with the increase of axial compression ratio. And when axial compression ratio was 0.8 and 0.9, the bearing capacity was close relatively.

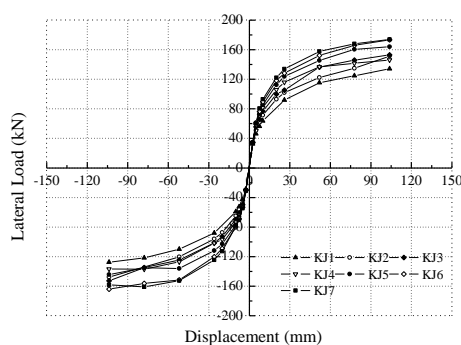


Fig.7 – Envelope curves

Tab.2 - Loads at each stage

| Specimens | Cracking load /kN | Yield load /kN | The maximum load /kN |
|-----------|-------------------|----------------|----------------------|
| KJ1 | 32.75 | 85.76 | 134.24 |
| KJ2 | 33.87 | 98.82 | 151.37 |
| KJ3 | 34.42 | 102.02 | 152.92 |
| KJ4 | 34.30 | 104.17 | 146.08 |
| KJ5 | 34.44 | 117.01 | 163.99 |
| KJ6 | 35.06 | 123.85 | 173.34 |
| KJ7 | 35.89 | 127.09 | 173.99 |

Rigidity degeneration

Rigidity degeneration curves of Specimens KJ1-KJ7 are shown in Figure 8. The initial and ultimate stiffness values are shown in Table 3. The secant stiffness [14] was adopted to describe stiffness degradation of specimens. At the initial stage of loading, concrete cracks developed quickly and stiffness degradation dropped fast. When the displacement reached 20 mm, the stiffness degradation rate slowed down. The initial stiffness of Specimens KJ1-KJ7 were 12.27 kN/mm, 12.71 kN/mm, 12.89 kN/mm, 12.93 kN/mm, 12.90 kN/mm, 12.93 kN/mm, 12.98 kN/mm, respectively. The ultimate stiffness of KJ1-KJ5 (axial compression ratio was 0.3-0.7) was 1.26 kN/mm-1.48 kN/mm. When axial compression ratio reached to 0.8-0.9, the ultimate stiffness of KJ6 and KJ7 reached 1.6 kN/mm.

With the increase of displacement, the rate of stiffness degradation of the Specimen KJ1-KJ7 approximated each other. Large axial compression ratio gained bigger initial stiffness. The reason was that the larger vertical load had stronger binding effect on the concrete, which improved the mechanical properties of the concrete and maintained the high lateral stiffness.

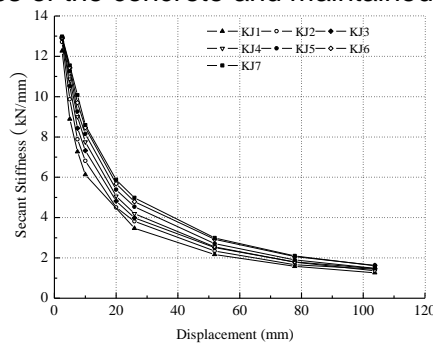


Fig.8 – Envelope curves

Tab.3 - Initial stiffness and ultimate stiffness

| Specimens | KJ1 | KJ2 | KJ3 | KJ4 | KJ5 | KJ6 | KJ7 |
|------------------------------------|-------|-------|-------|-------|-------|-------|-------|
| Initial stiffness/ (kN/mm) | 12.27 | 12.71 | 12.89 | 12.93 | 12.90 | 12.93 | 12.98 |
| Ultimate stiffness / (kN/mm) | 1.26 | 1.44 | 1.47 | 1.36 | 1.48 | 1.63 | 1.61 |

Ductility

Ductility curves of Specimens KJ1-KJ7 are shown in Figure 9. It can be seen that ductility factors [14] were 4.59, 4.32, 4.87, 5.31, 4.61, 4.41, 4.58 in the axial compression ratio 0.3-0.7. The ductility factor was all above 4.0. It indicated that profiled steel sheet bracing and infilled RC frame worked well together, which improved the ductility of the structure significantly. It can be seen from Figure 9, the ductility enhanced with the increase of axial compression ratio when axial compression ratio was between 0.4 and 0.6. However, the ductility decreased with the increase of axial compression ratio when axial compression ratio was greater than 0.6.

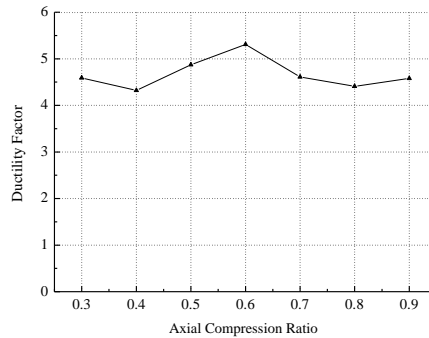


Fig.9 – Ductility curve

Energy dissipation

Energy dissipation curves of Specimens KJ1-KJ7 are shown in Figure 10. It can be seen that the higher the value of equivalent viscous damping coefficient [14], the higher the ability of energy dissipating. In Figure 10, the equivalent viscous damping coefficient improved gradually with the increase of the displacement. The trend showed that the infilled RC frame structure strengthening with profiled steel sheet bracing obtained good energy dissipation capacity.

When the axial compression ratio was 0.3, the equivalent viscous damping coefficient gained a larger value. When the axial compression ratio is 0.4-0.9, the equivalent viscous damping coefficient decreased with the increase of axial compression ratio. It can be seen from that the lower axial compression ratio could get higher energy dissipation capacity. At the same time, the higher axial compression ratio decreased energy dissipating.

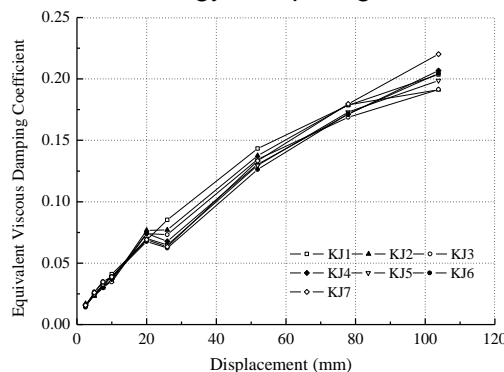


Fig.10 – Energy dissipation curve

Conclusion

In this research, finite element models are verified by comparing with test results. Seven infilled RC frames strengthening with profiled steel sheet bracing specimens are studied in different axial compression ratio. The conclusions are as follows:

- (1) When the axial compression ratio was within the range of 0.3-0.6, the bearing capacity has been improved with the increase of axial compression ratio. The maximum bearing capacity range

was 134.24 kN-152.92 kN. Meanwhile, when the axial compression ratio was within the range of 0.7-0.9, the bearing capacity was enhanced with the increase of axial compression ratio. The maximum bearing capacity was 163.99 kN-173.99 kN. The maximum bearing capacity of the specimen was increased by 13.78 %-22.16 %. The infilled RC frame structure with high axial compression ratio was able to obtain higher seismic bearing capacity.

(2) The rate of stiffness degradation of seven specimens was almost the same under different axial compression ratio. When the axial compression ratio was 0.3-0.9, the initial stiffness value ranged from 12.27 kN/mm to 12.98 kN/mm and the ultimate stiffness ranged from 1.26 kN/mm to 1.61 kN/mm. With the increase of axial compression ratio, the initial stiffness and ultimate stiffness showed an increasing trend. However, the amplitude of increasing trend is not large. The effect of axial compression ratio on infilled RC frame structure was not significant.

(3) When the axial compression ratio was between 0.3 and 0.6, the ductility of infilled RC frame showed well. However, when the axial compression ratio was between 0.6 and 0.9, the ductility decreased. It showed that the smaller axial compression ratio, the better ductility of infilled RC frame. Excellent ductility can be achieved within the axial compression ratio of 0.6.

(4) The equivalent viscous damping coefficient and the energy dissipation capacity of Specimen KJ1-KJ7 were enhanced with the increase of displacement. It could get better energy dissipation capacity when the axial compression ratio was 0.3.

Acknowledgment

The authors would like to acknowledge the Natural Science Foundation of the Jiangsu Higher Education Institutions of China (No: 18KJB560002), the Research Project of Ministry of Housing and Urban-Rural Development of Jiangsu province (No: 2017ZD233), Research Project of Changzhou institute of technology (No: YN1722), Student Research Training Program of Changzhou Institute of Technology (No: 2017079Z) and the National Program on Key Basic Research Project of China (973Program) (2015CB057803), which collectively funded this project.

REFERENCES

- [1] ZHANG W. L., 2016. Seismic Behavior of RC Braced Frame Structures Research and Comparison Model Selection. PhD dissertation, Civil engineering, Lanzhou University of Technology, Lanzhou. (In China)
- [2] ZHAO B. C., WANG J. L., YU A. L., Gu Q., 2015. Design method of RC frame filled with Y-eccentrically steel brace. Journal of Xi'an university of architecture and technology (natural science edition), vol. 47(6): 799-803. (In China)
- [3] Maheri M. R., Akbari R., 2003. Seismic behaviour factor, R, for steel X-braced and knee-braced RC buildings. Engineering Structures, vol. 25(12): 1505-1513
- [4] Dubey S. K. D., Kute S. Y., 2013. Experimental investigation on the ultimate strength of partially infilled and steel-braced reinforced concrete frames. International Journal of Advanced Structural Engineering (IJASE), vol. 5(1): 1-10.
- [5] TahamouliRoudsaria M., Entezarib A., Hadidia M. H., Gandomian O., 2017. Experimental assessment of retrofitted RC frames with different steel braces. Structures, vol. 11(1): 206-217.
- [6] GUO J., FAN H. T., 2015. Seismic response properties of steel concentric X-centrally steel braced RC frames. Journal of Central South University (Science and Technology), vol. 46(6): 2299-2308. (In China)
- [7] YANG X., HE X. G., ZHAO Z. Z., QIAN J. R., 2015. The conception of RC frame structures with a few steel braces. Engineering Mechanics, vol. 32(S1): 129-135. (In China)
- [8] FAN H. T., WANG Z. X., ZHAO H. J., SUN A. F., 2013. Analysis of seismic performance of RC frame structure with X-bracings. Journal of Architecture and Civil Engineering, vol. (2): 35-41. (In China)
- [9] Cao P., Feng N., Wu K., 2014. Experimental study on infilled frames strengthened by profiled steel sheet bracing. Steel & Composite Structures, vol. 17(6): 777-790.

- [10] WANG J. L., ZHAO B. C., 2012. The effect of axial compression ratio on seismic property of Y-type eccentrically braced RC frames. *Journal of Suzhou University of Science and Technology (Engineering and Technology)*, vol. 25(4): 31-35. (In China)
- [11] WANG T. C., LU M. Q., 2005. The Finite element analysis of effect of axial load level on ductility of CFRT frames. *Journal of Jilin University (Engineering and Technology Edition)*, vol. 35(1): 70-75. (In China)
- [12] Feng N. N., CAO P. Z., QI Y. S., ZHAO F. H., 2017. Finite element analysis of infilled RC frames reinforced by profiled steel sheet bracing. *Steel Construction*, vol. 32(11): 37-41. (In China)
- [13] Polyakov, S. V., 1956. On the interactions between masonry filler walls and enclosing frame when loaded in the plane of the wall. *Translations in Earthquake Engineering Research Institute, Moscow, Russia.*
- [14] JGJ 101-2015, 2015. *Specification for seismic test of buildings.* China Architecture & Building Press, Beijing. (In China)

IN-SERVICE CONDITION ASSESSMENT OF LONG-SPAN BRIDGES BASED ON TRAFFIC LOAD EFFECTS USING MONITORING DATA

Rui-feng Nie, Yi-jie Huang and Song-hui Li*

Shandong University of Science and Technology, Department of Civil Engineering, Qingdao 266590, China; 302huangyijie@163.com

ABSTRACT

Long span bridges are widely equipped with structural health monitoring (SHM) systems. Using SHM, a wide range of real-time structural responses under ambient loading could be recorded, which provides the basis for bridge load rating and structural performance assessment. During these structural responses, displacement is an important index to represent the bridge in-service condition. In the paper, monitored girder displacements of a cable-stayed bridge are examined to assess the bridge in-service condition. The finite element model of the studied bridge is first updated based on monitored natural frequencies. Realistic influence lines of the bridge could be obtained based on the updated model, which is the baseline for assessment. Then, moving average method and window smoothing method are employed to extract the displacement induced only by traffic loading from that by wind, temperature, and environmental noise. Finally, using the extracted traffic load effects of girder displacements, the characteristic values under various remaining lives are extrapolated through constructing the limit distribution using block maxima based generalized extreme value (GEV) model fitting. Results show the predicted displacements would exceed the design level of the Chinese code after the bridge serves for another 10 years, indicating potential risk. At that time, the management of traffic loads and maintenance of bridge components should be enhanced to ensure the bridge in-service condition.

KEYWORDS

Long span bridge, Structural health monitoring (SHM), Traffic load, Extreme extrapolation, Load effect

INTRODUCTION

Traffic load is a main variable action during the service of bridges. Nowadays, there are many techniques to collect realistic traffic load information on bridges, such as weigh-in-motion (WIM), bridge weigh-in-motion (BWIM), and high-definition video (HDV) etc. [1-2]. In China, the transportation industry explosively grows in recent years, and vehicle overloading is very serious. Therefore, precise assessment of traffic load effects on bridges is very critical, which becomes a hot research topic [3-5].

The current research interest of traffic load effects mainly focuses on short and medium span bridges. Yuan et al. [4] collected heavy truck data to analyse the structural safety of short to medium span bridges. Ji et al. [5] used measured traffic flow to construct fatigue truck model for the assessment of steel decks in a suspension bridge. Getachew & O'Brien [6] used measured traffic data to establish load model for the assessment of short and medium span bridges in remaining lifetime. However, these measurement techniques show some deficiencies for long span

bridges: (1) the traffic data from WIM are based on sectional measurement and thus impossible to infer the vehicle load sequences over spatial bridge spans; (2) BWIM is applicable to short span bridges or culverts but difficult to clarify the loading case of multiple presence of vehicles over long length; (3) video recording could capture the dynamical behavior of individual vehicles but is hard to collect vehicle load information. Therefore, it is necessary to develop a new technical methodology for the evaluation of traffic loading effects on long-span bridges.

For the study of traffic load effects on long-span bridges, the main existing approach is to construct load sequences over long loading length through traffic microsimulation [7-8]. However, whether traffic simulation could accurately reflect realistic traffic loading is still a controversial topic. Liu et al. [9] filtered the effect of wind, temperature, and environmental noise on the cable force, and analyse the relationship between cable force and these environmental actions. Xia et al. [10] applied similar filtering algorithms to extract displacement induced by traffic loading based on monitoring GPS displacement data of a long span bridge, and extrapolated extreme traffic load effects to evaluate bridge condition.

In the paper, structural health monitoring data are utilized to assess the bridge in-service condition through the case study of a double-pylon cable-stayed bridge. First, the basic information of the studied bridge is introduced and the finite element model of the bridge is updated based on monitored dynamic properties. Then, girder displacements in several important locations are studied, and traffic load effects are maintained with the filtering of load responses induced by temperature, wind, and environmental noise. Finally, characteristic traffic load effects are extrapolated using extreme value theory, which are compared with designed values to assess the in-service condition of the bridge.

DESCRIPTION OF THE BRIDGE

Bridge overview

The studied case is a double-pylon cable-stayed bridge with the span arrangement of 70+160+448+160+70 m as shown in Figure 1. The bridge carries six-lane bidirectional traffic. The height of the concrete diamond pylon is 170 m. The width of the streamline flat steel box girder is 28 m. There are 56 pairs of stayed-cables with four spatial cable planes.

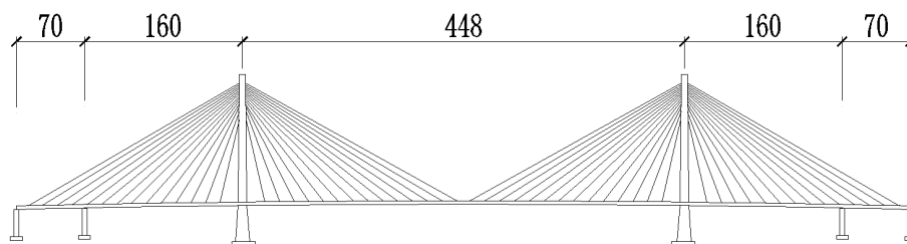


Fig. 1 – Overall layout of studied cable-stayed bridge (unit: m)

Finite element model updating

The studied bridge has been in service for almost 20 years. Though there are no serious diseases observed during bridge operation, there are still some cracks detected in the top plate of the steel box girder, anchorage zone of the stayed-cables, and water leakage in the pavement. Therefore, the actual state of the bridge may be different from design drawings, and should be updated based on structural monitoring.

The finite element model of the studied bridge is established using ANSYS based on design drawings. As shown in Figure 2, the girder and the pylon are modelled by beam 4 and the stayed-cable is modelled by link 10. The structure uses a semi-floating system.

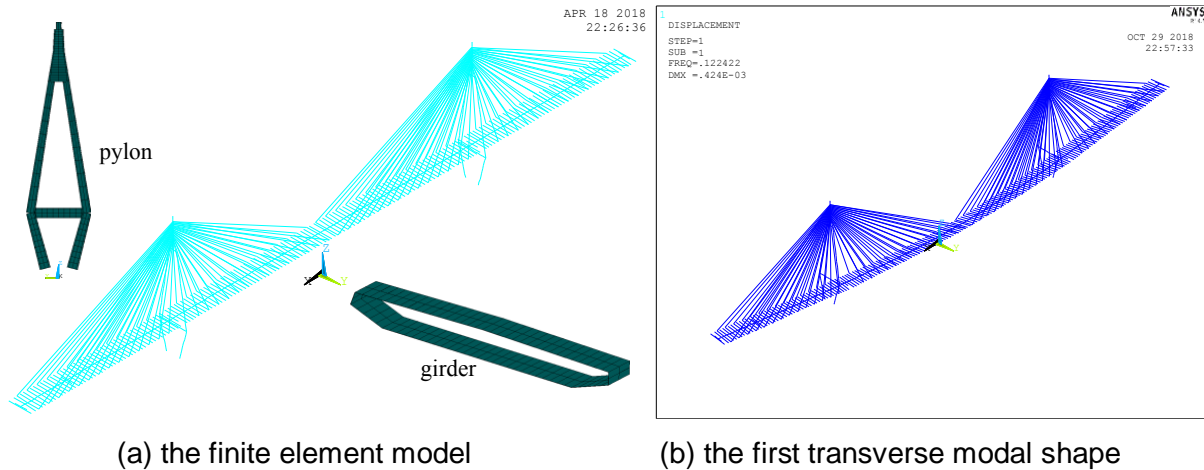


Fig. 2 – FE model and first model shape of the bridge

Based on the dynamical features from structural health monitoring, the first six-order modes of the bridge are obtained as shown in Table 1. The frequencies and modal shape of the bridge were measured using accelerometers installed on the bridge through ambient excitation. Since the realistic bridge state may be different from that of design drawings, the objective of model updating is to make the modified FE model be in consistent with monitoring results regarding these six-order mode frequencies. In the model updating, the well-known girder stiffness, concrete modulus of elasticity, structural boundary condition are taken as the updating parameters [11-12]. The updating results are shown in Table 1, and the first transverse modal shape is shown in Figure 2(b). Results indicate the analytical frequencies of modified FE model are well consistent with monitoring results with relative error basically no more than 8%. Therefore, it can be considered that the updated FE model could represent the realistic condition of the bridge. Note that small damage and crack of local component do not affect the overall performance of the bridge, and thus global vibration characteristics of the bridge are applied in the FE model updating.

Tab. 1 - FE model updating based on structural natural frequencies

| Vibration order | Mode direction | Monitoring | FE model Updating | Relative error /% |
|-----------------|----------------|------------|-------------------|-------------------|
| 1 | Transverse | 0.114 | 0.122 | 7.02 |
| 2 | Vertical | 0.234 | 0.253 | 8.12 |
| 3 | Transverse | 0.351 | 0.334 | -4.84 |
| 4 | Vertical | 0.354 | 0.351 | -0.85 |
| 5 | Longitudinal | 0.454 | 0.491 | 8.15 |
| 6 | Torsional | 0.482 | 0.503 | 4.36 |

Finally, the updated FE model is the baseline for the investigation of traffic loading effects on the bridge. According to the Chinese bridge design code [13], denoted D60, the lane load model shown in Figure 3 is used to calculate the girder displacement, where multi-lane factor, longitudinal reduction factor and impact factor are all considered. The influence lines of girder displacement in the quarter and middle positions of the central span are shown in Figure 4.

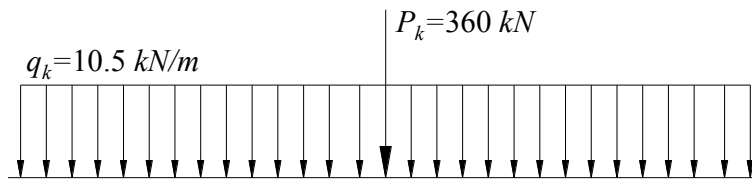


Fig. 3 – Lane load model defined in D60.

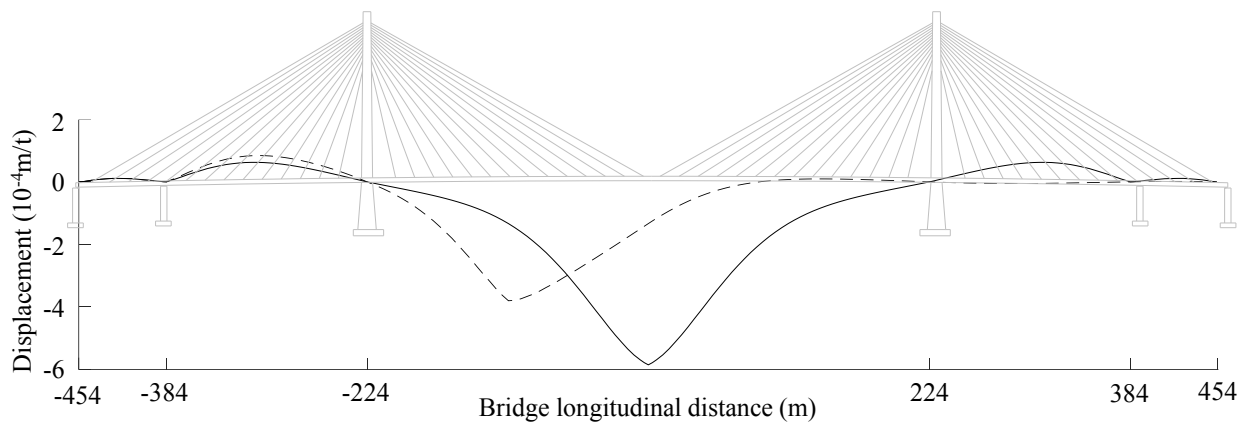


Fig. 4 – Influence lines of girder displacements of in the quarter and middle positions of the central span.

EXTRACTION OF TRAFFIC LOAD EFFECTS

The studied bridge has installed structural health monitoring system since 2014, which includes displacement monitoring of girder and pylon, stress monitoring of steel deck, and accelerometer of girder etc. In the paper, the displacement monitoring of main girder in the quarter and middle positions of the central span is illustrated in the paper. Figure 5(a) shows time-history of one-day displacement in the middle of the central span. It is well known that monitoring data include the effects of environmental noise, wind, temperature, and traffic. Therefore, load effects induced by factors expect traffic should be filtered so that the bridge in-service condition could be estimated.

Filtering of environmental noise

Realistic measured displacements are affected by testing equipment and environment, which means the measured data cover a large number of residuals and fluctuate within a certain range. Therefore, it is necessary to filter these residuals, and the common approach is utilizing moving average method. Using moving average algorithm could smooth out the effect of sudden fluctuations on the measurements. Furthermore, there is some environmental noise, which could be addressed through the 3σ principle to filter the influence of environmental noise on the results of measured displacements. Figure 5(b) shows the filtered time history of one hour after employing moving average method and the 3σ principle. Results indicate the outliers are all filtered.

Filtering of quasi-static effect

Bridge load effects are not only induced by traffic but also wind and temperature. The effect of temperature is a quasi-static process that load effect from temperature is slowly distributed. The change process of temperature load effect could be regarded as static, which is equivalent to the self-equilibrium position of bridge without vehicle action. Load effect induced by wind includes

static and dynamical impact. Load effect under static wind changes slowly than that of traffic flow, which could also be regarded as quasi-static effect. While, the dynamic effect of wind load is largely smaller than that of vehicle load in normal condition, therefore they are ignored hereon.

The load effects induced by traffic on bridges change rapidly with time. In order to filter these quasi-static effects, the time history of displacements should be subtracted from the equilibrium positions of the bridge under wind and temperature loading. Therefore, the average value of load effects in a certain time interval could be chosen as the equilibrium position of the bridge and a time interval of 10 min is used hereon [10]. The corresponding time-history results of load effects only induced by traffic over one hour are shown in Figure 5(c), which includes the static and dynamic traffic load effects. The displacements induced by traffic loading varied generally in the range of -0.3~0.2 m.

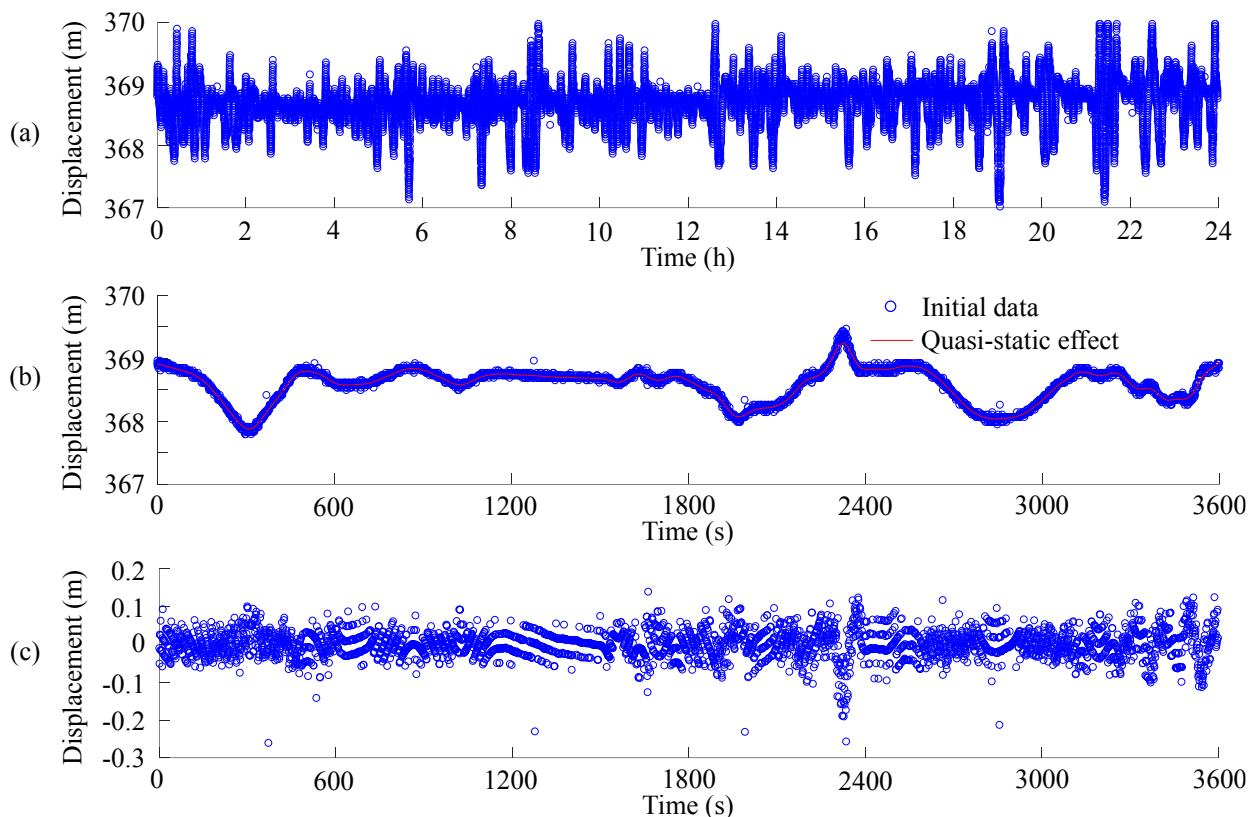


Fig. 5 – Data analysis of the time history of girder displacement: (a) initial data; (b) data filtering; (c) extracted data

BRIDGE IN-SERVICE CONDITION ASSESSMENT

Extrapolation of traffic load effects

Structural health monitoring system is installed from 2014, and total 16 months of monitoring data of girder displacement from 2014 to 2015 are used. Girder displacements in the quarter and middle positions of the central span are investigated to extract traffic loading effects to evaluate bridge in-service condition. Obviously, the 16-month test results are not sufficient to reflect the variable and extreme characteristics of vehicle load in long return period. Therefore, the extreme value theory is employed to predict the extreme value of bridge traffic load effect under any evaluation period based on existing monitoring data.

According to classical extreme value theory [14], the constructed samples using block maxima could be described through generalized extreme value (GEV) distribution, and the distribution model is as following

$$G(x; \xi, \sigma, \mu) = \exp \left\{ - \left(1 + \xi \frac{x - \mu}{\sigma} \right)^{-1/\xi} \right\} \quad (1)$$

where μ, σ, ξ are the location, the scale, and the shape parameters of the generalized extreme value distribution, $\xi=0, \xi > 0$ and $\xi < 0$ represent the type I (Gumbel), II (Frechet), and III (Weibull) GEV model.

GEV is established on the basis of the progressive extreme value model, and samples from block maxima should satisfy the following three conditions: (a) the observation could be simplified as a random variable, i.e. independent of time; (b) these random variables meet the same underlying distribution; (c) the observed variables are independent to each other. For traffic load effects on bridges, it is necessary to select a rational interval so that the requirement of independent and identical distribution could be satisfied. Generally, a day is selected as the block size for extreme value analysis. GEV is used to build the limit distribution of traffic load effects, and maximum likelihood is used to estimate parameters of GEV.

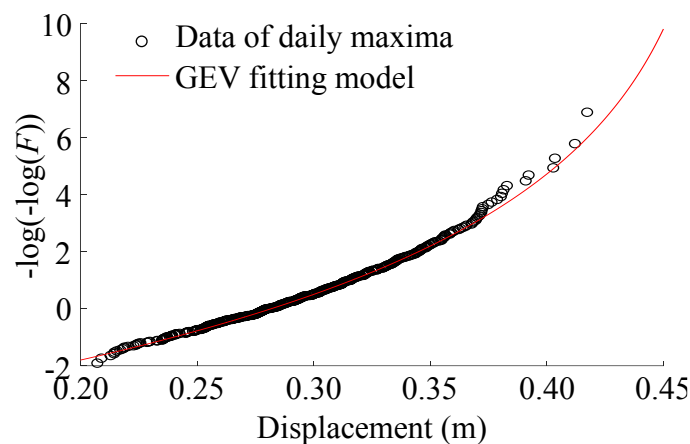


Fig. 6 – GEV fitting on daily maxima of girder displacement in the middle of the central span

Figure 6 shows GEV fitting on daily maxima of girder displacement in the middle of the central span. Totally 480 daily maxima are plotted in the probability paper. The fitting GEV model is estimated through maximum likelihood algorithm, and the shape, scale, location parameters of the GEV model are -0.1922, 0.0381 and 0.2822 respectively. It is known from Figure 6 that GEV could well describe the data. Based on the GEV distribution, characteristic value of any reference period could be easily obtained.

In-service condition assessment

The calculated displacements through deterministic traffic load model in D60 are 457 mm and 268 mm for the quarter and middle positions of the central span.

The specified level of traffic load in the design code is 95% quantile assurance in the design life of 100 y. Therefore, the characteristic value of displacement from monitoring should be in consistent with that design level regarding remaining life. Table 2 shows the extrapolated characteristic values of traffic load effects through GEV modelling under various remaining lives with 95% quantile assurance, and they are compared with the design level to assess bridge in-service condition.

Table 2 shows the changing of girder displacements in the quarter and middle positions of the central span. With the increase of the remaining lives, characteristic traffic load effects increase but the increasing tendency tends to be gentle. This tail tendency is consistent with the results of GEV fitting in Figure 6, where the tail curves upward, indicating the change of deflection prediction in remaining lives is small. Note that the predicted characteristic displacement is highly related with the variation of traffic loads on the bridge. If traffic loads on the bridge are incorporated with high randomness, then the change of future displacement prediction will be large. Based on the results, it can be revealed the traffic loads on the bridge are less randomness.

The characteristic values of displacements induced by traffic loading within 10 y are all lower than the calculated values from the design code. While, realistic traffic load effects of the bridge beyond 10 y are greater than those of the design code. Since displacement represents bridge in-service condition, the results indicate the bridge is in good condition within 10 y. However, the displacement of the bridge may exceed the design level when the evaluation period is greater than 10 y, and the good in-service condition could not be ensured. Therefore, management of traffic loads and maintenance of bridge components should be enhanced after the bridge further been in service for ten years.

Tab. 2 - Comparison of extrapolated traffic load effects and calculation results from design code under various remaining lives

| Remaining life | Displacement in the middle of the central span /mm | | Displacement in the quarter position of the central span /mm | |
|----------------|--|--------------|--|--------------|
| | Extrapolated value | Design value | Extrapolated value | Design value |
| 5 y | 452 | | 261 | |
| 10 y | 457 | | 267 | |
| 20 y | 460 | 457 | 271 | 268 |
| 50 y | 463 | | 275 | |
| 80 y | 464 | | 277 | |

CONCLUSION

The assessment of girder displacement under traffic loading in remaining life provides knowledge on bridge in-service condition. Based on monitoring data of displacement from the health monitoring system, the time-history of displacements induced only by traffic loading is obtained. Characteristic traffic load effects under various remaining lives are extrapolated and quantitatively analysed, to assess bridge in-service condition. The major conclusions are as follows:

- (1) Moving average method and window smoothing method could extract load effects induced by traffic based on monitored data from those produced by wind, temperature, and environmental noise. The extracted traffic load effects provide the basis for the operational analysis of vehicle load on bridges.
- (2) Based on extracted displacement induced by traffic loading, daily maxima based GEV extrapolation could be utilized to build the limit distribution of any return period.
- (3) According to the monitoring displacement of the studied bridge over 16 months, the extreme value prediction of girder displacement caused by traffic loading shows the realistic values are larger than the design level after being in service for another decade. Therefore, it is necessary

to enhance the management of traffic loads and maintenance of bridge components to ensure the bridge in-service condition.

ACKNOWLEDGEMENTS

This work was supported by Shandong Provincial Natural Science Foundation, China [grant number ZR2018PEE019]; Scientific Research Foundation of Shandong University of Science and Technology for Recruited Talents, China [grant number 2016RCJJ040]

REFERENCES

- [1] Hallenbeck ME, Weinblatt H. Equipment for collecting traffic load data. Transportation Research Board, 2004.
- [2] Lydon M, Taylor S E, Robinson D, et al. Recent developments in bridge weigh in motion (B-WIM). *Journal of Civil Structural Health Monitoring*, 2016, 6(1): 69-81.
- [3] Ruan X, Zhou J, Shi X, et al. A site-specific traffic load model for long-span multi-pylon cable-stayed bridges. *Structure and Infrastructure Engineering*, 2017, 13(4): 494-504.
- [4] Yuan Y, Han W, Huang P, et al. Structure safety assessment under heavy traffic based on weigh in motion and simulation analysis. *Advances in Structural Engineering*, 2017, 20(12): 1864-1878.
- [5] Ji B, Chen D, Ma L, et al. Research on stress spectrum of steel decks in suspension bridge considering measured traffic flow. *Journal of Performance of Constructed Facilities*, 2011, 26(1): 65-75.
- [6] Getachew A, O'Brien EJ. Simplified site-specific traffic load models for bridge assessment. *Structure and Infrastructure Engineering*, 2007, 3(4): 303-311.
- [7] Ruan X, Zhou J, Tu H, Jin Z, Shi X. An improved cellular automaton with axis information for microscopic traffic simulation. *Transportation Research Part C: Emerging Technologies*, 2017, 78: 63-77.
- [8] O'Brien EJ, Hayrapetova A, Walsh C. The use of micro-simulation for congested traffic load modeling of medium-and long-span bridges. *Structure and Infrastructure Engineering*, 2012, 8(3): 269-276.
- [9] Liu X, Huang Q, Ren Y, et al. Extraction of cable forces due to dead load in cable-stayed bridges under random vehicle loads. *Journal of Southeast University (English Edition)*, 2015, 31(3): 407-411.
- [10] Xia J, Zong Z, Yang Z, et al. Vehicle load model of large-span cable-stayed bridge based on GPS. *China Journal of Highway and Transport*, 2016, 29(1): 44-52. (In Chinese)
- [11] Brownjohn JMW, Moyo P, Omenzetter P, et al. Assessment of highway bridge upgrading by dynamic testing and finite-element model updating. *Journal of Bridge Engineering*, 2003, 8(3).
- [12] Jaishi B, Ren W X. Structural finite element model updating using ambient vibration test results. *Journal of Structural Engineering*, 2005, 131(4): 617-628.
- [13] Ministry of Communications and Transportation. General code for design of highway bridges and culverts JTG D60-2015, 2015, Beijing (In Chinese: China Communications Press).
- [14] O'Brien E J, Schmidt F, Hajjalizadeh D, et al. A review of probabilistic methods of assessment of load effects in bridges. *Structural safety*, 2015, 53: 44-56.

OPTIMIZATION OF RECLAIMED ASPHALT AND FT PARAFFIN FOR PERMANENT DEFORMATION AND MOISTURE DAMAGE OF ASPHALT MIXES

Fazal Haq¹, Arshad Hussain² and Muhammad Bilal Khurshid³

1. Post Graduate Student & Research Assistant (Corresponding Author), National Institute of Transportation, SCEE, NUST Campus H- 12, Islamabad, Pakistan
l;fhaq.tn15@nit.nust.edu.pk
2. Assistant Professor, National Institute of Transportation, SCEE, NUST Campus H-12, Islamabad, Pakistan; drarshad@nit.nust.edu.pk
3. Associate Professor, National Institute of Transportation, SCEE, NUST Campus H-12, Islamabad, Pakistan; bilal-nit@nust.edu.pk

ABSTRACT

Recycling of Reclaimed Asphalt Pavement (RAP) provides us the need to save valuable aggregate and the help of which the use of expensive bituminous binder will be reduced as well. In this study we have considered one WMA additive (Sasobit). The rut resistance of mixes was improved by adding either RAP or Sasobit or both as compared to control asphalt mixes. For lower contents of RAP i.e. up to 15 %, highest rut resistances was observed at 2 % Sasobit addition, and for higher content of RAP highest rut resistance was observed at 3 % Sasobit addition. On the other hand, increasing RAP and Sasobit content increased the moisture susceptibility of mixes, so best recommended combination is to use 30-40 % RAP in addition of 3 % Sasobit as far as permanent deformation and moisture susceptibility criteria are concerned.

KEYWORDS

HMA, WMA, Sasobit, Permanent deformation, Rutting, Moisture damage

INTRODUCTION

The increasing plea on our thoroughfares over the past couple of decade's results in a decrease of budgetary funds and to offer a cost effective, safe and efficient system of roads has steered to intense growth in the need to rehabilitate our present roadways.

Moreover, historical data revealed that the RAP mixes could have similar performance as virgin HMA mixtures, when accurately designed and constructed [1]. Many innovative products and procedures are available having proficiency of dropping the mixing temperature of HMA without negotiating the concert and harmony of the pavement. About 40 % reductions in mixing and compaction temperatures are possible by using these products. With the lower operating temperature another aided benefit is that it will reduce the oxidative hardening of the binder and this will help in increased performance of the pavement, such as averting the mix from being tender when placed, reduced block cracking and thermal cracking [2].

FT waxes is a long-chain hydrocarbon (aliphatic poly-methylene), fine crystalline, formed from the gasification of natural gas or coal feed stocks by the Fischer-Tropsch (FT) synthesis (in which partial oxidation of methane to carbon monoxide (CO) takes place, and later on reacting with hydrogen (H) manufacturing a combination of hydrocarbons under catalytic conditions. The carbon chain length in Sasobit ranges from plus C₅ to C₁₀₀ carbon atoms.

Sasobit is an “asphalt flow improver” with melting point of 102 °C and because of this reason Sasobit is perfectly soluble in bitumen at a temperature higher than 120 °C. At a down temperature it forms a crystalline grid structure in the binder that leads to additional permanency [3].

The range for Sasobit use is 0.8 % to 3 % by mass of binder. In marketable applications in Asia, Europe, the United States and South Africa Sasobit has been mixed straight with aggregate mix as melted liquid through a dosing meter or solid prills (small pellets). Marshall tests executed on blends prepared in this way signposted no variance in flow or stability values as associated to premixing with the binder [4]. For the purpose of comparing with conventional HMA technology, we need to carry out an inclusive laboratory and field examination to explore permanent deformation and moisture damage of WMA technology. The temperature regimes at which WMA are produced will help to distinguish it from other asphalt mixtures and then by comparing the strength and durability of final product [5]. There are extensive conclusions for WMA additives. Info obtained from industrialists and materials traders specify that there is a possibility to reduce CO₂ emissions and energy consumption to about 30 % as compared to standard HMA [6]. A positive influence on pavement performance may be demonstrated by these technologies, as they allow reduced HMA mixing and compaction temperature [7]. Using Sasobit there is an opportunity of dropping the production temperatures by 18–54 °C [8]. By lowering the production temperature, we can extend the paving season as the capability to perform late/early-season paving will be enhanced. This is due to the asphalt mix preparation occurs at a reduced temperature, will not cool as quickly, thus allow a longer production time period [9].

Rutting is the accumulation of small amount of irrecoverable strain due to applied load on the pavement, also known as permanent deformation [9]. Rutting has become the major mode of flexible pavement failure because of increase in truck pressure in the last decades. Rutting is principally caused by the accumulation of permanent deformation in different layers and in different portion of layers in the pavement structure. There are two types of rutting: instability rutting, which is caused by weak asphalt layers and structural rutting, which is caused by weak subgrade [11]. It has been revealed that for the larger part of the lifetime of the pavement, shear deformation is considered to be the primary mechanism of rutting [10]. Using some of WMA products along with high content of RAP may badly affect the rutting potential, because of reduced stiffness due to lower production temperature [12]. Physical behaviour of HMA changes when RAP is added. RAP binder's increased stiffness is thought to be the reason for higher modulus of HMA. In the same way it also disturbs the mixture's low temperature cracking as well as its fatigue behaviour [1].

Moisture damage is the loss of strength and durability of asphalt mix affected by moisture. Moisture damage is caused due to the interaction of moisture with the adhesion between asphalt binder and aggregate, and thus during cyclic loading it becomes more susceptible to moisture. It means that asphalt mixture can result moisture damage because of reduced bond strength between the fine aggregate and the asphalt binder [10]. Moisture present in air voids adversely affects the durability and strength of asphalt mixes and causes moisture damage. Moisture damage can occur in two different types: cohesive failure and adhesive failure. Cohesive failure is the strength reduction of the binder due to moisture damage, while adhesive failure is in between the aggregate and binder [13]. Conventional measure of moisture susceptibility can be reinforced by the consideration of contact angle measurements and dynamic modulus results, which were proposed recently to be promising alternatives to assess moisture susceptibility of asphalt mixes [14]. According to Washington State Department of Transportation (2009), indirect tensile strength testing of asphalt is a very common and easy way to check the performance of asphalt, which aid in measuring the asphalt mix susceptibility to moisture. In Indirect tensile strength testing, we test conditioned and unconditioned samples, which provide a consistent crack potential indication. For producing WMA lower production temperatures are used and thus moisture susceptibility increases. Incomplete

drying of aggregate causes moisture damage of a mix as water remains confined in the aggregate skeleton [15].

PROPOSED METHODOLOGY

Selection and laboratory testing of materials

Materials used in this research had all the results within the specified limits as per American and British standards and the aggregate gradation with nominal maximum aggregate size of 19 mm was used as per Marshall Mix Design.

Properties of asphalt mix are greatly influenced by gradation, surface texture and shape of the aggregates, as higher shear strength is provided by aggregates which are rough-textured and angular as compared to rounded shaped aggregate with smooth-textured and almost 95 % of the mixture is composed of aggregate and remaining 5 % is the asphalt binder, so aggregate is the component that provides resistance to deformation and provide a strong stone skeleton. Asphalt content in RAP was determined using Ignition method in accordance with ASTM D 6307 – 98 and it was found that 4.46 % of the total re-graded mass of RAP was aged-binder. While using Abson method in accordance with ASTM D1856 – 09, to extract aged bitumen from RAP for testing.

The selected aggregate gradation is shown in Table 1 and Figure 1 shows aggregate gradation which is plotted with percentage passing versus sieve sizes.

Tab. 1- NHA Class-B Gradation Selected for Testing

| S. NO | Sieve Size (mm) | NHA Specification Range (% Passing) | Our Selection | Retained (%) |
|-------|-----------------|-------------------------------------|---------------|--------------|
| 1 | 19 | 100 | 100 | 0.00 |
| 2 | 12.5 | 75-90 | 82.5 | 17.50 |
| 3 | 9.5 | 60-80 | 70 | 12.50 |
| 4 | 4.75 | 40-60 | 50 | 20.00 |
| 5 | 2.38 | 20-40 | 30 | 20.00 |
| 6 | 1.18 | 5-15 | 10.00 | 20.00 |
| 7 | 0.075 | 3-8 | 5.5 | 4.50 |
| 8 | Pan | ... | ... | 5.50 |

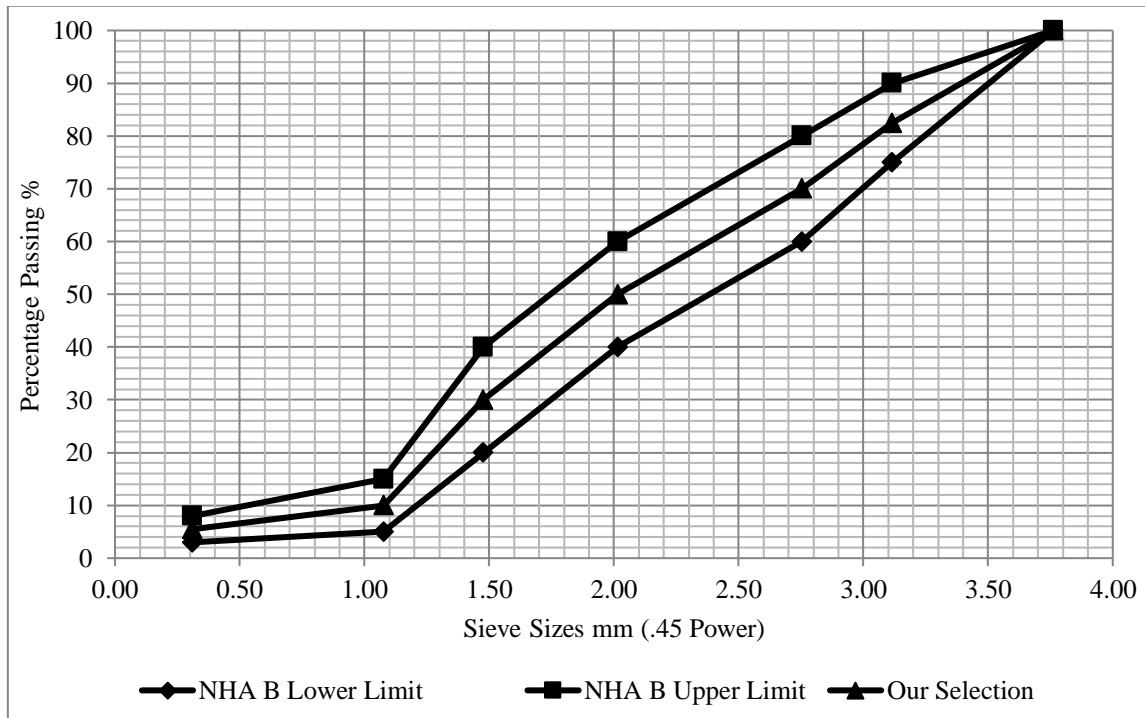


Fig. 1 – Class-B Gradation plot with NHA Specified limit

The amount of RAP was varied by content of 0 %, 15 %, 25 %, 35 % and 50 % in asphalt mix. Stability, flow values and volumetric were calculated using Marshall mix design procedure. Therefore, five different RAP contents and corresponding aggregate on different sieves were found which are shown in Table 2 and Table 3 while Figure 2 shows gradation which is plotted with percentage passing verses sieve sizes for mentioned percentages of RAP.

Tab. 2 - RAP gradation

| Sieve Dia (mm) | RAP (% Retained) |
|----------------|------------------|
| 19 | 0.00% |
| 12.5 | 7.02% |
| 9.5 | 11.15% |
| 4.75 | 20% |
| 2.38 | 18% |
| 1.18 | 31% |
| 0.075 | 10.25% |
| Pan | 2.70% |

Tab. 3 - Weight of Aggregate as per Gradation

| Sieve (mm) | % Passing | | | | | | |
|------------|-------------------|-------------------|---------------|----------|----------|----------|----------|
| | NHA B Lower Limit | NHA B Upper Limit | Our Selection | 15 % RAP | 25 % RAP | 35 % RAP | 50 % RAP |
| 19 | 100 | 100 | 100 | 100 | 100 | 100 | 100 |
| 12.5 | 75 | 90 | 82.5 | 85.2 | 85.9 | 86.5 | 87.3 |
| 9.5 | 60 | 80 | 70.0 | 69.0 | 69.7 | 70.1 | 70.7 |
| 4.75 | 40 | 60 | 50.0 | 50.2 | 50.8 | 51.0 | 51.4 |
| 2.38 | 20 | 40 | 30.0 | 32.5 | 33.7 | 34.5 | 35.3 |
| 1.18 | 5 | 15 | 10.0 | 10.9 | 12.8 | 13.6 | 14 |
| 0.075 | 3 | 8 | 5.5 | 5.0 | 5.3 | 5.5 | 6.3 |

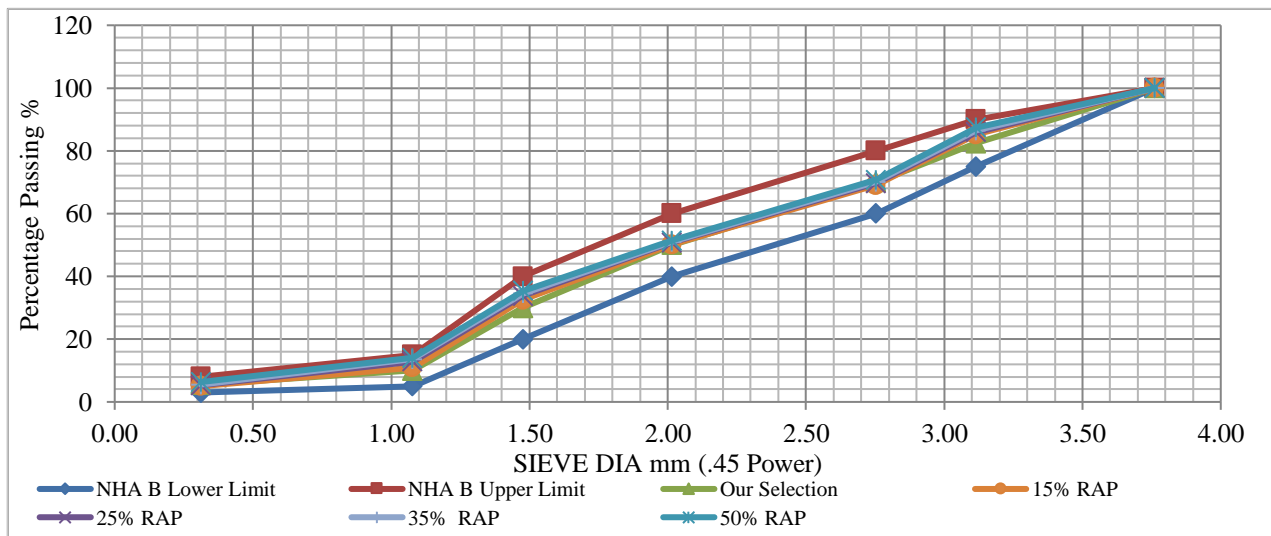


Fig. 2 – Gradation plot of RAP Percentages with Specified limit of NHA Class B

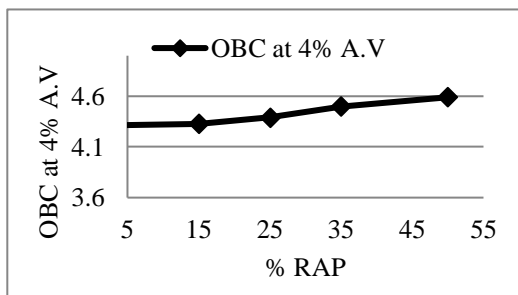
Optimum Bitumen Content determination

After the process of sieve analysis, aggregates were placed in oven to make it dry at a temperature of 105 °C to 110 °C. The amount of aggregates needed for the preparation of Marshall compacted specimen of 101.6 mm diameter, by Marshall Mix design method (ASTM D6926), should be approximately 1200g. As there were five types of gradations with respect to percentage of RAP i.e. 0 %, 15 %, 25 %, 35 %, and 50 %. Specimens were prepared at five different binder contents of 3.5, 4.0, 4.5, 5.0 and 5.5 %. The amount of asphalt cement added to each specimen was taken as the percentage of total weight of the mix. The reason of five trial blend was to select an asphalt mix that performs optimal at minimum bitumen content reaching voids of 4 %. The volumetric properties, stability and flow were measured and verified in light of Marshall Mix design criterion by revising the Marshall Mix design procedure thrice for each mix, thus fifteen specimens for each mentioned percentage of RAP were prepared for optimum binder content (OBC) determination and thus a total of 75 specimens were prepared for determination of five OBCs, based on varying

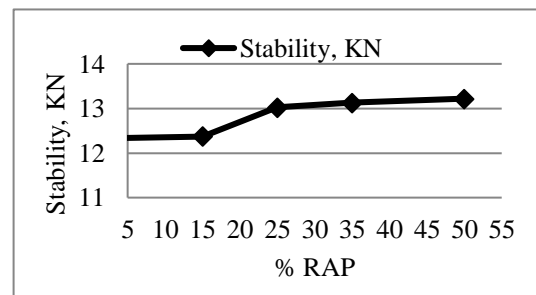
percentage of RAP. Separate graphical plots for all values were drawn as tabulated in Table 4 and shown in Figure 3 (a, b, c, d, e, and f).

Tab. 4 - Volumetric for Different Percentages of RAP

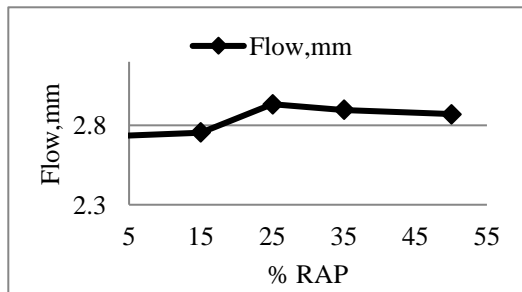
| (%) RAP | OBC at 4 % Air Voids | VMA, (%) | VFA, (%) | Stability, (KN) | Flow, (mm) | Unit Weight, (mg/cm ³) |
|---------|----------------------|----------|----------|-----------------|------------|------------------------------------|
| 0 | 4.31 | 13.49 | 70.04 | 12.32 | 2.72 | 2.37 |
| 15 | 4.33 | 13.56 | 70.19 | 12.37 | 2.75 | 2.37 |
| 25 | 4.39 | 13.96 | 71.10 | 13.02 | 2.93 | 2.36 |
| 35 | 4.5 | 13.66 | 70.7 | 13.12 | 2.89 | 2.37 |
| 50 | 4.59 | 13.79 | 71.07 | 13.22 | 2.87 | 2.37 |



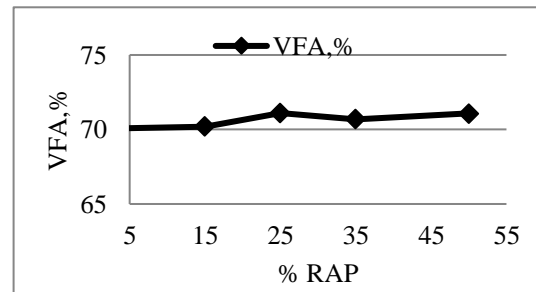
(a)



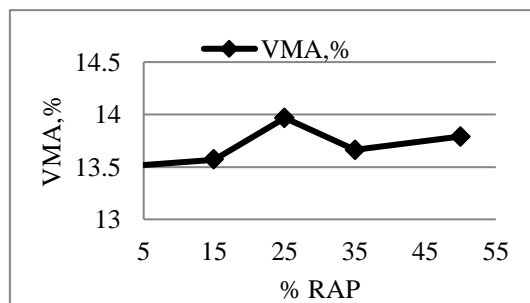
(b)



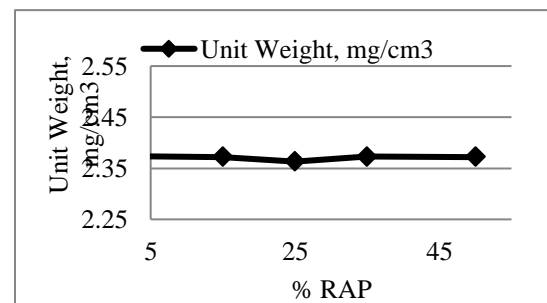
(c)



(d)



(e)



(f)

Fig. 3 – (a, b, c, d, e & f) – Plots between RAP percentages Vs Volumetric

Sample preparation for performance tests

Sasobit utilized in the study was in the form of prills as shown in Figure 4, and was imported through an authorized product distributor. In this study Sasobit was pre-blended with the binder in appropriate amount; samples were prepared with 0 %, 1 %, 2 % and 3 % Sasobit of OBC. Thus based on five percentages of RAP and with further addition of Sasobit percentages to each of the RAP percentage there were total of twenty mixes.



Fig. 4 – Sasobit Prills

Superpave mix design procedure was used to prepare specimens for performance testing. After sieving, similar to Marshal mix design, the aggregates were heated to a temperature of 105 °C to 110 °C. Mixing temperature of (160±5 °C) and compaction temperature of 135 °C was used for HMA, while using (125±5 °C) and 100°C as mixing and compaction temperature for WMA respectively, as obtained from the viscosity plots of binders through RV test at 135 °C and 160 °C and also 93 °C to 135 °C is the general used manufacturing temperature range for WMA. The required quantity of aggregate for preparing 152.4 mm diameter gyratory compacted specimens was 5000 g. Before compaction, conditioning of loose mix for short term aging was carried out for 2 hours at compaction temperature. Samples were prepared as per Superpave Mix Design method. Further, resizing of asphalt samples for testing were carried out by utilizing saw cutter and core cutter, to obtain standard sample of 38.1 mm height and 152.4 mm diameter for wheel tracker test and 63±2.5 mm height and 101.6 mm diameter for moisture damage testing through UTM as shown in Figure 5 and 6 respectively.



Fig. 5 – HWT Tested Sample

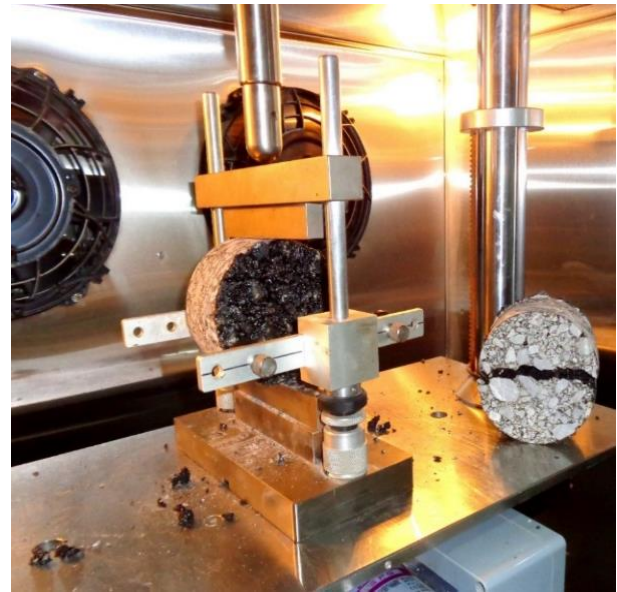


Fig. 6 – UTM Tested Sample

Permanent deformation (Wheel tracking test results)

Wheel tracking tests were conducted on specimens prepared for rutting under wet condition. For wheel tracking test a total of sixty samples were prepared for the twenty mixes. All the controlled specimens showed good resistance to rutting, whereas the specimens with 0 % and 15 % RAP shows higher resistance to rutting at 2 % Sasobit addition and at 3 % Sasobit addition these samples have less rut resistance than that of samples having 2 % Sasobit. But samples with higher contents of RAP that is 25 %, 35 % and 50 % showed higher rut resistance at 3% Sasobit. All of the specimens passed the wheel tracking test criteria of 12.5 mm rut depth at a temperature of 45 °C, which is the required testing temperature for bitumen of 58 grades (ARL 60/70) used in the study, while the numbers of passes were fixed to ten thousand which is the required criteria for rutting. The wheel tracking tests results are tabulated in Table 5 and graphically presented in Figure 7.

Moisture Damage (ITS Test Results)

Moisture susceptibility testing was carried out on asphalt mixtures according to ALDOT. For the twenty different mixes a total of 120 gyratory samples at 4 % air voids were prepared and tested for Indirect Tensile Strength (ITS). Thus six samples per mix were prepared, three of them were tested unconditioned by only placing in water at a temperature of 25 °C for one hour right before testing, while the other three specimens per mix were soaked in warm water at a temperature of 60 °C for 24 hours followed by placing in water at 25 °C for one hour before being tested for Indirect Tensile Strength. The raw wet (conditioned) and dry (unconditioned) strength values for the 20 mixtures are shown in Figure 8 while the tensile strength ratios are shown in Figure 9. From the results it is clear that as we increase the RAP percentage the strength of the asphalt mixes increases.

Tab. 8 - HWTD & ITS Tests Results

| Specification | Codes | Average RUT Depth (mm) | S1, (kPa) | S2, (kPa) | TSR=S2/S1 |
|---------------------|-------|------------------------|-----------|-----------|-----------|
| 0% RAP, 0% SASOBIT | R0S0 | 4.455 | 777.85 | 777.5 | 99.96 |
| 0% RAP, 1% SASOBIT | R0S1 | 4.410 | 779.35 | 777.35 | 99.74 |
| 0% RAP, 2% SASOBIT | R0S2 | 4.383 | 780.2 | 776.3 | 99.50 |
| 0% RAP, 3% SASOBIT | R0S3 | 4.420 | 781.3 | 774.15 | 99.08 |
| 15% RAP, 0% SASOBIT | R15S0 | 3.690 | 783.05 | 770.55 | 98.40 |
| 15% RAP, 1% SASOBIT | R15S1 | 3.545 | 785.15 | 768.7 | 97.90 |
| 15% RAP, 2% SASOBIT | R15S2 | 2.855 | 787.9 | 767.2 | 97.37 |
| 15% RAP, 3% SASOBIT | R15S3 | 2.965 | 789.25 | 766.45 | 97.11 |
| 25% RAP, 0% SASOBIT | R25S0 | 2.820 | 791.8 | 764.7 | 96.58 |
| 25% RAP, 1% SASOBIT | R25S1 | 2.680 | 794.15 | 763.65 | 96.16 |
| 25% RAP, 2% SASOBIT | R25S2 | 2.615 | 796.75 | 763.3 | 95.80 |
| 25% RAP, 3% SASOBIT | R25S3 | 2.405 | 802.45 | 761.7 | 94.92 |
| 35% RAP, 0% SASOBIT | R35S0 | 2.130 | 806.85 | 759.1 | 94.08 |
| 35% RAP, 1% SASOBIT | R35S1 | 1.940 | 817.2 | 757.35 | 92.68 |
| 35% RAP, 2% SASOBIT | R35S2 | 1.845 | 820.75 | 748.4 | 91.18 |
| 35% RAP, 3% SASOBIT | R35S3 | 1.655 | 828.2 | 739.15 | 89.25 |
| 50% RAP, 0% SASOBIT | R50S0 | 1.530 | 835.1 | 730.85 | 87.52 |
| 50% RAP, 1% SASOBIT | R50S1 | 1.410 | 842.3 | 715.6 | 84.96 |
| 50% RAP, 2% SASOBIT | R50S2 | 1.060 | 858.7 | 710.3 | 82.72 |
| 50% RAP, 3% SASOBIT | R50S3 | 0.850 | 877.6 | 692.45 | 78.90 |

S1 = Average Strength of Un- Conditioned samples, S2 = Average Strength of Conditioned samples

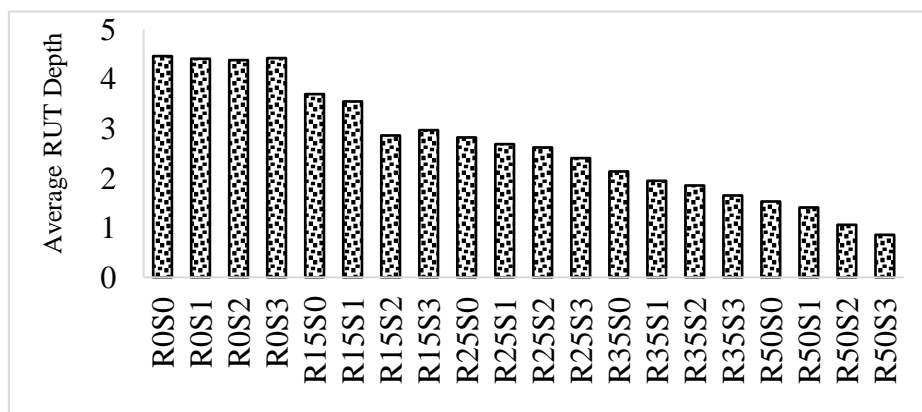


Fig. 7 – Average Rut depth from HWTD testing

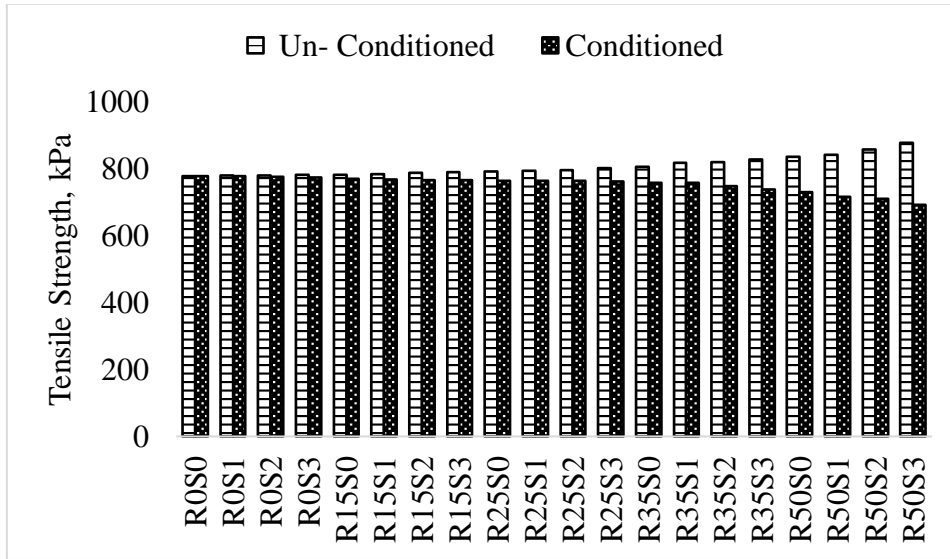


Fig.8 – Tensile Strength of different mixes

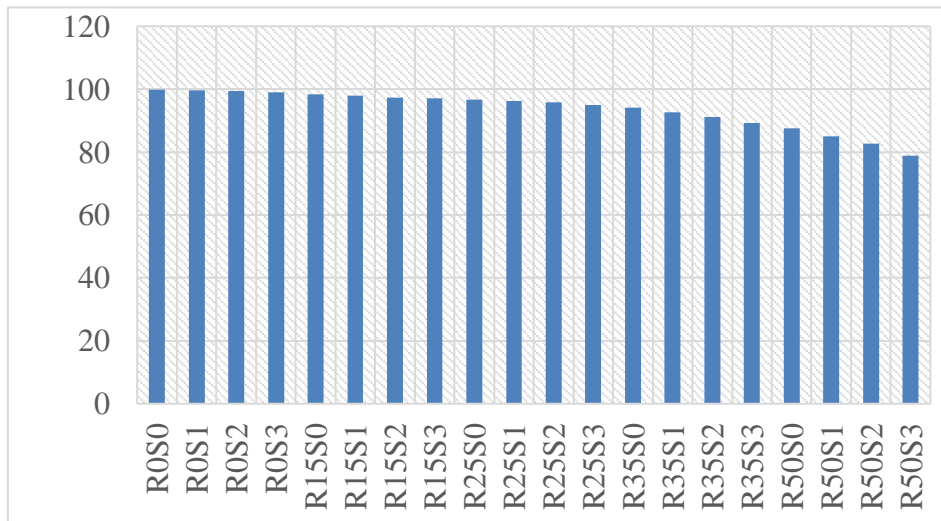


Fig. 9 – Average TSR for different mixes

The minimum tensile strength ratio specified by Superpave for mixes having no anti-stripping agent is 80 %. The calculated tensile strength ratios for the 20 mixes were all above 80 percent, except for the mix having 3 % Sasobit and 50 % RAP which was 78.9 %. Also, the ITS values show that all the conditioned samples give strength value lower than that of unconditioned samples, showing that, Sasobit increases the moisture susceptibility of an asphalt mix. Figure 10 shows Gyrotary Samples Before and After Testing.

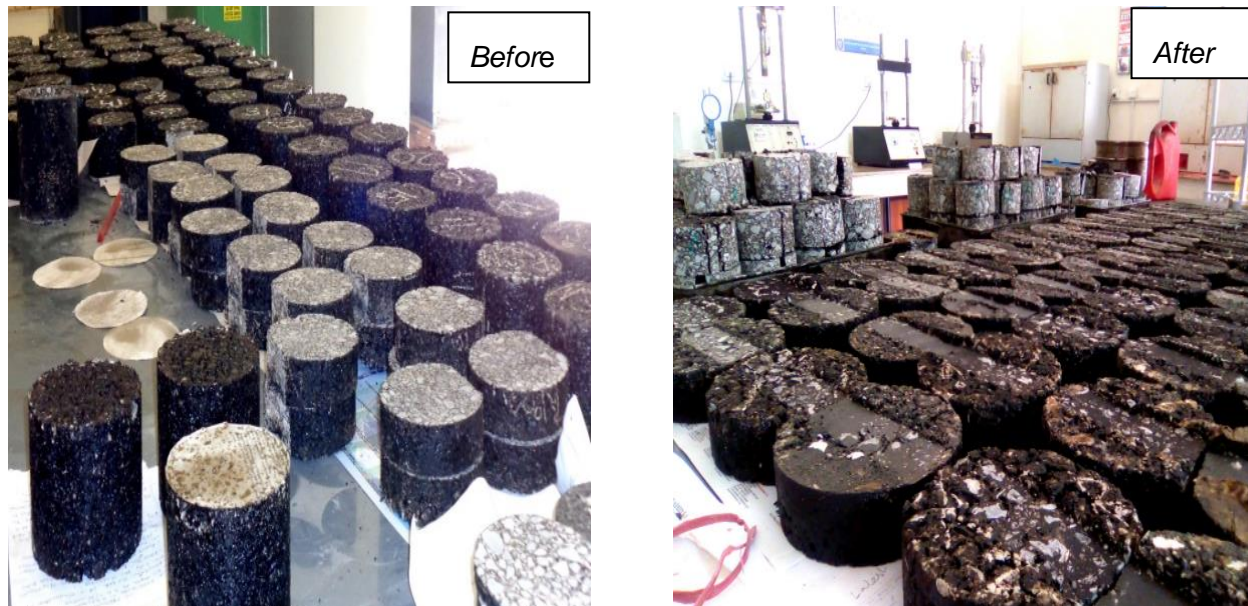


Fig. 10 – Gyratory Samples Before and After Testing

CONCLUSIONS

The conclusions drawn from laboratory tests are listed as follows:

- Resistance of HMA to rutting containing RAP increases by increasing RAP content.
- Rut resistance of controlled asphalt mixes and asphalt mixes containing RAP increases by increasing Sasobit content as compared to controlled mixes and mixes containing RAP only. The increase in rut resistance is due to decreased production temperature and this may be associated more to the reduced binder aging.
- Asphalt mixes having low contents of RAP i.e. up to 15 % give best rut resistance at 2 % Sasobit addition and then decreases unlike for mixes with higher contents of RAP i.e. above 15 % for which rut resistance increases linearly up to 3 % Sasobit. The decreased in rut resistance may be due to increased workability and viscosity.
- The indirect tensile strength for mixes with either Sasobit alone or both Sasobit and RAP were slightly higher as compared to the control mixes, which may be the reason that sasobit form lattice structure.
- The indirect tensile strength for mixes with Sasobit plus RAP was slightly higher, as compared to mix containing RAP only.
- The resistance against moisture damage of asphalt mixes containing RAP or Sasobit or both is lower than control specimens, which is the reason of reduced mixing and compaction temperatures and moisture damage increases due to incomplete drying of aggregate in the resultant asphalt mix using WMA technology. The moisture damage may be due to water trapped in the coated aggregate.
- For any percentage of RAP and Sasobit the values of tensile strength ratio are above the minimum range of 80 % except for 50 % RAP and 3 % Sasobit which is 78.90 %. While for the mix with 3 % sasobit and 35 % RAP the tensile strength ratio is 82.72 % which is close to the lower limit as well.

- As far as rutting resistance and moisture susceptibility is concerned to be the most prevalent forms of asphalt concrete distresses in our region and also in most of developing countries with no control on wheel axle loads, the recommended contents are 3 % Sasobit and 30-40 % RAP for adequate resistance to rutting and moisture damage. Further it is recommended that it is a better option to use 2 % sasobit with control mixes and mixes containing lower percentages of RAP i.e. up to 15 %, while for higher percentages of RAP better option is to use 3 % Sasobit.

Conflict of Interest Statement

The authors of this research paper, whose names are listed on title page, certify that they have conducted this research as a part of project financially supported by Pakistan Higher Education Commission with the title Characterization of Reclaimed Asphalt Pavement (RAP) for use in pavement construction industry in Pakistan.

Acknowledgement and Disclaimer

The researchers appreciatively recognize the support of Pakistan Higher Education Commission for sponsoring this research project under National Research Program for Universities (NRPU) with award No.20-45%/R&D/HEC/14/1067. This is only a technical article for experimental investigation along with optimization of RAP and Sasobit for permanent deformation and moisture damage of asphalt mixes. The mixture durability (moisture susceptibility) was measured by the Universal Testing Machine (UTM) performing Indirect Tensile Strength (ITS) test and permanent deformation (Rutting) by Hamburg Wheel Tracking device (HWTD). This research study does not establish a standard, specification, or a regulation.

REFERENCES

- [1] Al-Qadi I.L., Aurangzeb Q. and Carpenter, S.H., (2012), "Impact of High RAP Content on Structural and performance Properties of Asphalt Mixtures", Research Report FHWA-ICT-12-002, Illinois Center for Transportation.
- [2] Hurley, G.C. and Prowell, B. D. (2006b) "Evaluation of Evotherm for Use in Warm Mix Asphalt," Report NCAT 06-02, National Center for Asphalt Technology, Auburn University, Auburn, Alabama.
- [3] Abraham, E. (2014). Effects of Aggregate and Mixture Properties on the Rutting Performance of HMA Wearing Course (A Case Study on the Gohatsion-Dejen Trunk Road Segment) (Doctoral dissertation, AAU).
- [4] Hurley, G. C., & Prowell, B. D. (2005). Evaluation of Aspha-Min zeolite for use in warm mix asphalt. NCAT report, 5(04).
- [5] MAHA, I., SUBAGIO, B. S., EFFENDHI, F., & RAHMAN, H. (2015). Performance of Warm Mix Asphalt Concrete Binder Course (AC-BC) With Reclaimed Asphalt Pavement. Journal of the Eastern Asia Society for Transportation Studies, 11(0), 1745-1753.
- [6] McCormack, S. M., Sturgill, R. E., Howell, B., Van Dyke, C. W., & Kreis, D. (2014). Green Infrastructure.
- [7] Rossi, D., Filippi, S., Merusi, F., Giuliani, F., & Polacco, G. (2013). Internal structure of bitumen/polymer/wax ternary mixtures for warm mix asphalts. Journal of Applied Polymer Science, 129(6), 3341-3354.
- [8] Capitão, S. D., Picado-Santos, L. G., & Martinho, F. (2012). Pavement engineering materials: Review on the use of warm-mix asphalt. Construction and Building Materials, 36, 1016-1024.
- [9] Chowdhury, A., & Button, J. W. (2008). A review of warm mix asphalt (No. SWUTC/08/473700-00080-1). Texas Transportation Institute, the Texas A & M University System.

- [10] Ahmed, T. A. H. (2014). Investigating the rutting and moisture sensitivity of warm mix asphalt with varying contents of recycled asphalt pavement.
- [11] Hussain, S. (2012). Determining the Contribution of Different Structural Layers of Asphalt Pavement to Rutting using Transverse Profile Analysis. MS Thesis, National University of Sciences and Technology, Pakistan.
- [12] Mogawer, W., Austerman, A., Kluttz, R., & Roussel, M. (2012). High-Performance Thin-Lift Overlays with High Reclaimed Asphalt Pavement Content and Warm-Mix Asphalt Technology: Performance and Workability Characteristics. Transportation Research Record: Journal of the Transportation Research Board, (2293), 18-28.
- [13] O'Sullivan, K. A. (2009). The effects of warm mix asphalt additives on recycled asphalt pavement (Doctoral dissertation, WORCESTER POLYTECHNIC INSTITUTE).
- [14] Zhao, S., Huang, B., Shu, X., & Woods, M. (2013). Comparative evaluation of warm mix asphalt containing high percentages of reclaimed asphalt pavement. Construction and Building Materials, 44, 92-100.
- [15] Washington State Department of Transportation. (2009). 5.6 HMA Mix Design - Testing. Retrieved January 2009, from PTC Training Guides: http://training.ce.washington.edu/WSDOT/Modules/05_mix_design/05-6_body.htm